Transactions of the ASME

Transactions of the ASME, Journal of Fluids Engineering (ISSN 0098-2202) is published quarterly (Mar., June, Sept., Dec.) for $100 per year by The American Society of Mechanical Engineers, 345 East 47th Street, New York, NY 10017. Second class postage paid at New York, NY and additional mailing offices. POSTMASTER: Send address changes to Transactions of the ASME, Journal of Fluids Engineering, c/o THE AMERICAN SOCIETY OF MECHANICAL ENGINEERS, 22 Law Drive, Box 2300, Fairfield, NJ 07007-2300.
CHANGES OF ADDRESS must be received at Society headquarters seven weeks before they are to be effective. Please send old label and new address.
PRICES: To members, $29.00, annually; to nonmembers, $100. Add $15.00 for postage to countries outside the United States and Canada.
STATEMENT from By-Laws. The Society shall not be responsible for statements or opinions advanced in papers or . . . printed in its publications (B7.1, Par. 3).

INDEXED by Applied Mechanics Reviews and Engineering Information, Inc.

Journal of Fluids Engineering

Published Quarterly by The American Society of Mechanical Engineers

VOLUME 112 • NUMBER 1 • MARCH 1990

(Contents continued on page 39)

Contents (continued)

Journal of Fluids Engineering

Editorial

New Technical Editor

At the December 1989 Winter Annual Meeting in San Francisco, following nomination by the Fluids Engineering Division, the ASME Board on Communications approved a new Technical Editor for this Journal, to take office on July 1, 1990, for a term of five years.

He is *Demetri Pyrros Telionis*, Professor of Engineering Science and Mechanics, Virginia Polytechnic Institute and State University, Blacksburg, VA 24061. Dr. Telionis has served ably as Associate Editor of this Journal for three years and will undoubtably be an outstanding Technical Editor—only the third, after Bob Dean and myself, in the history of the Journal.

After graduating in 1964 from the National Technical University of Greece, Demetri Telionis served in the Greek Navy as a Technical Ensign Officer. He entered Cornell University in 1967 and received the Ph.D. degree in 1970. He then joined, and remains, on the faculty at VPI&SU, where he has received the Institute's Teaching Excellence Award and has participated with many graduate students in notable research projects and publications. He was one of the lead organizers for the First National Fluid Dynamics Congress in 1988 and, in 1987, received an ASEE Research Award for best paper. He is the author of the book *Unsteady Viscous Flow* (Springer-Verlag, 1981). Over the years he has had close contact with and has consulted for various industries.

Professor Telionis' research interests and publications span many subjects: unsteady flow separation, acoustic propagation in ducts, computational fluid dynamics, airfoil aerodynamics, convection heat transfer, three-dimensional boundary layers, vortex shedding, flow over delta wings, and tube-bundle vibrations. If there were 12 of him, they could do all the Journal's editorial work! Upon accepting the editorship, Prof. Telionis has some proposals for improving the quality, efficiency, and readership of the Journal—but I will let him tell you later in his own words.

The writer, first appointed Technical Editor in the fall of 1978, has thoroughly enjoyed his tenure with the Journal and with the ASME Transactions Board of Editors. The opportunity to work with so many fine Associate Editors, authors, and reviewers has been most educational. One hopes that the Journal quality was maintained in the spirit of the founding editor, Robert C. Dean. Of paramount importance to the Journal's success was the work of our Executive Secretary, (Mrs.) L.T. Brown, and the ASME Managing Editor, Cornelia Monahan. Without their expertise and continuous assistance, publication of the JOURNAL OF FLUIDS ENGINEERING would have been impossible during the writer's tenure.

Until June 1990, authors are requested to submit their papers as usual to my University of Rhode Island address. The June 1990 issue will then ask for new papers to be submitted to Prof. Telionis.

Frank M. White

Viscous Flow Analysis as a Design Tool for Hydraulic Turbine Components

T. C. Vu
Dominion Engineering Works,
GE Canada
Lachine, Québec, H8S 2S8 Canada

W. Shyy
University of Florida,
Department of Aerospace Engineering,
Mechanics and Engineering Science,
Gainesville, Fl. 32611

Viscous flow analysis based on the full Reynolds-averaged Navier-Stokes equations is being applied to successfully predict turbulent flow characteristics and energy losses in different hydraulic turbine components. It allows the designer to evaluate the hydraulic performance of alternative designs before proceeding with laboratory testing or to perform elaborate parametric study to optimize the hydraulic design. In this paper, the applications of three-dimensional viscous flow analysis as an analytical design tool for elbow draft tube and spiral casing are presented and their impact on engineering design assessed.

1 Introduction

Hydraulic turbines of the reaction type extract work from a fluid in a continuous manner by having it flow through a series of fixed and moving vanes. The flow, coming from the dam through the penstock, enters the casing which transforms the rectilinear flow into an inwardly swirling flow surrounding the turbine. Then it passes through a series of stay vanes and wicket gates which control the admission of water into the runner. At the runner, the potential energy of the water head is converted to mechanical energy (torque and speed). The flow then is decelerated in the draft tube, which recovers the kinetic energy leaving the runner as pressure potential energy [16]. As always, the energy conversion process is accompanied by some loss of energy. Hydraulic losses, which take place in all the hydraulic components of the turbine, come from different sources such as wall frictional loss, secondary flow, flow separation, profile drag, seal leakage, etc. The task of the hydraulic designer is to minimize all the above losses by judiciously choosing the dimensions and shapes of those hydraulic components. Traditionally, the design and development of hydraulic turbines has been based mostly on existing components and the performance assessment of the units has relied only on laboratory model testing. Recently, computation methods based on the first principles have been developed and applied to aid the design optimization of hydraulic turbine components [1, 2, 13]. For example, full three-dimensional finite element potential flow analysis has been used as a design tool for the runner and casing [1, 2]. However, potential flow analysis, assuming inviscid and irrotational flow inside the turbine components, cannot represent the complex behavior of truly turbulent viscous flows and cannot predict the associated energy losses.

Recently, intensive efforts have been devoted to developing a suitable numerical algorithm for computing general Navier-Stokes flows bounded by complex geometries [3, 4, 6, 7]. The flow analysis is based on the full Reynolds-averaged Navier-Stokes equations. The $k-\epsilon$ two equation turbulence model [8] has been utilized to analyze highly turbulent flow either in turbine models or in prototypes. The Navier-Stokes flow analyses have been applied to successfully predict flow characteristics and energy losses in different hydraulic turbine components [5, 9, 10, 11]. It is used regularly by our hydraulic designers to optimize distributor and draft tube geometries. Presently, further application of the Navier-Stokes flow analysis is being made for hydraulic turbine spiral cases. In this paper, the applications of the three-dimensional viscous flow analysis as an analytical design tool for elbow draft tubes and spiral casings are presented and their impact on engineering design assessed.

2 Numerical Algorithm and Boundary Conditions

The viscous flow analysis is based on the full Reynolds-averaged Navier-Stokes equations. The $k-\epsilon$ two equation turbulence model [8] is adopted here as closure form. The numerical formulation comprises a linearized, semi-implicit, conservative finite volume algorithm implemented in a general curvilinear coordinate system. No-slip conditions are applied to all the nodes at solid walls. At the nodal position next to the solid wall, the so-called wall function treatment [8] is used. At the inlet of the flow domain, the velocity profiles have to be specified. At the exit, zero value of the first order derivatives along the streamwise direction is adopted for all the dependent variables, except for the static pressure which does not require numerical boundary conditions due to the nature of the staggered grid system. This procedure has been studied in depth and found appropriate for the numerical procedure adopted here [14].

Contributed by the Fluids Engineering Division for publication in the JOURNAL OF FLUIDS ENGINEERING. Manuscript received by the Fluids Engineering Division January 24, 1989.

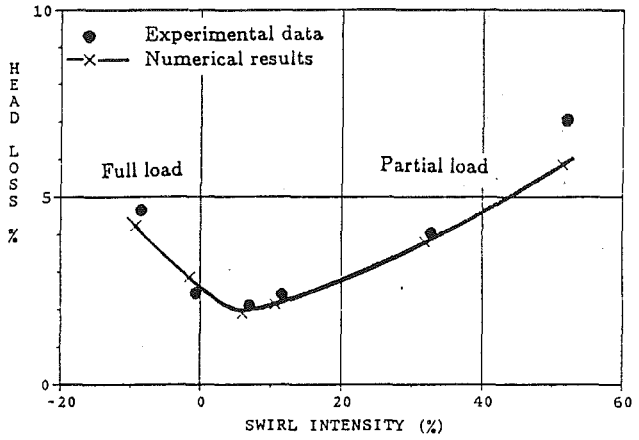

Fig. 1 Head losses in an elbow draft tube for different turbine operating conditions. Comparison between numerical results and experimental data.

Fig. 2(*a*) Francis runner exit flow characteristics at full load condition

Fig. 2(*b*) Francis runner exit flow characteristics at partial load condition

3 Viscous Flow Analysis for Elbow Draft Tubes

The role of the draft tube is to decelerate the velocity of the water leaving the turbine runner, thereby converting the excess kinetic energy of the outlet stream into a rise in static pressure [15]. The draft tube geometry consists essentially of a short conical diffuser followed by a 90 deg elbow of varying cross section and then a rectangular diffuser section. The shape of the cross section changes from being circular at the inlet end through elliptical within the elbow to rectangular at the exit. Also, the cross-sectional area of the draft tube mostly increases from inlet to outlet by a factor of 4 to 5.

The application of the flow analysis as a design tool can be made in different ways. The geometry of the draft tube could be optimized for a given draft tube inlet flow profile obtained from the runner exit flow conditions. On the other hand, for an existing draft tube geometry, the draft tube inlet flow profile could be optimized to achieve the best static pressure recovery factor. The influence of both the inlet flow profile and the geometrical design parameters on the draft tube pressure recovery factor is investigated. Typical grid size used for the draft tube flow analysis is $61 \times 19 \times 15$ which requires about 10 hours of CPU time on a VAX8600 or about 0.5 hour on a CRAY XMP. This grid size was found to yield satisfactory result after a series of grid independency test as reported in [11].

3.1 Influence of Inlet Flow Profile. The flow behavior and the static pressure recovery factor of the draft tube depend on the inlet flow conditions which are imposed by the turbine runner exit velocity profiles. As an example, flow analyses are performed to predict the head loss of an elbow draft tube at different operating conditions of a Francis turbine. The presence of a pier in the exit section is taken into account by reducing the draft tube width at that location a same amount as the pier thickness. A total of 6 pitot traverse measurements at the runner exit are used as inlet flow conditions for the draft tube flow analyses. It is noted that due to the use of the staggered grid system [3], there is no need to prescribe the static pressure distribution either at inlet or at outlet; only the velocity distribution at the inlet is needed to facilitate the computation. The comparison of the predicted total pressure losses or head losses with experimental data is shown in Fig. 1. The head loss is about 2 percent for optimal load, but it increases rapidly for off-design conditions. The numerical result agrees very well with laboratory measurements for the whole range of the runner operating conditions, except for very high swirl intensity at partial load where flow instability was observed during the test. The swirl intensity can be measured by the axial flux of swirl momentum divided by axial flux of axial momentum [16]. Figures 2(*a*) and 2(*b*) show direct photographic information of two different operating conditions, full load and partial load. In Fig. 2, the core flow is visible because it is a low pressure region that is cavitating. In the numerical computations, the flow is considered to be single phase with no account for cavitation. However, it is believed that based on the computed solution, flow pattern can be studied and compared to the experimental observation qualitatively to shed the light to the dynamic process under different loads.

Figure 3(*a*) illustrates a three-dimensional view of the draft tube flow characteristics at full load conditions. The velocity vectors are shown at the inlet and outlet sections. In Fig. 3(*c*), the top of the computational domain appears conical; this choice is taken to match the computational inlet with the locations of the measurement. All the solid lines starting at the center region of the inlet section and finishing at the outlet section represent the streaklines of the mean velocity flow field. The twisted streakline starting at the draft tube inlet center simulates correctly the straight rope observed at full load condition as shown in Fig. 2(*a*). The typical contra-rotating (opposite to the runner direction) free vortex flow at the draft tube inlet is shown in Fig. 3(*b*). The display of the velocity vectors in the main stream direction at the mid-section is represented in Fig. 3(*c*). The very weak velocity core, observed at the middle of the conical section, also indicates the presence of a rope at the center.

In Figs. 4(*a*) to 4(*c*) the draft tube flow behavior for optimal load condition is presented. Observation from velocity and streaklines indicates that no flow recirculation is occurring.

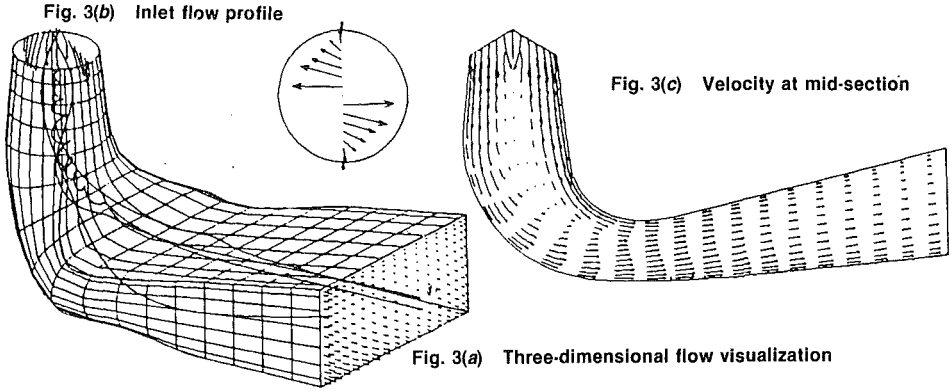

Fig. 3 Draft tube flow characteristics at full load condition

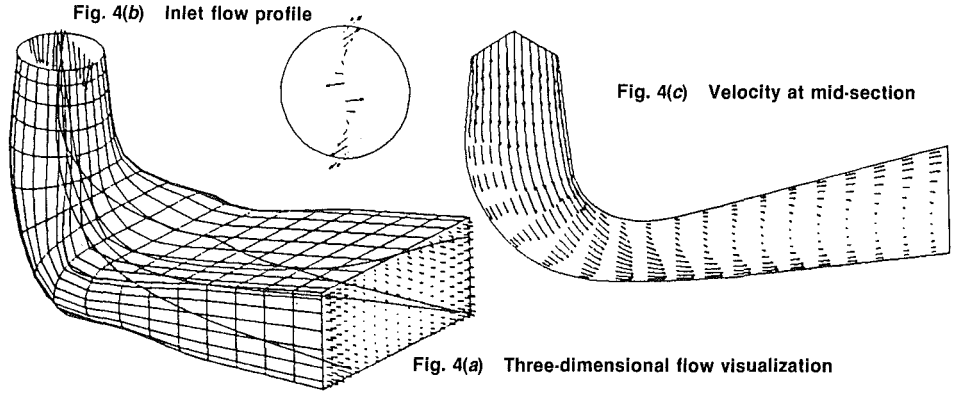

Fig. 4 Draft tube flow characteristics at optimal load condition

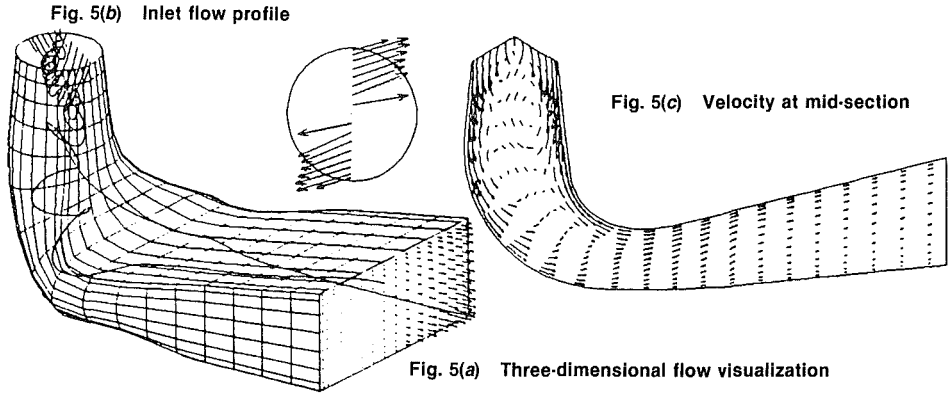

Fig. 5 Draft tube flow characteristics at partial load condition

Figure 4(*b*) represents the inlet flow profile of the optimal load condition. In this particular case, the inlet velocity profile is a combination of a co-rotative solid swirl and a small core of contra rotative free vortex swirl at the inlet center.

Figures 5(*a*) to 5(*c*) illustrate the draft tube behavior at partial load condition with a very high co-rotative swirl. The display of the velocity vectors in the main stream direction at the mid-section indicates that a large flow recirculation zone is taking place at the conical section. The twisted spiral streakline starting from the draft tube inlet center is very similar to the spiral rope observed in the Laboratory as shown in Fig. 2(*b*).

3.2 Influence of Geometrical Design Parameters. The geometry of an elbow draft tube can simply be defined by a series of cross sections connected from their center to the draft

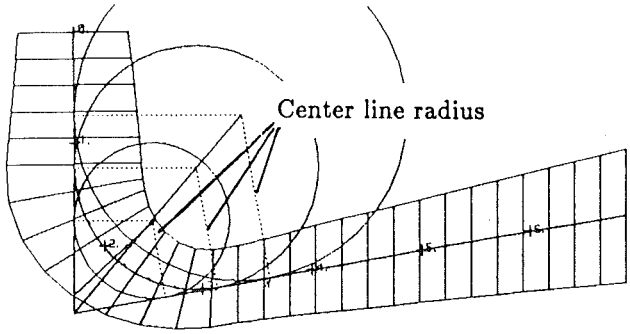

Fig. 6 Definition of elbow draft tube geometry by a series of cross sections connected to center line

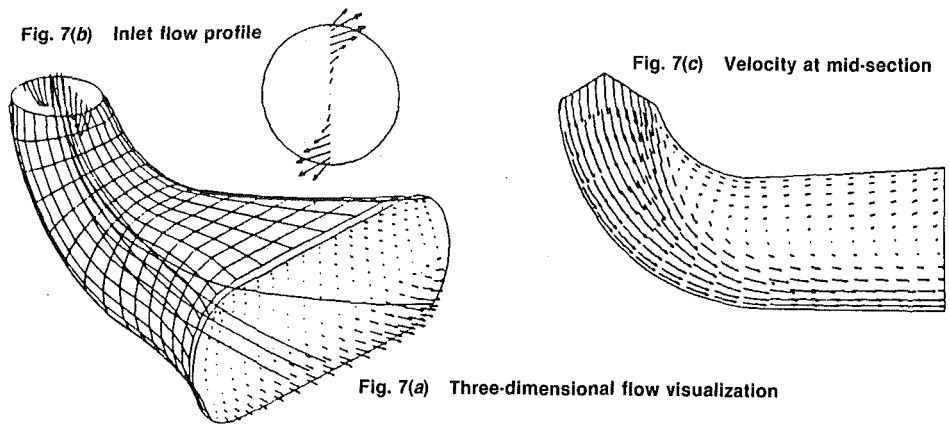

Fig. 7 Flow characteristics of a bad draft tube design at optimal load

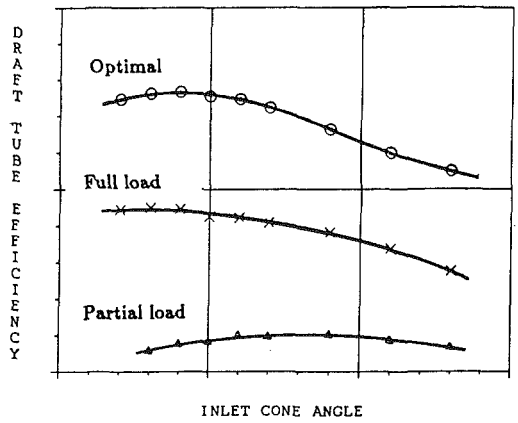

Fig. 8 Effect of inlet cone angle on draft tube efficiency

tube center line, as shown in Fig. 6. The variation of the cross-sectional area along the center line is defined by the commonly called diffusion curve. Also the variations of the shape and the aspect ratio of the cross section can be parameterized along the center line. The definition of the draft tube geometry by basic design parameters allows us to perform parametric studies in order to optimize the geometry. As an example, the effects of the inlet cone angle and the center line radius at the elbow section on the draft tube efficiency are presented here. The same elbow draft tube geometry used for the study of inlet flow profile is selected. The investigation is made for three different types of inlet flow profile corresponding to full load, optimal and partial load conditions, as shown in Figs. 3(*b*), 4(*b*), and 5(*b*). As demonstrated in the following, the present computational tool is being utilized to aid the design process through parametric variation.

• *Effect of Center-Line Radius.* The center line of the draft tube can be defined as a combination of a straight vertical line corresponding to the straight diffuser section, a circular arc for the elbow section and finally another straight line corresponding to the outlet section, as shown in Fig. 6. Flow analyses performed for different center line radii indicate that there is an optimal center line radius for each inlet flow profiles. A too large radius promotes early secondary flow in the elbow section which impairs the draft tube efficiency and a too small center line radius will provoke a large flow separation at downstream of the elbow section. Figures 7 show the flow behavior of a bad draft tube design which has a very large center line radius and no conical section at the inlet. Although a favorable solid swirl is specified at the inlet, a large flow recirculation zone occurs starting from the beginning of the elbow toward the outlet section.

• *Effect of Inlet Cone Angle.* Since the static pressure is recovered mostly in the straight vertical section of an elbow draft tube, it is important to select a correct inlet cone angle. Figure 8 shows the influence of the inlet cone angle on the draft tube efficiency for three different turbine operating conditions. The efficiency here is defined as the ratio of the actual draft tube pressure recovery factor and the theoretical pressure recovery factor. As shown, to obtain an optimal efficiency, a slightly smaller cone angle is required for full load condition compared to the cone angle required by optimal load. For higher inlet swirl condition such as at partial load, a much higher cone angle is required to obtain optimal draft tube efficiency.

4 Viscous Flow Analysis for Spiral Casing

The role of the casing is to transform the rectilinear flow coming from the penstocks into an inwardly swirling flow around the distributor, which has been analysed and reported in [10]. The spiral casing is essentially a 360 deg curved channel with decreasing cross sectional area and fluid extraction along the inner wall. Figure 9 illustrates the plan and elevation views of a typical spiral casing with Piguet type distributor stay rings.

The flow domain comprises the intake section, the casing itself and the distributor housing. Figure 10 shows a three dimensional view of the spiral casing flow domain with the body fitted grid system. Uniform flow is assumed at the casing inlet for the present study, but any particular flow velocity profile coming from the penstocks could be used as inlet flow condition. At the outlet portion of the flow domain, special treatments have to be applied to simulate the presence of the two series of stay vanes and wicket gates in order to properly account for the resistance yielded here.

Presently, this portion is considered as a porous medium where the porosity and the frictional loss could be adjusted to simulate the head loss in the distributor, depending highly on flow attack angles at the stay vane leading edges and orientation of the wicket gates. By doing this manner, the overall flow behavior can be predicted without having to model the presence of every stay vane and wicket gate. The spiral casing used for the flow analysis is a decelerated flow type. The Reynolds number based on the throat diameter and the axial velocity is 10^6. Typical CPU time required for a $95 \times 21 \times 13$ grid size is about 27 hours on a VAX8600.

Figure 11(*a*) shows the velocity vectors at the mid-section of the casing in the main stream direction. The uniform flat

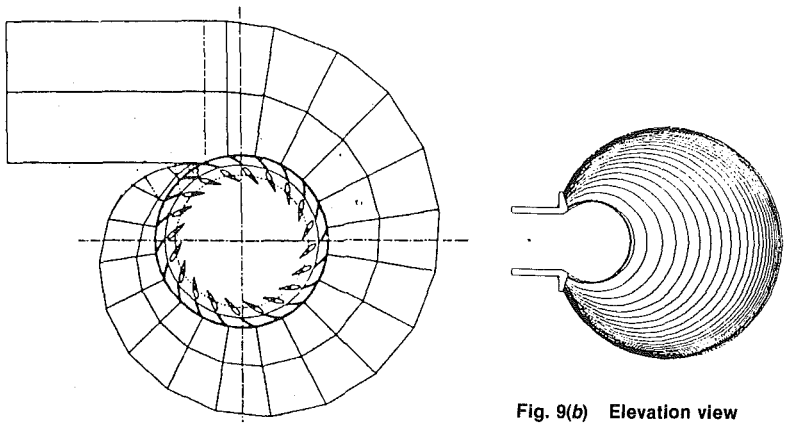

Fig. 9(*b*) Elevation view

Fig. 9(*a*) Plan view

Fig. 9 Plan view and elevation view of a spiral case

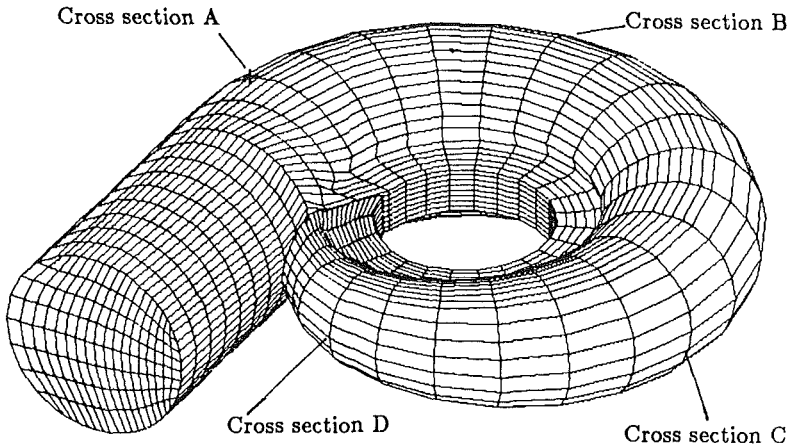

Fig. 10 Flow domain and body-fitted grid system of a spiral case

profile at the intake region is transformed gradually into a free vortex flow profile, as shown in Fig. 11(*b*). Toward the end of the casing, the free vortex flow profile disappears. The difference between the flow direction at the casing mid-section, represented by solid line, and the flow direction near the top of the casing, represented by broken line, is well illustrated in Fig. 11(*c*). Near the casing mid-section, the flow is mostly tangential to the casing circumference whereas the flow near the top is accelerated toward the inner radius. The distribution of the flow angle near the distributor entrance is also highly three-dimensional. An average calculation of the flow angle along the distributor height is necessary to obtain correct stay vane orientations. The static pressure contour curves, as shown in Fig. 11(*d*) for the mid-section, are distributed quite evenly around the casing and decreases rapidly toward the inner radius. Especially in the distributor section which is treated as a porous medium, the static pressure distribution is much more dense than in the casing. In Fig. 11(*d*), the pressure contours are of wavy pattern near the outside wall. This waviness is caused by the slope discontinuities between adjacent segments which are manufactured in straight pieces. Studies have also been conducted to compute the flow through a smooth casing, i.e., no slope discontinuities are present in top view. It is found that no pressure oscillations are present in such a smooth domain [17], hence confirms that the waviness shown in Fig. 11(*d*) is not a numerical phenomenon.

The display of velocity vectors at different cross sections of the casing, as shown in Fig. 12, illustrates well the evolution of the secondary flow in the spiral casing. At the beginning of the spiral casing, as shown in Fig. 12(*a*) for cross section A, the flow is accelerated evenly along the casing height. After a first 90 deg turn, as shown in Fig. 12(*b*) for the cross section B, the existence of double swirls generated by the casing curvature is observed. The radial component is very strong near the top and bottom of the casing and very weak near the center of the casing. At the cross section C, as shown in Fig. 12(*c*) the core of the double swirls becomes smaller. Near the end of the casing where the flow is more accelerated, the double swirls disappear as shown in Fig. 12(*d*) for the cross section D. These predicted flow characteristics for the spiral casing agree well with observations from experimental data obtained by Kurokawa and Nagahara [12].

5 Concluding Remarks

Viscous flow analysis, when it is well validated, is a powerful analytical design tool. As we have seen, viscous flow analysis can simulate correctly the flow characteristics and predict accurately head losses in different hydraulic turbine components. This allows us to visualize the whole flow field of complex geometries instead of just a few locally conducted experimental measurements. It allows designer to evaluate the hydraulic performance of alternative designs before preceeding with testing in laboratory or to perform elaborate parametric studies to optimize the hydraulic design.

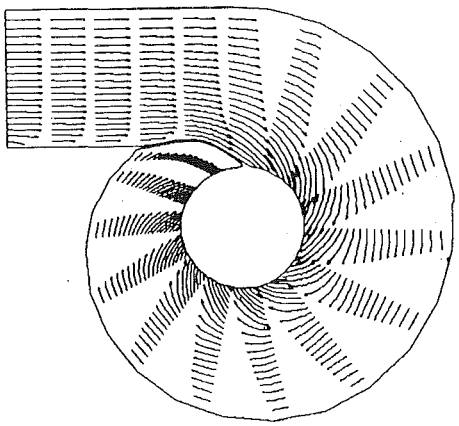

Fig. 11(*a*) Velocity vectors

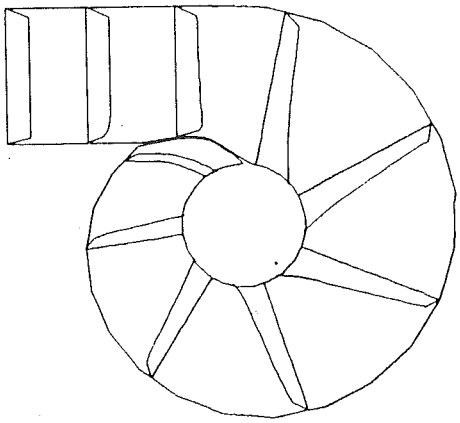

Fig. 11(*b*) Velocity profile

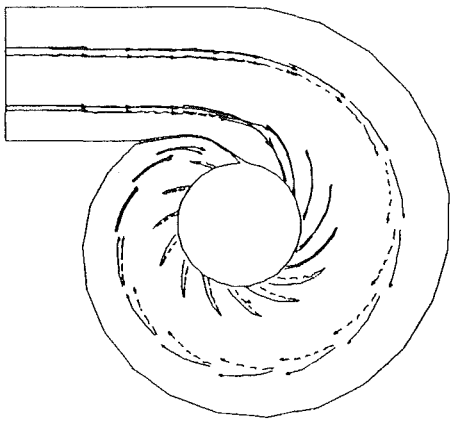

Fig. 11(*c*) Flow direction at mid-section (solid line) and near the top (dotted line)

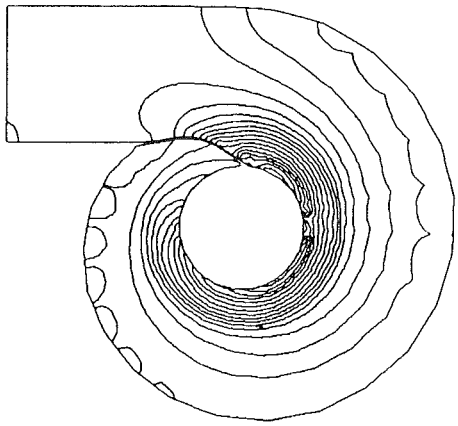

Fig. 11(*d*) Static pressure contour curves

Fig. 11 Spiral case main flow characteristics at mid-section

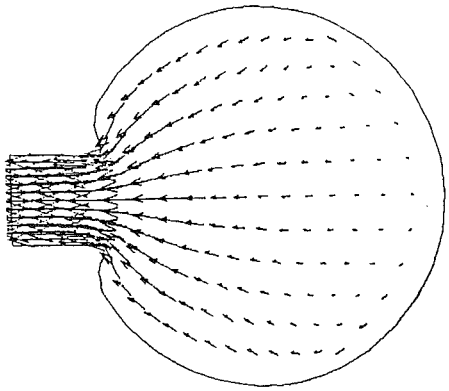

Fig. 12(*a*) Cross section A

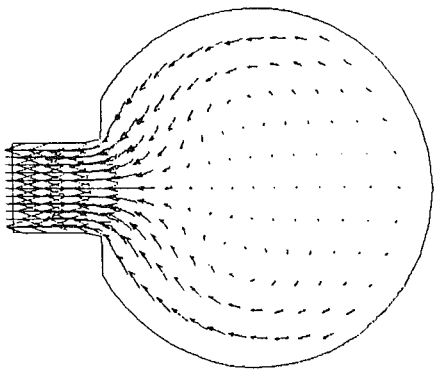

Fig. 12(*b*) Cross section B

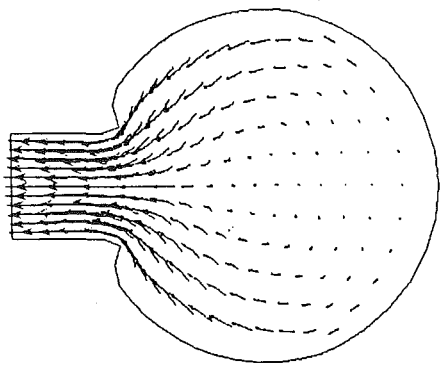

Fig. 12(*c*) Cross section C

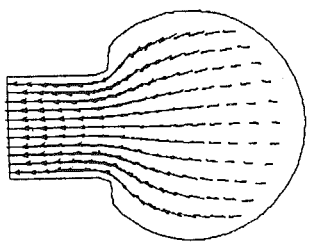

Fig. 12(*d*) Cross section D

Fig. 12 Spiral case secondary flow characteristics at different cross sections

References

1 Holmes, G., and McNabb, J., "Application of Three Dimensional Finite Element Potential Flow Analysis to Hydraulic Turbines," *IAHR Symposium 1982*, Paris, France, 1982.

2 Désy, N., Do, H., and Nuon, N., "Turbine Casing and Distributor Design," *Water Power 1987*, International Conference on Hydropower, Portland, Oregon, Vol. 3, 1987, pp. 1865–1872.

3 Shyy, W., Tong, S. S., and Correa, S. M., "Numerical Recirculating Flow Calculation Using a Body-fitted Coordinate System," *Numerical Heat Transfer*, Vol. 8, 1985, pp. 99–113.

4 Braaten, M. E., and Shyy, W., "A Study of Recirculating Flow Computation Using Body-Fitted Coordinates: Consistency Aspects and Skewness," *Numerical Heat Transfer*, Vol. 9, 1985, pp. 559–574.

5 Shyy, W., and Vu, T. C., "A Numerical Study of Incompressible Navier-Stokes Flow Through Rectilinear and Radial Cascade of Turbine Blades," *Comp. Mech.*, Vol. 1, 1986, pp. 269–279.

6 Shyy, W,. and Braaten, M. E., "Three-Dimensional Analysis of the Flow in a Curved Hydraulic Turbine Draft Tube," *Int. J. Num. Meth. Fluids*, Vol. 6, 1986, pp. 861–882.

7 Shyy, W., "A Study of Finite Difference Approximations to Steady State, Convection Dominated Flow Problems," *J. Comp. Physics*, Vol. 57, 1985, pp. 415–438.

8 Launder, B. E., and Spalding, D. B., "The Numerical Calculation of Turbulence Flows," *Comp. Meth. Appl. Mech. Eng.*, Vol. 3, 1974, pp. 269–289.

9 Vu, T. C., Shyy, W., Braaten, M. E., Reggio, M., "Recent Development in Viscous Flow Analysis for Hydraulic Turbine Components," *IAHR Symposium 1986*, Vol. 2, Montreal, Canada, 1986.

10 Vu, T. C., and Shyy, W., "Navier-Stokes Computation of Radial Inflow Turbine Distributor," ASME JOURNAL OF FLUIDS ENGINEERING, Vol. 110, 1988, pp. 29–32.

11 Vu, T. C., and Shyy, W., "Viscous Flow Analysis for Hydraulic Turbine Draft Tubes," *IAHR Symposium 1988*, Trondheim, Norway, 1988, also ASME JOURNAL OF FLUIDS ENGINEERING (accepted for publication).

12 Kurokawa, J., and Nagahara, H., "Flow Characteristics in Spiral Casings of Water Turbines," *IAHR Symposium 1986*, Vol. 2, Montreal, Canada, 1986.

13 Chacour, S. A., and Webb, D. R., 'LILLY'—A Computerized System for the Analysis, Design and Manufacture of Fluid Machinery, ASME Paper No. 84-WAFM-6, 1984.

14 Shyy, W., "Effect of Open Boundary on Incompressible Navier-Stokes Flow Computation: Numerical Experiments," *Numerical Heat Transfer*, Vol. 12, 1987, pp. 157–178.

15 Baumeister, T., "Turbomachinery," Streeter, V. L., ed, *Handbook of Fluid Dynamics*, Section 19, McGraw-Hill, New York, 1961.

16 Gupta, A. K., Lilley, D. G., and Syred, N., *Swirl Flows*, Abacus Press, Tunbridge Wells, Kent, UK, 1984.

17 Shyy, W., and Vu, T. C., "On the Adoption of Velocity Variable and Grid System for Fluid Flow Computation in Curvilinear Coordinates," *J. Comput. Physics* (accepted for publication).

Acknowledgments

The authors gratefully acknowledge the assistance of Mr. S. Coulson and the personnel of the Hydraulic Laboratory of Dominion Engineering Works for providing the experimental data. Also many thanks are due to Cray Canada for granting several hours of CPU time on a CRAY XMP. The software for grid generation and 3D flow visualization was developed by the CASTOR project of Ecole Polytechnique de Montréal.

A Transient Electromagnetic Flowmeter and Calibration Facility

P.J. Lefebvre
Naval Underwater Systems Center,
Newport, R.I.

W. W. Durgin
Worcester Polytechnic Institute,
Worcester, Mass.

An electromagnetic flowmeter was developed to measure transient flows at a data rate of 60 Hz. The approach taken was to develop suitable electronics to replace the electronics of a commercially available electromagnetic flowmeter normally used for steady-state operation. Use of the commercially available flowmeter body, which includes the magnetic coils, core, and signal electrodes, provided a relatively economical means of fabricating the transient flowmeter. A transient flow calibration facility consisting of a free-falling water column was also designed and built. Results of the calibrations are presented and show that the flowmeter can accurately measure transient flows up to the maximum observed acceleration of approximately 1 g.

Introduction

In the study of transient pipe flows, a need exists for the accurate measurement of the mean volumetric flow rate as a function of time. To date, very few flowmeters have been built that have the capability to measure transient flows. In addition, to the authors' knowledge, there are no commercially available flowmeters that can accurately measure transient flow rates at a high data rate.

Many of the existing flowmeters used for steady-state applications are inherently not applicable to transient flow measurements. For example, turbine meters, even though they have a fast signal response time and consequently provide output at an apparent high data rate, are momentum devices and the meter calibration is inherently a function of not only velocity profile but also rate of change of flow rate.

Head type meters, such as orifice plates, are dependent on the response of the pressure transducer(s) used in the differential pressure measurement. In addition, the flow field in the vicinity of the orifice can change considerably under high flow transients leading to changes in the orifice's calibration.

A few special-purpose meters have been developed over the past 25 years that have had some transient flow measurement capabilities. In 1950, Arnold [(1)] described an electromagnetic flowmeter for small flow rates that responded to very short transients of 0.001 second in duration. Since a circular cross section proved unsatisfactory for the design, a small rectangular cross section of 0.48 × 1.58 cm was chosen.

In 1960, Iwanicki and Fontaine [(2)] described an electromagnetic flowmeter, which was also designed to respond to very short transients of low flow rates. The meter, with a 1.2-cm diameter, could not be operated for more than a few seconds due to polarization of the flowing liquid at the signal electrodes. In each of the references, it was shown that the meters responded to large flow transients. Unfortunately, the facilities used to validate meter performance could not provide information on the accuracy of the flowmeter output.

Contributed by the Fluids Engineering Division for publication in the JOURNAL OF FLUIDS ENGINEERING. Manuscript received by the Fluids Engineering Division April 4, 1988.

To fulfill the need for accurate transient flow measurement during future experimental studies, the Naval Underwater Systems Center (NUSC) developed the transient flowmeter discussed herein. Criteria for this meter included accurate measurement of the mean volumetric flowrate (cross-sectional averaged velocity) with the meter being insensitive to changes in velocity profile, especially varying axi-symmetric profiles.

The resulting flowmeter is based on electromagnetic flowmeter principles and has the capability to accurately measure transient flows with a data rate of at least 60 Hz. The meter has a 5-cm diameter and can be used, with one common meter calibration factor, for both steady-state flows and for transient flows of either short or long duration. It also can operate accurately over a 30:1 flow rate range.

To evaluate the flowmeter's accuracy, a transient calibration facility was designed by NUSC and the Worcester Polytechnic Institute (WPI) and fabricated at WPI.

This paper describes the flowmeter, the calibration facility and also presents data on the flowmeter calibration.

Flowmeter Description

Electromagnetic technology was chosen as the basis for the transient flowmeter because of inherent fast response to transients and the general insensitivity of electromagnetic flowmeters to changes in velocity profile.

By using a weighting function, Shercliff [(3)] showed mathematically that the signal generated at the electrodes represents the average velocity for axisymmetric profiles. Reinhold [(4)] presented experimental data that showed errors of less than 0.5 percent when large unsymmetric flow disturbances were placed only five pipe diameters upstream of an electromagnetic flowmeter. Typical disturbances were a concentric orifice plate with 50 percent blockage and a segmental orifice with a 50 percent blockage. Obviously, the high performance observed is dependent on the design of the flowmeter itself, primarily the flowmeter's ability to generate a suitable magnetic field.

The electromagnetic flowmeter is based on Faraday's law of induction. As a conducting fluid passes through a magnetic

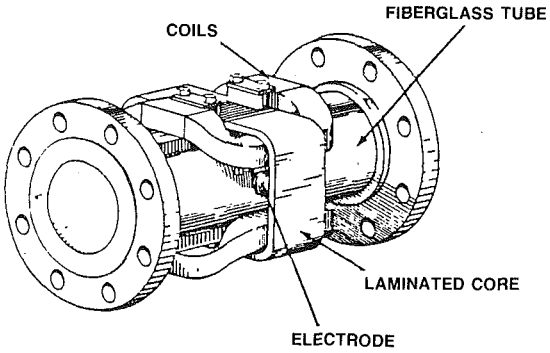

Fig. 1 Flowmeter body

field, an electric voltage is generated in a plane perpendicular to the plane of the magnetic flux vector and the conducting fluid's velocity vector. The generated potential E (volts) given by Faraday's law is shown in equation (1) as

$$E = KDBV, \tag{1}$$

where K is the meter's calibration factor, D is the distance between signal electrodes (or meter diameter), B is the magnetic flux density, and V is the cross-sectional average fluid velocity.

The approach taken in the development of the flowmeter was to utilize as much of a commercially available electromagnetic flowmeter as was feasible. The final version of he transient flowmeter, therefore, consists of the flow tube (or body) portion of a Foxboro Co. ac-powered electromagnetic flowmeter and the NUSC-designed electronics transmitter. The flow tube, as shown in Fig. 1, consists of the magnetic coils and core (which generates the magnetic flux), and the signal electrodes mounted flush with the inner wall of a 5-cm-diameter fiberglass tube.

In operation, the coil which produces the magnetic field is powered by line voltage (120 volts, 60 hz), thereby producing a magnetic field which oscillates sinusoidally at 60 Hz. Consequently, the signal from the electrodes is also sinusoidal at the same frequency as the magnetic field.

The electronic unit, which is essentially digital, samples the resulting sinusoidal output voltage from the signal electrodes during each cycle. The electronic unit monitors the change in voltage (flow rate) from the previous cycle and then incorporates that value into the aggregate sum to obtain the current value of voltage (flow rate).

Changes in the magnitude and frequency of the induced magnetic flux due to fluctuations in line voltage are compensated for in the design. A reference coil located on the external wall of the flow tube and in the vicinity of the magnetic coils monitors the instantaneous magnetic flux. By comparing the voltage from the signal electrodes to that induced in the reference coil in a unique manner, the effect of line voltage changes are eliminated. The electronic circuits were designed to operate at frequencies up to approximately 1000 Hz. However, at these higher frequencies, a commercially available flowtube would be unsatisfactory; a special flowtube would be needed.

The design of the electronics includes many novel features which act together to circumvent the usual problems associated with the high noise inherent in the signal generated at the electrodes of magnetic flowmeters. The flowmeter output provides both an analog and a digital signal corresponding to the instantaneous flow rate. Since the magnetic field is cycled and not maintained at a constant dc value, polarization of the fluid at the signal electrodes does not occur and the flowmeter can be operated for an indefinite period of time.

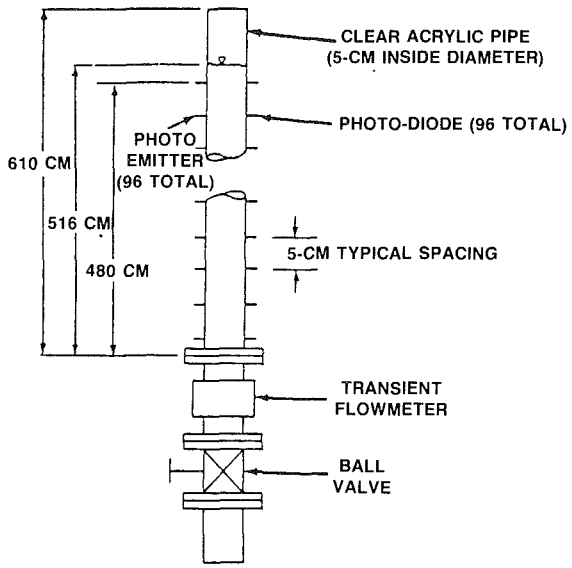

Fig. 2 Transient flow calibration facility

Calibration Facility

The purpose of the calibration facility at WPI was to establish the accuracy to which the flowmeter could measure transient volumetric flow rates under accelerations up to 1 g. The general concept of the facility was to accurately measure the transient velocity of a free-falling vertical column of water to which the output from the transient flowmeter could be compared. The velocity of the water column (calibration velocity) was measured by monitoring the rate of change in elevation of the free surface of the column.

As shown in Fig. 2, the water column is contained within a clear acrylic pipe having an inside diameter of 5 cm. The transient flowmeter was installed at the lower end of this pipe. Each test was initiated by manually opening a ball valve placed below the flowmeter. To measure the free surface velocity, a total of 96 photo-emitter/photo-diode optical pairs were distributed every 5 cm along the lowermost 480 cm of the acrylic pipe. As the surface of the water column passed a sensor station, a change in the intensity of light transmitted from the photo-emitter to the photo-diode occurred, resulting in a sharp jump in the voltage generated at the photo-diode. This change in voltage level was used to trigger a flip-flop in the facility's electronic circuitry to which all of the optical sensors were multiplexed. The analog output of this electronic system was a square wave with a varying half-period equal to the time between consecutive trigger pulses.

An IBM personal computer with a Data Translations analog-to-digital data acquisition board was used to detect the trigger pulses by sampling the analog output of the electronics at a rate of 5000 Hz. At that rate, the time that the water surface passed each of the optical sensor pairs was known to within ± 0.0002 second.

The effective vertical distance between optical sensor pairs

Nomenclature

A = cross-sectional area
B = magnetic flux density
D = meter diameter
E = voltage generated at electrodes
K = meter calibration factor
L = effective distance between optical pairs
V = cross-sectional average fluid velocity
W = weight
ρ = fluid density
σ = standard deviation

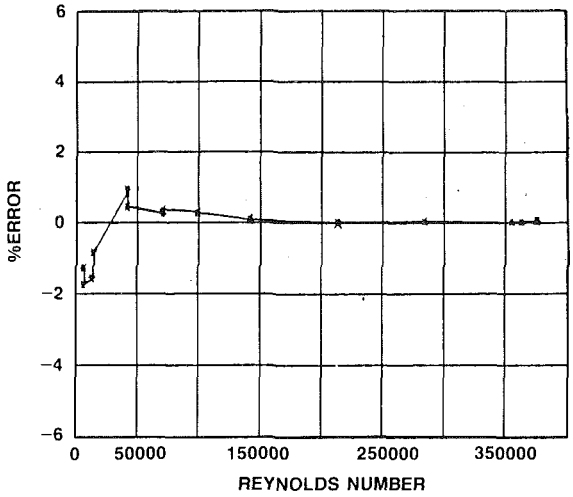

Fig. 3 Steady-state calibration curve

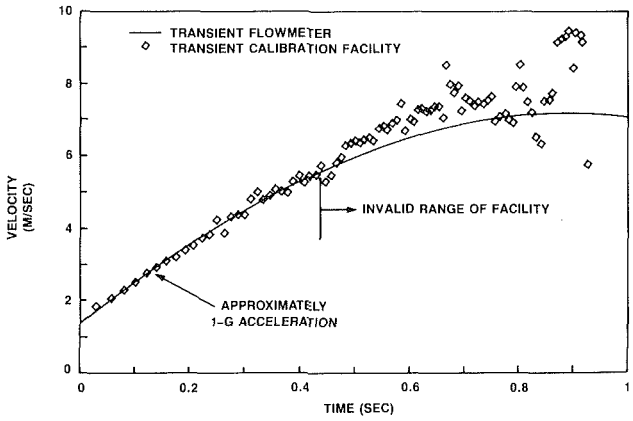

Fig. 4 Typical transient calibration curve (uncertainty in flow rate = ± 5 percent, in time = ± 0.0002 sec

was established by draining the water at a very slow rate and weighing the amount of water collected between trigger pulses. The weight was converted into an effective distance between optical sensor pairs based on a constant 5-cm internal pipe diameter, as shown in equation (2)

$$L = W/(A\rho), \tag{2}$$

where ρ is the density of the water, A is the cross-sectional area based on a 5 cm diameter, and W is the weight of the water between optical sensor pairs. This method accounted for variations in vertical distance between optical sensors pairs and also variations in diameter along the pipe.

Following each calibration run, post-processing software scanned the raw data file and created a file of the time at which each optical sensor pair was triggered. Velocity, based on a 5-cm diameter, was subsequently calculated from the time and effective distance values between optical pairs.

During a calibration, the analog output from the transient flowmeter was sampled simultaneously with the facility electronics at the 5000-Hz sampling rate. Since the output of the flowmeter was updated at a rate of 60 Hz, post-processing software scanned the raw data file and established the time corresponding to the updated flowmeter output to within ±0.0002 second. For each of these update times, the corresponding calibration velocity was calculated from the calibration velocity versus time data file by linearly interpolating between adjacent points. A comparison of the calibration velocity and the flowmeter velocity was then made.

Table 1 Calibration Summary

Run number	Mean Error (%)	σ
1	1.370	2.55
2	−0.946	2.56
3	−0.740	2.54
4	0.276	2.67
5	−0.575	2.47
6	0.776	2.62
7	−0.536	1.78
8	0.378	2.88
9	0.352	1.88
10	0.807	3.33
11	−1.318	2.36
12	−1.191	2.88
Average for all runs:	−0.041	2.57

Results

Prior to conducting any of the transient calibrations, a steady-state calibration of the meter was conducted at the Alden Research Laboratory's Flowmeter Calibration Facility, Holden, MA. This calibration was performed by using the gravimetric method and is considered accurate to ± 0.25 percent. The calibration was conducted over a velocity range of 0.15 to 9.1 m/s in the 5-cm diameter flowmeter. The corresponding Reynolds number range was 7100 to 375,000.

The steady-state calibration curve is shown in Fig. 3. The curve is presented as percent error from actual velocity when flowmeter velocity is calculated with a constant meter factor (K). As shown, accuracy (linearity) was within ±1.7 percent over the complete flow range and within ±0.5 percent over the 40,000 to 375,000 Reynolds number range, which is a substantial portion of the total range.

Twelve transient calibration runs were conducted. Even though each run was initiated by manually opening the valve at the bottom of the facility, the velocity versus time curve was fairly consistent between runs.

Results for a representative run are shown in the cross-sectional averaged velocity versus time curve of Fig. 4. The run lasted approximately 1 second. From 0.0 to approximately 0.43 second, the flow experienced an almost constant acceleration of approximately 1 g, reaching a velocity of approximately 5.5 m/s. Beyond 0.43 second, the free surface of the water column experienced considerable instability precluding any accurate measurements. The flowmeter, however, appears to have followed the water column velocity throughout the transient. All further discussions are limited to the 0.0-second to 0.43-second range of each run, which corresponds to the first 29 data points from the flowmeter.

Results for all 12 of the calibration runs are presented in Table 1. Mean error and standard deviation between the calibration facility and flowmeter measured flow velocities are presented separately for each run and also for the total of all data points. As shown, the absolute value of the mean error ranged from 0.276 to 1.370 percent, while the standard deviation of the error ranged from 1.78 to 3.33 percent. The mean error for all the data points was −0.041 percent with a standard deviation of 2.57 percent.

Using the results from the total of all data points, the difference between the calibration facility and the flowmeter measurements is expected to be within ±5.2 percent for 95 percent of measurements to be taken.

Inspection of the transient calibration curves (similar to Fig. 4) for each of the twelve runs showed that the flowmeter output exhibited a smooth transition throughout the transient with negligible fluctuations about the mean curve. Furthermore, for a major portion of each individual run, the flowmeter curve is essentially the mean curve for the calibration facility data.

Considering that the facility data for all runs fluctuated about the mean curves with a standard deviation of approximately 2.5 percent, it is believed that the accuracy (95 percent confidence level) of the facility is approximately ± 5 percent. An error analysis showed that errors due to factors other than the data fluctuations were negligible relative to the 5 percent error due to the fluctuations.

Considering the above estimated facility accuracy, the flowmeter accuracy cannot be stated to be any better than the facility's ± 5 percent accuracy during a transient run. However, considering that the mean difference between the facility and the flowmeter when all points are included is only −0.041 percent, and also considering the fact that the fluctuations in the flowmeter output about its mean curve are essentially negligible, it is expected that the true accuracy of the flowmeter in monitoring transient flows is approximately equal to the steady-state accuracy previously stated.

For the present meter, inaccuracies resulting from transient effects are essentially caused by the immediate rate of change of velocity profile and not its total past history. Therefore, even though the present tests were conducted with the fluid initially at rest, the above accuracy statements are applicable to other initial conditions.

Conclusions

An electromagnetic flowmeter has been developed that can accurately measure transient flow rates up to at least 1-*g* acceleration (maximum tested) with a data rate to 60 Hz. A calibration facility using a free-falling column of water has been shown to be a viable means of evaluating transient flowmeter performance up to 1 g.

Acknowledgment

Support for this project was provided through the Independent Research Program at the Naval Underwater Systems Center, Newport, RI.

References

1 Arnold, J. S., "An Electromagnetic Flowmeter for Transient Flow Studies," *The Review of Scientific Instruments*, Vol. 22, No. 1, Jan. 1950.

2 Iwanicki, L. R., and Fontaine, R. J., "Application of an Electromagnetic Flowmeter in Unsteady Flow," ASME Symposium on Measurement in Unsteady Flow, May 1962.

3 Shercliff, J. A., *The Theory of Electromagnetic Flow Measurement*, Cambridge University Press, Cambridge, England, 1961.

4 Reinhold, I., "Velocity Profile Influence on Electromagnetic Flowmeter Accuracy," *Flow Measurement of Fluids*, North-Holland Publishing Co., 1978.

The Mean Flow Structure on the Symmetry Plane of a Turbulent Junction Vortex

F. J. Pierce
Mechanical Engineering Department,
Virginia Polytechnic Institute
and State University,
Blacksburg, VA 24061
Fellow ASME

I. K. Tree
Engineering Specialist,
General Dynamics Corporation,
Fort Worth, TX 76101

The mean flow structure on the symmetry plane of a turbulent junction vortex is documented. A two-channel, two-color LDV system allowed nonintrusive measurements of the two velocity components on the symmetry plane. Extensive measurements were made in and around the separation point and within the junction vortex system, both very close to the floor and to the leading edge of the body generating the vortex system. Real-time smoke visualizations confirmed a region of strongly time-variant flow with large changes in the scale and position of the principal vortex structure. The extensive velocity field data are correlated with high quality surface visualizations and surface pressure measurements. The mean velocity measurements show one large well-defined vortex structure and one singular saddle point of separation on the symmetry plane. The transverse vorticity field computed from the extensive velocity field suggests a very strong but small second, counter rotating vortex located in the extreme corner formed by the floor and leading edge of the body. The surface flow visualization suggests only one clear separation line. The single pair of counter rotating vortices revealed by these detailed LDV velocity measurements is in agreement with two independent studies which used multiple orifice pressure probes. This measured two vortex model is not in agreement with the frequently pictured four vortex flow model, inferred from surface flow visualizations, showing two pairs of counter rotating vortices.

Introduction

The details of the mean flow structure on the symmetry plane of a turbulent junction vortex are of interest both from a fluid mechanic and a heat transfer point of view. The classical model of the velocity field on the symmetry plane of a low speed, turbulent junction vortex results from the work of Hunt, Abell, Peterka, and Woo [1] and Baker [2, 3]. Hunt et al. interpreted surface flow visualizations around blunt bodies in low speed flows with the aid of kinematic considerations for the flow field above the surface. This model was extended to turbulent flows both in reference [1] and by Baker [3], as displayed in Fig. 1. The essential features of Fig. 1(*a*) are a pair of separation and attachment lines which lie between multiple vortex structures in a four vortex system. Baker [3] modeled these vortex structures as shown in Fig. 1(*b*). The essential feature of Fig. 1(*b*) is the four vortex system with two relatively large and two relatively small vortex structures. The suggested attachment and separation lines consistent with such a mean flow model are shown in the figures. This four vortex flow model is also presented by Ishii and Honami [4] based on smoke wire visualizations.

The multiple vortex model with four vortices and two separation-attachment line pairs in Fig. 1 is similar to the four vortex separation model shown in Sedney and Kitchens [5] in their excellent summary of their extensive flow visualizations for obstacle-boundary layer interactions in supersonic turbulent flows. It is worth noting that for their supersonic turbulent flows, Sedney and Kitchens found the number of vortex pairs and corresponding separation and attachment line pairs was Reynolds number dependent. They present junction vortex systems with 2, 4, and 6 vortices with corresponding multiple separation-attachment line pairs.

While a number of more recent surface flow visualizations for low speed turbulent junction vortex systems appear in the literature [6–8], there appears to be limited documentation of the actual velocity field over such flow visualizations. One of the difficulties in documenting the velocity field is the strong time-variant character of such a flow field as documented by real-time smoke flow visualizations [9], and time resolved hot wire measurements [10], as well as the present time resolved LDV measurements. Typically very large velocity fluctuations occur, including complete flow reversals. In these situations probes may interfere with the flow field, and the question of flow phenomena such as separation being influenced by a physical probe can be raised. The nonintrusive LDV offered the opportunity to examine this flow field with essentially zero disturbance. Pierce, Kim, and Harsh [11], Pierce and Harsh [12], and Eckerle and Langston [13] have reported pressure probe measurements, and Dickinson [8] and Abid and Schmitt [14] have reported LDV velocity field measurements in a turbulent junction vortex.

Contributed by the Fluids Engineering Division for publication in the JOURNAL OF FLUIDS ENGINEERING. Manuscript received by the Fluids Engineering Division October 25, 1988.

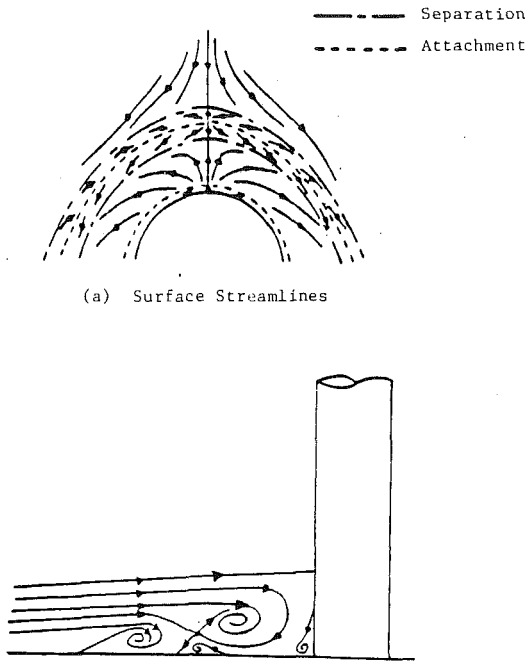

Fig. 1 Junction vortex flow patterns (taken from Baker [3])

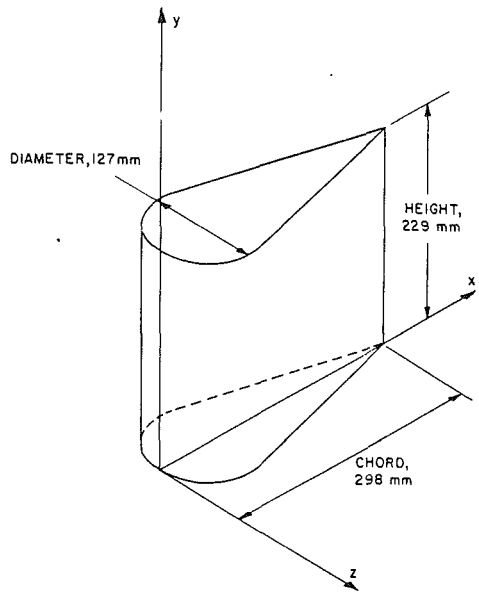

Fig. 2 The streamline cylindrical body and coordinate system

Experiment

A low-speed turbulent junction vortex system was generated by placing a streamlined cylinder as shown in Fig. 2 normal to a highly polished flat floor. Body dimensions and the coordinate system are shown in the figure. The 229 mm high cylinder was placed in a two-dimensional turbulent boundary layer nominally 90 mm thick, which developed over the 5 m long floor upstream of the test section of the 3.66 m wide by 2.44 m high rectangular cross section wind tunnel. The body Reynolds number of 183,000 based on the diameter or maximum thickness of the model was fixed with a typical test section velocity of about 24 m/s. The upstream momentum Reynolds number was 12,500. More details of the experimental facility can be found in Pierce, Kim, and Harsh [11], Pierce and Harsh [12], and Tree [15].

Velocity measurements on the upstream symmetry plane of a turbulent junction vortex are difficult to make. Real-time smoke visualizations showed the flow to be strongly time-variant with large changes in the size and position of the dominant vortex structure. Measurements made with physical velocity probes, such as hot wires or pressure probes, can be questioned because of the unknown influence such probes might have on the flow field itself, and because of the very large velocity fluctuations, including flow reversals, encountered by such probes. Additionally, a physical probe might tend to anchor or stabilize a time-variant flow event, e.g., separation points on the symmetry plane might tend to become fixed at the probe.

Unlike conventional physical probes, the nonintrusive LDV method does not disturb the flow field being measured. In recirculating flows and separating flows, the LDV often appears to be the most reliable measurement technique. In addition to its nonintrusive nature, the LDV is also a linear device. Thus the need for calibration and the various problems associated with instrument calibrations can be eliminated.

A two-component, two-channel system was used to measure the streamwise and normal (to the floor) components of the velocity field on the symmetry plane. The LDV system used a 2-watt Argon-ion laser utilizing the 488.0 nm (blue) and 514.5 nm (green) lines. A Dantec 55X modular, 3-beam, 2 component, frequency shifted system operated in the backscatter mode was used. A 40 MHz optical frequency shift was utilized to minimize fringe bias and determine flow direction. The front lens had a focal length of 600 mm. The scattering volume was approximately 0.15 mm × 5.3 mm, very small compared to the upstream boundary layer thickness of approximately 90 mm. This allowed very fine spatial resolution for the measurements. A block diagram of the LDV instrumentation system and data processing is shown in Fig. 3.

The LDV system output was processed with a Dantec model 55L90a counterprocessor which uses period averaging for velocity bias correction. Some additional signal filtering, amplification, and in-house signal splitting electronics were used to permit closer monitoring and improvement of the signal-to-noise ratio of the signal being processed. An Analogic Data 6000 digital waveform analyzer was used to monitor the Doppler bursts and provide frequency spectra of post-processed signals for the selection of optimum filter windows.

Forty-four profiles of two components of velocity were measured throughout the separation and vortex region for a total of 1792 velocity pairs. To insure meaningful averages for the strongly time variant flow shown by both real time smoke

Nomenclature

c_p = static pressure coefficient
D = leading edge diameter or body thickness
h = body height
R_D = Reynolds number based on body dimension
R_θ = Reynolds number based on approach boundary layer momentum thickness
$\overline{V}$ = velocity magnitude on symmetry plane
V^* = tunnel inlet throat speed used to nondimensionalize velocities
u, v, w = components of velocity
x, y, z = coordinates
δ = boundary layer thickness
δ^* = boundary-layer displacement thickness
θ = boundary-layer momentum thickness

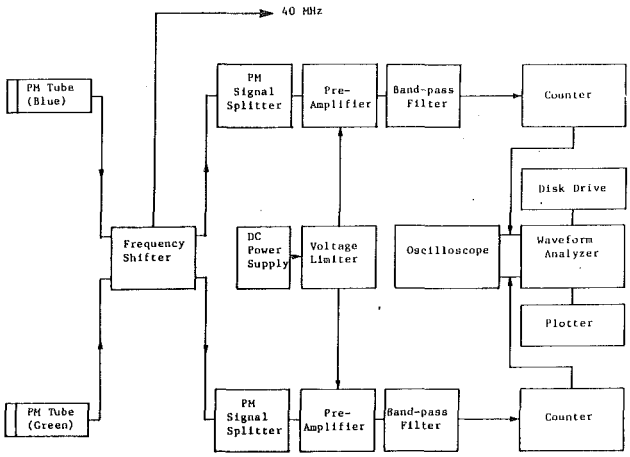

Fig. 3 Block diagram of LDV system

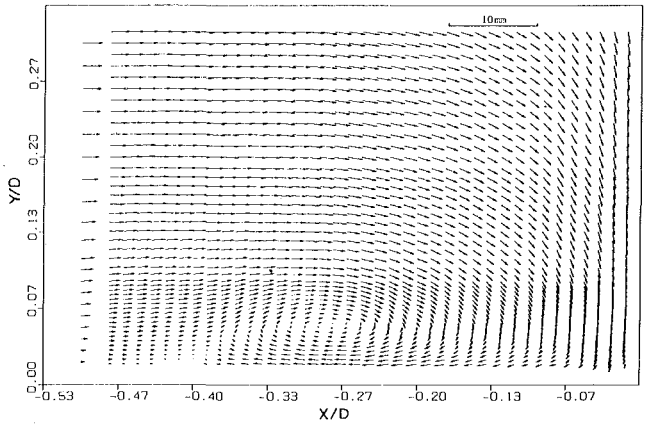

Fig. 5 LDV velocity field in the junction vortex flow field. Typical uncertainty in $\bar{V}/V^*$ is ± 0.009 or less.

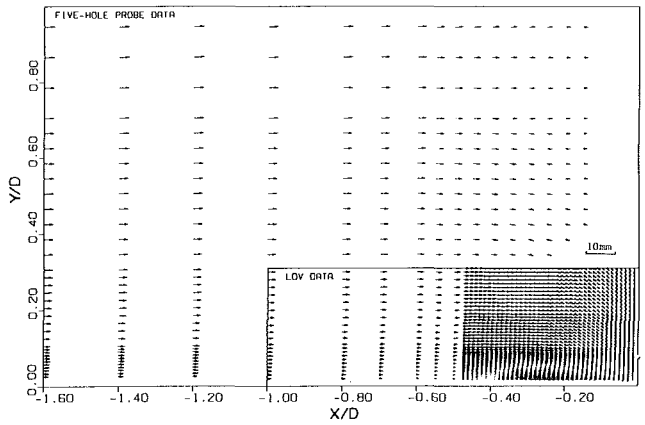

Fig. 4 Combined LDV and five-hole probe results on the plane of symmetry. Typical uncertainty in $\bar{V}/V^*$ is ± 0.009 or less.

visualizations and earlier hot wire measurements, each component of each velocity pair was computed from over 16,000 individual LDV realizations.

The scattering volume was accurately positioned in the tunnel by passing it through a 0.2 mm diameter pinhole carefully located from two orthogonal reference edges on a machinist's block placed in the tunnel. The laser optics, configured in the backscatter mode, were traversed as a unit on a milling machine table modified for use as a traversing device.

Several seeding materials were tried. The ultimate choice of seed was atomized from a solution made up of 20 percent cane sugar and 80 percent water (by volume). The seed was generated by a TSI model 9306, six jet atomizer, with the seed injected into the wall boundary layer approximately 5 m upstream of the test section. Based on the manufacturer's published data, the atomized liquid droplets were generally spherical in shape, and were estimated to be approximately 1 micron in diameter.

Results

Forty-four velocity profiles of two components of the mean velocity were made throughout the separation and vortex region for a total of 1792 velocity pairs. These detailed mean velocity measurements accurately define the size, shape, and location of the junction vortex, and the position of the upstream singular saddle point of separation. The region of the LDV measurements was selected to fit into the earlier extensive plane of symmetry measurements reported by Pierce, Kim and Harsh [11], and Pierce and Harsh [12] made with an extensively calibrated 5-hole probe. The region of the LDV measurements was confined to the portion of the upstream symmetry plane where separation and the large flow reversals of the junction vortex were known to exist from the earlier studies. Figure 4 shows the LDV measurement region relative to the earlier documented upstream symmetry plane. The forward portion of the LDV measurement region, which is well ahead of the saddle point of separation, showed excellent agreement with the earlier 5-hole probe measurements.

The mean velocity field measured consisted of six profiles upstream of the singular separation point and the junction vortex flow field, and 38 profiles in the separation and vortex flow field itself.

Data shown in the first six profiles is characterized by low pitch angles with the absence of any signs of flow separation. The velocity profiles shown are similar to those found in a typical two-dimensional turbulent boundary layer.

The flow field described by the remaining 38 profiles in Fig. 5 shows one singular saddle point of separation, followed by a single, relatively large, well-defined junction vortex. Velocity field vectors in Figs. 4, 5, and 6 have been nondimensionalized using the tunnel inlet speed. Velocity values including statistically meaningful uncertainties are given in Tree [15].

The entire flow field of Fig. 5 is constructed from 1,692 discrete ensemble average velocity component pairs. The actual length and height of the measurement region shown in Fig. 4 are 127 mm long and 39.4 mm high. Velocity measurements were made as close as 2.3 mm from the wall and 1.6 mm to the body leading edge. Accurate measurements any closer to the wall were precluded by a poor signal-to-noise ratio due to wall reflections. The scattering volume of nominally 0.15 mm dia. $\times$ 5.3 mm length and the clearance distances above the floor and ahead of the leading edge of the body are small relative to the size of the measurement region. Significant features of this figure are (1) the presence of only one saddle point of separation, and (2) the presence of a single relatively larger vortex structure. It is noted that the flow in the body-floor corner is suggestive of and consistent with the presence of a small, counter rotating corner vortex.

Figure 6 shows a magnified region of the flow centered about the perceived singular saddle point of separation. This magnified figure is included to confirm the absence of any other vortex structures in the neighborhood of the singular upstream separation point. Significant features of this figure, are as for Fig. 5, (1) the presence of only one separation point, and (2) the absence of any lesser vortex structures around this separation point.

Figure 7 shows a surface flow visualization for the floor below the junction vortex. Significant features of this flow visualization are (1) the perceived singular saddle point of

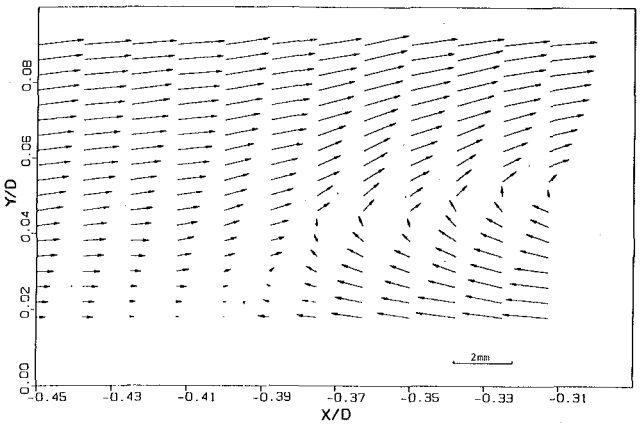

Fig. 6 LDV velocity field near the singular separation point. Typical uncertainty in $\bar{V}/V^*$ is ±0.009 or less.

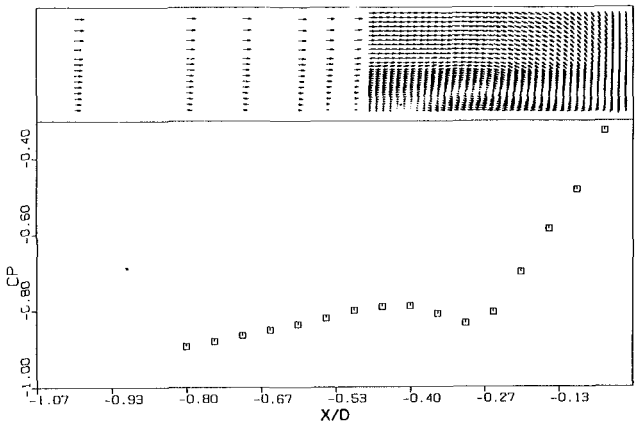

Fig. 8 Surface pressure distribution. Typical uncertainty in c_p is ±0.02.

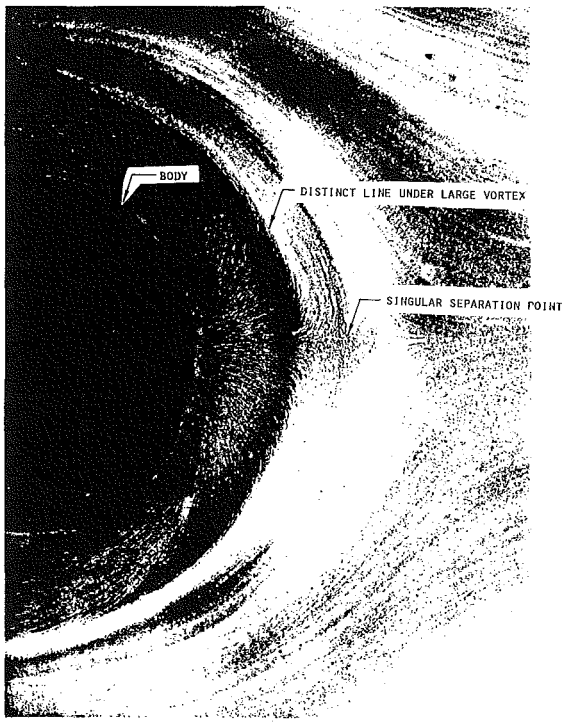

Fig. 7 Surface flow visualization

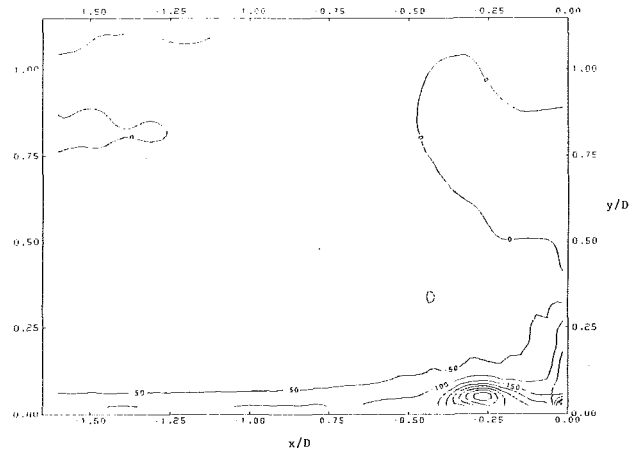

Fig. 9 Vorticity field computed from the measured LDV velocity field. Estimated typical uncertainty is ±10 percent.

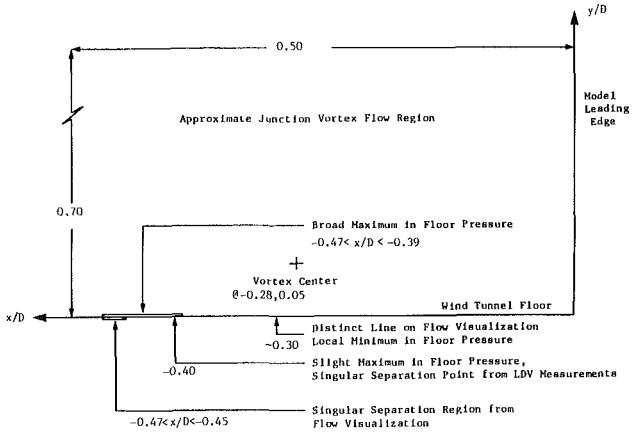

Fig. 10 Summary of junction vortex plane of symmetry flow observations

separation upstream of the junction vortex, and (2) the distinct line identified with the nominal center of the vortex structure above the floor. Additional details are presented in Pierce and Harsh [6, 12]. These two features are in agreement with the flow visualizations reported in Eckerle and Langston [13]. While additional separation and attachment lines might be speculated on, particularly if one looks to the sides of the figures away from the plane of symmetry, their existence is not well defined in the original, generally high quality, visualization. No clear evidence of an attachment line is seen in the body-floor corner.

Figure 8 shows the surface pressure coefficient along the symmetry plane relative to the LDV measured velocity field. The upper portion of this figure shows the relative position of the perceived separation point and vortex center relative to the local maxima and minima of the floor pressure field.

Figure 9 shows the transverse vorticity field computed from the measured velocity field. Significant features of this figure are (1) the presence of a large vortex approximately coincident with that seen in the velocity field of Figs. 4, 5, and 6, (2) the absence of any smaller vortices upstream of this larger, dominant vortex structure, and (3) the vorticity contours in the extreme corner of the junction which suggest the presence of a small, tightly wound corner vortex. The rotation of this corner vortex is opposite to the dominant vortex as it should be for a vortex pair. The computed vorticity field has local approximately equal minima and maxima values of −400 and 400/s for the principle vortex and the tightly wound corner vortex, respectively.

Figure 10 summarizes the features of the mean flow structure, based on results from the velocity measurements, surface visualizations, and surface pressure measurements.

Discussion

Hunt et al. [1] have proposed the four vortex plane of symmetry flow field model for a low speed turbulent junction vortex region essentially identical to that shown in Fig. 1. The model for the floor flow pattern was based on the application of kinematic principles and theorems in interpreting surface flow visualization results from surface mounted cubes and cuboids in a turbulent boundary layer. These same principles were also applied in constructing a model of the plane of symmetry velocity field. The Reynolds number of the experiments was of the order of 7×10^4, somewhat lower than the Reynolds number of 1.8×10^5 for the current experiment. It is noted, however, that the authors describe the streamline pattern shown for the turbulent horseshoe vortex system upstream of the obstacle in Fig. 1(*b*) as "inferred from the mean surface shear-stress pattern and smoke visualization studies in laminar boundary layers."

A similar flow model for the floor or surface flow and for the plane of symmetry velocity field has also been presented by Baker [3] and is shown in Fig. 1. Baker performed oil-flow visualization experiments of surface mounted cylinders for a wide range of Reynolds numbers ($4 \times 10^3 < R_D < 9 \times 10^4$). Typical surface streamlines from Baker's experiments are shown in Fig. 1(*a*). The flow pattern presumed for the plane of symmetry velocity field is shown in Fig. 1(*b*) and is essentially the same as given by Hunt et al. [1]. The floor flow model and the symmetry plane velocity field model of Hunt et al. [1] and Baker [3], are essentially identical in all respects. The floor or surface model consists of two pairs of separation/attachment lines. For a cylindrical body a separation point is typically seen at approximately one cylinder radius upstream of the leading edge. A separation line originating from this point wraps around the body approximately parallel to the forward half of the cylinder. This is followed closely by an attachment point on the symmetry plane, and an attachment line around the body. This is followed by a second pair of lines, with a second separation point on the symmetry plane and a corresponding separation line. Well beyond this, and very close to the body-surface corner, is a second attachment point and line. Kinematic considerations require these separation and attachment points and lines to occur in pairs [1]. Each of the separation and reattachment lines tends to wrap about the forward half of the body. For blunt bodies the same sequence of events is modeled, though a generalization on the approximate location of the first (and subsequent) singular points appears to be not easily made.

The symmetry plane velocity field model of Hunt et al. [1] and Baker [3], is consistent with the floor flow model. A large horseshoe or junction vortex dominates the flow, with a pair of smaller counter rotating vortices upstream of the large dominant vortex, and a third smaller corner vortex at the body-surface junction. These vortices occur as counter rotating pairs. Assuming the flow model figures given by the respective authors to be approximately correct in the relative physical sizes of the members of the vortex system, Hunt et al. [1] show the three smaller vortices to be about the same size, while Baker [3] shows the more remote upstream vortex, while clearly smaller than a dominant vortex, still significantly larger than the remaining two smaller vortices and as shown in Fig. 1(*b*). Both references [1 and 3] show figures which suggest that evidence of at least one of these secondary vortices in each of the models should be seen at a distance from the floor corresponding to the center of the dominant vortex.

Measurements in the current experiment were made at a body Reynolds number, R_D, of 183,000, and a momentum Reynolds number, R_θ, of 12,500. Measurements were made as close as 2.3 mm above the floor and 1.6 mm in front of the body leading edge. The most significant differences between the flow patterns proposed by Hunt et al. [1] and Baker [3], and the current velocity measurements, are that in the present work (1) only one vortex pair, and (2) only one singular saddle point of separation are clearly seen. Note that in Fig. 6 the velocity field measurements closest to the floor show no evidence of the presence of even a small vortex pair around the apparent separation point. Since velocity measurements were made as close to the wall as 2.3 mm, the pair of counter rotating vortices upstream of the primary horseshoe vortex in the four vortex flow field model [1, 3] would have to be contained within a wall layer with a characteristic scale of less than 2.3 mm, and could not be substantiated by the current measurements. While no clear evidence of a small corner vortex appears, the velocity field near the model is consistent with the presence of such a vortex, albeit a very small one.

Velocity vectors in the vicinity of the separation point are shown in Fig. 5. By projecting the vanishing streamwise velocity component onto the floor, the singular saddle point of separation is estimated to be at approximately 51 mm upstream of the body. It should be noted that the measured velocity vectors shown in Fig. 5 are all directed upward and away from the floor. This is the expected flow pattern near such a singular separation point. Assuming the relative scale to be approximately correct, the velocity field sketches in references 1 and 3 (see Fig. 1), one would expect to find in Fig. 5, between the upstream singular separation point and a vortex centerline, evidence of (1) a counter rotating vortex pair, (2) an attachment point, (3) a saddle point in the flow field preceding the primary vortex, and (4) a second separation point.

The measured velocity field shown in Fig. 5 shows only one singular separation point with no evidence of the additional flow features described above. This is also supported by the flow visualization of Harsh and Pierce [4] shown in Fig. 7 which indicates only one clear singular saddle point of separation on the symmetry plane at approximately one body radius upstream of the body leading edge. On or near the symmetry plane there is little evidence of either a reattachment point or a second separation point. From the nearest wall measurement upward throughout the measurement field the velocity vectors all show a positive vertical component. No evidence of a negative vertical component of velocity occurs in any local region as would be required in the neighborhood of an attachment point. Also absent in the measured flow field is any evidence of the counter rotating vortex pair, or the saddle point upstream of the primary vortex, where impinging flow vectors would be expected to connect the saddle point to any attachment point below.

The velocity field data were used to generate transverse vorticity contours shown in Fig. 9. This figure shows the single large vortex approximately in agreement with its position as indicated by the velocity field. The concentric contours in the corner of the body floor junction does strongly support the existence of a tightly wound counter rotating corner vortex. Evidence of such a vortex is not seen clearly in the velocity field data. Note, however, that no indications of a vortex pair upstream of the large vortex structure is predicted by the velocity data in these vorticity contours.

Earlier 5-hole probe studies of the mean velocity field of this junction vortex system reported in Pierce, Kim and Harsh [11] and Pierce and Harsh [12] also confirm the existence of a single large dominant vortex which appears to increase in scale with flow distance around the body. Eckerle and Langston [13] reported five-hole probe measurements for a larger circular cylinder at a somewhat higher Reynolds number, $R_D = 5.5 \times 10^5$. They also report a single vortex pair, with a dominant upstream vortex and a tightly wound corner vortex.

Dickinson [8] did not include detailed plane of symmetry measurements in his LDV work. Abid and Schmitt [14] used a similar shaped but larger body, with a yet higher Reynolds number, $R_D = 1.05 \times 10^6$ (and a momentum Reynolds number of 15,000). Their results are somewhat difficult to interpret.

While the symmetry plane results clearly show a single dominant vortex, there is evidence of three smaller vortices as in the Baker [3] four vortex model. The floor flow visualization appears to show only a single primary separation line, although the authors present two pairs of separation and reattachment lines in their interpretation of the floor flow visualizations. No computed vorticity field is presented although the velocity component contours presented do suggest such a vorticity figure would be useful in interpreting the velocity results further. Nonetheless, Abid and Schmitt show evidence of the smaller vortex pair which Hunt et al. [1] and Baker [3] model as occurring just upstream of the larger and dominant junction vortex. The existence of this vortex pair would also be consistent with additional separation and reattachment lines, though little evidence of these lines is seen in the floor flow visualization presented in [14].

Ishii and Honami [4] performed smoke wire visualization studies in an impinging jet geometry, simulating flow encountering a body of infinite diameter. For an $R_\theta = 2900$, one frame of a smoke wire visualization shows what appears to be a separation vortex upstream of the dominant junction vortex, consistent with a four vortex flow model.

For junction vortex flows, the number of vortex pairs and corresponding separation-attachment lines have been demonstrated to be Reynolds number dependent for both laminar [16] and supersonic turbulent [5] flows.The number of vortex pairs increases with Reynolds number in both cases. For laminar flows, increasing the body height/boundary layer thickness ratio, h/δ, also increases the number of vortex pairs [16]. It would seem reasonable to suspect that for the low speed turbulent case the junction vortex system structure may also be Reynolds number and possibly h/δ ratio dependent.

Table 1 summarizes six experiments on the symmetry plane flow for low speed turbulent junction vortex flows. Five of the six cases reviewed show consistency with a two vortex system for $R_D < 10^6$ and a four vortex system for $R_D > 10^6$. It should be noted that the documentation of the four vortex structures was not as detailed and convincing as in the studies showing a two vortex system. In the case of the exception, it is not clear whether the number of vortices reported in the model was verified by flow field measurements or smoke visualizations. This is noted since surface flow visualizations can be difficult to interpret.

Real-time smoke visualization studies on the plane of symmetry by Pierce, Kim, and Frangistas [9] have been made with the present model at 12 values of R_D over a wide range of Reynolds number, with $10^3 < Re_D < 1.8 \times 10^5$. Even at the lowest Reynolds number values, the vortex system was characterized as highly-time variant. For the entire R_D range studied, the flow was dominated by only one, relatively large, strongly time variant vortex. In virtually all cases, there were fleeting glimpses of smaller vortex structures, often in counter rotating pairs. However these appear to occur at random and for only fleeting views. This was in contrast to the time variant but clear view of the single large vortex that dominated the flow. Single frame viewing taken out of time context proved to be potentially misleading. An occasional single frame that could be interpreted as a multiple vortex structure looks very supportive of a four or six vortex model. However, when viewed in a continuous time context, such frames did not support the existence of multiple vortex structures. No evidence of a corner vortex was seen in any of the smoke visualizations.

Table 1

Source	R_D	R_θ	D/δ^*	Number of vortices
Baker [3]	1.1×10^5		11.3	4
Pierce, Kim and Harsh [11]	1.83×10^5	12500	11.2	2
Present LDV results	1.83×10^5	12500	11.2	2
Eckerle and Langston [13]	5.5×10^5	6150	65.	2
Abid and Schmitt [14]	1.05×10^6	15000	54[a]	4
Ishii and Honami [4]	∞	2900	∞	4[b]

[a] Assumes $\delta^*/\theta = 1.3$, representative of a near zero pressure gradient 2DTBL.

[b] Three vortices are shown in smoke wire figures, the number 4 is consistent with existence of vortex pairs.

Summary

The mean velocity field on the symmetry plane of a turbulent junction vortex was documented with a two-channel LDV system. This nonintrusive system precludes concerns over the effect of any physical probe inserted in the flow field. The velocity field was correlated with surface pressure measurements and surface visualizations.

A single large vortex dominated the flow and appeared to have its time average center lie over a local minimum in the surface pressure. The time average center position of this vortex also appeared to coincide with a clear, well scoured line around the body in the surface flow visualization and identified as a line of relatively high wall shear stress. The flow visualization suggests only one clear separation line.

A transverse vorticity field computed from the measured velocity field gives evidence of a small corner vortex at the junction of the body and floor. Neither the velocity field measurements nor the computed vorticity field indicate the presence of any other vortex structures for the flow conditions of the experiment.

A singular saddle point of separation indicated by the velocity field appears to coincide approximately with a local maximum in the floor pressure measurements, and these appear to be slightly behind the singular separation point inferred from the surface flow visualizations. This would suggest large gradients in the fluid layer immediately adjacent to the wall.

At the flow conditions of this experiment, a two vortex symmetry plane flow field is confirmed with one large vortex dominating the flow. A second, very small counter rotating vortex appears to exist in the extreme corner of the flow.

A survey of six studies of low speed turbulent junction vortex flows suggests that the number of vortex structures present appears to be body Reynolds number dependent, with the number of vortex structures increasing with R_D. While for laminar and supersonic junction vortex systems, multiple vortices, in pairs, of 2, 4, and 6 have been reported, the studies surveyed here report only 2 or 4 vortices.

Further study on (1) the number of vortex structures possible in a system, (2) the Reynolds number range over which the various multiple structures exist, and (3) the manner or means whereby the computational fluid mechanicist could expect a solver to predict the proper number of such vortex structures should be further examined.

For the flow conditions of this particular complex flow, including separation and flow reversal, the agreement between the nonintrusive LDV and intrusive multiple orifice pressure probe velocity measurements showed a high degree of agreement.

References

1 Hunt, J. C., Abell, C. J., Peterka, J. A., and Woo, H., "Kinematical Studies of the Flows Around Free and Surface-Mounted Obstacles; Applying Topology to Flow Visualization," *Journal of Fluid Mechanics*, Vol. 86, Part 1, 1978, pp. 179–200.

2 Baker, C. J., "The Laminar Horseshoe Vortex," *Journal of Fluid Mechanics*, Vol. 95, Part 2, Nov. 1979, pp. 347–368.

3 Baker, C. J., "The Turbulent Horseshoe Vortex," *Journal of Wind Engineering and Industrial Aerodynamics*, Vol. 6, No. 1–2, July 1980, pp. 9–23.

4 Ishii, J., and Honami, S., "A Three-Dimensional Turbulent Detached Flow with a Horseshoe Vortex," ASME *Journal of Engineering for Gas Turbines and Power*, Vol. 108, 1986, pp. 125–130.

5 Sidney, R., and Kitchens, C. W., "The Structure of Three-Dimensional Separated Flows in Obstacle-Boundary Layer Interactions," BRL Rpt. 1791, Aberdeen Proving Ground, June 1975.

6 Pierce, F. J., and Harsh, M. D., "Three-Dimensional Turbulent Boundary Layer Separation at the Junction of a Streamlined Cylinder with a Flat Plate," *Proceedings of the Third International Symposium on Flow Visualization*, Sept. 1983, pp. 59–63.

7 Langston, L. S., and Boyle, M. T., "A New Surface-Streamline Flow-Visualization Technique," *Journal of Fluid Mechanics*, 125, Dec. 1982.

8 Dickinson, S. C., "Flow Visualization and Velocity Measurements in the Separated Region of an Appendage-Flat Plate Junction," *Proceedings of the Ninth Biennial Symposium on Turbulence,* held at University of Missouri-Rolla, Oct. 1–3, 1984.

9 Pierce, F. J., Kim, C. M., and Frangistas,, G., Unpublished films, Mechanical Engineering, VPI&SU, Apr. 1987.

10 Pierce, F. J., Frangistas, G. A., and Nelson, D. J., "Geometry Modification Effects on a Junction Vortex Flow," *Proceedings of the Symposium on Hydrodynamic Performance Enhancement for Marine Application*, Naval Underwater Systems Center, Newport, RI, Nov. 1988.

11 Pierce, J. F., Kim, C. M., and Harsh, M. D., "The Mean Flow Structure of a Turbulent Junction Vortex," VPI-E-87-6, Mechanical Engineering, Virginia Polytechnic Institute and State University, Blacksburg, VA, Apr. 1987 (Available NTIS).

12 Pierce, F. J., and Harsh, M. D., "The Mean Flow Structure Around and Within a Turbulent Junction Vortex—Part II. The Separated and Junction Vortex Flow," ASME JOURNAL OF FLUIDS ENGINEERING, 110, Dec. 1988, pp. 415–423.

13 Eckerle, W. A., and Langston, L. S., "Horseshoe Vortex Formation Around a Cylinder," ASME *Journal of Turbomachinery*, Vol. 109, Apr. 1987, pp. 278–285.

14 Abid, R., and Schmitt, R., "Experimental Study of a Turbulent Horseshoe Vortex Using a Three-Component Laser Velocimeter," AIAA Paper 86-1069, May 1986.

15 Tree, I. K., "Laser Doppler Velocimeter Measurements in a Turbulent Junction Vortex," Dissertation, Mechanical Engineering, Virginia Polytechnic Institute and State University, Blacksburg, VA, June 1986. (Available University Microfilms)

16 Norman, R. S., "On Obstacle Generated Secondary Flows in Laminar Boundary Layers and Transition to Turbulence," Ph.D. dissertation,IIT, Dec. 1972.

Experimental Study of Flow Oscillation in a Rectangular Jet-Driven Tube

J. Iwamoto

Professor,
Department of Mechanical Engineering,
Tokyo Denki University,
Tokyo 101, Japan
Mem. ASME

Several papers, mainly of a theoretical nature, have been published on the oscillatory flow in a Hartmann-Sprenger tube. Quantitative exploration of the flow field has proved difficult and details are lacking. In the present work, using a rectangular tube, synchronous shadowphotography has been applied to visualize the flow field during stable oscillatory flow. The measurement of pressure has also been made for the case of steady flow when both ends of the tube are open. From these experimental results the necessary conditions for starting and maintaining a stable oscillatory flow in an H-S tube have been established.

1 Introduction

The arrangement known as the Hartmann-Sprenger tube (H-S tube) comprises a convergent nozzle aligned coaxially with a tube in which the end further from the nozzle is closed. When an underexpanded sonic jet is directed against the open end of the H-S tube, a violent oscillation of the air column in the tube occurs and a high temperature is produced at the closed end. Since Sprenger [1] first published his experimental results in 1954, several investigations have been made into the oscillatory behavior of the flow and, in particular, into the mechanism by which a stable high temperature is attained and into the practical application of the temperature effect [2].

It is now well known that the thermal effect is due to irreversible heating by shock waves and by wall friction. However, in order to maintain a constant high temperature, there must be a balance between the heat generated and that removed. With regard to the removal of heat generated, in addition to the heat transfer through the walls, it has been shown in reference [3], that the exchange of mass in the boundary layer at the contact surface between the so-called indigenous fluid which remains in the tube near the closed end and extraneous fluid is important.

The mechanism by which stable oscillation of the air column in the tube is initiated and maintained has not yet been satisfactorily explained. A theoretical analysis by Kawahashi and Suzuki [4] based on linear theory has shown that it is a self-excited oscillation due to the existence of a negative impedance. The results of experiments and theoretical analysis using a plugged tube or, what has been described as a Hartmann-Sprenger tube of zero length, have been reported by other investigators [5-7]. With this configuration, also, it is known that a stable oscillation of the flow field occurs when the plugged tube is placed in the underexpanded jet at a critical distance from the convergent nozzle. But in this case also the mechanism by which the stable oscillation is initiated and maintained has not been well established.

Iwamoto concluded in his paper [8] that the necessary conditions for flow oscillation in the H-S tube are the existence of a low pressure region and a positive pressure gradient near the open end during the period of inflow. But, since this conclusion was derived based on qualitative discussion of the experimental results, the explanation is unsatisfactory.

In the present paper, using a rectangular tube, synchronous shadowphotography has been applied to visualize the flow field in the space between the nozzle and H-S tube during stable oscillatory flow. The measurement of pressure has also been made for the case of steady flow when both ends of the tube are open. From these experimental results, the necessary conditions for oscillatory flow in an H-S tube have been established.

2 Experimental Arrangement

The apparatus used in the experiments is shown schematically in Fig. 1. Dry air is supplied to the plenum chamber in the side of which a convergent nozzle is fitted.

It is well known that the flow behavior in the flow field between the nozzle and open end of the tube and in its neighborhood plays an important role in understanding the mechanism of the self-excited flow oscillation in the tube. Since the flow in these fields is very complicated, it is difficult to make quantitative measurements of flow properties using an axially symmetric tube. Therefore in the present experiment a rectangular tube is used. With the rectangular tube the pressure distribution in the flow field between the nozzle and tube can easily be obtained by pressure taps on the side walls.

The height, H, of the convergent, or forcing nozzle is 8 mm and is equal to the height of the driven tube which is 170 mm long. The external angle of the tube wall at the open end is 10 degrees. The width of the nozzle and tube is constant and is equal to 8 mm. Larger sizes of the nozzle and tube are more

Contributed by the Fluids Engineering Division for publication in the JOURNAL OF FLUIDS ENGINEERING. Manuscript received by the Fluids Engineering Division October 4, 1988, revised manuscript received April, 1989.

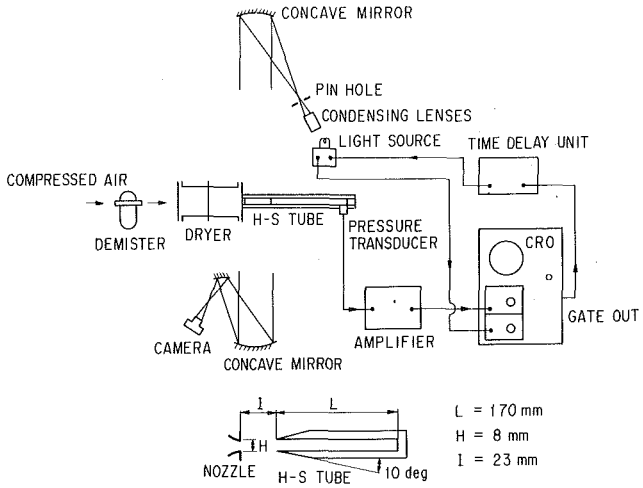

Fig. 1 Experimental apparatus

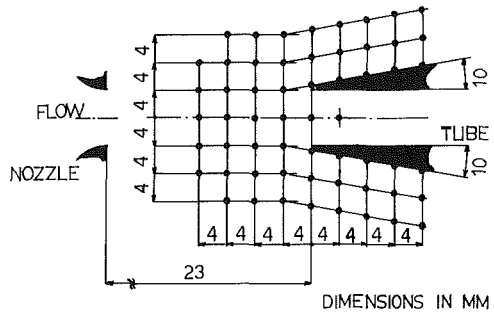

Fig. 2 Static pressure tap locations

favorable for quantitative measurements of the flow properties, but due to the capacity of the air source, these sizes are limited to the above values.

Whether the periodic flow oscillation takes place in the H-S tube or not depends upon the ratio of the stagnation pressure of the jet p_0 to the ambient pressure p_a and the tube separation distance l. In the present experiment the forcing nozzle, the internal surface of which is well finished, is underexpanded with the pressure ratio $p_0/p_a = 3.3$. Under this condition periodic flow oscillation is obtained at the tube separation distance $l = 23$ mm which is fixed during the experiment.

The flow in the space between the forcing nozzle and the driven tube has been visualized by synchronous shadowphotography. The window for the flow visualization is made of lucite, which can be replaced by side walls made of brass with taps for steady-flow pressure measurements for the tube with both ends open.

A pressure transducer located in the closed end of the tube gives a very periodic pressure history, and the discontinuous pressure rise due to the shock wave in the pressure history is used to trigger the light source. Thus, the time when each shadowgraph is taken is measured from the instant when the shock wave in the tube reaches the closed end.

The open tube, i.e., the tube with both ends open, is also used to obtain shadowgraph pictures and the static pressure distributions of the steady flow field in the vicinity of the end

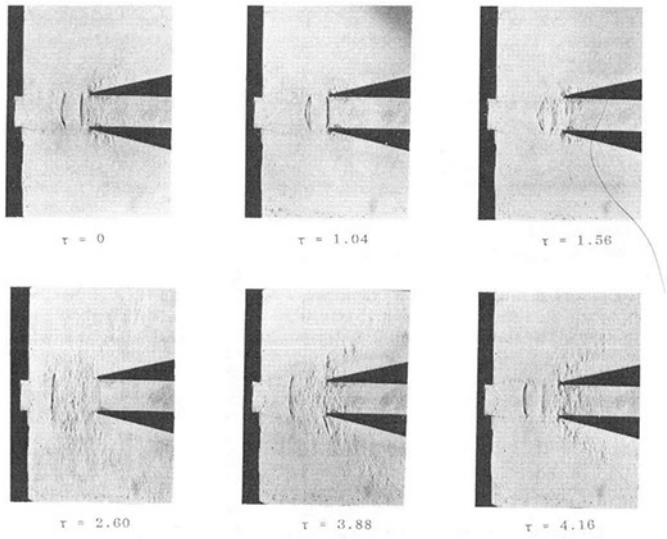

Fig. 3(*a*) Shadowgraphs of flow pattern during one cycle of oscillation; $p_0/p_a = 3.3$

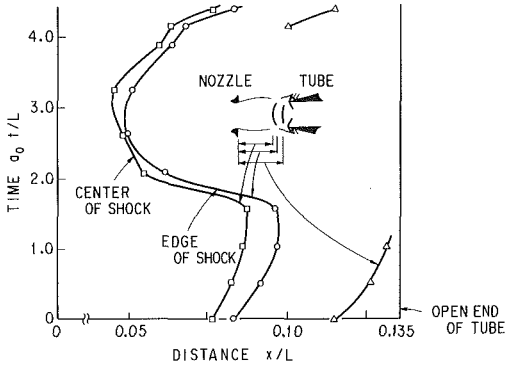

Fig. 3(*b*) Paths of the shock waves in the space between the nozzle exit and the open end of the tube; $p_0/p_a = 3.3$ (uncertainty in $x/L = \pm 0.002$ and in $\tau = a_0 t/L \simeq \pm 0.044$)

closer to the nozzle under the same arrangement. Static pressure taps, which are 0.4 mm in diameter, are located on the side wall of the nozzle and tube, as shown in Fig. 2.

3 Results and Discussion

3.1 Flow Visualization. Studies on the visualization of the axially symmetric flow field have already been published [8,9]. The present study concerns the flow field due to a rectangular tube and nozzle.

Typical shadowgraphs which reveal the characteristic features of the flow field between the nozzle exit and the open end of the tube, in a sequence of events within one cycle, are shown in Fig. 3(*a*). The observed frequency of the periodic flow was 454.5 Hz (periodic time 2.20 ms), and the calculated fundamental resonance frequency of the air column in the tube based on the length of the tube L and the stagnation speed of sound of the jet a_0 is 489 Hz. Since the average temperature

Nomenclature

a_0 = stagnation speed of sound of the jet
H = height of the nozzle and the tube
l = nozzle-tube spacing
L = length of the tube
p_a = atmospheric pressure
p_0 = stagnation pressure of the jet
t = time
x = distance measured from the nozzle exit plane
τ = nondimensional time = $a_0 t/L$

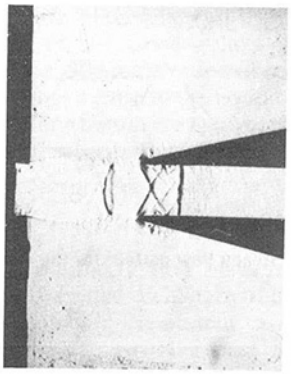

Fig. 4 Shadowgraph of flow pattern for the tube with both ends open; $p_0/p_a = 3.3$

of flow in the tube is actually higher than the stagnation temperature of the jet, the calculated frequency is higher than this value. The difference between these two frequencies implies that the open end correction made to the actual length of the tube for the estimation of the frequency is large because of the large amplitude oscillation. The time t is nondimensionalized by L/a_0 (a_0 is the stagnation speed of sound of the jet and L the length of the tube). The nondimensional time τ shown below each picture in the figure is measured from the instant when the shock wave in the tube reaches the closed end. Nondimensional periodic time is $\tau = 4.40$.

In each shadowgraph the nozzle can be seen in the left-hand side and the part of the tube near the open end in the right-hand side. All the shock waves in the nozzle jet are curved, while in axially symmetric flow an oblique shock and Mach disk are observed under similar conditions [9].

Figure 3(*b*) shows the trajectories of the shock waves in the space between the nozzle and open end of the driven tube, which are obtained from the shadowgraphs in Fig. 3 (*a*). In this figure the abscissa is the nondimensional distance x/L, where x is the axial distance measured from the nozzle exit plane. The open end of the tube is at $x/L = 0.135$.

The shadowgraphs at $\tau = 0$ and 1.04 in Fig. 3(*a*) show the flow field when the nozzle jet is flowing into the tube. It can be seen from these shadowgraphs that a bow shock and almost normal shock stand in the nozzle jet, and some wavelets can be seen along the outside surfaces of the tube walls. As can be seen in Fig. 3(*b*), during the period between $\tau = 0$ and 1.04 the location of the shock in the jet and the distance between the paths of the shock at the center and the jet boundary do not vary much with time compared with that between $\tau = 2.60$ and 4.16, during which the outflow from the tube takes place. This means that during the period of inflow the flow is relatively steady and stable compared with that during the outflow.

The shadowgraph at $\tau = 1.56$ shows the flow pattern at an instant during the time that flow into the tube is about to change into an outflow. Since the flow pattern in the flow field at this time and thereafter until the outflow pattern is established changes very quickly, the shadowgraph does not show the flow pattern clearly. Toward the end of the inflow phase, the shock wave reflected from the closed end of the tube reaches the open end and it comes out of the tube. And then, it merges with the almost normal shock which stands in front of the open end during inflow. This merged shock moves toward the curved shock in the nozzle jet and merges again with it, so that a strong single shock is formed by the time $\tau = 2.60$, when the almost steady outflow pattern is established. The shadowgraphs at $\tau = 2.60$ and 3.88 show almost steady outflow pattern. During the almost steady outflow period the jets from the nozzle and tube impinge on one another and are deflected sideward. So, there must be a collision layer between the standing shock in the nozzle jet and the open end (or the interface between two jets) which is not clearly seen in the shadowgraphs, while in the axially symmetric flow field, the collision layer can be easily located [9]. It is known that when a choked jet impinges upon a solid object, a shock wave always stands in the jet. That there is no shock wave in the outflowing jet from the tube means that the tube jet may be subsonic and unchoked. During the period of outflow no waves are observed along the outside surface of the wall. This flow pattern is not always as stable as that associated with inflow because the shock wave may fluctuate with a small amplitude of excursion on the axis.

As the outflow weakens with time, the flow pattern begins to change into that for inflow. As seen in the shadowgraph at time $\tau = 3.88$, the disturbed flow in the tube near the open end gives the indication that the outflow from the tube is starting to weaken. In the later stages of this transitional phase, at time $\tau = 4.16$, another shock wave appears in the space between the curved shock in the nozzle jet and the open end of the tube. This signals the start of the regime of quasi-steady flow into the tube. The inflow starts apparently at a time between $\tau = 4.16$ and 4.4.

Figure 4 shows the shadowgraph of the steady-state flow field when the jet blows into the tube with both ends open. Comparison of this with the shadowgraph taken at time $\tau = 1.04$ in Fig. 3(*a*) shows that these flow patterns are very similar as far as those features in the flow field outside the tube are concerned. In particular, the shock waves in both flow fields stand at almost the same position in the jet. Similar results are known to be obtained for axially symmetric flow [8].

Thus, in establishing the mechanism of the initiation and maintenance of the flow oscillation in an H-S tube, the following are considered and discussed. As a starting point, the jet from the nozzle may be assumed to be directed against a tube that has both ends open and that the steady-state flow pattern of Fig. 4 has been attained. If the right-hand end of the open tube is now suddenly closed, the flow pattern in the space between the nozzle and the open end of the tube will change. What has to be considered here is whether or not the same flow pattern as that of the original steady flow can be restored after the lapse of a certain time. If the flow pattern reverts to that of the steady state, then a periodic oscillation of the flow could result, since quasi-steady inflow could be one phase of a possible periodic oscillation.

In reference [8] it is mentioned that necessary conditions for the initiation and maintenance of the oscillatory flow in the tube are two-fold: the existence of a low pressure region near the open end along the outside surface of the tube wall and a positive pressure gradient along the center axis immediately upstream of the open end. This will be discussed in the next section.

3.2 Pressure Distribution for the Open Tube. As mentioned in the previous section, the necessary conditions for the initiation and maintenance of the flow oscillation in the H-S tube are derived from the qualitative point of view in reference [8]. These conditions are as follows. When the end of the open tube (the tube with both ends open) further from the nozzle is suddenly closed, while the open tube is blown steadily by the nozzle jet, a shock wave, or hammer wave, is produced at the closed end and travels upstream in the tube toward the open end. If the pressure gradient in the flow field upstream of the open end is positive, this shock wave can move across the open end and go further upstream in the nozzle jet. At the same time the low pressure region caused by the waves outside the tube, which is located outside the tube at a small distance downstream of the open end, moves upstream together with the above shock and takes the position at the edge of the open end. Therefore, the expansion wave reflected from the open end when the shock comes out becomes stronger because of the existence of the low pressure region at the edge of the open end. This reflected expansion wave moves toward the closed

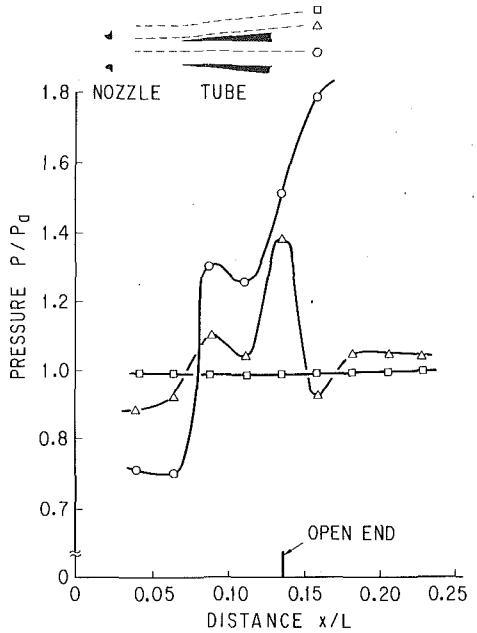

Fig. 5 Pressure distributions in the space between the nozzle exit and the open end of the tube; p_0/p_a = 3.3 (Uncertainty in p/p_a = ±0.025 and in x/L = ±0.002)

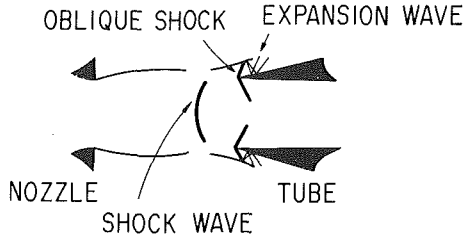

Fig. 6 Steady flow pattern for the open tube

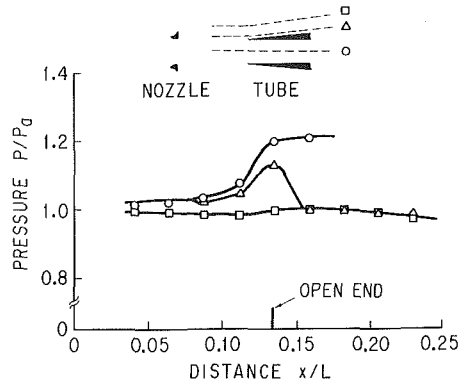

Fig. 7 Pressure distributions in the space between the nozzle exit and the open end of the open tube p_0/p_a = 2.0 (Uncertainty in p/p_a = ±0.025 and in x/L = ±0.002)

end, and when this expansion wave comes back to the open end from the closed end, a shock of enough strength is reflected from the open end for the oscillation not to die down. Thus, the low pressure region outside the tube near the open end is necessary for an expansion wave of enough strength to be reflected, as well as the positive pressure gradient in the flow field upstream of the open end.

In this section these conditions are discussed based on the pressure measurements for the steady flow case with both ends of the tube open.

Figure 5 shows the pressure distributions along lines parallel to the centerline of the nozzle and tube, and also, along the outside surface of the tube wall. Since the measured pressures are almost symmetrical about the centerline of the jet, the averages of the pressures along the upper lines and the corresponding lower lines are shown in the figure. The open end of the tube is located at $x/L = 0.135$ and the standing shock in the jet is at around $x/L = 0.087$.

The pressure distribution along the centerline shows the almost discontinuous pressure rise at $x/L = 0.087$ due to the shock wave and the continuous pressure rise in the tube due to the pseudo-shock waves consisting of some oblique shocks which originate at the edge of the open end. The slight pressure decrease at around $x/L = 0.112$ may be caused by the rarefaction waves which are reflected from the jet boundary as a result of the interaction of the shock at $x/L = 0.087$ with the jet boundary.

The pressure distribution along the outside surface of the tube wall shows the maximum pressure at the open end and the minimum pressure lower than atmospheric pressure at $x/L = 0.159$. This distribution suggests the existence of a wave system developed along the outside surface of the tube wall, which is not clearly shown in the shadowgraph (Fig. 4). As shown in the sketch in Fig. 6, the oblique shock attached to the edge of the open end extends outward to the jet boundary and a rarefaction wave is reflected from it, which is again reflected from the tube wall. Thus, the pressure downstream of the reflected rarefaction wave becomes lower than atmospheric pressure; this location approximately corresponding to that of the minimum pressure on the curve in Fig. 5.

As regards the other condition, i.e., the existence of the positive pressure gradient in the jet near the open end, the pressure distribution along the centerline of the jet in Fig. 5 shows the negative gradient which starts at $x/L = 0.088$ and is followed by the positive gradient at $x/L = 0.112$. Since the open end is located at $x/L = 0.135$, the positive part of the pressure gradient is present outside the tube. The negative pressure gradient is not large enough to stem an upstream movement of the shock wave in the nozzle jet.

In order to confirm that flow oscillation does not occur when the above conditions are not satisfied, the experiment was carried out with the nozzle pressure ratio p_0/p_a reduced to 2.0 and the nozzle-tube spacing kept constant. In this case flow oscillation does not occur when the end further from the nozzle is closed. The steady flow pressure distributions in the flow field for the tube with both ends open are shown in Fig. 7. The pressure distribution along the centerline of the jet shows the positive gradient just upstream of the open end, which is mostly due to the shock wave in the jet, although the pressure rise is smaller than that in Fig. 5. Thus, the shock wave which originates at the right-hand end when the end is suddenly closed can move out through the open end and travel upstream in the nozzle jet.

However, as can be seen from the pressure distribution along the outside surface of the tube wall, the pressure downstream of the position where peak pressure is reached is almost equal to the atmospheric pressure. Therefore, a region of low pressure as shown in Fig. 5 does not exist under this condition and a rarefaction wave of enough strength is not reflected from the open end for the oscillation to continue.

Thus, it can be concluded that the conditions necessary for the initiation and maintenance of flow oscillation of the H-S tube are the existence of a low pressure region along the outside surface of the wall near the open end and a positive pressure gradient in the jet upstream of the open end.

These findings can also be corroborated by the experiments on the oscillatory flow in an H-S tube using the hydraulic analogy by Iwamoto and Deckker [10]. In their water table experiments it was found that if a thin plate is inserted into

the oscillating flow field in the plane of the tube entrance, in contact with its edge, so as to remove the region of low depth (i.e., low pressure), the oscillation ceases abruptly. Also, when the open end is brought so close to the nozzle that the pressure gradient on the centerline becomes negative, then the flow does not oscillate, even if there is a region of low depth outside the tube.

5 Conclusions

Using a rectangular tube, a flow visualization study was made to reveal the self-excited oscillation of an H-S tube flow. From the results obtained in the present experiment the temporal change in the flow pattern in the space between the nozzle exit and the open end of the tube was discussed.

From static pressure measurements made for the open tube and the examination of the results developed in the previous work in reference [8], necessary conditions for the flow oscillation of the H-S tube were derived and established; i.e., they are the existence of a low pressure region on the outside surface of the tube wall and of a positive pressure gradient near the open end of the tube.

Acknowledgments

The work described was carried out by Mr. Y. Arai and Mr. K. Oshigane under the author's supervision. The author wishes to record his thanks to them for the use of their experimental results.

References

1 Sprenger, H., "Ueber thermische Effekte in Resonanzrohren," *Mitteil. Inst. Aerodynamik. E.T.H.*, Nr. 21, 1954, p.18.

2 Iwamoto, J., "Thermal Effect of Resonance Tube," Research Reports from Tokyo Denki University, No. 22, Dec. 1974, pp. 113–125.

3 Brocher, E., and Maresca, C., "Etude des phenomenes thermiques dans un tube de Hartmann-Sprenger," *Int. J. Heat Mass Transfer*, Vol. 16, 1973, pp. 529–548.

4 Kawahashi, M., and Suzuki, M., "Generative Mechanism of Air Column Oscillation in a Hartmann-Sprenger Tube Excited by an Air Jet Issuing from a Convergent Nozzle," *J. Appl. Math. and Phys.* (*ZAMP*), Vol. 30, 1979, pp. 797–810.

5 Moerch, K. A., "A Theory for the Mode of Operation of the Hartmann Air Jet Generator," *J. Fluid Mech.*, Vol. 20, Part 1, 1964, pp. 141–159.

6 Kukita, Y., "Impingement of Supersonic Jet on a Flat Plate," JSME Preprint, No. 750–16, 1975, pp. 229–231 (in Japanese).

7 Iwamoto, J., "Stability of a Resonance Flow," Research Reports from Tokyo Denki University, No. 17, Dec. 1969, pp. 135–143.

8 Iwamoto, J., "Necessary Conditions for Starting and Maintaining a Stable Oscillatory Flow in a Hartmann-Sprenger Tube," *Flow Visualization*, Vol. 4, 1986, pp. 507–512.

9 Iwamoto, J., and Deckker, B. E. L., "Cyclic Wave Action in the Stable Operation of a Hartmann-Sprenger Tube," *Proc. 13th Int. Symp. on Shock Tubes and Waves*, 1981, pp. 216–223.

10 Iwamoto, J., and Deckker, B. E. L., "A Study of the Hartmann-Sprenger Tube Using the Hydraulic Analogy," *Experiments in Fluids*, Vol. 3, 1985, pp. 245–252.

The Outflow of Buoyant Releases Including Fire Gases From a Long Corridor Closed at One End

M. A. Delichatsios
Factory Mutual Research Corporation,
Norwood, MA 02062

A new simple model is presented for the outflow of buoyant releases, including fire gases, from a long corridor closed at one end. A physical description of the model and application to well-documented data justify and validate the present model. The analysis incorporates the interaction of gravity (buoyancy) forces, turbulence, and entrainment rates into the plume rising from the fire. The model provides equations for predicting the temperature rise and the velocity in the ceiling layer if one knows the heat release rate from the fire and the air entrainment into the fire plume before the plume is submerged in the ceiling layer. Limited data and analysis indicate that the present flow situation allows a maximum entrainment rate into the fire beyond which the rate of the flow entering the corridor at the open end cannot further increase, i.e., the flow is choked. Although the data analyzed in this paper could not include buoyant outflows produced by fires at the end of a long corridor, the present model can be extended to apply for such flows as it is suggested by a recent Japanese paper [6] and other similar flows [3]. Of course, more experiments using fires in corridors are desirable to validate the present model.

Introduction

The objective of this paper is to identify the main parameters that can characterize flows of fire gases in long corridors and to present a method for calculating the temperature and velocities of the ceiling layer gases originating from a fire in a corridor.

The phenomena that control the motion of fire gases under a ceiling are mainly 1) the initial flow turbulence and momentum produced in the fire plume, and 2) the buoyancy forces in the ceiling layer, which act to stabilize the flow by reducing the turbulence levels (friction at the ceiling walls is, in general, small relative to gravity forces). Buoyancy in a horizontal stably stratified layer (e.g., a layer of hot fire gases) can generate permanent waves at the interface between hot and cold gases, can transform a (fast) supercritical flow to a subcritical flow by a hydraulic jump, and can destroy the turbulent fluctuations owing to its stabilizing influence on vertical displacements. Note that the buoyancy flow in the ceiling layer will be reduced by heat losses to the ceiling which are usually a significant amount of the enthalpy flow.

For the sake of illustration, we discuss several ceiling flows of gases investigated previously. The axisymmetric ceiling jet flow from a fire under an unobstructed ceiling has been analyzed by Alpert [1]; the jet starts as a supercritical flow (the local Froude number is greater than one); subsequently, its turbulence is decreased by the opposing buoyancy forces while, at the same time, entrainment rates to the ceiling jet continuously decrease. Entrainment, also, causes decay of the velocity until the flow becomes critical or subcritical (the local Froude number is equal or less than one). If the flow is obstructed (e.g., by a cylindrical curtain) or restricted (between ceiling beams), one observes that a hydraulic jump (which is similar to compressible gas shock) occurs to accommodate the flow under the obstruction (see Wilkinson [2], Delichatsios [3]). After the hydraulic jump, which may extend to a length of two to three times the layer thickness, the flow becomes critical or subcritical and entrainment to the ceiling layer ceases; waves may also develop or amplify after the hydraulic jump [4].

These simple concepts have been applied by the author to describing the flow of fire gases under a beamed ceiling [3]. We mention here that in that analysis [3] we ignored the possibility of having permanent interfacial gravity waves after the hydraulic jump even though the experimental results indicated the existence of such waves.

In this paper, we extend the application of the previous concepts to the flow of fire gases from a long corridor closed at one end. An important difference from other applications is that the corridor situation involves the counterflow of two layers of fluid having different densities: a cold incoming air layer and a hot outflow of fire gases. We illustrate the analysis and comparison with experimental results for a case representing a plane fire located at the closed end of the corridor (Section II). Then, we indicate in Section III, how these concepts can be applied to an arbitrary fire near the closed end of a corridor.

Contributed by the Fluids Engineering Division for publication in the JOURNAL OF FLUIDS ENGINEERING. Manuscript received by the Fluids Engineering Division April 4, 1988.

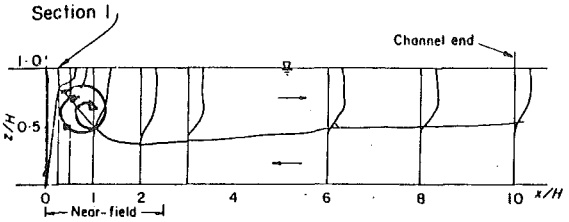

Fig. 1 Temperature field for buoyancy sources (e.g., fires) at one end of a channel or corridor

Description of the Physics

Figure 1 shows a diagram of the contours of the fire plume and the hot layer from a steady plane fire at the closed end of a corridor. The fire is assumed to have small flame height relative to the corridor height. It follows that such fires can be represented by a point buoyancy source having buoyancy flux $q_{\Theta,0}$ *per unit width of the corridor*

$$q_{\Theta 0} = \frac{\dot{Q}g}{\rho_\infty C_p T_\infty W} \tag{1}$$

where $\dot{Q}$ is the heat release from the fire, g is the gravitational constant, ρ_∞ is the ambient density, C_p is the specific heat, T_∞ is the ambient temperature, and W is the width of the corridor. The diagram in Fig. 1 is supported by experimental observations and measurements of turbulent buoyant jets in water discharging vertically into a two-dimensional channel [5].

The ceiling layer develops in the following way. Just after the hot fire products impinge on the ceiling, they form a ceiling jet which flows toward the open end of the corridor. During the initial transient flow development, the ceiling jet starts as a "shooting" flow wherein inertia forces are much greater than buoyancy forces (i.e., a characteristic Froude number is much greater than one). The depth of the ceiling jet layer increases by entrainment with increasing distance from the impingement area. The increasing depth of the ceiling layer causes a restriction to the flow area available to the counterflowing incoming entrainment air. Such a restriction of the flow area produces disturbances (gravity waves) at the interface between the hot and cold layers. These waves may induce the formation of a hydraulic jump which transforms the "shooting" ceiling-jet flow to "quiescent" ceiling jet flow (i.e., Froude number less or equal to one). Thus, the flow reaches a quasi-steady state.

In general, the location of the hydraulic jump in the ceiling jet flow depends on the entrainment characteristics and geometry of the flow [2, 3]. For the present two-dimensional plane flow geometry in a corridor, a hydraulic jump seems to occur near the impingement area according to experimental evidence [5–7]. It follows that a recirculating flow is formed near the impingement region. Following the flow transition near the impingement area, a "quiescent" ceiling flow is developed wherein entrainment of air is negligible so that the temperature in the ceiling layer may decrease only because of heat losses.

Best experiments for the present situation depicted in Fig. 1 have been reported by Jirka and Harleman [5] who conducted experiments in water using free turbulent plane buoyant jets with variable momentum flux at the source in two-dimensional channel flows. They claim in their analysis that a recirculating zone, as shown in Fig. 1, occurs only for high momentum fluxes at the source of the buoyant fluid [5].

It is proposed in this paper, based on observations of the experimental configurations [2, 5, 6] (see Fig. 1), that a recirculating zone is formed near the top of the turbulent buoyant jet. (Jirka and Harleman [5] suggest that for low momentum flows a hydraulic jump forms just after the impingement region. This hydraulic jump, however, is so close to the impingement region [5] that the ceiling flow must be "flooded" according to the definition of Wilkinson [2]). It should be emphasized that at the hydraulic jump, momentum is not lost but the convective part of the momentum is transformed to buoyant head (see, e.g., reference [2]). Experiments with buoyant flows [6] corroborate this observation. I am very gratified to point out that this conclusion has been independently corroborated in a recent paper by J. Andreopoulos, A. Paturi, and W. Rodi [11]. The size of the recirculating zone increases as the Froude number increases, i.e., as the momentum forces of the discharged jet become even larger than the buoyant forces. Finally, for high Froude numbers the vertical size of the recirculation zone becomes almost equal to the height of the channel. In every configuration, the recirculation zone is followed by a surface layer of hot fluid near the ceiling, since the channel communicates with a water reservoir (cf, with description of the experiments in reference [5]). Entrainment of fresh fluid occurs at the bottom part of the vertical buoyant jet. The turbulent fluctuations are dissipated in the recirculation zone. Therefore, no dilution is expected to occur in the surface layer of the hot fluid away from the jet axis.

Dimensional Analysis and an Analytical Model for the Flow

Before we present an analytical model for predicting temperatures in the ceiling layer, we replot the data for water in reference [5] by using simple dimensional analysis. The only length scale of the problem is the channel height, H, if one neglects the width of the buoyancy source. The independent variables of the source are its momentum flux, m_0, and its buoyancy flux, $q_{\theta 0}$ (see equation [1]), whereas, in consistence with the virtual source approximation, the flow rate at the source is zero. The momentum flux is defined per unit channel width, W, as

$$m_o = \frac{\rho_f u_f^2 B W}{W} = \rho_f u_f^2 B \tag{2}$$

wherein ρf is the density of the fluid at the source, u_f its velocity, and B is the width of the two-dimensional source slit.

The dependent variable is the density defect in the hot surface layer away from the buoyant jet axis. It is important to emphasize that the density defect should be introduced in the form of $\beta g \Theta_2$, where β is the thermal expansion coefficient of water, g is the gravitational constant, and Θ_2 is the temperature rise (over the cold layer) in the surface layer. The density defect in the form of $\beta g \Theta_2$, which has the dimensions of gravitational acceleration, is the appropriate term present in the momentum equation, while it also satisfies the heat transfer equation for a constant (i.e., independent of temperature) expansion coefficient. (Note that for gases $\beta\theta_2 = \frac{\theta_2}{T_\infty}$, if one assumes that the Boussinesqu approximation applies.)

The density defect in the surface layer away from the jet axis and the recirculation cell will be constant and independent of the distance from the jet axis because no entrainment occurs in this region of the ceiling layer and heat losses are ignored (cf, with discussion at the end of Section 1). By dimensional arguments the following relation can be deployed by using the independent variables (H, m_0, $q_{\Theta 0}$) and the dependent variable $g\beta\Theta_2$ of the present physical situation:

$$\frac{(\beta g \Theta_2)\, H}{q_{\Theta 0}^{2/3}} = fcn\left(\frac{m_0^{3/4}}{q_{\Theta 0}^{1/2} H^{3/4}}\right) \tag{3}$$

The dimensionless group at the RHS of equation (3) is a Froude number of the source with a characteristic length equal to the channel height.

All the experimental results (Table 1 in reference [5]) are

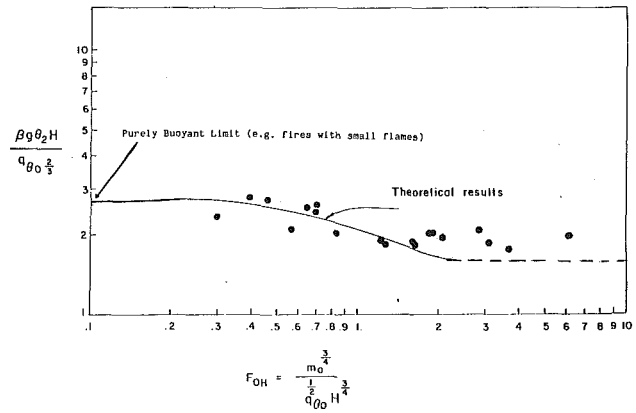

Fig. 2 Dimensionless density defect in the surface layer as a function of a discharged jet Froude number, equation (1) (Data from reference [5])

plotted on a log-log paper in Fig. 2 using the dimensionless variables in equation (3).

It is obvious that the correlation of all the experimental results is very good based on the simple hypothesis expressed by equation (3). Based on dimensional analysis, it can be observed, as corroborated by the experimental results (Fig. 2), that 1) for pure buoyant release (source momentum $= m_0 = 0$) as in small fires the dimensionless density defect, $\frac{\beta g \Theta_2 H}{q_{\Theta 0}^{2/3}}$, is expected to be constant; 2) when the recirculation cell covers the height of the channel the source term, $\frac{m_0^{3/4}}{q_{\Theta 0}^{1/2} H^{3/4}}$, should not influence appreciably the density defect. Therefore, it is expected that the dimensionless density defect $\frac{g\,\beta\Theta_2\,H}{q_{\Theta 0}^{2/3}}$, will take again a constant value but different from the value corresponding to purely buoyant flows.

The hypothesis expressed by equation (3), based on dimensional arguments, has been shown in Fig. 2 to correlate satisfactorily the experimental results. However, it is worthwhile to present a simple analysis of the discharge of a vertical buoyant jet in confined depth based on the physical model proposed in the introduction. The analysis will help generalize the model results, especially for the important case where significant heat (buoyancy flow) losses occur in the ceiling layer. Figure 3 is a sketch of the flow field in accordance with the physical model presented in this work. The plane turbulent buoyant jet released at 0 in Fig. 3 grows up to a height H-H_e; then a recirculation cell of height H_e is formed; subsequently a steady surface layer of hot fluid flows into a water reservoir at the end of the channel at Section 2.

All the turbulence is dissipated in the recirculation cell; therefore, no entrainment occurs in the surface layer flow. The mechanical energy, the mass, and buoyancy (thermal) conservation equations can be applied between the end of recirculation cell (Section 1 in Fig. 3) and the end of the channel (Section 2 in Fig. 3); *friction and heat losses along the channel are neglected for the present application*. Moreover, since no information about the discharge coefficients at the end of the channel is available, it is assumed that critical gravity flow conditions [5] exist at the end of the channel regarding the flow of the surface layer and its counterflow at the bottom of the channel. In the following analysis we assume that the property profiles in the ceiling layer are uniform.

The complete energy equation for the incoming and outgoing flow have the following form:

$$(g\beta\theta_e)\,H_e = \beta g\theta_2 h_2 + \frac{U_2^2}{2} + \frac{1}{2}\left(U_{b,e}^2 - \frac{1}{2}\,U_{b,2}^2\right) - \frac{1}{2}\,U_e^2$$

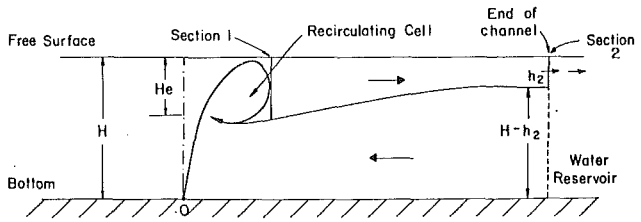

Fig. 3 Sketch of the flow of a plane buoyant turbulent jet discharging into a two-dimensional channel or corridor

wherein $U_{b,2}$, $U_{b,e}$ are the velocities of the incoming flow at the exit and near the recirculation cell, respectively, and U_e is the velocity of the outgoing flow just after the recirculation cell. The contributions of the last three terms at the RHS of the energy equation is negligible compared to the remaining terms. Therefore, the energy equation takes the following form for uniform property profiles

$$(\beta g\Theta_e)\,H_e = (\beta g\,\Theta_2)\,h_2 + \frac{U_2^2}{2} \tag{4a}$$

Here, h_2 and U_2 are the depth and the velocity in the surface layer at the end of the channel (see Fig. 3). At the LHS of equation (4*a*), we have neglected the kinetic energy of the flow going out of the recirculating zone as being small relative to the buoyancy (potential) energy. Note that this velocity cannot be calculated by using the apparent cross section of the flow in this region (H_eW); instead, the effective outflow area in this region is larger than the apparent area (H_eW) owing to the development of the recirculation cell (see Fig. 3). Observe, also, that the density defect in the recirculation cell is equal to the density defect in the surface layer, $(\beta g\ \Theta_e) = (\beta g\ \Theta_2)$, since no dilution occurs in the channel flow.

The mass flow (per unit mass and unit channel width) conservation in the ceiling layer can be written as:

$$q_2 = h_2 U_2 \tag{4b}$$

while the buoyancy ($\sim$ thermal energy) flow conservation gives:

$$q_{\theta 0}\ (\text{at the source}) = 2\ q_2 \beta g \theta_2 \tag{4c}$$

since no thermal losses occur in the present circumstances. The factor two at the RHS of equation (4*c*) accounts for the symmetry of the flow (see Fig. 1). Finally, the postulate of critical flow conditions (see also reference [5]) near the end of the channel provides the following equation:

$$F_1^2 + F_2^2 = 1 \tag{4d}$$

wherein F_1^2 is the Froude number of the incoming flow and F_2^2 is the Froude number of the ceiling layer flow:

$$F_1^2 = \frac{U_1^2}{(g\beta\theta_2\,(H-h_2)} = \frac{[U_1\,(H-h_2)]^2}{g\beta\theta_2\,(H-h_2)^3} = \frac{q_2^2}{g\beta\theta_2\,(H-h_2)^3} \tag{4e}$$

while

$$F_2^2 = \frac{U_2^2}{g\beta\theta_2 h_2} = \frac{q_2^2}{g\theta_2\beta\,h_2^3} = \frac{q_2^3}{(q_{\theta 0/2})\,h_2^3} \tag{4f}$$

To derive equations (4*e*) and (4*f*) we have used the fact that the incoming flow is equal to the outgoing flow as well as relations (4*b*) and (4*c*).

By using the conservation equations for mass and buoyancy flow and the assumptions of critical flow condition at the end of the channel, together with equations (4*e*) and (4*f*), one can show that

$$\frac{h_2}{H} = \frac{2}{F_2^2 + 2}\ \frac{H_e}{H} \qquad \text{(energy equation (4}a\text{))} \tag{5}$$

$$\frac{q_2}{q_{\Theta 0}^{1/3} H} = \frac{2\,F_2^{2/3}}{2^{1/3}(F_2^2 + 2)}\ \frac{H_e}{H} \qquad \begin{matrix}(q_2 = h_2 U_2)\\ (q_{\Theta 0} = 2\,q_2 \beta g\ \theta_2)\end{matrix} \tag{6}$$

$$F_2^2\left[\left(\frac{h_2}{H-h_2}\right)^3+1\right]=1 \text{ (critical flow conditions)} \quad (7)$$

A final relationship which closes the system of equations (5), (6), and (7) is provided by the expression of air entrainment into the flow from the floor ($Z=0$) to the height ($H-H_e$). The entrainment to a buoyant plane jet is conveniently provided by the following expression [5]:

$$\frac{q_1}{q_{\Theta 0}^{1/3}H}=\frac{I_1}{I_2^{1/2}}F_{0H}^{2/3}k^{1/2}\left(1+\frac{I_2^{1/2}I_4}{I_3}\frac{k^{1/2}}{F_{0H}{}^2}\left(1-\frac{H_e}{H}\right)^{3/2}\right)^{1/3}\left(1-\frac{H_e}{H}\right)^{1/2} \quad (8)$$

where I_1, I_2, I_3, and I_4 are profile-dependent coefficients defined in reference [1]; k is a constant growth factor for the width of the jet [5]; and F^2_{0H} is a Froude number characteristic of the source $\equiv \frac{m_0^{3/2}}{q_{\Theta 0}H^{3/2}}$, which is the square of the dimensionless group defined in equation (3). Note that because of symmetry, $q_2=\frac{q_1}{2}$.

The numerical values of the constants used in the present analysis are the following (5):

$$I_1=\sqrt{\pi}\,,\ I_2=\sqrt{\pi/2}\,,\ I_3=\lambda\sqrt{\frac{\pi}{1+\lambda^2}}\,,\ I_4=\lambda\sqrt{\pi}\,,$$

where $\lambda = 1.24$, $k = .147$. The following method was used for the solution of equations (5), (6), (7), and (8): first one chooses a value of $\frac{h_2}{H}$, then one finds the Froude number F_2^2 from equation (7) and $\frac{H_e}{H}$ from equation (5); finally, by equating equation (6) to half the values of RHS of equation (8), one can determine F^2_{0H}.

The analytical results are plotted in Fig. 2 using the same ordinates as before. Notwithstanding the simplicity of the model, it is obvious that there is good agreement of the experimental results with the theoretical predictions. Observe that for small values of the source Froude number (abscissa in Fig. 2) the theory predicts, in agreement with the experiments, a constant value of the dimensionless temperature rise $\frac{g\beta\Theta_2 H}{q_{\Theta 0}^{2/3}}$ $\simeq 2.76$; a physically acceptable solution of equations (2) to (7) exists up to the value of the Froude number $\frac{m_0^{3/4}}{q_{\Theta 0}^{1/2}H^{3/4}}=2.29$ (see Fig. 2). At this value the layer thickness is $h_2=\frac{H}{2}$, that is half the corridor depth. No physically acceptable solution for the system of equations (5), (6), (7), and (8) exists for larger values of the source Froude number. Subsequently, the depth layer depth, h_2 near the exit remains fixed and the entrainment to the jet is now controlled by the exit conditions and not by the characteristic jet entrainment requirements so that the flow rate into the corridor cannot further increase, i.e., the inflow is "choked." The experimental data [5] support this observation.

The results shown in Fig. 2 (with the abscissa set $\equiv 0$) can be directly applied to fires located at the closed end of a corridor, if one accounts appropriately for the presence of the wall. However, an additional consideration which must be taken into account is the *significant reduction by a factor of about two of the entrainment coefficient* for convective flows attached to a vertical wall[8]. Possible heat losses from the fire to the vertical wall should also be accounted for.

One may conclude that an answer to the fire problem in a corridor can be provided by solving the simple model represented by equations (4), (5), and (6) together with an appropriate equation for the entrainment (replacing equation (8)) into the fire. Such a model, which also includes heat losses, is outlined in the next section.

Application to Outflow of Gases in Corridor From Any Fire at the Closed End

A diagram of the smoke layer as shown in Fig. 3 is still applicable. We assume that the length of the corridor is larger than the length of the recirculation region. A steady fire is burning near the closed end of the corridor. The source fire may be a pan, a pool or a burning wall. We assume that we know the total heat release rate from the fire per unit width of the corridor in the form of a buoyancy flux $q_{\theta 0}$ (see equation (1)). The energy, buoyancy flow and mass flow equations take a form similar to equations (4), (5), (6), and (7) with the exception that in the present case the buoyancy flow in the ceiling layer is (cf with equation (4*c*))

$$q_{\theta 0}=q_2\beta\theta_2 g \quad (9)$$

These equations must be supplemented by an equation which provides the entrainment into the fire, $\dot{m}_{ent}/\rho_\infty$; if there are not other air supplies

$$q_2=\frac{\dot{m}_{ent}}{\rho_\infty}. \quad (10)$$

Note that the entrainment rate will depend on the fire size, geometry and flame height. One must use different expressions for pool fires [8], or wall fires [9]. It is out of the scope of the present work to carry out these calculations here. However, it is significant to notice, as we have observed in the previous section, that if the entrainment requirements to a specific fire are very high (so that $h_2/H = 1/2$), the flow into the corridor cannot further increase, and burning may become unstable.

The system of equations (5), (6), (7), (9), and (10) provides the (top-hat) velocity, temperature and depth in the hot ceiling layer. We mention again that heat losses from the hot gases to the ceiling have been neglected in the present model. These losses can be included by using a convective heat transfer coefficient to the ceiling in a way similar to the analysis presented earlier by the author [3]. In these circumstances the buoyancy ($\sim$ thermal energy) flow in the ceiling will decrease because of heat losses. A method for estimating such heat losses is sketched below. If one neglects the heat losses around the impingement area of the fire at the ceiling, convective heat losses to the ceiling can be calculated by the following integral heat transfer relation:

$$\frac{d}{dx}(q_2\theta_2)=-\frac{h_c}{\rho C_p}\theta_2 \quad (11)$$

Since $\theta_2 = T - T_{\text{amb}}$, equation (11) implicitly includes the specific assumption that the ceiling temperature is equal to the ambient temperature. The heat transfer coefficient can be modeled by considering a constant Stanton number [3, 10] $\frac{h_c}{\rho C_p U_2}=K$. Since the ceiling has constant depth over most of its length and $q_2 = h_2U_2$, equation (11) implies that the temperature decays exponentially with distance; such a result agrees with previous experiments [3], new experiments in tunnel fires [6] and new experimental evidence on the heat transfer to ceilings in corridors [10].

Conclusions

The major achievement of this work is the development of

simple algebraic equations for the prediction of temperatures and velocities in the ceiling gas layer produced by a fire at the closed end of a corridor; see equations (8*a*), (8*b*), and (8*c*) together with an entrainment equation (9) which depends on the geometry (pool, wall fire) and size of the fire (e.g., flame height). These equations represent the model shown in Fig. 3 and they have been validated by comparison with well documented data (see Fig. 2). Another important conclusion from the analysis and experimental data is the observation that for high air entrainment requirements into the fire, the inflow is restricted, i.e., the flow is choked and instabilities may develop in the burning behavior of the fire. Although the data analyzed in this paper could not include buoyant outflows produced by fires at the end of a long corridor, the present model can be extended to apply for such flows as it is suggested by a recent Japanese paper [6] and other similar flows [3]. Of course, more experiments using fires in corridors are desirable to validate the present model.

References

1 Alpert, R. A., "Turbulent Ceiling-Jet Induced by Large-Scale Fires," *Comb. Science and Technology*, Vol. 11, 1975, p. 197.

2 Wilkinson, D. L., and Wood, I. R., *Journal of Fluid Mechanics*, Vol. 47, 1971, p. 241.

3 Delichatsios, M. A., "The Flow of Fire Gases Under a Beamed Ceiling," *Combustion and Flame*, Vol. 43, 1981, pp. 1–10.

4 Chin, Wilson, C., "Kinematic Wave Approach to Hydraulic Jumps with Waves," *J. Hydronautics*, Vol. 13, No. 4, 1979, p. 120.

5 Jirka, G. H., and Harleman, D. R. F., "Stability and Mixing of a Vertical Buoyant Jet in Confined Depth," *J. Fluid Mech*, Vol. 94, 1979, pp. 275–304.

6 Kitahara, R., and Umezu, M., "Tunnel Fires," *Bulletin of Japan Association of Fire Science and Eng.*, Vol. 34, No. 1, 1984.

7 Miller, D. S., and Brighouse, B. A., "Therman Discharges," BHRA, The Fluids Engineering Centre.

8 Delichatsios, M. A., "A Simplified Algebraic Model for Turbulent Wall Fires," *21st Symposium (International) on Combustion*, Munich, Germany, Aug., 1986.

9 Delichatsios, M. A., "Air Entrainment into Buoyant Jets and Pool Fires," to be published in *Fire Science Handbook*, ed. by C. Beyler, 1986.

10 Zukoski, E., Private Communication, 1986.

11 Andreopoulos, J., Paturi, A., and Rodi, W., *JFM*, Vol. 168, 1986.

Y. Nagano
Professor.
Mem. ASME

M. Tagawa
Research Associate.

Department of Mechanical Engineering,
Nagoya Institute of Technology,
Nagoya 466, Japan

An Improved k-ϵ Model for Boundary Layer Flows

An improvement of the k-ϵ model has been made in conjunction with an accurate prediction of the near-wall limiting behavior of turbulence and the final period of the decay law of free turbulence. The present improved k-ϵ model has been extended to predict the effects of adverse pressure gradients on shear layers, which most previously proposed models failed to do correctly. The proposed model was tested by application to a turbulent pipe flow, a flat plate boundary layer, a relaminarizing flow, and a diffuser flow with a strong adverse pressure gradient. Agreement with the experiments was generally very satisfactory.

1 Introduction

Among the two-equation turbulence models, the k-ϵ model is currently most often used for turbulence predictions. However, not a few problems remain to be corrected (Patel et al., 1981, 1985). On the basis of the conclusions reached at the 1980–1981 Stanford Conference (Kline et al., 1981), Nagano and Hishida (1987) proposed an improved form of the k-ϵ model, which predicts very accurately various kinds of wall turbulent shear flows such as a pipe flow, a flat-plate boundary layer, a diffuser flow, a relaminarizing flow, etc. While this model seems to be satisfactory for the prediction of ordinary turbulent flows, even with heat transfer (Nagano and Kim, 1988), the wall limiting behavior of velocity fluctuations (Chapman and Kuhn, 1986) is not sufficiently considered in its modeling. Therefore, in the numerical analysis where an accurate prediction of near-wall turbulence is required, e.g., heat transfer analysis of high Prandtl number fluids (Myong et al., 1987), some errors may appear in the predictions. Also, the k-ϵ model is generally poor when applied in the calculation of shear flows with strong adverse pressure gradients (Patel et al., 1981, 1985). Even in the recent model of Nagano and Hishida (NH model, 1987), improvements to overcome this drawback have yet to be sufficient, and the rigorous prediction as to separation may result in failure.

The necessity to reflect the limiting behavior of turbulence on its modeling was pointed out by Patel et al. (1981, 1985), and details of the wall limiting behavior were discussed by Chapman and Kuhn (1986). Based on these studies, Myong and Kasagi (1988) performed an improvement of the k-ϵ model so as to reproduce the wall limiting behavior.

In the present study, we evolve the NH model and propose an improved version, in which the limiting behavior of turbulence and the effect of an adverse pressure gradient on shear layers are fully considered. The problems involved in the existing similar models (Lam and Bremhorst (LB), 1981; Myong and Kasagi (MK), 1988) are made clear from comparison of model results. Furthermore, the limiting behavior of free turbulence, such as the decay law of the final period of grid-generated turbulence, is shown to be incorrectly reproduced with the conventional k-ϵ model, and the solution to this problem is given.

2 k-ϵ Model for Wall Turbulence

2.1 Governing Equations. In the k-ϵ model, the reference velocity of turbulence is represented by $k^{1/2}$ determined from the turbulent kinetic energy k, and the characteristic length scale is given by $L_e = k^{3/2}/\epsilon$, which is the typical length scale of energy-containing eddies. Using the concept of eddy viscosity ν_t, the governing equations of the k-ϵ model for wall turbulence may be written as:

$$\frac{Dk}{D\tau} = \frac{\partial}{\partial x_j}\left\{\left(\nu + \frac{\nu_t}{\sigma_k}\right)\frac{\partial k}{\partial x_j}\right\} - \overline{u_i u_j}\frac{\partial \overline{U}_i}{\partial x_j} - \epsilon \tag{1}$$

$$\frac{D\epsilon}{D\tau} = \frac{\partial}{\partial x_j}\left\{\left(\nu + \frac{\nu_t}{\sigma_\epsilon}\right)\frac{\partial \epsilon}{\partial x_j}\right\} - C_{\epsilon 1} f_1 \frac{\epsilon}{k}\overline{u_i u_j}\frac{\partial \overline{U}_i}{\partial x_j} - C_{\epsilon 2} f_2 \frac{\epsilon^2}{k} \tag{2}$$

where

$$-\overline{u_i u_j} = \nu_t\left(\frac{\partial \overline{U}_i}{\partial x_j} + \frac{\partial \overline{U}_j}{\partial x_i}\right) - \frac{2}{3}\delta_{ij}k \tag{3}$$

$$\nu_t = C_\mu f_\mu k^2/\epsilon \tag{4}$$

and $D/D\tau = \partial/\partial\tau + \overline{U}_j\partial/\partial x_j$.

The determination of the model constants (C_μ, $C_{\epsilon 1}$, $C_{\epsilon 2}$, σ_k, σ_ϵ) and the model functions (f_μ, f_1, f_2) in equations (1)–(4) are discussed in Section 2.4. The turbulence quantities can be obtained from equations (1)–(4) together with the following continuity and momentum equations:

$$\partial \overline{U}_i/\partial x_i = 0 \tag{5}$$

$$\frac{D\overline{U}_i}{D\tau} = -\frac{1}{\rho}\frac{\partial \overline{P}}{\partial x_i} + \frac{\partial}{\partial x_j}\left(\nu\frac{\partial \overline{U}_i}{\partial x_j} - \overline{u_i u_j}\right) \tag{6}$$

2.2 Modeling of Limiting Behavior of Wall Turbulence. In the vicinity of the wall, the relations $\overline{U}^+ = y^+$, $u \propto y$, $v \propto$

Contributed by the Fluids Engineering Division for publication in the JOURNAL OF FLUIDS ENGINEERING. Manuscript received by the Fluids Engineering Division December 13, 1988.

y^2 and $w \propto y$ hold, as does $\epsilon = \nu \overline{(\partial u_i/\partial x_j)(\partial u_i/\partial x_j)} \rightarrow \epsilon_w$ for $y \rightarrow 0$. Consequently, the limiting behavior of wall turbulence is represented by the relations $k \propto y^2$, $-\overline{uv} \propto y^3$ and $\nu_t \propto y^3$. Then, from equation (4), the model function f_μ has to satisfy $f_\mu \propto y^{-1}$. As noted by Chapman and Kuhn (1986), none of the existing k-ϵ models summarized by Patel et al. (1981, 1985) meet this requirement. Myong and Kasagi (1988) concentrated on this problem and proposed the following model function:

$$f_\mu = (1 + 3.45/R_t^{1/2})\{1 - \exp(-y^+/70)\} \quad (7)$$

where $R_t = k^2/\nu\epsilon$ is the turbulence Reynolds number.

Nagano and Hishida (1987) have pointed out that appropriate modeling of ν_t from the buffer to log-law regions is crucial for accurate prediction of the well-known logarithmic velocity profile:

$$\overline{U}^+ = 2.5 \ln y^+ + 5.5 \quad (8)$$

They also validated the effectiveness of the following Van Driest damping function for f_μ:

$$f_\mu = \{1 - \exp(-y^+/A_\mu)\}^2, \; A_\mu = 26 \sim 27 \quad (9)$$

However, equation (9) changes as $f_\mu \propto y^2$ in the near-wall region and does not satisfy the limiting behavior $f_\mu \propto y^{-1}$. Thus, considering the characteristics of near-wall turbulence, we improve f_μ as follows to comply with the condition $f_\mu \propto y^{-1}$:

$$f_\mu = \{1 - \exp(-y^+/A_\mu)\}^2(1 + B_\mu/R_t^{3/4}) \quad (10)$$

The physical meaning of equation (10) is clear from equation (4). Thus, away from the wall (where R_t becomes large), the relation $\nu_t \propto k^{1/2} L_e$ holds and the eddy viscosity is thereby determined by the comparatively large-scale energy-containing eddies; but as the wall is approached, the eddy viscosity is reduced to $\nu_t \propto (k^2/\epsilon)/R_t^{3/4} = k^{1/2}\eta$ ($\eta = (\nu^3/\epsilon)^{1/4}$ is the Kolmogorov microscale) and determined by the small-scale eddies dominating mainly the dissipation process. This corresponds closely to the fact that the energy conservation law is maintained by dissipating almost all the energy which is diffusively transported from the region away from the wall (Nagano and Hishida, 1985).

On the other hand, from equation (2), the following equation holds at $y = 0$:

$$\nu\partial^2\epsilon/\partial y^2 = C_{\epsilon 2} f_2 \epsilon^2/k \quad (11)$$

Considering the limiting behavior of wall turbulence, $f_2 \propto y^2$ is required to satisfy equation (11). In free turbulence, as described in Section 2.3, the limiting behavior requires:

$$f_2 = 1 - 0.3\exp\{-(R_t/A_u)^2\} \quad (12)$$

Near the wall, we have $R_t = k^2/(\nu\epsilon) \propto y^4$, so that equation (12) reaches y^0. Thus, in the present study, the following equation is proposed after considering all possible items relating to the limiting behavior of wall and free turbulence as well.

$$f_2 = [1 - 0.3\exp\{-(R_t/A_u)^2\}]\{1 - \exp(-y^+/B_u)\}^2 \quad (13)$$

2.3 Modeling of Limiting Behavior of Free Turbulence. The decay law of the final period of homogeneous turbulence should be reproduced by a turbulence model as the limiting behavior of free turbulence. As is well known (Batchelor and Townsend, 1948a, 1948b; Comte-Bellot and Corrsin, 1966; Corrsin, 1951), the decay law of homogeneous turbulence is given by

$$k \propto x^{-n} \quad (14)$$

where the x axis is taken in the flow direction. The exponent n takes the value of $1 \sim 1.25$ during the initial period (Batchelor and Townsend, 1948a; Comte-Bellot and Corrsin, 1966) and 2.5 during the final period (Corrsin, 1951), respectively. In a homogeneous decaying turbulent flow, equations (1) and (2) become simply

$$\overline{U}\, dk/dx = -\epsilon \quad (15)$$

$$\overline{U}\, d\epsilon/dx = -C_{\epsilon 2} f_2 \epsilon^2/k \quad (16)$$

Thus, from equations (14), (15) and (16), we obtain

$$C_{\epsilon 2} f_2 = (n+1)/n \quad (17)$$

If we take $n = 1.1$ for the initial period ($f_2 = 1$), the model constant $C_{\epsilon 2}$ becomes 1.9. This is a typical value with the conventional k-ϵ models. In the final period, we obtain $f_2 = 0.7$ by substituting $n = 2.5$ and $C_{\epsilon 2} = 1.9$ into equation (17). Equation (12) has been derived from these relations.

2.4 Model Constants. In accordance with the conventional models (Patel et al., 1985; Nagano and Hishida, 1987), the model constants C_μ, $C_{\epsilon 1}$, $C_{\epsilon 2}$ and the model function f_1 are set to $C_\mu = 0.09$, $C_{\epsilon 1} = 1.45$, $C_{\epsilon 2} = 1.9$ and $f_1 = 1.0$. Usually, the constants σ_k and σ_ϵ are assigned to $\sigma_k = 1.0$ and $\sigma_\epsilon = 1.3$, but in the present study we adopt $\sigma_k = 1.4$ and $\sigma_\epsilon = 1.3$ in virtue of the results of the Reynolds stress equation modeling

Nomenclature

A_μ, B_μ, A_u, B_u = turbulence model constants
C_f = skin-friction coefficient = $\tau_w/(\rho \tilde{U}_e^2/2)$
C_μ, $C_{\epsilon 1}$, $C_{\epsilon 2}$ = turbulence model constants
DIFF(χ) = turbulent diffusion of χ
d = pipe diameter
f_μ, f_1, f_2 = turbulence model functions
k = turbulent kinetic energy = $\overline{u_i u_i}/2$
L_e = length scale of energy-containing eddies
M = mesh length
$\overline{P}$ = mean pressure
P_{ij} = generation rate of $\overline{u_i u_j}$
Re = Reynolds number = $\overline{U}_m d/\nu$
R_t = turbulence Reynolds number = $k^2/(\nu\epsilon)$
r_0 = pipe radius
$\overline{U}$, u = mean and fluctuating velocity components in x direction
$\overline{U}_i$, u_i = mean and fluctuating velocity components in x_i direction
$\overline{U}_e$, $\overline{U}_m$ = velocity external to boundary layer, and bulk velocity
$\overline{U}^+$ = dimensionless velocity = $\overline{U}/u_\tau$
u_τ = friction velocity = $\sqrt{\tau_w/\rho}$
v = fluctuating velocity component in y direction
x, y = coordinates
y^+ = dimensionless distance from wall = $u_\tau y/\nu$
δ_{ij} = Kronecker delta
ϵ = dissipation rate of k
ϵ_{ij} = dissipation rate of $\overline{u_i u_j}$
η = Kolmogorov microscale = $(\nu^3/\epsilon)^{1/4}$
ν, ν_t = molecular and eddy viscosities
ρ = density
σ_k, σ_ϵ = turbulence model constants for diffusion of k and ϵ
τ, τ_w = time and wall shear stress
ϕ_{ij} = pressure-strain rate
$\overline{(\ )}$ = time mean value

Subscripts

e = boundary-layer edge
m = bulk-mean
w = wall

Table 1 Constants and functions in the proposed k-ϵ model

C_μ	$C_{\epsilon 1}$	$C_{\epsilon 2}$	σ_k	σ_ϵ	f_μ	f_1	f_2
0.09	1.45	1.9	1.4	1.3	$\{1-\exp(-\frac{y^*}{26})\}^2\{1+\frac{4.1}{Rt^{3/4}}\}$	1.0	$[1-0.3\exp\{-(\frac{Rt}{6.5})^2\}]\{1-\exp(-\frac{y^+}{6})\}^2$

($\sigma_k/\sigma_\epsilon = 1.09$) by Hanjalić and Launder (1976). The effect of such manipulation is described in detail in Section 2.6.

With the asymptotic expansion for $-\overline{uv}$ near the wall and f_μ given by equation (10), we obtain:

$$-\overline{uv} \propto C_\mu(B_\mu/A_\mu^2)y^3 \tag{18}$$

If the experimental values of $-\overline{uv}$ near the wall are available, the best combination of the model constants A_μ and B_μ can be determined. In the meantime, to obtain the solution for the universal velocity profile in the log region (equation (8)), the model constant A_μ should match the Van Driest constant (Nagano and Hishida, 1987). Moreover, since the ratio of the Kolmogorov microscale, η, to the scale of eddies responsible for the turbulence dissipation, L_d, is about $\eta/L_d = 0.2 \sim 0.25$ (Nagano and Hishida, 1985), B_μ is eventually equal to $1/0.25 \sim 1/0.2 = 4 \sim 5$. Thus, we put: $A_\mu = 26$ and $B_\mu = 4.1$.

So far, the model constant A_u in equation (12) has been set at $A_u = 1.0$ (Patel et al., 1985). However, as described later, the use of this value does not follow the decay law of homogeneous turbulence. Therefore, the constants A_u and B_u in equation (13) are assigned to $A_u = 6.5$ and $B_u = 6.0$ so as to satisfy the limiting behavior of free and wall turbulence. The model constants and functions of the proposed k-ϵ model are summarized in Table 1.

2.5 Numerical Scheme. The numerics sometimes affect the results of the turbulence models both in the algorithm chosen and the number and distribution of grid points (Kline et al., 1981). Therefore attention was paid to the numerics so as to make model appraisal more meaningful. The numerical technique used is a well-tested Keller's Box method (Bradshaw et al., 1981). It is known that this method is unconditionally stable and the accuracy of a solution is high. The coordinate for regions of very large gradients should be expanded near the wall. Thus, for internal flows, a transformation is introduced so that $\zeta = (y/r_0)^{1/2}$. For external flows, the following nonuniform grid (Bradshaw et al., 1981) across the layer is employed:

$$y_j = \Delta y_1 (K^j - 1)/(K - 1) \tag{19}$$

where Δy_1, the length of the first step, and K, the ratio of two successive steps, are chosen as 10^{-5} and 1.03, respectively. For both internal and external flow cases, 201 cross-stream grid points were used to obtain grid-independent solutions. The first grid point was normally located well into the viscous sublayer: e.g., less than $y^+ = 0.03$ in the case of internal flows. To confirm the numerical accuracy, the cross-stream grid interval was cut in half for the internal flow cases. No significant differences were seen in the results. In order to resolve the streamwise changes in the viscous sublayer sufficiently, the maximum streamwise step-size was restricted to a sublayer thickness, i.e., $\Delta x < \nu/u_\tau$.

The boundary conditions are: $\overline{U} = k = \partial k/\partial y = 0$ and $\epsilon_w = \nu(\partial^2 k/\partial y^2)_w$ at $y = 0$ (wall); $\partial\overline{U}/\partial y = \partial k/\partial y = \partial\epsilon/\partial y = 0$ at the axis for internal flows (symmetry); $\overline{U} = \overline{U}_e$, $\overline{U}_e dk/dx = -\epsilon$ and $\overline{U}_e d\epsilon/dx = -C_{\epsilon 2} f_2 \epsilon^2/k$ at the free stream for external flows where $\overline{U}_e$ or $d\overline{P}/dx$ is prescribed from experiments.

The criteria for convergence are:

$$\mathrm{Max}|Y^{(i+1)} - Y^{(i)}|/\mathrm{Max}|Y^{(i)}| < 10^{-5} \tag{20}$$

where $Y = \partial X/\partial y$ (X: $\overline{U}$, k, and ϵ),

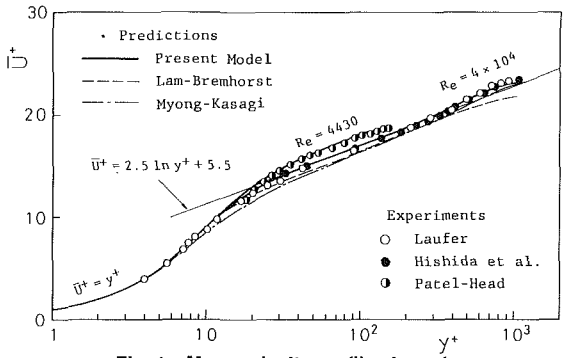

Fig. 1 Mean velocity profiles in a pipe

and

$$|U_\tau^{(i+1)} - U_\tau^{(i)}| < 10^{-5} \tag{21}$$

where $U_\tau = u_\tau/\overline{U}_m$ or $u_\tau/\overline{U}_e$, $u_\tau = \sqrt{\tau_w/\rho}$ with $\tau_w/\rho = \nu(\partial\overline{U}/\partial y)_{y=0}$, and i denotes the number of iterations. Calculations stop when both criteria are satisfied. The computations were performed on a FACOM M-780/20 computer.

2.6 Results and Discussion. The predictions of the universal velocity profile in a pipe are shown in Fig. 1. The present model predicts exactly the universal velocity profile given by equation (8), and agreement with the experiments (Laufer, 1954; Hishida et al., 1980) is almost perfect. The models of MK and LB slightly undershoot the universal velocity profile given by equation (8). In addition, the present model can predict progressive deviation from equation (8) with decreasing Reynolds numbers (Patel and Head, 1969). To identify the performance of the present model for lower Reynolds-number flows, the calculations of a channel flow at Re = 1835 were made and compared with the experimental data of Patel and Head (1969). Agreement with the experiment was virtually complete (not shown).

The calculated profiles of turbulence energy k near the wall are shown in Fig. 2. The wall limiting behavior of k predicted by the present model becomes $k/u_\tau^2 \simeq 0.03y^{+2}$. Obviously, this is almost in agreement with the result of the MK model and the value estimated from the experiments (Derksen and Azad, 1981). The LB model gives a little smaller prediction than the present and MK models.

The predictions of the Reynolds shear stress $-\overline{uv}$ near the wall are shown in Fig. 3. The present near-wall profile of $-\overline{uv}$ may be represented by $-\overline{uv}/u_\tau^2 \simeq 2 \times 10^{-4}y^{+3}$. On the other hand, the result of the MK model is $-\overline{uv}/u_\tau^2 \simeq 6 \times 10^{-4}y^{+3}$, which agrees with $-\overline{uv}/u_\tau^2 = (5 \sim 7) \times 10^{-4}y^{+3}$ calculated from the coherent eddy model (Chapman and Kuhn, 1986). As seen from equation (18), the present model does provide the same coefficient of y^{+3} as these values by using a smaller value for A_μ. However, if A_μ is made smaller, the universal "law of the wall" given by equation (8) cannot be reproduced correctly and the prediction becomes a bit smaller than equation (8). Whether or not a turbulence model can reproduce the law of the wall correctly is one important criterion to judge the quality of the model (Patel et al., 1981, 1985). Therefore, in the present study, we attach greatest importance to the accuracy of a velocity profile prediction. As mentioned previously, the MK model seems to be constructed

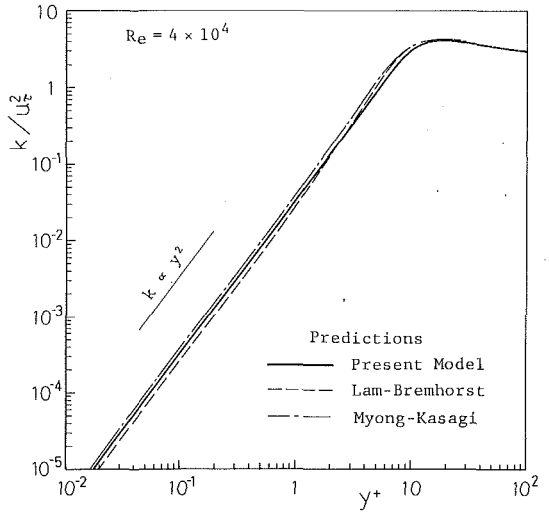

Fig. 2 Near-wall behavior of turbulent kinetic energy

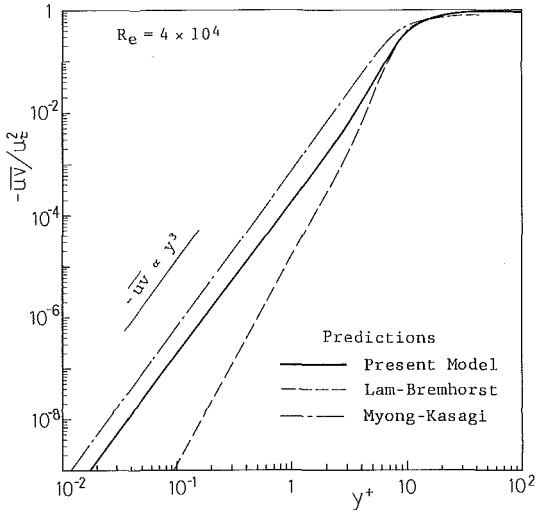

Fig. 3 Near-wall behavior of Reynolds shear stress

at a certain sacrifice of the accuracy of the velocity profile prediction. Also, there are no direct experimental results which prove the coefficient of y^{+3} to be $(5 \sim 7) \times 10^{-4}$. For these reasons, we have judged it meaningless to further refine the model at this stage. It should be mentioned here that the LB model does not satisfy the wall limiting behavior of $-\overline{uv} \propto y^3$.

Another important criterion of the appropriateness of a turbulence model was emphasized by Patel et al. (1985), namely, the examination of the model function f_μ. As shown in Fig. 4, the present model function follows closely the actual measurements (see Patel et al. (1985) for full details). However, a significant discrepancy is observed in the model functions of the MK and LB models, at least in the log region.

In the near-centerline region, the production terms in equations (1) and (2) are negligible because of $\partial\overline{U}/\partial y \simeq 0$, and the turbulent diffusion terms balance mainly with the dissipation terms. Since the model constants σ_k and σ_ϵ are set as $\sigma_k < \sigma_\epsilon$ (i.e., $\sigma_k = 1.0$ and $\sigma_\epsilon = 1.3$) in the conventional models, the turbulent diffusion of k from the wall region overwhelms that of ϵ. Consequently, as illustrated in Fig. 5, the predicted values of k in the core region become larger than the experiment. However, this problem is resolved simply by putting $\sigma_k = 1.4$ and $\sigma_\epsilon = 1.3$ as in the proposed model.

Unrealistic behavior of ν_t in the core region of the flow

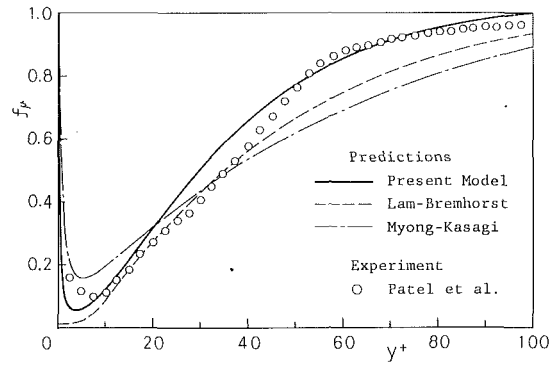

Fig. 4 Variation of the model function f_μ with wall distance

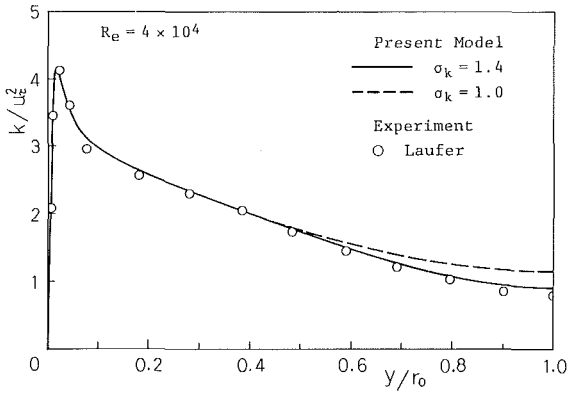

Fig. 5 Turbulent energy profiles in a pipe

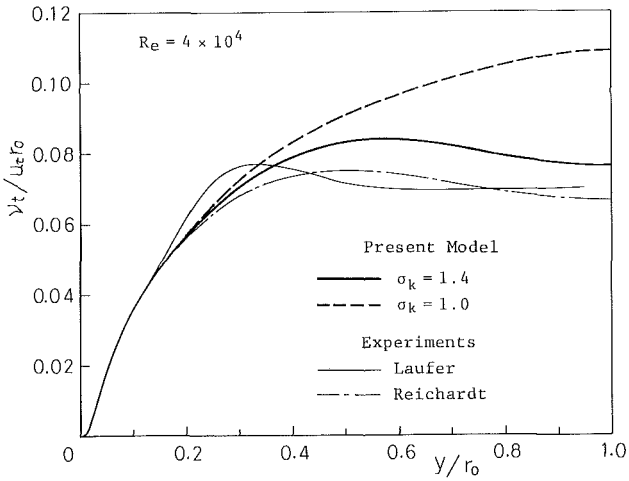

Fig. 6 Variation of eddy viscosity in the core region

(Takemitsu, 1987), known as a common drawback of the k-ϵ models, can be corrected, as shown in Fig. 6, by altering $\sigma_k = 1.0$ to 1.4. Thus the experimental profile (Laufer, 1954; Reichardt, 1951) is well reproduced with the k-ϵ model.

In the constant-stress layer, σ_ϵ is related to other model constants such as:

$$C_{\epsilon 1} = C_{\epsilon 2} - \kappa^2/\sigma_\epsilon \sqrt{C_\mu} \tag{22}$$

Therefore, in order to minimize the modification of model constants, it is desirable to retain the typical σ_ϵ value.

To assess the performance of the present model for the prediction of external flows, the calculations of a flat-plate boundary layer are compared with the experimental data (Gibson et al., 1982; Verriopoulos, 1983). The prediction of mean

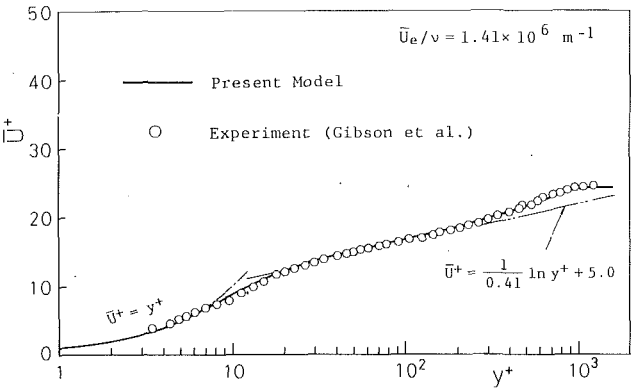

Fig. 7 Mean velocity profile in a flat-plate boundary layer

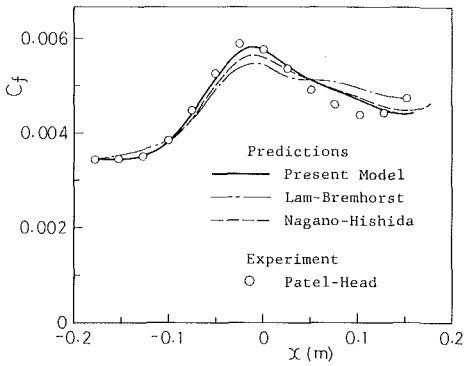

Fig. 8 Comparison of model results for relaminarizing flow

velocity profile in the turbulent boundary layer is presented in Fig. 7, compared with the experimental result (with streamwise location at x = 971 mm downstream from leading edge). Obviously, agreement with the experiment is virtually perfect, and the predictions of the turbulent kinetic energy k and the Reynolds stress $-\overline{uv}$ reproduce very accurately the experimental results of Verriopoulos (1983) (not shown).

To examine the accuracy of the prediction for more complex turbulent flows, a relaminarizing flow was analyzed with the proposed model. Relaminarization or retransition is the phenomenon by which upstream turbulence changes into a laminar flow under a sustained steep, streamwise acceleration. Numerical calculation was performed under the same condition as the experiment of Patel and Head (1968). The prediction of the skin-friction coefficient C_f is presented in Fig. 8, compared with the measurements (Patel and Head, 1968). In order to predict the correct value of C_f with a turbulence model, accurate calculation of wall shear stress $\tau_w = \mu(\partial\overline{U}/\partial y)_w$ is crucial. Hence, adequacy of modeling for near-wall turbulence reflects seriously on the C_f result. From Fig. 8 it is clear that the calculations with the proposed model reproduce accurately the succession of stages that occur in a relaminarizing flow: the initial increase in C_f under a steep acceleration of streamwise velocity accompanied by a strong favorable pressure gradient $d\overline{P}/dx < 0$, and the subsequent decrease in C_f associated with retransition. The accuracy of prediction is generally good in comparison with the LB and NH models.

In two-equation turbulence modeling, the limiting behavior of free turbulence has not yet been sufficiently discussed. As mentioned in Section 2.3, the decay law of homogeneous turbulence is given by equation (14). From equation (1), this leads to $\epsilon \propto x^{-(n+1)}$, and the decay law is rewritten in terms of the turbulent Reynolds number R_t as:

$$R_t \propto x^{-(n-1)} \tag{23}$$

Substituting n = 1.1 for the initial period and n = 2.5 for the final period into equation (23) yields:

$$\left.\begin{aligned} R_t &\propto x^{-0.1} \quad \text{(initial period)} \\ R_t &\propto x^{-1.5} \quad \text{(final period)} \end{aligned}\right\} \tag{24}$$

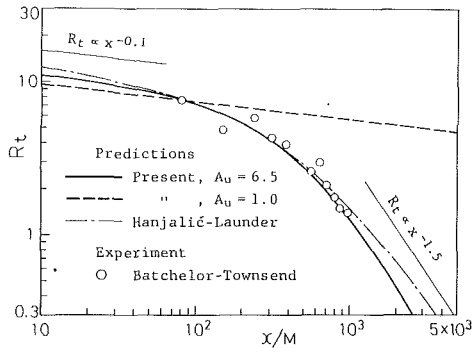

Fig. 9 Decay law of homogeneous turbulence

Figure 9 shows the present calculations, compared with the experimental result (Batchelor and Townsend, 1948a). In the existing k-ϵ models, the constant A_u in f_2 (equation (12)) is assigned the value of 1.0 (Patel et al., 1985; Nagano and Hishida, 1987). However, as seen from Fig. 9, this modeling cannot analyze the decay law of homogeneous turbulence. Replacement of A_u = 1.0 with 6.5, as in the proposed model, makes it possible to predict this decay law. Hanjalić and Launder (1976) proposed the following function for f_2 in their Reynolds-stress equation model.

$$f_2 = 1 - (0.4/1.8)\exp\{-(R_t/6)^2\} \tag{25}$$

with $C_{\epsilon 2}$ = 1.8. Using equation (25) with $C_{\epsilon 2}$ = 1.8, almost the same result can be obtained as with the present model ($C_{\epsilon 2}$ = 1.9).

3 Effects of Adverse Pressure Gradients

3.1 Model Improvement. In a flow under adverse pressure gradient conditions ($d\overline{P}/dx > 0$), the additional production of ϵ due to deceleration becomes significant (Hanjalić and Launder, 1980). Hence, adding this effect to equation (2), the transport equations of k and ϵ are given by:

$$\frac{Dk}{D\tau} = \frac{\partial}{\partial y}\left\{\left(\nu + \frac{\nu_t}{\sigma_k}\right)\frac{\partial k}{\partial y}\right\} - \overline{uv}\frac{\partial \overline{U}}{\partial y} - (\overline{u^2} - \overline{v^2})\frac{\partial \overline{U}}{\partial x} - \epsilon \tag{26}$$

$$\frac{D\epsilon}{D\tau} = \frac{\partial}{\partial y}\left\{\left(\nu + \frac{\nu_t}{\sigma_\epsilon}\right)\frac{\partial \epsilon}{\partial y}\right\} - C_{\epsilon 1} f_1 \frac{\epsilon}{k}\overline{uv}\frac{\partial \overline{U}}{\partial y}$$

$$- C'_{\epsilon 1} f_1 \frac{\epsilon}{k}(\overline{u^2} - \overline{v^2})\frac{\partial \overline{U}}{\partial x} - C_{\epsilon 2} f_2 \frac{\epsilon^2}{k} \tag{27}$$

where x denotes the streamwise coordinate. Since the model constant $C'_{\epsilon 1}$ in equation (27) is required to satisfy $C'_{\epsilon 1} > C_{\epsilon 1}$, we take $C'_{\epsilon 1} = 2.5C_{\epsilon 1}$ with reference to Hanjalić and Launder (1980). All other model constants and functions are the same as in Section 2.

Equations (26) and (27) are not closed because these equations involve unknown turbulence quantities $\overline{u^2}$ and $\overline{v^2}$. Bradshaw (1967) revealed from his experiments that the structural parameter $a_1 = -\overline{uv}/k$ remains nearly constant even in strong adverse pressure gradient flows. From this finding, for closing equations (26) and (27), we can use the following algebraic stress model (ASM) constructed on condition that the variation of a_1 is negligible (Rodi and Scheuerer, 1983).

$$\frac{D\overline{u_i u_j}}{D\tau} - \mathrm{DIFF}(\overline{u_i u_j}) = P_{ij} + \phi_{ij} - \epsilon_{ij} \tag{28}$$

where

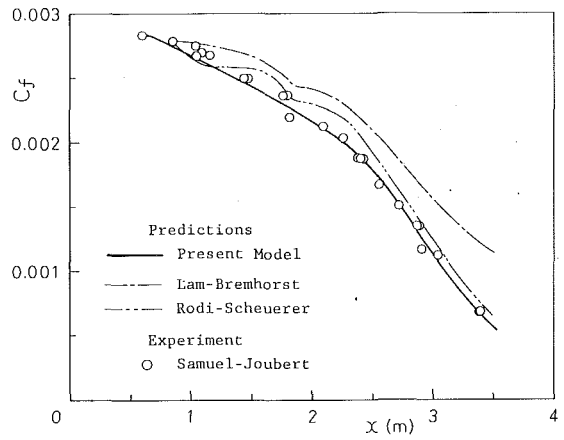

Fig. 10 Comparison of model results for strong adverse pressure gradient flow

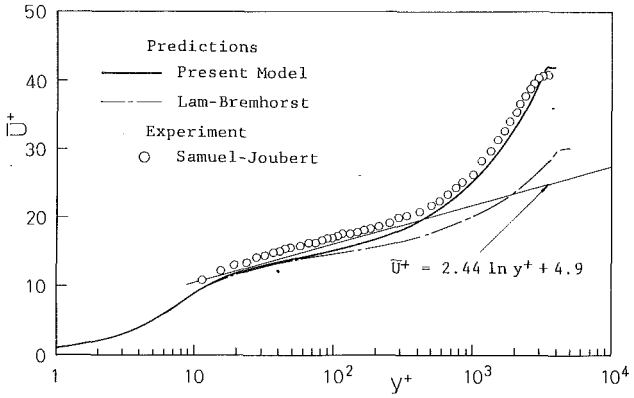

Fig. 11 Mean velocity profiles in a strong adverse pressure gradient flow

$$\frac{D\overline{u_iu_j}}{D\tau} - \mathrm{DIFF}(\overline{u_iu_j}) = \frac{\overline{u_iu_j}}{k}\left\{\frac{Dk}{D\tau} - \mathrm{DIFF}(k)\right\} = \frac{\overline{u_iu_j}}{k}(P_k - \epsilon) \tag{29}$$

and

$$P_{ij} = -(\overline{u_iu_k}\,\partial\overline{U}_j/\partial x_k + \overline{u_ju_k}\,\partial\overline{U}_i/\partial x_k),\ P_k = P_{ii}/2,$$

$$\epsilon_{ij} = (2/3)\delta_{ij}\epsilon.$$

The isotropization of the production model (Launder, 1985) is used for the pressure-strain term (redistribution term) ϕ_{ij}.

$$\phi_{ij} = \phi_{ij,1} + \phi_{ij,2} + \phi_{ij,w} \tag{30}$$

$$\phi_{ij,1} = -C_1(\epsilon/k)(\overline{u_iu_j} - 2/3\cdot\delta_{ij}k) \tag{31}$$

$$\phi_{ij,2} = -C_2(P_{ij} - 2/3\cdot\delta_{ij}P_k) \tag{32}$$

The wall-proximity effect on ϕ_{ij} is expressed (Gibson and Launder, 1978) as:

$$\phi_{ij,w} = \phi'_{ij,1} + \phi'_{ij,2} \tag{33}$$

$$\phi'_{ij,1} = C'_1(\epsilon/k)(\overline{u_ku_m}n_kn_m\delta_{ij} - 3/2\cdot\overline{u_ku_i}n_kn_j - 3/2\cdot\overline{u_ku_j}n_kn_i)f \tag{34}$$

$$\phi'_{ij,2} = C'_2(\phi_{km,2}n_kn_m\delta_{ij} - 3/2\cdot\phi_{ik,2}n_kn_j - 3/2\cdot\phi_{jk,2}n_kn_i)f \tag{35}$$

where $f = k^{3/2}C_\mu^{3/4}/\epsilon y\kappa$, $n_i = 1$ (in the direction normal to the wall) and $n_i = 0$ (otherwise). The model constants C_1 and C_2 in $\phi_{ij,1}$ and $\phi_{ij,2}$ are $C_1 = 3.0$ and $C_2 = 0.3$, which are the optimum values determined through Younis's systematic investigation (Launder, 1985). With these values, the constants C_1' and C_2' in $\phi'_{ij,1}$ and $\phi'_{ij,2}$ are chosen as C_1' $= 0.75$ and C_2' $= 0.5$ (Gibson and Younis, 1986). The Kármán constant κ is given as $\kappa = 0.4$.

3.2 Results and Discussion. To judge the quality of the proposed model, we have calculated the strong adverse pressure gradient flow. This test case is identical to Flow Case 0141 of the 1980–1981 Stanford Conference (Kline et al., 1981). The distribution of the skin-friction coefficient C_f is shown in Fig. 10, compared with the experiments (in this figure, the model results of LB and Rodi and Scheuerer (RS) are cited from Rodi and Scheuerer (1986)). Until now, the predictions for this flow with the k-ϵ models have been very unsatisfactory (Patel et al., 1981; Nagano and Hishida, 1987). The present model overcomes this drawback and provides a good prediction. Rodi and Scheuerer (1986) added the production terms originating from the extra strain $\partial\overline{U}/\partial x$ to the k and ϵ transport equations, and used the wall functions as the boundary conditions. They also fixed the values of $\overline{u^2}$ and $\overline{v^2}$ with the experimental data $\overline{u^2}/k = 1.1$ and $\overline{v^2}/k = 0.25$. Accordingly, it is quite natural for this model to yield a good prediction, because the mean velocity is artificially fitted to the universal velocity profile at one point at least in the wall region over the entire streamwise location. However, from the standpoint of numerical "prediction," this seems less than desirable. In contrast, the proposed model has universality because of no restricted conditions. Moreover, as shown in Fig. 10, the present result is by no means inferior to that of the RS model.

A more concrete improvement of the present model is seen in Fig. 11, in which comparison of model results is made for the velocity profiles in wall coordinates. The LB model gives a considerable underprediction for the measurements, whereas good overall agreement is obtained with the proposed model. The results of the RS model are not shown here, since the velocity of this model ineluctably had to have the correct value in the log region (where the wall functions were specified).

4 Concluding Remarks

An improved form of the k-ϵ model, which reproduces strictly the limiting behavior of wall and free turbulence, has been developed. Through the revision of the model constants and functions, many of the defects of the k-ϵ models noted so far have been removed. With the present model, we have calculated a pipe flow, a turbulent boundary layer and a relaminarizing flow, and have verified the validity of the proposed model in the light of the experimental facts.

Flows with adverse pressure gradients have not been predicted correctly by the existing k-ϵ models. In the calculations of such flows, the prediction of a separation point (with $C_f = 0$) is particularly important, but it has been almost impossible to obtain even an approximate estimate with the previous k-ϵ models. On the other hand, the proposed model assures a good estimation with the aid of the algebraic stress model. Furthermore, governing equations are not so complex, and thus the computing time required is usually comparable with that for the existing near wall k-ϵ models.

Acknowledgment

This research was partially supported by a Grant-in-Aid for Scientific Research on Priority Areas from the Ministry of Education, Science and Culture of Japan (No. 62613503).

References

Batchelor, G. K., and Townsend, A. A., 1948a, "Decay of Isotropic Turbulence in the Initial Period," *Proceedings of the Royal Society, London*, Series A, Vol. 193, pp. 539–558.

Batchelor, G. K., and Townsend, A.A., 1948b, "Decay of Isotropic Turbulence in the Final Period," *Proceedings of the Royal Society*, London, Series A, Vol. 194, pp. 527–543.

Bradshaw, P., 1967, "The Turbulence Structure of Equilibrium Boundary Layers," *Journal of Fluid Mechanics*, Vol. 29, pp. 625–645.

Bradshaw, P., Cebeci,T., and Whitelaw, J. H., 1981, *Engineering Calculation Methods for Turbulent Flow*, Academic Press, London.

Chapman, D. R., and Kuhn, G. D., 1986, "The Limiting Behaviour of Turbulence Near the Wall," *Journal of Fluid Mechanics*, Vol. 170, pp. 265–292.

Comte-Bellot, G., and Corrsin, S., 1966, "The Use of a Contraction to Improve the Isotropy of Grid-Generated Turbulence," *Journal of Fluid Mechanics*, Vol. 25, pp. 657–682.

Corrsin, S., 1951, "The Decay of Isotropic Temperature Fluctuations in an Isotropic Turbulence," *Journal of Aeronautical Sciences*, Vol. 18, No. 6, pp. 417–423.

Derksen, R. W., and Azad, R. S., 1981,"Behavior of the Turbulent Energy Equation at a Fixed Boundary," *AIAA Journal*, Vol. 19, pp. 238–239.

Gibson, M. M., and Launder, B. E., 1978, "Ground Effects on Pressure Fluctuations in the Atmospheric Boundary Layer," *Journal of Fluid Mechanics*, Vol. 86, pp. 491–511.

Gibson, M. M., Verriopoulos, C. A., and Nagano, Y., 1982, "Measurements in the Heated Turbulent Boundary Layer on a Mildly Curved Convex Surface," *Turbulent Shear Flows 3*, L. J. S. Bradbury et al., eds., Springer-Verlag, Berlin, pp. 80–89.

Gibson, M. M., and Younis, B. A., 1986, "Calculation of Boundary Layers With Sudden Transverse Strain," ASME JOURNAL OF FLUIDS ENGINEERING, Vol. 108, pp. 470–475.

Hanjalić, K., and Launder, B. E., 1976, "Contribution Towards a Reynolds-Stress Closure for Low-Reynolds-Number Turbulence," *Journal of Fluid Mechanics*, Vol. 74, pp. 593–610.

Hanjalić, K., and Launder, B. E., 1980, "Sensitizing the Dissipation Equation to Irrotational Strains," ASME JOURNAL OF FLUIDS ENGINEERING, Vol. 102, pp. 34–40.

Hishida, M., Nagano, Y., and Morimoto, Y., 1980, "Structure of Pipe Flow Turbulence. 1st Report, Characteristics of Velocity Fluctuations and Reynolds Shear Stress," *Trans. Japan Soc. Mech. Engrs.*, Series B, Vol. 46, pp. 1455–1466.

Kline, S. J., Cantwell, B. J., and Lilley, G. M., 1981, The 1980–1981 AFOSR-HTTM-Stanford Conference on Complex Turbulent Flow: Comparison of Computation and Experiment I, II and III, Thermosciences Division, Mechanical Engineering Department, Stanford University, Stanford, Calif.

Lam, C. K. G., and Bremhorst, K., 1981, "A Modified Form of the k-ϵ Model for Predicting Wall Turbulence," ASME JOURNAL OF FLUIDS ENGINEERING, Vol. 103, pp. 456–460.

Laufer, J., 1954, "The Structure of Turbulence in Fully Developed Pipe Flow," NACA Report 1174.

Launder, B. E., 1985, "Progress and Prospects in Phenomenological Turbulence Models," *Theoretical Approaches to Turbulence*, D. L. Dwoyer et al., eds., Springer-Verlag, Berlin, pp. 155–186.

Myong, H. K., Kasagi, N., and Hirata, M., 1987, "Prediction of Turbulent Heat Transfer by the Modified k-ϵ Model Taking into Account the Near-Wall Behavior of Turbulence," *Proceedings, 24th National Heat Transfer Symposium of Japan*, pp. 10–12.

Myong, H. K., and Kasagi, N., 1988, "A New Proposal for a k-ϵ Turbulence Model and Its Evaluation. 1st Report, Development of the Model," *Trans. Japan Soc. Mech. Engrs.*, Series B, Vol. 54, pp. 3003–3009.

Nagano, Y., and Hishida, M., 1985, "Production and Dissipation of Turbulent Velocity and Temperature Fluctuations in Fully Developed Pipe Flow," *Fifth Symposium on Turbulent Shear Flows*, Cornell University, Ithaca, pp. 14.19–14.24.

Nagano, Y., and Hishida, M., 1987, "Improved Form of the k-ϵ Model for Wall Turbulent Shear Flows," ASME JOURNAL OF FLUIDS ENGINEERING, Vol. 109, pp. 156–160.

Nagano, Y., and Kim, C., 1988, "A Two-Equation Model for Heat Transport in Wall Turbulent Shear Flows," ASME *Journal of Heat Transfer*, Vol. 110, pp. 583–589.

Patel, V. C., and Head, M. R., 1968, "Reversion of Turbulent to Laminar Flow," *Journal of Fluid Mechanics*, Vol. 34, pp. 371–392.

Patel, V. C., and Head, M. R., 1969, "Some Observations on Skin Friction and Velocity Profiles in Fully Developed Pipe and Channel Flows," *Journal of Fluid Mechanics*, Vol. 38, pp. 181–201.

Patel, V. C., Rodi, W., and Scheuerer, G., 1981, "Evaluation of Turbulence Models for Near-Wall and Low-Reynolds Number Flows," *Third Symposium on Turbulent Shear Flows*, University of California, Davis, Calif., pp. 1.1–1.8.

Patel, V. C., Rodi, W., and Scheuerer, G., 1985, "Turbulence Models for Near-Wall and Low Reynolds Number Flows: A Review," *AIAA Journal*, Vol. 23, pp. 1308–1319.

Reichardt, H., 1951, "Vollstandige Darstellung der turbulenten Geschwindigkeitsverteilung in glatten Leitungen," *Z. angew. Math. Mech.*, Vol. 31, pp. 208–219.

Rodi, W., and Scheuerer, G., 1983, "Calculation of Curved Shear Layers with Two-Equation Turbulence Models," *Physics of Fluids*, Vol. 26, pp. 1422–1436.

Rodi, W., and Scheuerer, G., 1986, "Scrutinizing the k-ϵ Turbulence Model Under Adverse Pressure Gradient Conditions," ASME JOURNAL OF FLUIDS ENGINEERING, Vol. 108, pp. 174–179.

Takemitsu, N., 1987, "A Revised k-ϵ Model," *Trans. Japan Soc. Mech. Engrs.*, Series B, Vol. 53, pp. 2928–2936.

Verriopoulos, C. A., 1983, "Effects of Convex Surface Curvature on Heat Transfer in Turbulent Flow," *Ph.D. Thesis*, Imperial College, London.

V. De Henau

G. D. Raithby

B. E. Thompson[1]

Department of Mechanical Engineering,
University of Waterloo,
Waterloo, Ontario,
Canada, N2L 3G1

Prediction of Flows With Strong Curvature and Pressure Gradient Using the $k-\epsilon$ Turbulence Model

The $k-\epsilon$ *turbulence model of Launder and Spalding has found widespread application in the computation of fluid flows. Under conditions of strong adverse pressure gradient or strong streamline curvature, the accuracy of the model is known to decrease. The present paper adds to the available case studies involving these types of flows by providing predictions for two problems. In the first problem, Simpson's flow, an adverse pressure gradient induces the flow along a planar surface to separate. The second problem is unseparated flow over an airfoil. In addition to predictions using the standard* $k-\epsilon$ *model, results are reported from another* $k-\epsilon$ *model by Hanjalic and Launder, that has been modified to account for adverse pressure gradients.*

1 Introduction

The critical uncertainty in the numerical simulation of turbulent shear flows is the estimation of the Reynolds stresses. Models in current use may be as simple as explicit algebraic relations that connect the stresses to the mean flow variables, or as complex as a set of differential transport equations with one equation for each stress. The $k-\epsilon$ model of Launder and Spalding [1] has emerged as a standard because it has been quite successful for predicting a wide variety of flows, yet is reasonably simple.

Some authors have, however, reported serious deficiencies in the $k-\epsilon$ model for particular flows. For flows with strong streamline curvature, Leschziner and Rodi [2] found that the measured anisotropy of the normal stresses and the magnitude of the shear stresses are not well predicted by the $k-\epsilon$ model. For flows in a strong adverse pressure gradient, Rodi and Scheuerer [3] found that the predicted dissipation is too small, with the result that turbulent stresses are too large.

Some attempts have been made to modify the $k-\epsilon$ model and improve its performance for such flows. Leschziner and Rodi [2], and Pourahmadi and Humphrey [4] suggested making the C_μ "constant" in the model dependent on the flow curvature. This improved the predictions for jet flows, but created convergence difficulties [5] for an internal flow. In their study of flows with strong adverse pressure gradients, Hanjalic and Launder [6] found that a higher production of dissipation was required to correctly predict the turbulence levels for cases where the mean flow is irrotational. This led to a proposal [6, 3] for increasing the coefficient that multiplies the production of turbulent kinetic energy by normal stresses in the ϵ equation.

The present study was undertaken to examine the performance of the $k-\epsilon$ model, and to evaluate the improvement of the performance obtained by the Hanjalic and Launder [6] modification[2], for two flows. Both cases were chosen because of their relevance to airfoil flows. The first case, Simpson's problem [7, 8, 9, 10], was flow along a wind tunnel wall with an imposed pressure distribution that approximated the pressure on an airfoil. The second case was the flow over a supercritical airfoil measured by Nakayama [11]. Simpson's flow experiences a strong adverse pressure gradient but no boundary-induced streamline curvature (internal streamline curvature does result from flow separation). Nakayama's flow is subject to both strong adverse pressure gradients and strong streamline curvature.

To choose an appropriate turbulence model for a computational fluid dynamics code, the analyst must know the strengths and weaknesses of all candidate models. This knowledge is gained through comparisons of predictions with data for a variety of flows. The aim of this paper is to add two case studies to the literature that will assist potential users to understand more completely the capabilities of the standard $k-\epsilon$ model, and the potential benefits of implementing the Hanjalic and Launder [6] modification.

2 Formulation and Solution Method

2.1 Equations of Motion. For a turbulent, incompressible, two-dimensional flow, the time-averaged differential equations of motion, written for a general orthogonal coordinate system, are [12]:

Conservation of mass

$$\frac{1}{h_1 h_2}\left[\frac{\partial}{\partial x_1}(\rho h_2 U)+\frac{\partial}{\partial x_2}(\rho h_1 V)\right]=0 \qquad (1)$$

[1] Current Address: Scientific Research Associates, Glastonbury, Conn.

Contributed by the Fluids Engineering Division for publication in the JOURNAL OF FLUIDS ENGINEERING. Manuscript received by the Fluids Engineering Division December 12, 1988.

[2] The model has been generalized in the present paper to make it coordinate system independent.

Conservation of momentum in the x_1 direction

$$\frac{\partial}{\partial t}(\rho U)+\frac{1}{h_1h_2}\left[\frac{\partial}{\partial x_1}(\rho h_2UU)+\frac{\partial}{\partial x_2}(\rho h_1VU)\right]$$
$$=-\frac{1}{h_1}\frac{\partial P}{\partial x_1}+\frac{1}{h_1h_2}\left[\frac{\partial}{\partial x_1}(h_2\sigma_{11})+\frac{\partial}{\partial x_2}(h_1\sigma_{21})\right]$$
$$+\frac{1}{h_1h_2}\left[\rho VV\frac{\partial h_2}{\partial x_1}-\rho UV\frac{\partial h_1}{\partial x_2}+\sigma_{12}\frac{\partial h_1}{\partial x_2}-\sigma_{22}\frac{\partial h_2}{\partial x_1}\right] \quad (2)$$

Conservation of momentum in the x_2 direction

$$\frac{\partial}{\partial t}(\rho V)+\frac{1}{h_1h_2}\left[\frac{\partial}{\partial x_1}(\rho h_2UV)+\frac{\partial}{\partial x_2}(\rho h_1VV)\right]$$
$$=-\frac{1}{h_2}\frac{\partial P}{\partial x_2}+\frac{1}{h_1h_2}\left[\frac{\partial}{\partial x_1}(h_2\sigma_{12})+\frac{\partial}{\partial x_2}(h_1\sigma_{22})\right]$$
$$+\frac{1}{h_1h_2}\left[\rho UU\frac{\partial h_1}{\partial x_2}-\rho UV\frac{\partial h_2}{\partial x_1}+\sigma_{21}\frac{\partial h_2}{\partial x_1}-\sigma_{11}\frac{\partial h_1}{\partial x_2}\right] \quad (3)$$

In the equations above, U and V are the mean velocity in the x_1 and x_2 directions, respectively, ρ is the density and h_1 and h_2 are the metrics. The local effective mean pressure P is defined as

$$P=P^*+\frac{2}{3}\rho k$$

where P^* is the mean pressure relative to the hydrostatic pressure and k is the turbulence kinetic energy. The turbulent viscosity approach relates the stresses σ_{ij} to the strain rates e_{ij} through the relations

$$\sigma_{11}=2(\mu+\mu_t)e_{11} \quad (4)$$

$$\sigma_{22}=2(\mu+\mu_t)e_{22} \quad (5)$$

$$\sigma_{12}=2(\mu+\mu_t)e_{12} \quad (6)$$

where μ_t is the turbulent viscosity. For incompressible flows,

$$e_{11}=\left(\frac{1}{h_1}\frac{\partial U}{\partial x_1}+\frac{V}{h_1h_2}\frac{\partial h_1}{\partial x_2}\right) \quad (7)$$

$$e_{22}=\left(\frac{1}{h_2}\frac{\partial V}{\partial x_2}+\frac{U}{h_1h_2}\frac{\partial h_2}{\partial x_1}\right) \quad (8)$$

$$e_{12}=\frac{1}{2}\left(\frac{1}{h_1}\frac{\partial V}{\partial x_1}+\frac{1}{h_2}\frac{\partial U}{\partial x_2}-\frac{V}{h_1h_2}\frac{\partial h_2}{\partial x_1}-\frac{U}{h_1h_2}\frac{\partial h_1}{\partial x_2}\right) \quad (9)$$

2.2 Turbulence Modelling. The standard $k-\epsilon$ turbulence model calculates the turbulent viscosity μ_t as [1]

$$\mu_t=C_\mu\frac{\rho k^2}{\epsilon} \quad (10)$$

where ϵ is the rate of dissipation and C_μ is taken as a constant. The transport equations for the turbulence kinetic energy and the dissipation rate in general orthogonal coordinates can be written as [13]:

Transport of turbulence kinetic energy k

$$\frac{\partial}{\partial t}(\rho k)+\frac{1}{h_1h_2}\left[\frac{\partial}{\partial x_1}(\rho h_2Uk)+\frac{\partial}{\partial x_2}(\rho h_1Vk)\right]$$
$$=\frac{1}{h_1h_2}\left[\frac{\partial}{\partial x_1}\left(\frac{h_2}{h_1}\left(\mu+\frac{\mu_t}{\sigma_k}\right)\frac{\partial k}{\partial x_1}\right)\right.$$
$$\left.+\frac{\partial}{\partial x_2}\left(\frac{h_1}{h_2}\left(\mu+\frac{\mu_t}{\sigma_k}\right)\frac{\partial k}{\partial x_2}\right)\right]+P_k-\rho k\tau \quad (11)$$

Transport of rate of dissipation ϵ

$$\frac{\partial}{\partial t}(\rho\epsilon)+\frac{1}{h_1h_2}\left[\frac{\partial}{\partial x_1}(\rho h_2U\epsilon)+\frac{\partial}{\partial x_2}(\rho h_1V\epsilon)\right]$$
$$=\frac{1}{h_1h_2}\left[\frac{\partial}{\partial x_1}\left(\frac{h_2}{h_1}\left(\mu+\frac{\mu_t}{\sigma_\epsilon}\right)\frac{\partial\epsilon}{\partial x_1}\right)\right.$$
$$\left.+\frac{\partial}{\partial x_2}\left(\frac{h_1}{h_2}\left(\mu+\frac{\mu_t}{\sigma_\epsilon}\right)\frac{\partial\epsilon}{\partial x_2}\right)\right]+P_\epsilon-C_{\epsilon2}\rho\epsilon\tau \quad (12)$$

Nomenclature

C = airfoil chord length
C_μ, $C_{\epsilon1}$, $C_{\epsilon2}$, $C_{\epsilon3}$ = constants for turbulence model
e = fluid strain
E = wall turbulence model constant, equation (21)
h_1, h_2 = metrics in x_1 and x_2 directions, respectively
h_s, h_n = metrics in s and n directions, respectively
H = height of calculation domain
k = turbulence kinetic energy
L = length of calculation domain
P^* = pressure
P = $P^*+\frac{2}{3}\rho k$
P_k, P_ϵ = production of turbulence energy and of dissipation, respectively
Re_x = Reynolds number based on characteristic length x
s, n = streamline coordinate directions
$\overline{uu}$, $\overline{vv}$, $\overline{uv}$ = turbulent Reynolds stresses
U, V = mean velocity components in the x_1 and x_2 directions, respectively
U_s, U_n = mean velocity components in the s and n directions, respectively
U_τ = shear velocity
U^+ = velocity non-dimensionalized by shear velocity
x_1, x_2 = generalized coordinates directions
y^+ = nondimensional distance normal from a wall
δ = boundary layer thickness
δ^* = displacement thickness
ϵ = rate of dissipation of turbulence energy
κ, κ_1 = wall turbulence model constants
μ, μ_t = laminar and turbulent viscosities
ν_t = turbulent kinematic viscosity
ρ = density
σ = fluid stress
σ_k, σ_ϵ = turbulent Prandtl number for k and ϵ, respectively
τ = inverse time scale = ϵ/k
τ_w = wall shear stress

Subscripts

1, 2 = denoting coordinate directions x_1 and x_2, respectively
s, n = denoting coordinate directions s and n, respectively
t = turbulent
∞ = referring to freestream condition

Acronyms

SKE = standard $k-\epsilon$ turbulence model
MKE = modified $k-\epsilon$ turbulence model with $C_{\epsilon3}=5.50$

The empirical constants in the standard $k-\epsilon$ model are given the following values [1]: $C_\mu = 0.09$, $\sigma_k = 1.0$, $\sigma_\epsilon = 1.3$, $C_{\epsilon 1} = 1.45$ and $C_{\epsilon 2} = 1.92$. τ is an inverse time scale defined as

$$\tau = \frac{\epsilon}{k}$$

The production of turbulence kinetic energy P_k is expressed in terms of Reynolds stresses and mean flow strain rates as

$$P_k = -\rho\overline{uv}(2e_{12}) - \rho\overline{uu}e_{11} - \rho\overline{vv}e_{22} \tag{13}$$

and the "production" of dissipation P_ϵ is approximated by

$$P_\epsilon = C_{\epsilon 1} P_k \tau \ . \tag{14}$$

To permit a different sensitivity of P_ϵ to the normal stresses, Hanjalic and Launder [6] substituted equation (13) into equation (14), eliminated e_{22} in favor of e_{11} using mass conservation, and then changed the coefficient multiplying the normal stresses from $C_{\epsilon 1}$ to $C_{\epsilon 3}$ to obtain the following equation.

$$P_\epsilon = \tau[-C_{\epsilon 1}\rho\overline{uv}(2e_{12}) - C_{\epsilon 3}\rho(\overline{uu} - \overline{vv})e_{11}] \tag{15}$$

To augment the production of dissipation by normal strains, $C_{\epsilon 3}$ is positive and greater than $C_{\epsilon 1}$. A value of $C_{\epsilon 3}$ of 4.44 was recommended by Hanjalic and Launder but Rodi and Scheuerer [3] used 2.5 for high adverse pressure gradient flows.

Hanjalic and Launder [6] use the following expression for $(\overline{uu} - \overline{vv})$,

$$(\overline{uu} - \overline{vv}) = 0.33k \tag{16}$$

The value of 0.33 is in agreement with experimental results for boundary layer flows in adverse pressure gradients [14]. Equation (16) is different from the expression

$$(\overline{uu} - \overline{vv}) = -4\frac{\mu_t}{\rho}\left(\frac{1}{h_1}\frac{\partial U}{\partial x_1} + \frac{V}{h_1 h_2}\frac{\partial h_1}{\partial x_2}\right)$$

which follows from the turbulent viscosity definition of stresses. For a fully developed flow between parallel plates, this equation yields $(\overline{uu} - \overline{vv}) = 0$, which is contrary to measurements. Therefore, the present study has followed Hanjalic and Launder by using equation (16).

To apply this model to a flow not aligned with the x_1 direction (assumed in equation (16)), the local $s-n$ coordinate system in Fig. 1 is introduced in a manner similar to that proposed by Leschziner and Rodi [2]. The expression for P_k in this coordinate system is

$$P_k = 4\mu_t(e_{sn})^2 - 0.33\rho k e_{ss} \tag{17}$$

where e_{ss} and e_{sn} are the normal and shear strains respectively. These are defined in Appendix A.

Equation (17) is used to calculate the production of turbulence kinetic energy in the k-equation (equation (11)) as well as in the ϵ-equation (equation (12)) where P_ϵ is expressed as

$$P_\epsilon = \tau[C_{\epsilon 1}P_k - (C_{\epsilon 3} - C_{\epsilon 1})0.33\rho k e_{ss}] \tag{18}$$

The derivation of equations (17) and (18) is given in Appendix A.

2.3 Boundary Conditions. This section deals with the application of the boundary conditions for flow along a turbulent wall.

Wall Boundary Conditions on Velocity. The velocity normal to a solid wall is set to zero. The boundary condition for the tangential velocity is specified by a shear stress based on a wall function approach described below.

In the derivation of the wall function, y^+ is taken as the non-dimensional distance normal to the wall

$$y^+ = \frac{\rho y U_\tau}{\mu} \tag{19}$$

If there is an equilibrium layer near the surface, in which the shear stress is nearly constant and the production of k is in balance with its dissipation, then

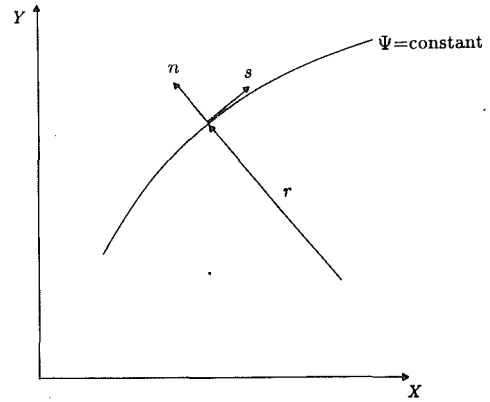

Fig. 1 Streamline coordinate system

$$U_\tau = C_\mu^{1/4} k^{1/2}$$

For the viscous and buffer layers ($y^+ \le 30$), Rannie [15] suggested that

$$U^+ = \frac{1}{\kappa_1}\tanh(\kappa_1 y^+) \tag{20}$$

where $\kappa_1 = 0.0688$ and $U^+ = U/U_\tau$. In the fully turbulent layer region ($y^+ > 30$), the standard logarithm velocity profile is adopted [1], i.e.,

$$U^+ = \frac{1}{\kappa}\ln(Ey^+) \tag{21}$$

where κ and E are the log-law constants equal to 0.41 and 9.0 (for a smooth wall), respectively [1].

Expressions for the shear stress at the wall are obtained from equations (20) and (21), assuming that for the region very near the wall the pressure gradient has no influence on the flow [16] and the flow is locally one-dimensional. The expressions are

for $y_P^+ \le y1^+$

$$\tau_w = \frac{\rho U_P C_\mu^{1/4} k_P^{1/2} \kappa_1}{\tanh(\kappa_1 y_P^+)} \tag{22}$$

for $y_P^+ > y1^+$

$$\tau_w = \frac{\rho U_P C_\mu^{1/4} k_P^{1/2} \kappa}{\ln(E y_P^+)} \tag{23}$$

The subscript P refers to the node in the flow that lies adjacent to the wall while $y1^+$ is the value of y^+ at which equations (22) and (23) give the same value of τ_w.

Wall Boundary Condition for k *and* ϵ. At the wall, $\partial k/\partial y = 0$. In addition, assuming that the dominant term in the near wall production is the shear stress, the following can be derived from equations (20) and (21)

for $y^+ \le y2^+$

$$P_k = \frac{\rho^2 U_\tau^4}{\mu}\frac{\tanh^2(\kappa_1 y^+)}{\cosh^2(\kappa_1 y^+)} \tag{24}$$

for $y^+ > y2^+$

$$P_k = \frac{\rho^2 U_\tau^4}{\mu}\frac{1}{\kappa y^+} \tag{25}$$

$y2^+$ is the value of y^+ at which equations (24) and (25) give the same value of P_k. The production of k for a given node that lies immediately adjacent to the wall is obtained by integrating equations (22) and (23) over the y^+ region occupied by the node.

Based on the assumption that the flow is in local equilibrium in the near wall region ($\rho\epsilon = P_k$), the variation of ϵ with distance normal to the wall is simply expressed as

for $5 < y^+ \le y2^+$

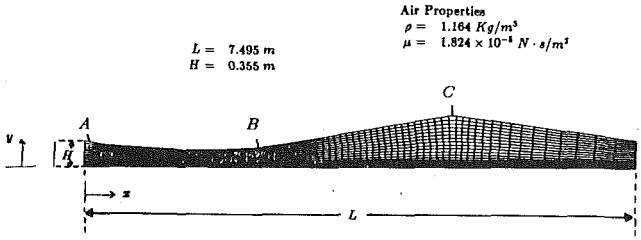

Fig. 2 Wind tunnel geometry and fluid properties for the turbulent separating boundary layer flow problem

Table 1 Experimental parameters of the mean flow development

x (m)	U_∞ (m/s)	δ (cm)	δ^* (cm)
2.778	17.038	6.066	1.601
2.858	16.599	6.760	—
2.934	16.185	7.219	2.317
3.123	15.228	8.828	—
3.273	14.661	11.877	5.245
3.448	14.158	14.818	7.889
3.604	13.868	17.191	10.191
3.896	13.594	25.568	15.888
3.996	13.517	27.861	—

$$\epsilon = \frac{\rho U_\tau^4}{\mu} \frac{\tanh^2(\kappa_1 y^+)}{\cosh^2(\kappa_1 y^+)} \tag{26}$$

for $y^+ > y2^+$

$$\epsilon = \frac{\rho U_\tau^4}{\mu} \frac{1}{\kappa y^+} \tag{27}$$

In the viscous sublayer ($y^+ \leq 5$), measurements indicate that the dissipation rate is constant [1]. The level of ϵ for that region is therefore given by the level of ϵ at $y^+ = 5$, that is

for $y^+ \leq 5$

$$\epsilon = \frac{\rho U_\tau^4}{\mu} \frac{\tanh^2(5\kappa_1)}{\cosh^2(5\kappa_1)} \tag{28}$$

Equations (26) to (28) replace the transport equation for the dissipation rate (equation (12)) at the nodes that lie immediately adjacent to the wall.

It is noted here that the treatment of the wall boundary conditions for the region $y^+ < 30$ is different from the standard wall function method [1]. When applied to the fully developed turbulent flow between parallel plates of Laufer [17], the standard wall model predicts a decrease in k near the wall which is more rapid than the one observed experimentally. The present wall model yields the correct trend for k near the wall and, for this reason, is adopted in this paper.

Summary: From known U and k fields (obtained from a previous iteration or from an initial guess), the values of y_P^+ are evaluated. Based on these values, the wall shear stress, as well as the production of k and the dissipation level at the wall, are calculated and used as boundary values in the appropriate equations.

2.4 Numerical Model and Solution Procedure. Information on the performance of the turbulence model presented in the previous section will be obtained by comparing the solution of the equations to measurements. For this information to be reliable, it is necessary that the numerical errors in the solution do not contaminate the comparison.

The discretization method used in the present study was extensively tested [18, 19] for a variety of external flows for which benchmark solutions were available. Furthermore, grid independence studies were conducted on the solutions to the two flows described in this paper. Results of these studies are discussed in the followng section.

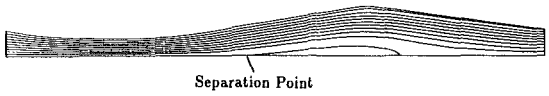

Fig. 3 Streamlines for turbulent separating boundary layer flow

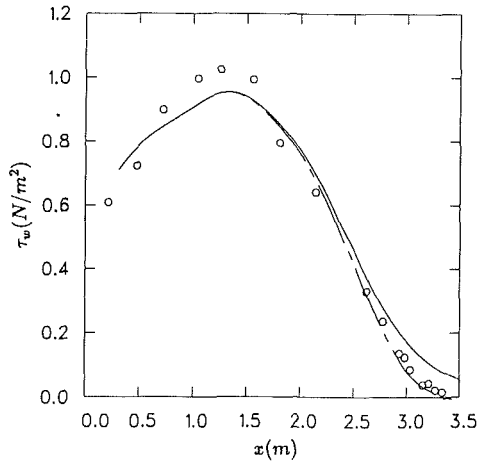

Fig. 4 Bottom wall shear stress distribution for turbulent separating boundary layer flow (60 × 35 grid).
Experimental Simpson: ○; SKE: ———; MKE: — —

It may be of interest here to alert analysts to the serious pressure errors that occur when upwind differences are used. These, of course, contaminate the velocity solution for external flows [20, 19]. The discretization used to obtain the solutions reported in this paper avoided this problem [18, 19].

Solutions to the non-linear equation set were obtained from successive iterations on a linear form of the equations. Iterations were performed until the following criterion was met

$$\left| \frac{\Phi^{n+1} - \Phi^n}{\Phi_{\max}^{n+1} - \Phi_{\min}^{n+1}} \right| \leq 0.00001$$

where Φ represents k, ϵ and the pressure P and n is the iteration number. This criterion is close to the round-off limit of a VAX 780 computer.

3 Numerical Results

3.1 Turbulent Separating Boundary Layer Flow

Description of the Problem. Simpson et al. [7-10] measured the two-dimensional flow in a wind tunnel with the cross-sectional shape shown in Fig. 2. The goal was to impress a pressure on the lower planar surface similar to that encountered on an airfoil. To avoid separation on the upper surface of the wind tunnel, mass was withdrawn through slots at locations A, B, and C. Separation was observed on the lower surface at about 40 percent of the distance to C from location B (between 3.10m to 3.45m from the inlet). The area of the tunnel was reduced past C to close off this recirculation bubble.

The measurements presented by Simpson et al. were normalized with respect to a velocity scale $U_\infty(x)$ and length scales of $\delta(x)$ and $\delta^*(x)$. The values of these quantities are required at the x-locations at which comparisons between the measurements and the predictions are made. The relevant quantities are reproduced in Table 1.

Implementation of the Numerical Model. The numerical model for the problem was run using the kind of orthogonal grid shown in Fig. 2. The results presented here were obtained with a grid of density (60×35).

In accordance with the experiment, the inlet velocity was prescribed as uniform ($U = 15.057$ m/s) in the x direction and zero ($V = 0$) in the y direction. k was specified to correspond to a uniform isotropic turbulence intensity of 0.1 percent.

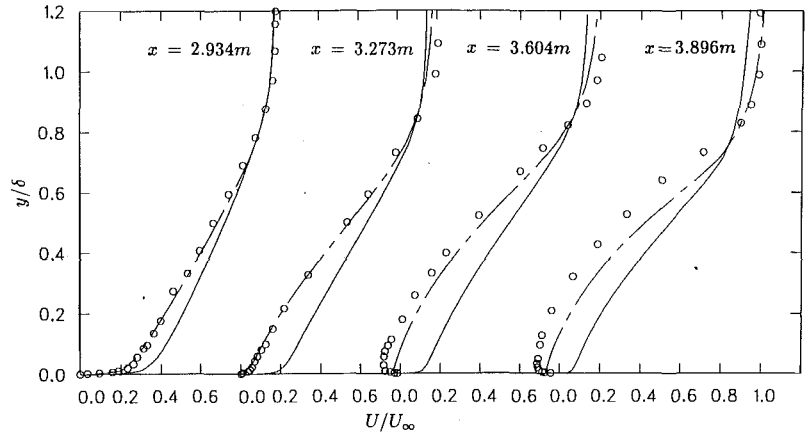

Fig. 5 Comparison of experimental and numerical mean velocity profiles (60 x 35 grid).
Experimental Simpson: ○; SKE: ———; MKE: – – –

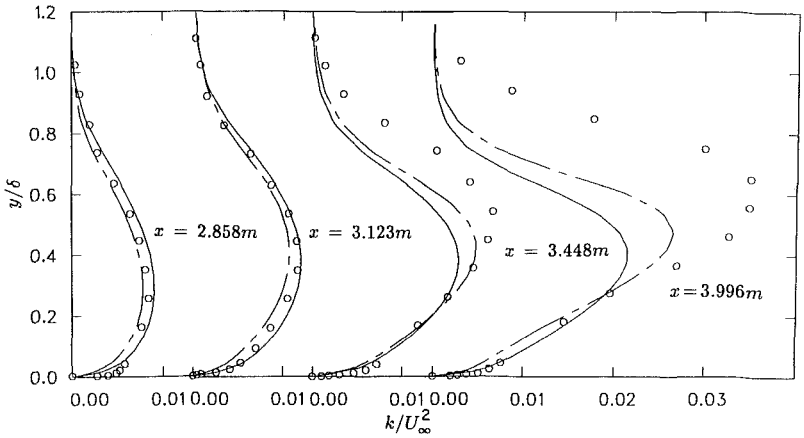

Fig. 6 Comparison of experimental and numerical turbulence kinetic energy profiles (60 x 35 grid).
Experimental Simpson: ○; SKE: ———; MKE: – – –

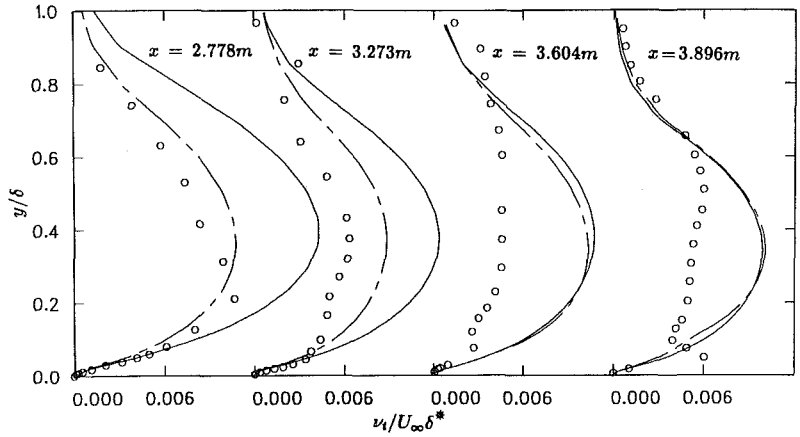

Fig. 7 Comparison of experimental and numerical turbulent kinematic viscosity profiles (60 x 35 grid).
Experimental Simpson: ○; SKE: ———; MKE: – – –

Following the recommendation of Cebeci et al. [21], an inlet dissipation rate of $\epsilon = k^{3/2}/(0.005H)$ was prescribed, were H is the wind tunnel height at the inlet. The wind tunnel walls were taken as hydraulically smooth. Separation on the upper surface was avoided in the computer model by withdrawing mass through the wall between B and C at a uniform rate which matched the measured total withdrawal. This produced velocities normal to the wall of about 0.7 percent of the inlet velocity.

Numerical solutions were obtained with the standard $k-\epsilon$ model (SKE), and with the modified model (MKE), in which $C_{\epsilon 3} = 5.50$.

Presentation and Discussion of the Results. The SKE model failed to predict separation on the lower surface. The MKE model predicted separation at $x \approx 3.4$m, which lies within the range of observed separation. To determine the sensitivity of the gross features of the flow to $C_{\epsilon 3}$, solutions were obtained for several different values of $C_{\epsilon 3}$. Flow separation was found for $C_{\epsilon 3} \geq 2.50$. As $C_{\epsilon 3}$ was increased above this

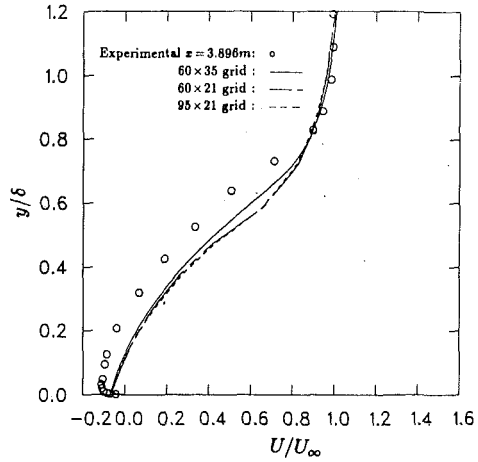

Fig. 8 Comparison of velocity profiles obtained with MKE for various grid sizes at a station located in the recirculating flow region.

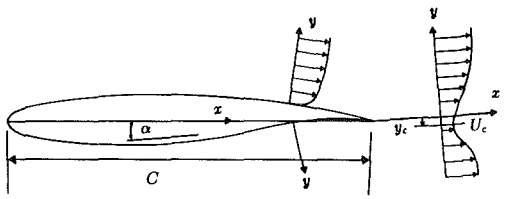

Fig. 9 Super critical airfoil profile and coordinates definition

value, the separation bubble increased. For $C_{\epsilon 3} > 5.50$, converged solutions could not be obtained. The streamline for the MKE model ($C_{\epsilon 3} = 5.50$) are shown in Fig. 3.

Comparisons of the wall stresses are shown in Fig. 4. The SKE model degrades in accuracy in the adverse pressure gradient zone as the separation point is approached and fails to change sign (i.e., no separation). The MKE model departs from the SKE predictions in the adverse pressure gradient region and agrees much better with the measurements near separation. The accurate prediction of the location of the separation point already discussed, is reflected in this plot by a change in the sign of τ_w at the correct x-location.

Profiles of the U-velocity comparison is shown in Fig. 5 at four stations, two of which are downstream of separation. The overall level of agreement is much better with the MKE model. The height of the backflow ($U<0$) region within the separation bubble, and the velocity defect within the boundary layer ($y/\delta<1$), are significantly underpredicted by both models.

The turbulent kinetic energy and turbulent viscosities are compared in Figs. 6 and 7, respectively. There is some improvement in the k profiles (Fig. 6) predicted by the MKE model, compared to SKE, only in the separated flow region, but there is generally poor agreement with the measurements in this region: the predicted level of k is too small, and the predicted region of high k is confined too close to the wall. The turbulent viscosity (Fig. 7) is greatly overpredicted by the SKE model upstream of the separation (this prevents the flow from separating). It is surprising that the ν_t profiles predicted downstream of separation are almost identical for the SKE and MKE models, even though flow separation has occurred with the MKE model.

Influence of Grid Refinement of the Predictions. Calculations of the Simpson flow were performed on various grid sizes in order to investigate the influence of grid refinement on the accuracy of the predictions. Figure 8 illustrates the velocity profiles obtained with MKE at a station located in the recirculating flow region for (60×35), (60×21) and (95×21) grids. Although a small effect of grid size on the predictions can be

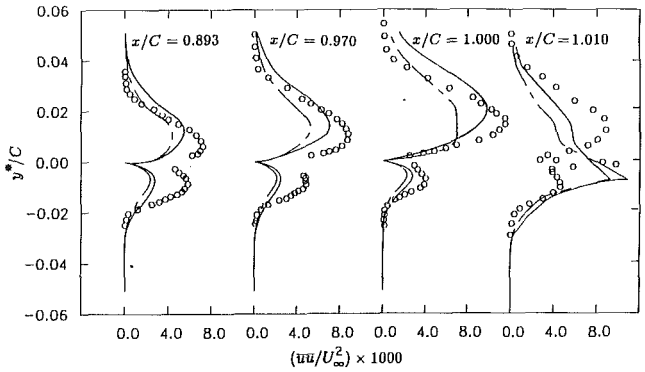

Fig. 10(a) $\overline{uu}$ Profiles for supercritical airfoil at 4 deg incidence. Experimental Nakayama: o; SKE: ———; MKE: ——— for $x/C \le 1.000$, $y^* = y$; for $x/C > 1.000$, $y^* = y - y_c$ Re = 1.2×10^6

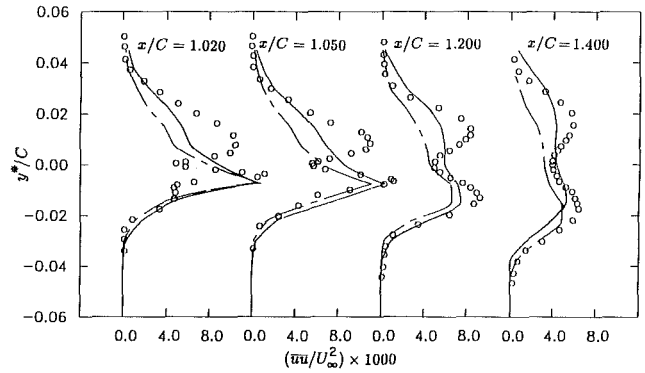

Fig. 10(b) $\overline{uu}$ Profiles for supercritical airfoil at 4 deg incidence. Experimental Nakayama: o; SKE: ———; MKE: ——— for $x/C \le 1.000$, $y^* = y$; for $x/C > 1.000$, $y^* = y - y_c$ Re = 1.2×10^6

observed, it is not responsible for the important discrepancies between the predictions and the experimental data. Similar conclusions can be drawn for the predictions of k and ν_t.

Summary. The MKE model provides much better agreement with the data than the SKE model for Simpson's problem. There are, however, very significant discrepancies between results from this model and the data, particularly in the separated flow region.

3.2 Turbulent Flow Past a Supercritical Airfoil With 4° Angle of Attack at $Re_c = 1.2 \times 10^6$

Description of the Problem. Nakayama [11] has provided measurements of flow over the supercritical airfoil shown in Fig. 9, with an angle of attack $\alpha = 4°$. Measurements were obtained in a wind tunnel with walls located at 0.79C above and below the airfoil. The inlet velocity was 30 m/s, so that the Reynolds number based on the chord length C was 1.2×10^6, and the turbulence intensity was 0.02 percent. The coordinate system in which the data were reported is also shown in Fig. 9.

Implementation of the Numerical Model. A 95×40 orthogonal grid extended 10 chord lengths upstream and downstream of the airfoil. The upper and lower boundaries were placed at the location of the wind tunnel wall, and the grid conformed to the airfoil surface. Of the 95 control volumes in the x_1 direction, 33 were clustered on both the top and the bottom surfaces of the airfoil. Such a grid was found to provide adequate resolution.

The inlet velocity and kinetic energy (isotropic turbulence assumed) were matched with the experiment. The inlet dissipation was selected to make the turbulent viscosity 3 to 4 orders of magnitude smaller than its maximum value near the airfoil. Zero normal velocity and slip conditions were applied on the

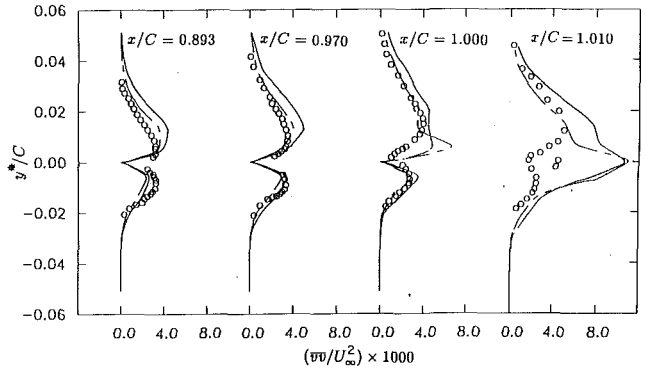

Fig. 11(a) $\overline{vv}$ Profiles for supercritical airfoil at 4 deg incidence. Experimental Nakayama: o; SKE: ———; MKE: — — for $x/C \le 1.000$, $y^* = y$; for $x/C > 1.000$, $y^* = y - y_c$ Re = 1.2×10^6

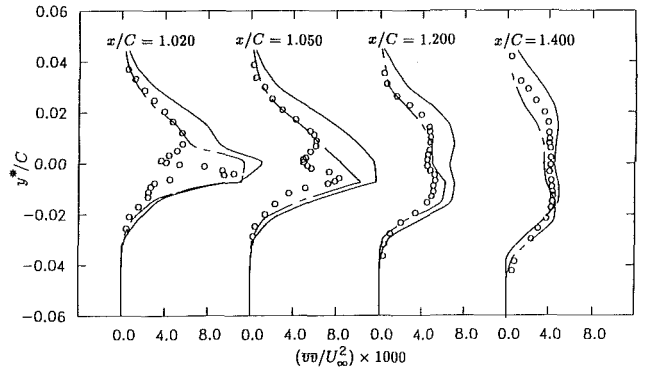

Fig. 11(b) $\overline{vv}$ Profiles for supercritical airfoil at 4 deg incidence. Experimental Nakayama: o; SKE: ———; MKE: — — for $x/C \le 1.000$, $y^* = y$; for $x/C > 1.000$, $y^* = y - y_c$ Re = 1.2×10^6

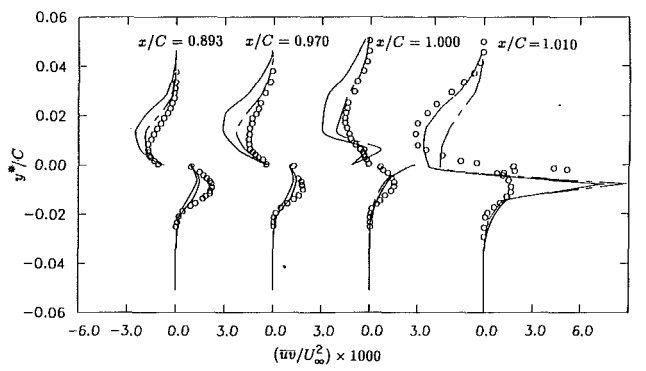

Fig. 12(a) $\overline{uv}$ Profiles for supercritical airfoil at 4 deg incidence. Experimental Nakayama: o; SKE: ———; MKE: — — for $x/C \le 1.000$, $y^* = y$; for $x/C > 1.000$, $y^* = y - y_c$ Re = 1.2×10^6

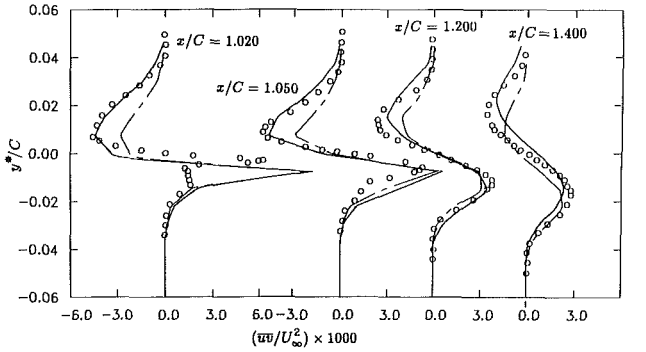

Fig. 12(b) $\overline{uv}$ Profiles for supercritical airfoil at 4 deg incidence. Experimental Nakayama: o; SKE: ———; MKE: — — for $x/C \le 1.000$, $y^* = y$; for $x/C > 1.000$, $y^* = y - y_c$ Re = 1.2×10^6

wind tunnel walls. With this boundary condition, the flow far away from the airfoil is nearly inviscid, but the disturbance of the pressure around the airfoil by the wall is accounted for in the model. It would have been too expensive, computationally, to resolve the viscous boundary layer growth along the tunnel wall.

Comparisons of turbulent stress measurements and predictions are presented along y-profiles at several x/C stations between 0.893 and 1.40. $x/C \le 1.0$ denotes stations on the airfoil and, at such stations, the y-coordinate lies normal to the surface of the airfoil (see Fig. 9).

Presentation and Discussion of the Results. Figures 10(a) and 10(b) compare the measured and predicted $\overline{uu}$ stress. For stations on the airfoil, the SKE model provides more accurate predictions, both above ($y/C > 0$) and below the airfoil. Just beyond the trailing edge ($x/C = 1.02$), both models give similar predictions, but further into the wake, the MKE stresses decay too quickly. Neither model however provides good agreement. For example, neither model predicts the double peak of $\overline{uu}$ in the wake, that probably results from the advection of $\overline{uu}$ by the streams from above and below the airfoil.

The levels of the normal stress $\overline{vv}$ are in better agreement with the measurements (Figs. 11(a), 11(b)), but the double peak peak that exist at the trailing edge again disappears within 1 percent of the chord length. Clearly, the eddy viscosity approach depends too strongly on local effects, with too little memory of upstream conditions. For this $\overline{vv}$ stress component, the MKE model predicts somewhat better levels than the SKE model.

Of particular interest are the $\overline{uv}$ stresses shown in Figs. 12(a) and 12(b). The MKE model is significantly better than the SKE model on the airfoil (Fig. 12(a)), while the reverse is true in the wake (Fig. 12(b)). The magnitude, and the decay rate behind the airfoil, of the shear stresses is better predicted than the normal stresses.

Summary. For Nakayama's problem, in which both strong streamline curvature and adverse pressure gradients occur, some stresses are better predicted by the MKE model and some by the SKE model. The MKE model tends to be better adjacent to the airfoil and the SKE is better in the wake. While the general stress levels are reasonably well predicted, the profiles are incorrect in the wake.

4 Conclusions

The performance of the standard $k-\epsilon$ model (SKE) as well as that of a modified $k-\epsilon$ model (MKE), is evaluated for two case studies that involve strong adverse pressure gradients and, for one of the cases, strong boundary induced streamline curvature. The purpose of the modification in the MKE model is to sensitize the dissipation equation to the normal stresses.

For the first problem, involving a sufficiently strong adverse pressure gradient to induce separation, but with no boundary induced curvature, the modified (MKE) model induced separation while the standard $k-\epsilon$ (SKE) model did not. The failure to predict such an important flow feature represents a major deficiency of the standard $k-\epsilon$ model.

The second problem, of flow over a supercritical airfoil at 4 deg angle of attack, has a strong boundary curvature and induces strong adverse pressure gradients on the suction surface. In this case, the stresses predicted by the MKE model were slightly more accurate for the flow near the surface, but the SKE model provided more accurate stresses in the wake. The level and wake decay rate of the stresses were roughly correct

for this problem. The profile shapes, especially in the wake, were poorly predicted.

The results presented in this paper underline the poor performance of the SKE model in predicting flows with adverse pressure gradient and strong streamline curvature. As expected, the MKE model offers an improvement over the SKE model for the case of the strong adverse pressure gradient flow but performs poorly for the curved flow. This is not surprising considering that the MKE model has not been enhanced to treat such flows. It was also found that the predicted turbulent stresses do not have sufficient memory of upstream conditions. This underlines the fundamental inadequacy of the turbulent viscosity formulation.

References

1 Launder, B. E., and Spalding, D. B., "The Numerical Computation of Turbulent Flows," *Comp. Methods Appl. Mech. Eng.*, Vol. 3, 1974, pp. 269–289.

2 Leschziner, M. A., and Rodi, W., "Calculation of Annular and Twin Parallel Jets Using Various Discretization Schemes and Turbulence-Model Variations," ASME JOURNAL OF FLUIDS ENGINEERING, Vol. 103, 1981, pp. 352–360.

3 Rodi, W., and Scheuerer, G., "Scrutinizing the $k-\epsilon$ Turbulence Model Under Adverse Pressure Gradient Conditions," ASME JOURNAL OF FLUIDS ENGINEERING, Vol. 108, 1986, pp. 174–179.

4 Pourahmadi, F., and Humphrey, J. A. C., "Prediction of Curved Channel Flow with an Extended $k-\epsilon$ Model of Turbulence," *AIAA Journal*, Vol. 21, 1983, pp. 1365–1373.

5 Hackman, L. P., "A Numerical Study of the Turbulent Flow Over a Backward Facing Step Using a Two Equation Turbulence Model," Ph.D. thesis, University of Waterloo, Waterloo, Ontario, Canada, 1982.

6 Hanjalic, K., and Launder, B. E., "Sensitizing the Dissipation Equation to Irrotational Strains," ASME JOURNAL OF FLUIDS ENGINEERING, Vol. 102, 1980, pp. 34–40.

7 Simpson, R. L., Chew, Y.-T., and Shivaprasad, B. G., "The Structure of a Separating Turbulent Boundary Layer. Part 1. Mean Flow and Reynolds Stresses," *J. Fluid Mech.*, Vol. 113, 1981, pp. 23–51.

8 Simpson, R. L., Chew, Y.-T., and Shivaprasad, B. G., "The Structure of a Separating Turbulent Boundary Layer. Part 2. Higher-Order Turbulence Results," *J. Fluid Mech.*, Vol. 113, 1981, pp. 53–73.

9 Shiloh, K., Shivaprasad, B. G., and Simpson, R. L., "The Structure of a Separating Turbulent Boundary Layer. Part 3. Transverse Velocity Measurements," *J. Fluid Mech.*, Vol. 113, 1981, pp. 75–90.

10 Simpson, R. L., Shivaprasad, B. G., and Chew, Y.-T., "The Structure of a Separating Turbulent Boundary Layer. Part 4. Effects of Periodic Free-Stream Unsteadiness," *J. Fluid Mech.*, Vol. 127, 1983, pp. 219–261.

11 Nakayama, A., "Characteristics of the Flow Around Conventional and Super Critical Airfoils," *J. Fluid Mech.*, Vol. 160, 1985, pp. 155–179.

12 Raithby, G. D., Galpin, P. F., and Van Doormal, J. P., "Prediction of Heat and Fluid Flow in Complex Geometries Using General Orthogonal Coordinates," *Numer. Heat Transfer*, Vol. 9, 1986, pp. 125–142.

13 Hackman, L. P., Raithby, G. D., and Strong, A. B., "Numerical Prediction of Flows Over Backward-Facing Steps," *Int. J. Num. Meth. Fluids*, Vol. 4, 1984, pp. 711–724.

14 Simpson, R. L., "Characteristics of a Separating Incompressible Turbulent Boundary Layer," AGARD CP 168, paper 14, 1975.

15 Rannie, W. D., "Heat Transfer in Turbulent Shear Flow," *J. Aeronaut. Sci.*, Vol. 23, 1956, pp. 485–489.

16 Lewis, J. P., and Pletcher, R. H., "A Boundary-Layer Computational Model for Predicting the Flow and Heat Transfer in Sudden Expansions," Technical Report No. HTL-26, CFD-14, ISU-ERI-Ames-87018, Engrg. Research Institute, Iowa State University, Ames, 1986.

17 Laufer, J., "Some Recent Measurements in a Two Dimensional Turbulent Channel Flow," *Journal of Aeronautical Sciences*, 1950, pp. 277–287.

18 De Henau, V., "A Numerical Study of the Turbulent Flow Around Airfoils," M.A.Sc. thesis, University of Waterloo, Waterloo, Ontario, Canada, 1987.

19 De Henau, V., Raithby, G. D., and Thompson, B. E., "A Total Pressure Correction for Upstream Weighted Schemes," *Int. J. Num. Meth. Fluids*, Vol. 9, 1989, pp. 855–864.

20 Castro, I. P., Cliffe, K. A., and Norgett, M. J., "Numerical Predictions of the Laminar Flow Over a Normal Flat Plate," *Int. J. Num. Meth. Fluids*, Vol. 2, 1982, pp. 61–88.

21 Cebeci, T., Khalil, E. E., and Whitelaw, J. H., "Calculation of Separated Boundary-Layer Flows," *AIAA J.*, Vol. 17, No. 12, 1979, pp. 1291–1292.

APPENDIX A

A Derivation of P_k and P_ϵ in the Streamline Coordinate System

Figure 1 illustrates the $s-n$ coordinate system. U_s is defined as the mean velocity along a streamline and U_n, the velocity normal to a streamline. Since, by definition, no mass flows across a streamline, U_s and U_n are given by

$$U_s = \sqrt{U^2 + V^2}$$

$$U_n = 0$$

Therefore, the continuity equation for a stream tube is

$$\frac{1}{h_s h_n}\frac{\partial}{\partial s}(\rho h_n U_s) = 0 \tag{29}$$

where h_s and h_n are the metrics in the s and n directions, respectively.

The strains are expressed as

$$e_{ss} = \frac{1}{h_s}\frac{\partial U_s}{\partial s} \tag{30}$$

$$e_{nn} = \frac{U_s}{h_n h_s}\frac{\partial h_n}{\partial s} \tag{31}$$

$$e_{sn} = \frac{1}{2}\left[\frac{1}{h_n}\frac{\partial U_s}{\partial n} - \frac{U_s}{h_s h_n}\frac{\partial h_s}{\partial n}\right] = \frac{1}{2}\left[\frac{h_s}{h_n}\frac{\partial}{\partial n}\left(\frac{U_s}{h_s}\right)\right] \tag{32}$$

By expanding equation (29), it can be easily shown that

$$e_{ss} = -e_{nn} \tag{33}$$

The Reynolds stresses are related to the mean flow gradients using the Boussinesq's approximation and are given by

$$-\rho\overline{u_s u_s} = 2\mu_t e_{ss} - \frac{2}{3}\rho k \tag{34}$$

$$-\rho\overline{u_n u_n} = 2\mu_t e_{nn} - \frac{2}{3}\rho k \tag{35}$$

$$-\rho\overline{u_s u_n} = 2\mu_t e_{sn} \tag{36}$$

A.1 Derivation of P_k

The expression of P_k is $s-n$ coordinates is given by

$$P_k = -\rho\overline{u_s u_n}(2e_{sn}) - \rho\overline{u_n u_n}e_{nn} - \rho\overline{u_s u_s}e_{ss}$$

From equation (33), P_k can be written as

$$P_k = -\rho\overline{u_s u_n}(2e_{sn}) - \rho(\overline{u_s u_s} - \overline{u_n u_n})e_{ss} \tag{37}$$

Following the proposal of Hanjalic and Launder [6], $(\overline{u_s u_s} - \overline{u_n u_n})$ is related to the turbulence kinetic energy k by

$$P_k = -\rho\overline{u_s u_n}(2e_{sn}) - 0.33\rho k e_{ss}$$

or, by substituting the equation for the Reynolds shear stress (equation (36)), we obtain

$$P_k = 4\mu_t(e_{sn})^2 - 0.33\rho k e_{ss} \tag{38}$$

A.2 Derivation of P_ϵ

In the standard $k-\epsilon$ model, the generation of dissipation is given by

$$P_\epsilon = C_{\epsilon 1} P_k \tau$$

By decomposing P_k into its components parts (equation (38)), Hanjalic and Launder [6] defined P_ϵ as

$$P_\epsilon = 4C_{\epsilon 1}\tau\mu_t(e_{sn})^2 - 0.33C_{\epsilon 3}\tau\rho k e_{ss} \tag{39}$$

Equation (39) can be rewritten as

$$P_\epsilon = 4C_{\epsilon 1}\tau\mu_t(e_{sn})^2 - 0.33C_{\epsilon 1}\tau\rho k e_{ss}$$

$$-0.33C_{\epsilon 3}\tau\rho k e_{ss} + 0.33C_{\epsilon 1}\tau\rho k e_{ss}$$

or, more conveniently

$$P_\epsilon = \tau[C_{\epsilon 1}P_k - (C_{\epsilon 3} - C_{\epsilon 1})0.33\rho k e_{ss}] \tag{40}$$

Numerical Simulation of Turbulent Shear Flow in an Isothermal Heat Exchanger Model

C. Zhang
Graduate Assistant.

A. C. M. Sousa
Professor.
Mem ASME.

Department of Mechanical Engineering,
University of New Brunswick,
Fredericton, N. B., Canada E3B 5A3

Numerical predictions of fluid flow are reported for the isothermal, two-dimensional, axisymmetric flow in a disk-doughnut heat exchanger. The system consists of alternating and equi-spaced doughnut and disk baffles located in a pipe with water flowing in a turbulent regime. The two-equation ($k-\epsilon$) turbulence model as proposed by Nagano and Hishida is modified to accommodate disc and doughnut baffles. The governing equations for steady-state flow are solved in primitive variable form using segregated pressure correction linked algorithm. Predictions are critically evaluated against available data for mean quantities.

Introduction

The accurate and detailed predictions of shell-side flow distribution are of primary importance in performing the hydraulic design analysis of heat exchangers. Design and performance could therefore be improved with such information. In a great number of engineering applications baffles are placed in shell-and-tube heat exchangers in order to increase levels of mixing and consequently enhance heat transfer. Therefore, a priori knowledge of the flow field may eliminate problems related with flow induced vibration and flow maldistribution to avoid potential structural damage, and eventually improve overall heat transfer coefficients.

Turbulence modeling plays an important role in the accuracy of the simulation. The popular ($k-\epsilon$) model has widespread use in several commercial codes, for instance PHOENICS [1]. Despite this, the open literature has given little attention to evaluating the predictive capability of this model in regions where baffles are located in the flow passage. Typically, the bulk of the literature is addressed to laminar flow (Berner et al. [2]), turbulent flow over a backward facing step (Autret et al. [3]) or turbulent flow over a single baffle (Ganesan et al. [4]).

The present study intends to fill this gap. It is an extension of recent publications presented by Zhang and Sousa [5–6], Theodossiou et al. [7] and Sousa and LeBlanc [8], in which predictive methods are tested and assessed by comparing their results with experimental data for flows under isothermal conditions.

The selected flow situation and experimental data are taken from Founti et al. [9] and Vafidis [10], in which a water model was constructed to simulate the shell-side flow in a disk-and-doughnut baffle, shell-and-tube heat exchanger. This particular model does not take into account exit effects, thermal effects, tube bundle, and secondary flow streams such as tube-baffle leakage flow and shell-baffle leakage flow. Two Reynolds numbers and two baffle spacings are used in this study.

The present configuration results in a considerable challenge in terms of modelling, and an appropriate benchmarking test, since the main flow features will not be masked by the presence of the tube bundle. As shown by Elphick and Currie [11] and Theodossiou et al. [7], the effect upon the flow of the tube bundle is to smooth out the velocity distribution and to reduce the recirculation regions.

In line with this rationale, the two-equation ($k-\epsilon$) model as proposed by Nagano and Hishida [12] in a modified form to handle the baffles is reported in the following sections and its predictions are compared against the experimental data. Required assumptions are also outlined and discussed.

Flow Configuration

The heat exchanger model is schematically shown in Fig. 1. The test section comprises a 74 mm + 1.0 mm internal diameter pipe and 475 mm length, and a system of four and eight alternating and equi-spaced disk and doughnut baffles for two baffle-pitch geometries, respectively. This system in the physical model is connected and kept on axis by six 3 mm diameter brass rods. These rods are not incorporated into the computational model and consequently neglected in the simulation.

The flow conditions, geometries and parameters investigated are given in Table 1.

Mathematical Formulation

Equations of Motion. The flow field in the configuration shown in Fig. 1 can be conveniently described in cylindrical polar coordinates. The steady, two-dimensional governing differential equations for the mean quantities as reported by Gupta and Lilley [13] are

Contributed by the Fluids Engineering Division for publication in the JOURNAL OF FLUIDS ENGINEERING. Manuscript received by the Fluids Engineering Division August 22, 1988.

Table 1 Flow configurations

Geometrical parameters (mm) Configuration	D_s	d_c	d_d	l_i	l_o	l/D_s
Geometry #1	74	50.8	54	100	118	1
Geometry #2	74	50.8	54	100	65	0.5

Flow parameters Configuration	U_b(ms^{-1})	Re_b*10^{-4}
Geometry #1	0.619	4.55
Geometry #2	0.497	3.66

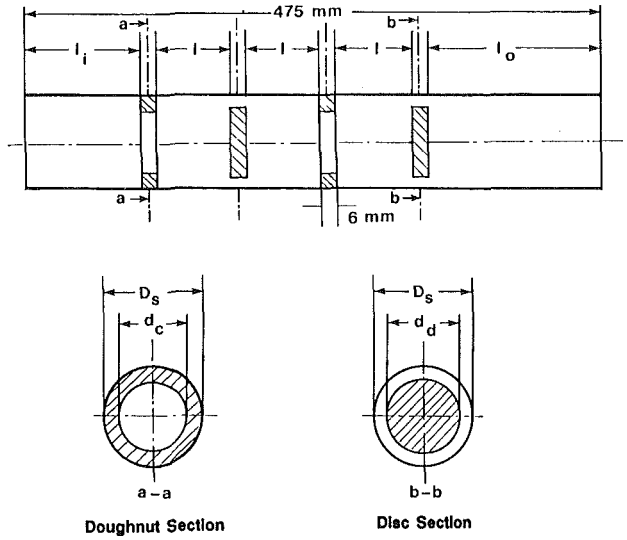

Fig. 1 Heat exchanger model

Continuity

$$\frac{\partial u}{\partial x}+\frac{1}{r}\frac{\partial (rv)}{\partial r}=0 \tag{1}$$

Momentum

$$\rho\left[\frac{\partial (uu)}{\partial x}+\frac{1}{r}\frac{\partial (rvu)}{\partial r}\right]=\frac{1}{r}\left[\frac{\partial}{\partial x}\left(r\mu_e\frac{\partial u}{\partial x}\right)+\frac{\partial}{\partial r}\left(r\mu_e\frac{\partial u}{\partial r}\right)\right]$$
$$-\frac{\partial p}{\partial x}+\frac{\partial}{\partial x}\left(\mu_e\frac{\partial u}{\partial x}\right)+\frac{1}{r}\frac{\partial}{\partial r}\left(r\mu_e\frac{\partial v}{\partial x}\right)-F_x \tag{2}$$

$$\rho\left[\frac{\partial (uv)}{\partial x}+\frac{1}{r}\frac{\partial (rvv)}{\partial r}\right]=\frac{1}{r}\left[\frac{\partial}{\partial x}\left(r\mu_e\frac{\partial v}{\partial x}\right)+\frac{\partial}{\partial r}\left(r\mu_e\frac{\partial v}{\partial r}\right)\right]$$
$$-\frac{\partial p}{\partial r}+\frac{\partial}{\partial x}\left(\mu_e\frac{\partial u}{\partial r}\right)+\frac{1}{r}\frac{\partial}{\partial r}\left(r\mu_e\frac{\partial v}{\partial r}\right)-2\mu_e\frac{v}{r^2}-F_r \tag{3}$$

The local hydraulic resistances, F_x and F_r, follow the general formulation proposed by Carlucci et al. [14], namely:

$$F_x=k_bU_p\mu \tag{4}$$

$$F_r=k_bU_pv \tag{5}$$

where k_b is a head loss coefficient and U_p is defined as $U_b=(u^2+v^2)^{1/2}$. For the particular cases of the baffles, which are assumed to be impervious to flow, the value of k_b is set to an arbitrarily large value (10^{20}). This means that the baffles are modelled as infinite hydraulic resistances.

The concept of an effective viscosity, defined as the sum of the laminar and turbulent viscosities,

$$\mu_e=\mu+\mu_t \tag{6}$$

is employed.

Nomenclature

C_1, C_2 = turbulent model constants
C_p = wall static pressure coefficient = $(p-p_{ref})/(\rho U_b^2/2)$
C_μ = turbulence model constant
D_s = internal diameter of the model heat exchanger
d_c = doughnut hole diameter of the model heat exchanger
d_d = disk diameter of the model heat exchanger
F = local hydraulic baffle resistance
f_μ, f_1, f_2 = turbulence model functions
G_k = volumetric rate of generation of turbulent dissipation rate
k = turbulent kinetic energy
L_m = the Nikuradse mixing length
l = baffle pitch of the model heat exchanger
l_1 = entrance length in the model heat exchanger before first battle
l_o = exit length in the model heat exchanger after last baffle
p = pressure
p_{ref} = reference pressure
R = internal radius of the model heat exchanger
Re_b = Reynolds number = $\rho U_b D/\mu$
R_{ky} = local turbulence Reynolds number = $\rho\sqrt{k}\,y/\mu$
R_{kz} = local turbulence Reynolds number = $\rho\sqrt{k}\,z/\mu$
R_t = turbulence Reynolds number = $\rho k^2/(\mu\epsilon)$
R_τ = local Reynolds number = $y^+=\rho u^* y/\mu$
r = radial coordinate
U_b = bulk velocity
U_p = streamwise velocity
u = axial velocity component
u^* = friction velocity = $\sqrt{\tau_w/\rho}$
v = radial velocity component
x = axial coordinate
y = radial location away from the walls
y^+ = radial dimensionless distance = $\rho u^* y/\mu$
z = axial location away from the walls
z^+ = axial dimensionless distance = $\rho u^* z/\mu$
ϵ = turbulent dissipation rate
μ = laminar dynamic viscosity
μ_e = effective dynamic viscosity
μ_t = turbulent dynamic viscosity
ν = laminar kinematic viscosity = μ/ρ
ν_e = effective kinematic viscosity = μ_e/ρ
ν_t = turbulent kinematic viscosity = μ_t/ρ
ρ = density
σ_k, σ_ϵ = turbulent Prandtl numbers for k and ϵ, respectively
τ_w = wall shear stress
χ = the von Karman constant

Subscripts

r = in radial direction
x = in axial direction

Nagano and Hishida's k-ϵ Model. This model permits the calculation to be carried out up to the wall without the use of universal wall functions. In what follows the model will be outlined as given originally by Nagano and Hishida [12].

Kinetic Energy

$$\rho\left(u\frac{\partial k}{\partial x}+v\frac{\partial k}{\partial r}\right)=\frac{\partial}{\partial x}\left[\left(\mu+\frac{\mu_t}{\sigma_k}\right)\frac{\partial k}{\partial x}\right]+\frac{1}{r}\frac{\partial}{\partial r}\left[r\left(\mu+\frac{\mu_t}{\sigma_k}\right)\frac{\partial k}{\partial r}\right]$$

$$+G_k-\rho\epsilon+\rho D \tag{7}$$

Dissipation Rate

$$\rho\left(u\frac{\partial \epsilon}{\partial x}+v\frac{\partial \epsilon}{\partial r}\right)=\frac{\partial}{\partial x}\left[\left(\mu+\frac{\mu_t}{\sigma_\epsilon}\right)\frac{\partial \epsilon}{\partial x}\right]+\frac{1}{r}\frac{\partial}{\partial r}\left[r\left(\mu+\frac{\mu_t}{\sigma_\epsilon}\right)\frac{\partial \epsilon}{\partial r}\right]$$

$$+C_1\frac{\epsilon}{k}G_k-C_2f_1\rho\frac{\epsilon^2}{k}+\rho E \tag{8}$$

where

$$G_k=\mu_t\left[2\left\{\left(\frac{\partial u}{\partial x}\right)^2+\left(\frac{\partial v}{\partial r}\right)^2+\left(\frac{v}{r}\right)^2\right\}+\left(\frac{\partial u}{\partial r}+\frac{\partial v}{\partial x}\right)^2\right] \tag{9}$$

$$D=-2\mu\left(\frac{\partial\sqrt{k}}{\partial r}\right)^2/\rho \tag{10}$$

$$E=\mu\mu_t(1-f_\mu)\left(\frac{\partial^2 u}{\partial r^2}\right)^2/\rho^2 \tag{11}$$

$$f_1=1-0.3\exp(-R_t^2) \tag{12}$$

$$R_t=\rho k^2/(\mu\epsilon) \tag{13}$$

$$f_\mu=[1-\exp(-y^+/26.5)]^2 \tag{14}$$

$$\mu_t=C_\mu f_\mu\rho k^2/\epsilon \tag{15}$$

$$y^+=\rho u^* y/\mu \tag{16}$$

$$u^*=\sqrt{\tau_w/\rho} \tag{17}$$

In the above equations, the values of the constants used for the computations are given in Table 2.

Modifications of Nagano and Hishida's k-ϵ Model. When the baffle effects are to be considered the following "ad hoc" modifications were made to the f_μ, D and E terms:

$$f_\mu=[1-\exp(-\mathrm{R}_{ky}/26.5)-\exp(-\mathrm{R}_{kz}/26.5)]^2 \tag{18}$$

$$D=-2\mu\left[\left(\frac{\partial\sqrt{k}}{\partial r}\right)^2+\left(\frac{\partial\sqrt{k}}{\partial x}\right)^2\right]/\rho \tag{19}$$

$$E=\mu\mu_t(1-f_\mu)\left[\left(\frac{\partial^2 u}{\partial r^2}\right)^2+\left(\frac{\partial^2 v}{\partial x^2}\right)^2\right]/\rho^2 \tag{20}$$

where

$$\mathrm{R}_{ky}=\rho\sqrt{k}\,y/\mu \tag{21}$$

$$\mathrm{R}_{kz}=\rho\sqrt{k}\,z/\mu \tag{22}$$

In the function f_μ of the present model, R_{ky} (or R_{kz}) is used instead of y^+ (or z^+) in the original function f_μ as reported by Nagano and Hishida [12]. As stated by these authors, turbulent velocities near the wall are usually of the same order of magnitude as the friction velocity u^*. Therefore, the local Reynolds number, $R_y(=y^+=\rho u^* y/\mu)$, is similar to the local turbulence Reynolds number, $R_k(=\rho\sqrt{k}y/\mu)$, in the wall region. For this particular flow situation where several baffles are inside the flow field, the calculation of the friction velocity u^* for all of the baffle walls is cumbersome, and the proposed change is a reasonable strategy.

The underlying assumption made when rewriting these terms is that the flow in the immediate vicinity of the baffles still holds the main Couette flow characteristics. Strictly speaking, this is not true in regions of adverse pressure gradients and stagnation points which take place on the pipe wall in the regions located just ahead and behind the doughnuts, and on the forward face of the disk baffles, respectively. However, the findings of a series of test runs reported by Zhang and Sousa [6] indicate that the above mentioned flow features are confined to relatively small regions, and the Couette flow assumption is acceptable.

Table 2 Turbulence model constants

Constant	C_μ	C_1	C_2	σ_k	σ_ϵ
Value	0.09	1.45	1.90	1.00	1.30

Solution Algorithm

The algorithm employed here is based on the method proposed by Theodossiou and Sousa [15]. The method uses a segregated solution with the equations discretized by a control volume formulation, in which the advective terms are modelled by a hybrid scheme and the diffusion terms are fitted with piecewise linear profiles. The momentum equations are linked to the continuity equation by the pressure correction. For completeness, a brief description of the method will be presented here.

The closed set of equations to be solved comprises:

(*i*) Two momentum equations.
(*ii*) One continuity equation.
(*iii*) Two turbulence quantity equations.

Since these equations are coupled together and are highly non-linear, an iterative approach is used for their solution. A cyclic outer iteration comprises the following sequence of operations:

(*a*) The momentum equations, equations (2) and (3), are solved based on a pressure field taken from the previous iteration.

(*b*) A Poisson equation for the pressure correction, derived from the continuity equation, equation (1), is solved, and at the end of each outer iteration loop, pressures and velocities are corrected.

(*c*) The two turbulent quantities k and ϵ are obtained from their transport equations, equations (7) and (8). To save computer time, however, these equations are only solved every fourth outer iteration loop of the momentum and pressure correction equations.

(*d*) A new cycle is started unless the prescribed accuracy has been reached.

Boundary Conditions. The set of equations being solved are of the elliptic type requiring boundary conditions on all the boundary surfaces of the flow domain. Four kinds of boundary conditions are described, they are: inlet, outlet, pipe wall and the plane of symmetry (here only half of the cross-section needs to be considered, as the flow is assumed to be symmetric about the pipe axis).

Inlet. At inlet, the profiles of all the field variables (except pressure) need to be specified. The axial velocity component was assumed to have a uniform or a parabolic profile, and the radial velocity component was set to zero. In any case, however, this inlet condition does not appear to affect much the flow beyond the first baffle. The levels of turbulent kinetic energy and its dissipation are not known, therefore, appropriate assumptions are required. The value of k is taken as a fraction, in the present case 0.012, of the inlet mean kinetic

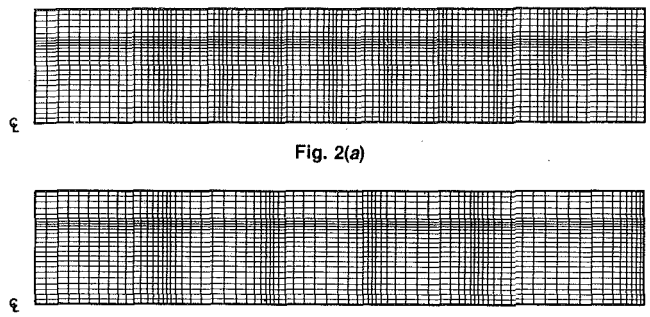

Fig. 2(*a*)

Fig. 2(*b*)

Fig. 2 Basic grids used for the simulations. (*a*) Geometry #1; (*b*) Geometry #2

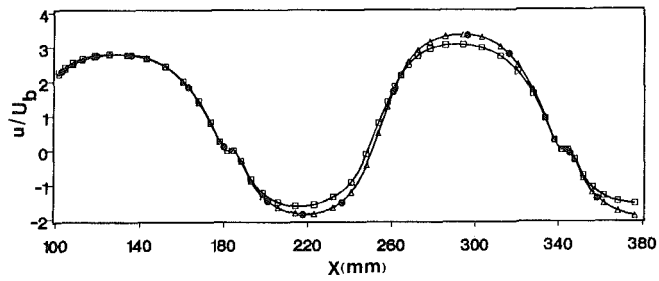

Fig. 3(*a*)

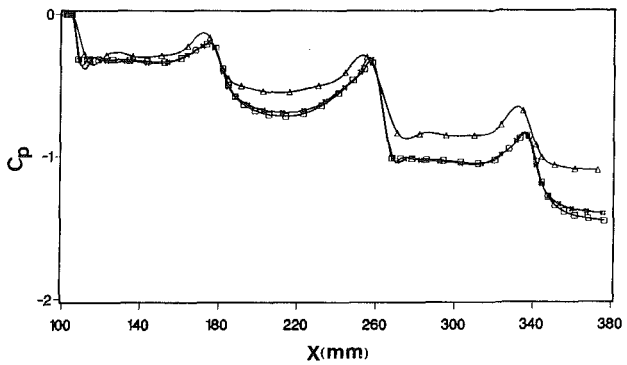

Fig. 3(*b*)

Fig. 3 Grid-independence tests for geometry #1 with grids 12*46, 18*64 and 24*76. (*a*) Centerline velocities; (*b*) wall static pressure coefficient, C_p. (▵-Grid 12*46; #-Grid 18*64; □-Grid 24*76)

energy, while the dissipation is calculated via the procedure suggested by Autret et al. [3], namely:

$$\epsilon = C_\mu \frac{\chi y k^2}{L_m^2 u^*} \tag{23}$$

where χ is the von Karman constant taken as 0.41 and L_m is the Nikuradse mixing length given by

$$\frac{L_m}{R} = 0.14 - 0.08\left(1 - \frac{y}{R}\right)^2 - 0.06\left(1 - \frac{y}{R}\right)^4 \tag{24}$$

Outlet. Information about the flow at the exit plane is not available, so the axial velocities at the outlet are allowed to vary according to the nearest upstream values but magnitudes are adjusted to satisfy continuity as described by Theodossiou et al. [7]. The other variables (k, ϵ, and v) have their streamwise derivatives set to zero. This treatment should be carefully employed, since it may lead to erroneous results as discussed by Zhang and Sousa [5].

Wall. The non-slip condition is applied at the wall to all fluid velocities. The values of k and ϵ are set equal to zero at the wall as proposed by Nagano and Hishida [12]. Since the walls are impervious to flow, the normal velocity components

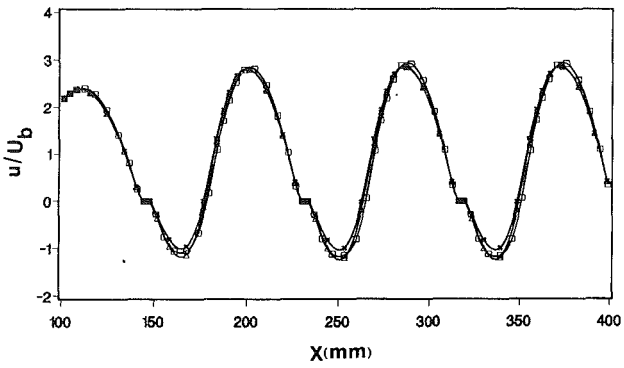

Fig. 4(*a*)

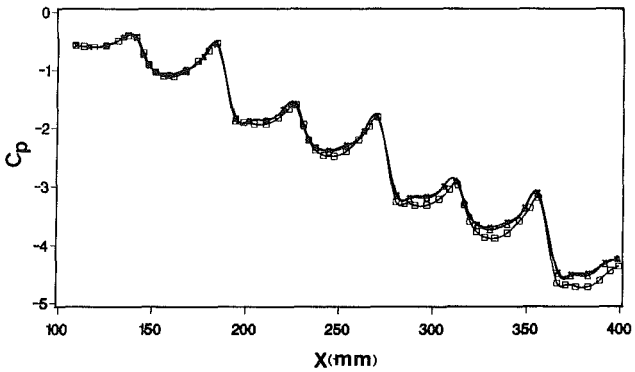

Fig. 4(*b*)

Fig. 4 Grid-independence tests for geometry #2 with grids 18*76, 24*76, and 24*92. (a) Centerline velocities; (b) wall static pressure coefficient, C_p. (#-Grid 18*76; ▵-Grid 24*76; □-Grid 24*92)

are equal to zero. Accordingly, pressure correction gradients normal to the walls are set to zero following the suggested treatment of Theodossiou and Sousa [15].

Plane of Symmetry. Along the pipe axis the derivatives with respect to the radial direction of all field variables are set to zero. This condition in the discretized conditions is modelled to be consistent with the piecewise linear profiles taken for the diffusion terms of the governing equations.

Results and Discussion

The computations were carried out in non-uniform, fixed, staggered grids of 24-radial by 76-axial and 24-radial by 92-axial for geometries #1 and #2, respectively, as shown in Figs. 2(*a*) and 2(*b*). To test the grid-independence of the solutions, three different grids were used for each case. These grids are 12*46, 18*64 and 24*76 for geometry #1, and 18*76, 24*76 and 24*92 for geometry #2. Convergence trends indicate an asymptotic behavior, but no extrapolation to zero-grid size was attempted.

Comparisons for the different grids were conducted for values of centerline velocities and wall static pressure coefficient. In each case, as depicted in Figs. 3 and 4, the maximum differences between the two smaller grids, i.e., 18*64 and 24*76 for geometry #1, and 24*76 and 24*92 for geometry #2, are approximately 1.5 percent, a value, which is well below the experimental systematic errors (10 percent for the mass flow rate).

Computing time per nodal point and iteration on the UNB IBM 3090/180-VF mainframe using the basic grids is approximately $7*10^{-4}$ s, and satisfactory convergence is obtained in 70 iterations. Solutions are judged to have converged when both the error norm for the momentum equations and the normalized ratio between the mass residual and inlet mass flow rate satisfy the condition of being less than 10^{-5}.

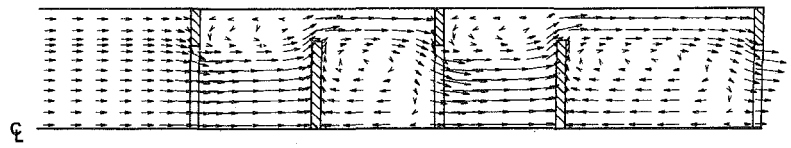

Fig. 5(*a*)

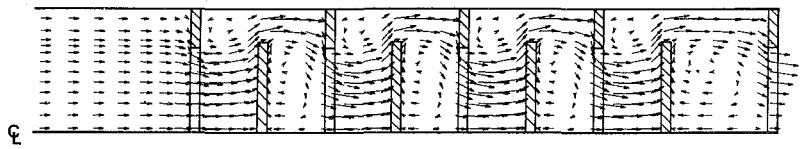

Fig. 5(*b*)

Fig. 5 Predicted mean velocity field for half cross-section. (*a*) Geometry #1, (*b*) Geometry #2.

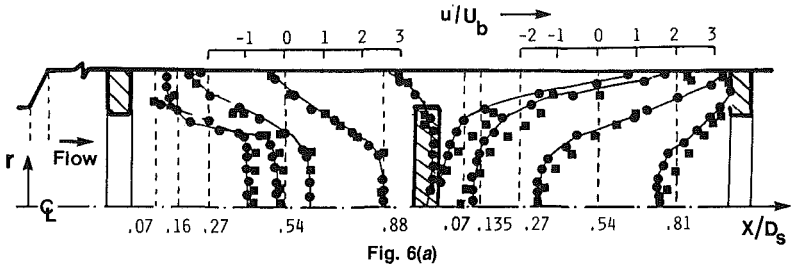

Fig. 6(*a*)

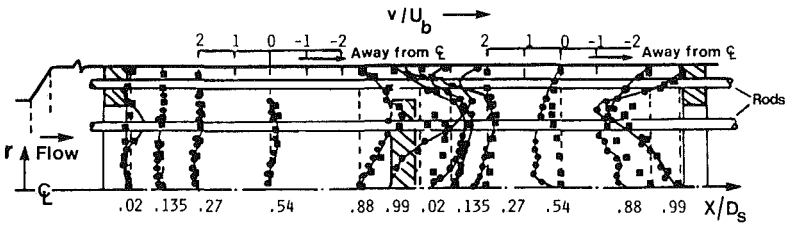

Fig. 6(*b*)

Fig. 6 Predictions and experimental data for geometry #1. (*a*) Mean axial velocities, (*b*) mean radial velocities. (● -Experiments; ■ -Predictions)

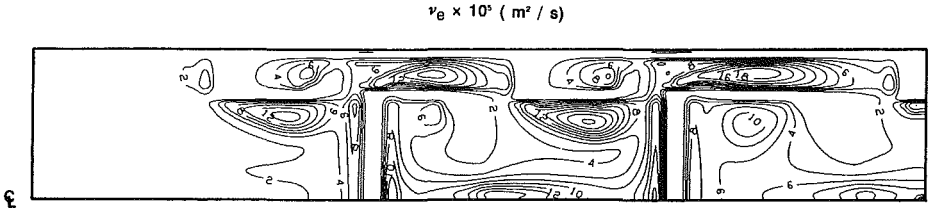

Fig. 7 Distribution of effective kinematic viscosity in geometry #1

The mean velocity distributions of the turbulent shear flow in the disc-and-doughnut heat exchanger is indicated on the vector plots in Fig. 5. The simulations were carried out for geometries #1 and #2 using the present (k–ϵ) formulation. The large recirculation zones and wakes behind the disk and doughnut baffles, as reported by Founti et al. [9], are clearly shown through Fig. 5. The reattachment length behind the doughnuts tends to be smaller for geometry #2 than for geometry #1, a finding also noted in the experimental study [9].

The predicted results for mean axial and radial velocities in geometry #1 are shown in Fig. 6. In Fig. 6(b), at x/D_s equal to 0.54 and beyond, some discrepancies between predictions and experimental data are shown. This may be attributed not only to the shortcomings for recirculation flows of any eddy viscosity based model, but also a result of the presence of the supporting brass rods, which may cause local increase of the radial velocity component. Overall the agreement between experimental and predicted values in very encouraging. This is further corroborated by noting that the predicted values for the width of the recirculation bubble (0.65 d_d at half the recirculation zone) and the reattachment length (1.17 d_d) compare well with the experimental values of 0.63 d_d and 1.24 d_d, respectively.

Figure 7 illustrates the typical distribution of the effective kinematic viscosity ν_e, predicted by the proposed model for geometry #1. It it interesting to note that in recirculation zones the effective viscosity gradients are relatively small.

The agreement between predictions and experiments for the centerline mean axial velocity is excellent as shown in Fig. 8.

The turbulent kinematic viscosity ν_t is given in Fig. 9 for locations $x/D_s = 0.27$ downstream doughnuts (Fig. 9(a)) and disks (Fig. 9(b)).

The predictions for the normalized turbulent kinetic energy for geometry #1 are shown in Fig. 10 at locations $x/D_s = 0.27$ downstream doughnuts (Fig. 10(a)) and disks (Figs. 10(b)). The peaks occur around log $(y^+) = 2.2 - 2.3$.

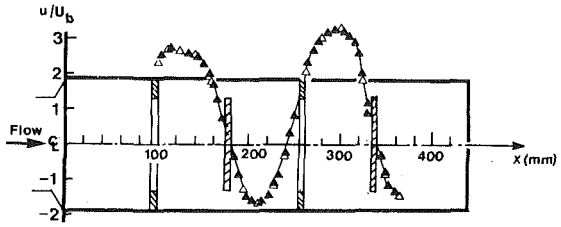

Fig. 8 Centerline mean axial velocity for geometry #1. (▲-Experiments; △-Predictions)

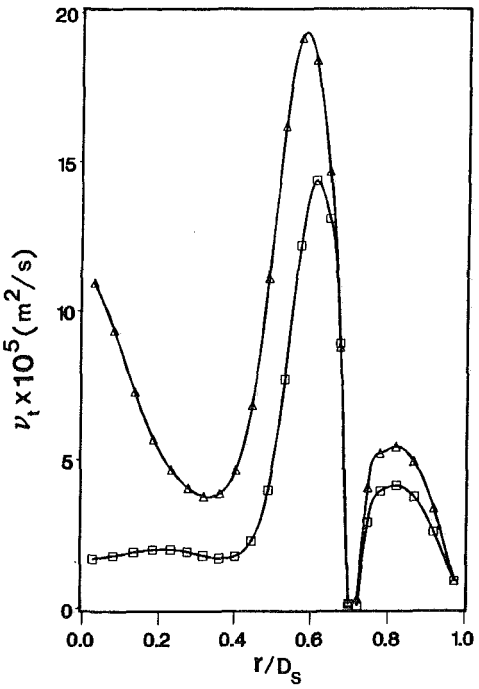

Fig. 9(a)

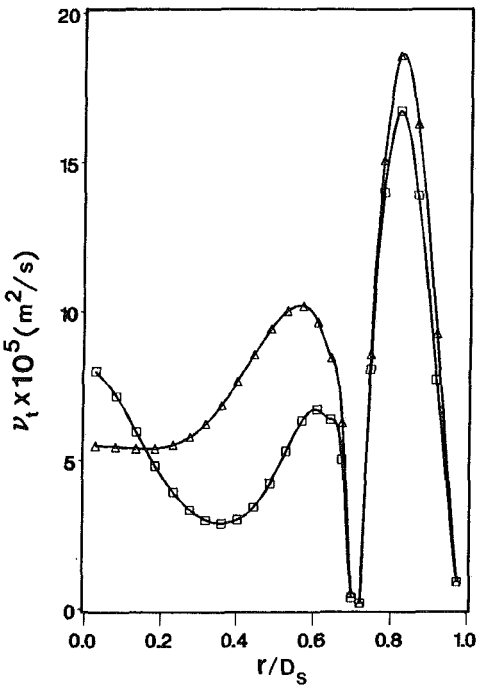

Fig. 9(b)

Fig. 9 Turbulent kinematic viscosity in geometry #1 at location $x/D_s = 0.27$ downstream. (*a*) Doughnuts, (*b*) disks. (□-1st disk (or doughnut); △-2nd disk (or doughnut))

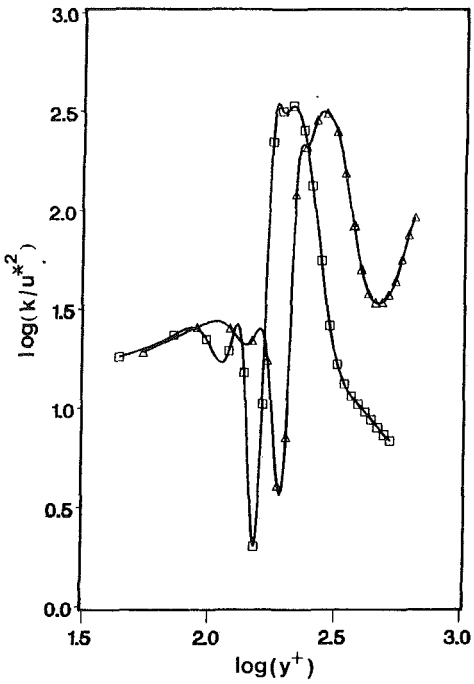

Fig. 10(a)

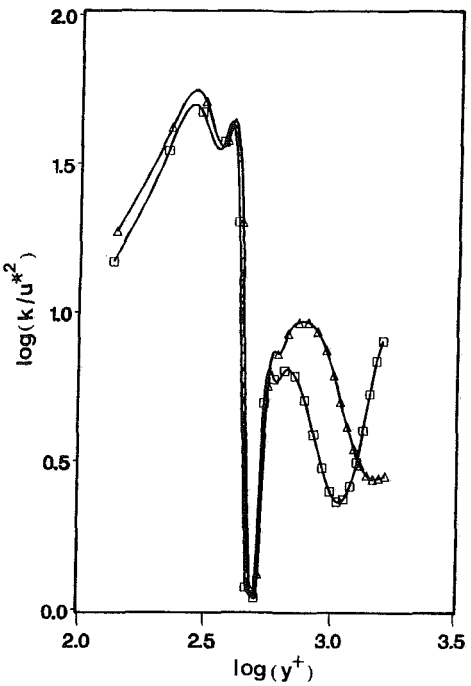

Fig. 10(b)

Fig. 10 Normalized turbulent kinetic energy distribution in geometry #1 at $x/D_s = 0.27$ downstream. (*a*) Doughnuts, (*b*) disks. (□-1st disk (or doughnut); △-2nd disk (or doughnut))

The results for the mean axial velocity distribution in geometry #2 are presented in Fig. 11, for locations $x/D_s = 0.27$ downstream doughnuts (Fig. 11(*a*)) and disks (Fig. 11(*b*)). A large change in flow quantities between the first and subsequent doughnuts, as reported by Founti et al. [9], is apparent. Figure 11 also indicates that the mean flow self-similarity is established by the second doughnut, which agrees with the experimental results [9]. However, the flow behind the fourth disk presents a major departure from this trend, which may be caused by the expansion of the outflow.

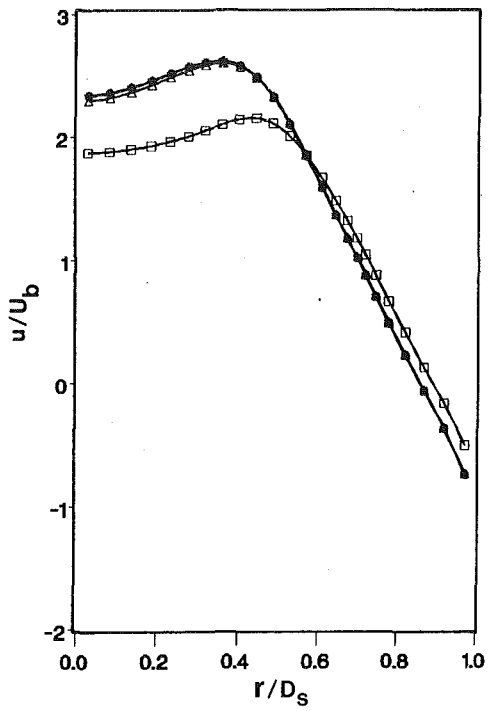

Fig. 11(*a*)

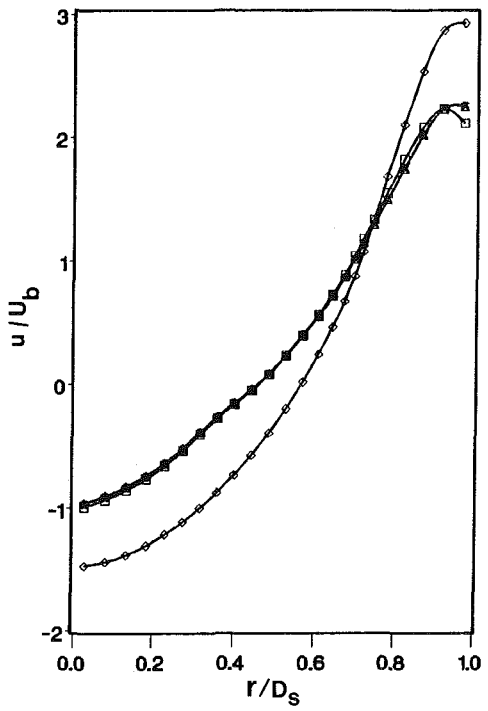

Fig. 11(*b*)

Fig. 11 Mean axial velocity distribution in geometry #2 at $x/D_s = 0.27$ downstream. (*a*) Doughnuts, (*b*) disks. (□-1st disk (or doughnut); △-2nd disk (or doughnut); #-3rd disk (or doughnut); ◇-4th disk (or doughnut))

The results for the wall static pressure coefficient (C_p) are shown in Fig. 12. The agreement between predictions and experimental data is good, considering the complexity of the flow configuration.

Finally, for the purpose of comparison, Fig. 13 shows the centerline mean axial velocities obtained by the proposed model and Nagano and Hishida's model, respectively. The comparison indicates that the proposed model predicts the velocity

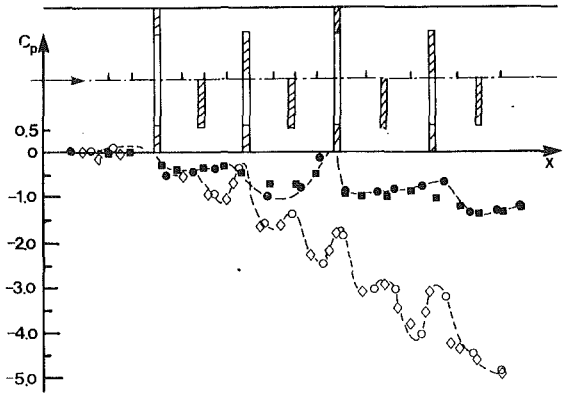

Fig. 12 Distribution of wall static pressure coefficient. Geometry #1: ●-Experiments; ■-Predictions. Geometry #2: ○-Experiments; ◇-Predictions.

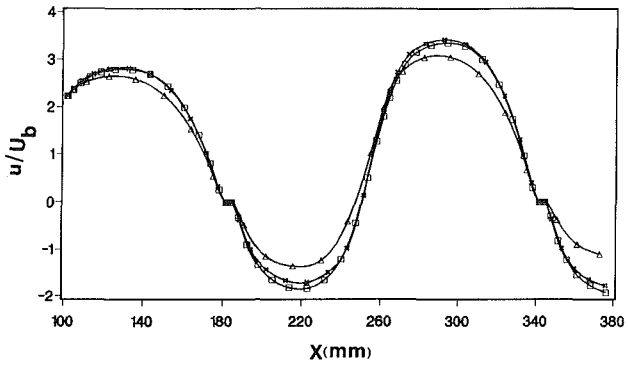

Fig. 13 Centerline mean axial velocity for geometry #1. (●-Exp; △-Proposed model; □-Nagano and Hishida's model)

field better than Nagano and Hishida's model. The latter tends to overestimate the velocity behind the disks and underestimate the velocity behind the doughnuts. This can be explained by the fact that the original Nagano and Hishida's model, which was designed for pipe flow, does not take into account the effects of shear stress of disk and doughnut walls.

As a final comment, it should be mentioned that the above results were obtained with no attempt of optimizing the turbulence model constants listed in Table 2. This may have enhanced the prediction capability of the numerical model, the immediate objective, hoever, was to evaluate the results produced by "ad hoc" modifications, somehow dictated by engineering common sense, to Nagano and Hishida's model [12].

Concluding Remarks

The modified (k–ϵ) model proposed in the present study performed well in predicting the mean flow quantities as assessed by the comparison with the experimental data. The modifications permit the calculations to be carried out up to the solid walls, including baffles, a feature that yields good numerical robustness. In addition, their implementation was found to be straightforward, requiring minimal effort in incorporating the baffles. Also, as compared to the Nagano and Hishida's model for multibaffled flow, the proposed model led to savings in computer time well above 40 percent.

The predictive capability of the model for the turbulent quantities, however, has to be futher assessed against experimental data before its overall potential can be evaluated.

Acknowledgment

Financial support for this work was received from the Uni-

versity of New Brunswick, and Natural Sciences and Engineering Research Council of Canada (NSERC grant No. A1398).

References

1 Gunton, M., Rosten, H. I., Spalding, D. B., and Tatchell, D. G., "PHOENICS-An Instruction Manual," CHAM TR/75 (1983).

2 Berner, C., Durst, F., and McEligot, D. M., "Flow Around Baffles," ASME Winter Annual Meeting, Boston, Mass., Paper No. 83-WA/HT-9.

3 Autret, A., Grandotto, M., and Dekeyser, I., "Finite Element Computation of a Turbulent Flow Over a Two-Dimensional Backward Facing Step," *International Journal for Numerical Methods in Fluids*, Vol. 7, 1987, pp. 89–102.

4 Ganesan, Y., Spalding, D. B., and Murthy, B. S., "Experimental and Theoretical Investigation of Flow Behind an Axi-Symmetrical Baffle in a Circular Duct," *J. Institute of Fuel*, Vol. 51, 1978, pp. 144–148.

5 Zhang, C., and Sousa, A. C. M., "Numerical Predictions of Shellside Flow in a Model of a Disc-and-Doughnut Heat Exchanger," *Proc. 9th Brazilian Congress of Mechanical Engineering*, Vol. 1, Florianopolis, S. C., Dec. 7–11, 1987, pp. 41–44.

6 Zhang, C., and Sousa, A. C. M., "Comparison of Different Turbulence Models for Shell-Side Flow in a Model Heat Exchanger," *Proc. 6th Italian Conference on Fluid Flow and Heat Transfer*, Bari, Italy, June 9–10, 1988, pp. 153–164.

7 Theodossiou, V. M., Sousa, A. C. M., and Carlucci, L. N., "Flow Field Predictions in a Model Heat Exchanger," *Int. J. Computational Mechanics*, Vol. 3, 1988, pp. 419–428.

8 Sousa, A. C. M., and LeBlanc, D. D., "Shell-Side Flow Prediction of an Experimental Heat Exchanger," *Numerical Methods for Non-Linear Problems*, Eds. C. Taylor, E. Hinton, D. R. J. Owen and W. Onate, Vol. 2, Pineridge Press, 1984, pp. 791–801.

9 Founti, M. A., Vafidis, C., and Whitelaw, J. H., "Shell-Side Distribution and the Influence of Inlet Conditions in a Model of a Disc-and-Doughnut Heat Exchanger," *Experiments in Fluids*, Vol. 3, 1985, pp. 293–300.

10 Vafidis, C., "The Influence of a Symmetric Inlet Flow on the Pressure and Velocity Characteristics of an Isothermal Heat Exchanger Model," AERE-Report, AERE-R, 19585, 1982.

11 Elphick, I. G., and Currie, I. G., "Flow Distribution Measurements in a Model Heat Exchanger, Phases #1 and #2," Reports to Atomic Energy of Canada Ltd. by Dept. of Mechanical Engineering, University of Toronto, 1982.

12 Nagano, Y., and Hishida, M., "Improved Form of the k–ϵ Model for Wall Turbulent Shear Flows," ASME JOURNAL OF FLUIDS ENGINEERING, Vol. 109, 1987, pp. 156–160.

13 Gupta, A. K., and Lilley, D. B., *Flowfield Modelling and Diagnostics*, Abacus House, Tunbridge Wells, U. K., 1985, pp. 34–74.

14 Carlucci, L. N., Galpin, P. F., and Brown, J. D., "Numerical Predictions of Shell-Side Heat Exchanger Flows," *A Reappraisal of Shell-Side Flow in Heat Exchangers*, Eds., W. J. Marner and J. M. Chenoweth, ASME, HTD-Vol. 36, New York, N.Y., 1984, pp. 19–26.

15 Theodossiou, V. M., and Sousa, A. C. M., "An Efficient Algorithm for Solving the Incompressible Fluid Flow Equations," *International Journal for Numerical Methods in Fluids*, Vol. 6, 1986, pp. 557–572.

A New Hydraulic Pressure Intensifier Using Oil Hammer

Katsumasa Suzuki
Associate Professor,
Musashi Institute of Technology,
Tamazutsumi Setagayaku,
Tokyo 158 Japan

An oil hammer generates a greater pressure than that supplied to a pipeline, and sometimes causes equipment breakdown. The author intends to actively utilize this pressure rise. A new type of pressure intensifier is proposed, which converts oil pressure into a value more than six times higher, by means of an oil hammer. The intensifier has advantages in simple structure and in easy control since it is controllable by switching only one solenoid operated valve. A theoretical analysis describing the performance and operation of this design is developed. Results of experimental work on this design are then compared with theoretical results.

1 Introduction

As an oil (water) hammer generates a pressure greater than that supplied to a pipeline, and sometimes causes equipment breakdown, many attempts have been made to predict such pressures and develop methods to reduce it. In the present work, however, the author proposes to actively utilize this pressure rise. A new type of hydraulic pressure intensifier is proposed, which operates on the principle that an oil hammer is generated continuously in a pipeline and only the high pressure oil is discharged through a check valve. The intensifier can convert oil pressure of several MPa produced by a low pressure pump, into a pressure which is more than six times higher.

In the case of water, a hydraulic ram utilizing this idea by means of a water hammer has been invented two hundred years ago, and is used to deliver water to higher elevations. Recent investigations show that the discharge pressure of hydraulic rams are of the order of several hundred kPa [1]. The new intensifier proposed here is intended to be used with an oil hydraulic equipment. The discharge pressure levels required are about 10–30 times greater than those encountered by a hydraulic ram. Consequently, a different structure is required for the new intensifier. This intensifier has the following advantages over the usual intensifier.

(*a*) Very simple structure. As the new intensifier is composed only of a pipeline, a check valve, a solenoid operated valve and the current switching device, the structure is simple and economical.

(*b*) Switching of only one solenoid operated valve makes it possible to start and stop the intensifier easily and to control the discharge at the output. This control is achieved by repeated switching of the solenoid valve. It is suitable for micro computer control.

In this paper the new intensifier construction is explained and its fundamental characteristics are clarified by experimental and theoretical results.

Contributed by the Fluids Engineering Division for publication in the JOURNAL OF FLUIDS ENGINEERING. Manuscript received by the Fluids Engineering Division April 4, 1988.

2 New Intensifier Construction

The construction of the new intensifier which has been developed in this research is shown in Fig. 1. The fluid at constant pressure is supplied to the upstream side of the pipeline (position 1). The switching of a solenoid operated valve located at the downstream end of the pipeline (position 2) generates an oil hammer in the pipeline.

When current is supplied to the solenoid valve, it is in the open state, the fluid path is free and the fluid flows at high speed through the pipeline and the solenoid valve to the tank. Immediately after the valve is closed rapidly, by cutting off the solenoid current, an oil hammer is generated in the pipeline. As long as the pressure at point 2 is higher than that at point 3, the check valve is open and high pressure fluid is discharged through the check valve. Soon the pressure at point 2 becomes lower than that at point 3, and the check valve closes preventing a reverse flow. Therefore, a pressure much higher than the supply can be obtained. The accumulator (II) resets from instantaneous and local pressure increase at point 3, and increases the discharge volume. The high pressure fluid is intended to be sent to a load through point 4 originally, but that path is shut for this study. A relief valve (II) is attached to keep the pressure constant at point 3. Because point 4 is shut, all of the high pressure fluid is discharged through the relief valve.

The solenoid operated valve is controlled by a micro com-

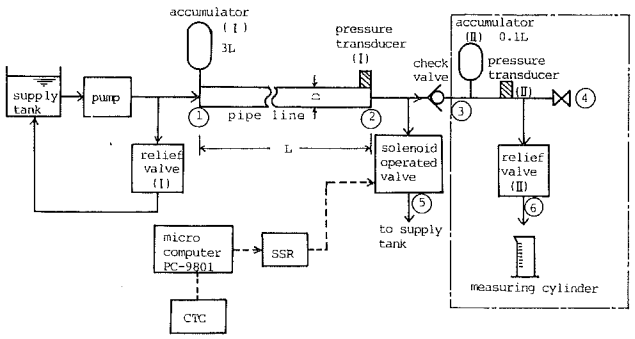

Fig. 1 Schematic diagram of the test rig

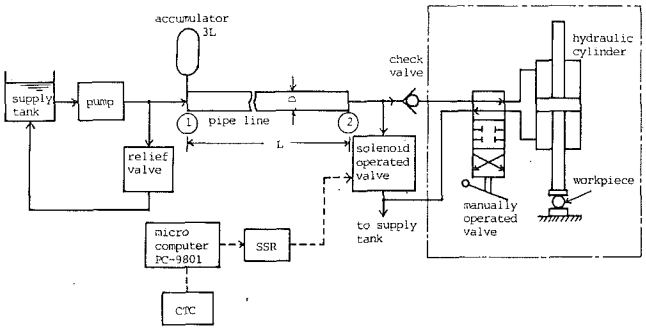

Fig. 2 Example of application

puter to obtain the desired switching pattern. The micro computer includes an LSI (CTC = Counter Timer Circuit) in order to detect time at intervals of 1.25 ms, and it switches the direct current of the solenoid operated valve at desired time intervals. The micro computer output signal is sent to the solid state relay (SSR) through an interface. This signal controls the OPEN | CLOSED status of the solenoid operated valve. The OPEN-CLOSED intervals and the total number of OPEN | CLOSED operations are entered interactively by the user at the keyboard.

This intensifier is applied to a hydraulic cylinder as a main application as shown in Fig. 2. The part enclosed by a line in Fig. 1 is replaced by a hydraulic cylinder and a manually operated valve. In this case, the hydraulic cylinder can be operated as usual by operating the manually operated valve. If an oil hammer is generated by the operation of the solenoid operated valve, the chamber of the cylinder is compressed by the discharged fluid. The pressure in the chamber can be raised gradually for every on-off of the solenoid operated valve. The detailed performance of this application is clarified in another publication [2].

3 Numerical Calculation

The model developed by Zielke [3] is applied to predict the pressure and fluid velocity of the system by numerical calculation, which considers the initial and the boundary conditions of the pipeline when an oil hammer occurs. Zielke's model considers frequency-dependent laminar friction in the pipeline and has been developed to predict the dynamic response of pipelines. The model combines both the method of characteristics and finite difference.

The following conditions are assumed for numerical calculation. At the beginning, the solenoid operated valve is in the closed position and the fluid in the line is at rest. The pressure in the line is equal to the supply pressure of the pump. The valve is then opened and closed according to the pulse output of the micro computer. The w in equation (4) is the ratio of the current open area of the solenoid valve to its total open area, and its value lies between zero and one. It is assumed that the flow through the check valve is discharged without any pressure drop when the pressure at point 2 is higher than that at point 3 due to an oil hammer.

Considering these conditions, the following equations are used for the calculations together with the equations developed by Zielke.

The initial conditions are:

$$v = 0 \tag{1}$$

$$p = P_s \tag{2}$$

where v and p are the average velocity and the pressure at a section, respectively, at all points along the pipeline.

The boundary conditions are:
at the upstream end:

$$p_1 = P_s \tag{3}$$

at the downstream end:

$$q_v = c_0 A_v w \sqrt{2p_2/\rho} \tag{4}$$

$$A_c v_2 = q_3 + q_v \tag{5}$$

$$p_3 = P_0 \tag{6}$$

due to the action of the check valve:

$$p_2 = P_0 \quad (q_3 > 0) \tag{7}$$

$$q_3 = 0 \quad (p_2 < P_0) \tag{8}$$

4 Experimental Results and Calculated Results

The differential transformer is connected to the spool of the solenoid operated valve to measure the valve (spool) displacement. The pressures p_2 and p_3 are measured by semiconductor pressure transducers (I) and (II). These signals and micro computer output e_c, solenoid voltage e_s and the signal of the current i are memorized rapidly by a digital memory device. Later these are recorded slowly by X-Y recorder. The parameter values of the test rig are tabulated in Table 1.

Figure 3 shows the calculated result of the fluid velocity v_2 after the solenoid operated valve starts to open. The velocity increases rapidly from zero and reaches almost steady state in approximately 100 ms. Therefore, referring to this velocity response, the solenoid operated valve is operated with suitable time intervals.

4.1 Dynamic Characteristics. First, the solenoid operated valve is operated continuously with pulse width of 125 ms and

Nomenclature

A_c = line cross-sectional area
A_v = total open area of solenoid operated valve
c = sonic velocity in fluid, $\sqrt{K/\rho}$
c_0 = discharge coefficient
D = inner diameter of line
D_v = $4\nu/D^2$
e_c = electric output signal of computer
e_s = solenoid voltage
i = solenoid current
K = bulk modulus of fluid
L = length of line
N = number of nodes along line
P_0 = output pressure
P_m = maximum output pressure
P_s = supply pressure
p = pressure
q = volumetric fluid flow rate
q_v = volumetric fluid flow rate through valve
T_1 = $2L/c$
t = time
t_w = pulse width
V_i = input volume through point 1 per cycle
V_0 = output volume through point 3 per cycle
v = average fluid velocity at line section
w = ratio of current open area of solenoid valve to its total open area
y = valve (spool) displacement
η = efficiency
ν = kinematic viscosity of fluid
ρ = fluid density

Subscripts

1,2,3,4,5,6 = flow positions (Fig. 1)

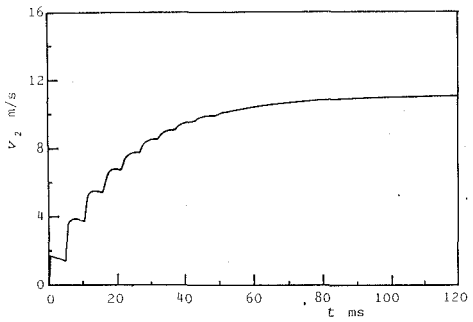

Fig. 3 v_2 after opening the valve

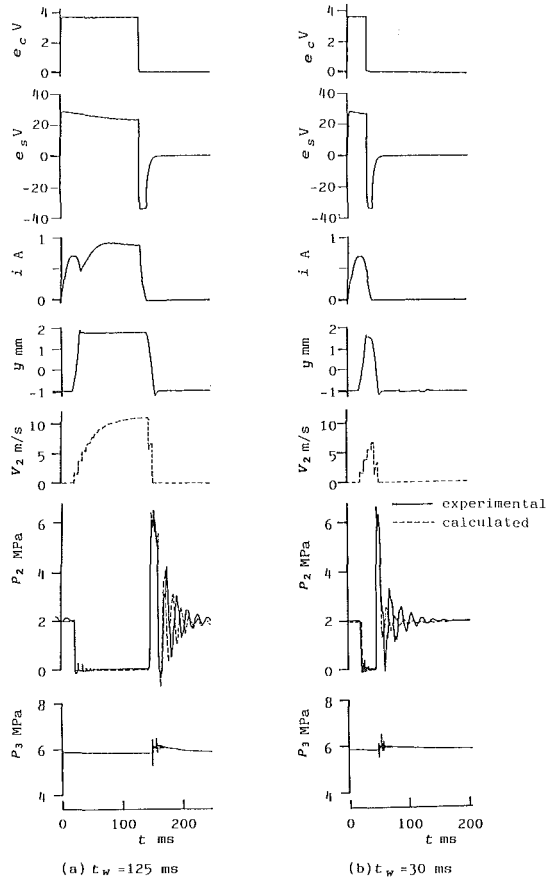

Fig. 4 Responses of the system to pulse input with different width

frequency of 4 Hz. The valve is intended to be closed after the flow velocity reaches sufficiently steady state. Figure 4(*a*) shows the micro computer signal and the response at each point for one cycle, illustrated with a common time axis. The solenoid operated valve begins to open 22.1 ms after turning on the computer signal. The pressure p_2 at the downstream end becomes almost zero and the fluid in the line is accelerated.

By the closure of the solenoid operated valve, the pressure p_2 increases suddenly and reaches a value $P_0(=p_3)$, which is kept constant at point 3. Because the check valve opens at this moment and the fluid is discharged through it, the pressure p_2 is maintained at this value for a short time and undergoes a damped oscillatory behavior which eventually converges to the value of the supply pressure P_s. When p_2 becomes lower than P_0, the check valve closes. The displacement of the poppet in the check valve is a few tenths of a mm. The fluctuation of the supply pressure P_s at the point 1 during the oil hammer is within 4 percent of the steady state pressure due to the relief valve (I) and the accumulator (I).

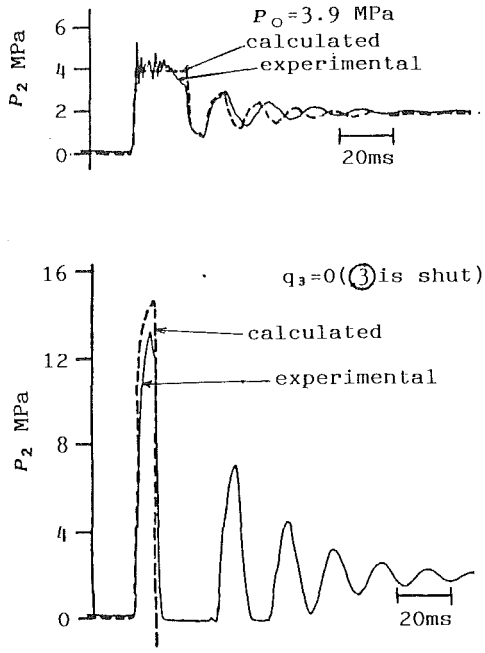

Fig. 5 Wave forms of pressure p_2 for various output conditions

For the numerical calculation, the observed form of the valve displacement is approximated by a trapezoidal wave. When y is greater than zero, the solenoid operated valve is open. In Fig. 4, the solid lines show the experimental results.

Figure 5 shows the pressure responses with different output conditions. If point 3 is shut, very high pressure is generated at first then decreases into a value lower than atmosphere. Therefore cavities seem to appear in the fluid.

The cycle period of the vibration in the experimental results for $P_0=3.9$ MPa is longer than the calculated result. When point 3 is shut, the maximum pressure of the experiment is lower than the calculated result. These are attributed to the unavoidable volume at the connection parts in the experimental equipment. Around point 2 the distances between the downstream end of the pipeline, the solenoid valve and the check valve and between the check valve and the accumulator (II) are made as small as possible. However, there are still some amount of unavoidable piping length between these points. The compressibility of the volume of fluid in these regions softens the abrupt change of the flow velocity and consequently weakens the oil hammer making the cycle period of the vibration longer. The extra piping length also produces time lags which reduce the output volume as mentioned in the next section.

4.2 Output Volume. Figures 6 and 7 show the output volume V_0 per cycle for a steady output pressure $P_0(=p_3)$. The value of the output pressure P_0 can be varied by the adjustment of the relief valve (II). Figure 6 shows the effect of the line length. Figure 7 shows the effect of the line diameter D. The uncertainty bands of the measurements represent odds of 20 to 1. These are indicated on the following figures.

On the whole, the output volume obtained by the experiment shows relatively lower value than that obtained by calculation. This may be attributed to the many kinds of small difference in the experimental conditions from the idealized conditions of the calculation. For example, the unavoidable small distance between each parts at downstream end 2 reduces the output volume. Dynamics of the poppet in the check valve seem complicated and need to be clarified precisely in the future, but they are idealized in the calculation since the purpose of the paper is to clarify the fundamental principles of the new intensifier. The time delay of the check valve

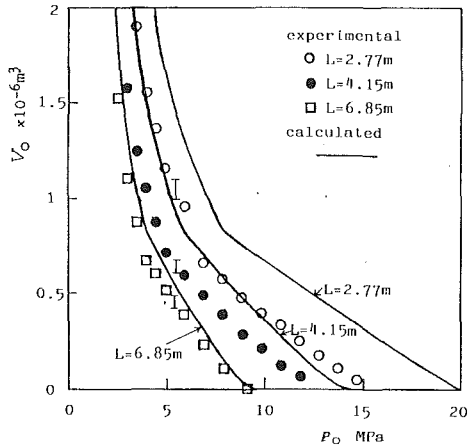

Fig. 6 Output volume V_0 versus output pressure P_0 for various line length L

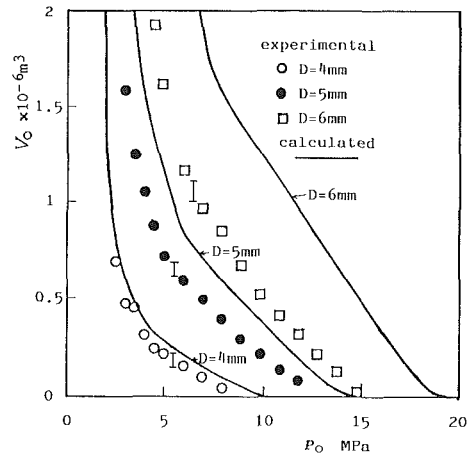

Fig. 7 Output volume V_0 versus output pressure P_0 for different inner diameter D

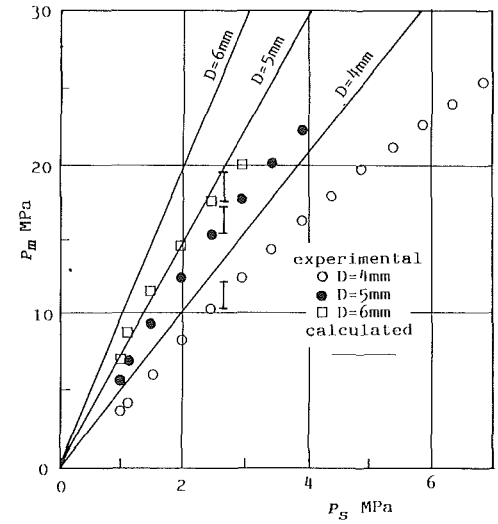

Fig. 8 Maximum output pressure P_m versus supply pressure P_s

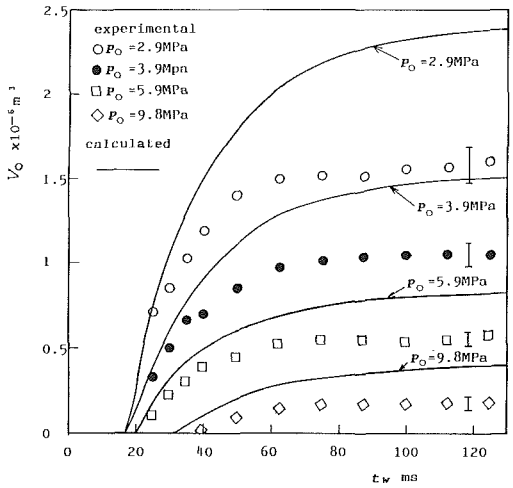

Fig. 9 Output volume V_0 versus pulse width t_w for various output pressure P_0

causes the output flow reduction when it begins to open and also causes a reverse flow when it begins to close. Therefore the output volume with the real check valve is less than that with the idealized check valve.

When the line length is reduced or the diameter is increased, the output volume increases and the maximum output pressure rises. However, in either case, the necessary output flow of the pump is increased, because the input volume to the line during time when the solenoid operated valve is open increases. Moreover if the line length is reduced further, the experimental results do not increase as much as expected from the calculation. This may be attributed strongly to the unavoidable piping lengths and volume between the components at the downstream end and the dynamics of the poppet in the check valve. The cycle period of the oil hammer becomes shorter with the reduced length, and the effect increases for rapid charge.

Another cause of the performance drop is that laminar flow is assumed in the calculation. The maximum Reynolds number is expected to be 2160 with $L=2.77$ m, $D=5$ mm and 2390 with $L=4.15$ m, $D=6$ mm. Around these Reynolds numbers the flow is expected to become turbulent, which results in the increase of resistance to the flow. Therefore the flow velocity does not become as high as expected by calculation.

4.3 Maximum Output Pressure. As the output pressure P_0 increases, the output volume V_0 decreases, and finally it becomes zero. At this state, the pressure P_0 is defined as a maximum output pressure P_m. Figure 8 shows the effect of the supply pressure P_s and line diameter D on the maximum output pressure P_m. P_m is almost proportional to P_s. A pressure that is about 4.2 times as high as the supply pressure is obtained in the experiment with a value of $D=4$ mm, about 6.1 times with $D=5$ mm, and about 7.4 times with $D=6$ mm. The experimental result is lower than calculated one due to the same reason as Fig. 5 for $q_3=0$.

If the pressure drop through the solenoid operated valve is ignored, the valve is assumed to be closed instantaneously after the steady flow velocity is obtained, and the output flow is zero, the maximum output pressure P_m is indicated generally by the equation (9) because it is typical in oil hammers [4]:

$$P_m=\frac{cD^2P_s}{32\nu L}\left(1+2\sqrt{\frac{D_vT_1}{\pi}}+D_vT_1\right) \tag{9}$$

The value indicated by equation (9) is a few percent higher than the calculated result of Fig. 8.

The assumption of instantaneous valve closure is reasonable in this case. Although the actual valve closure takes similar time as acoustic cycle ($2L/c$) after it starts to move, the pressure drop across the valve (p_2) is very small during almost all the process of the valve closure because the area of the

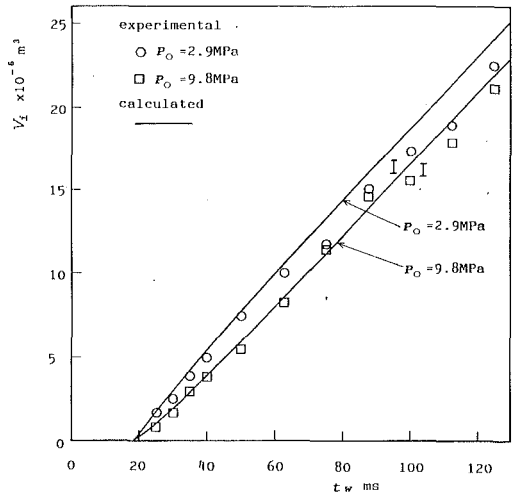

Fig. 10 Input volume V_i versus pulse width t_w

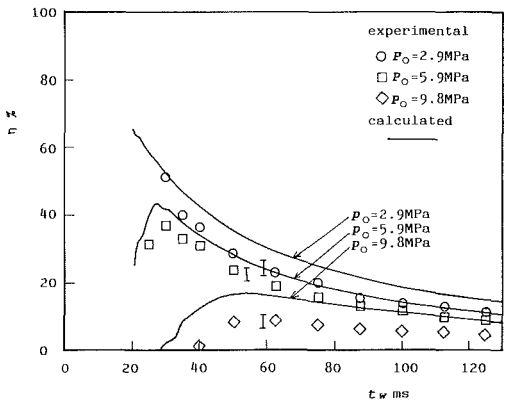

Fig. 11 Efficiency η versus pulse width t_w for various output pressure P_0

valve $A_v w$ is still big enough during it. In very short period before the valve is closed completely, the pressure drop becomes significant across the valve and stops the flow completely at last. Therefore, when the calculated result of p_2 with the assumption of instantaneous valve closure is compared with the result calculated using the observed valve displacement, only a slight difference is found at the beginning portion of the pressure rise.

4.4 Effect of Pulse Width. So far the pulse width has been kept at 125 ms. The following will be expected from Fig. 3, if the open time interval of the solenoid operated valve is varied. The maximum fluid velocity is increased and the oil hammer becomes stronger and results in the output volume increase as the interval increases. But the effect decreases when the interval is increased beyond 100 ms. Besides the input volume to the pipeline increases monotonically with the interval and flows away wastefully into a tank.

Now the input volume, the output volume and the efficiency are investigated when the pulse width of the micro computer output is varied. Figure 4 (*a*) and (*b*) show the relations amongst the micro computer signals and the response of each point for the pulse width, respectively 125 ms or 30 ms. For the short pulse width, the difference of the forms between the computer signal and the valve displacement is large. If the pulse width is shorter than 16 ms, the solenoid operated valve remains closed, because the valve displacement is too small to exceed the overlap region. If the pulse width is longer than this, the open time interval of the valve increases monotonically according to the increase of the pulse width.

Table 1 Parameters

Parameter	Value
A_V	7.76×10^{-5} m^2
c_0	0.6
D	5 mm except Fig. 7 & 8
K	1.36 GN/m^2
L	4.15 m except Fig. 6
N	20
P_s	1.96 MPa except Fig. 8
ν	$0.38.3 \times 10^{-4}$ m^2/s
ρ	853 kg/m^3

Figure 9 shows the relation between the output volume V_0 and the pulse width t_w. The output volume increases as the pulse width is increased. But the output volume increases slightly as the pulse width increases beyond 100 ms. The value of the experimental results is less than the calculated results in Fig. 9. This may be attributed to the similar reason mentioned in section 4.2. Figure 10 shows the relation between the input volume V_i and the pulse width t_w. V_i means the volume which flows during a cycle through the entrance of the line. V_i increases monotonically with t_w, and it is slightly more at the low output pressure than at the high output pressure.

The efficiency η is defined as:

$$\eta = \frac{P_0 V_0}{P_s V_i} \tag{10}$$

Figure 11 shows the relation between the efficiency and the pulse width. The figure shows that there exists a value of t_w at which the efficiency is a maximum.

5 Conclusion

A new type of intensifier has been invented and tested, which has the principle that an oil hammer is generted continuously in a pipeline and only the high pressure fluid is discharged through a check valve. As the performance has been investigated by experiments and numerical calculations, it has been verified that the fluid pressure of several MPa supplied by a low pressure pump can be converted into pressure several times higher. Though the possible output flow is not much, application is possible where high pressure is needed by a cylinder at the final stage of pressing or during cramping in a press or a cramp equipment. As the output volume per cycle is clearly determined by the condition, the total output volume can be controlled by the number of cycles. Therefore it is favorable for computer control because the intensifier can be controlled only by switching the solenoid current on and off.

Acknowledgment

The author expresses his thanks to Prof. S. Sato and Mr. K. Kobayashi of Musashi Institute of Technology for their support in performing this research.

References

1 Iversen, H. W., "An Analysis of the Hydraulic Ram," ASME JOURNAL OF FLUIDS ENGINEERING, Vol. 97, No. 2, 1975, pp. 191–196.

2 Suzuki, K., "Application of a New Pressure Intensifier Using Oil Hammer to Pressure Control of a Hydraulic Cylinder," ASME JOURNAL OF DYNAMIC SYSTEMS, MEASUREMENT, and Control, Vol. 111, No. 2, pp. 322–328.

3 Zielke, W., "Frequency-Dependent Friction in Transient Pipe Flow," ASME *Journal of Basic Engineering*, Vol. 90, No. 1, 1968, pp. 109–115.

4 Holmboe, E. L., Rouleau, W. T., "The Effect of Viscous Shear on Transients in Liquid Lines," ASME *Journal of Basic Engineering*, Vol. 89, No. 1, pp. 174–180.

Experimental Investigations of Annular Liquid Curtains

K. D. Kihm
Department of Mechanical Engineering,
Texas A&M University,
College Station, TX 77843

N. A. Chigier
Mechanical Engineering Department,
Carnegie-Mellon University,
Pittsburgh, PA 15213

Experiments have been performed to study the dynamics of vertical annular liquid curtains. Using a high and a low speed photographic recording technique, different modes of curtain formation have been visualized: (a) nonpressurized curtain, (b) pressurized steady curtain, (c) pressurized oscillating curtain, and (d) punctured curtain. The velocity of the liquid was measured by an argon-ion laser Doppler velocimeter, and results were compared with free falling motion. The convergence length of the curtain was measured as a function of the pressure differential for different Froude and Weber numbers, and for different nozzle gap widths. The experimental data agree well with existing theoretical predictions for steady curtains. For harmonically oscillating curtains, the average values of minimum and maximum convergence lengths show fairly good agreement with the theory.

Introduction

When liquid emerges vertically downward from an annular nozzle, a conical liquid sheet, which will be called a "liquid curtain," is formed due to the combined effects of the contractive action of surface tension, the elongative action of inertia and gravity, and the expanding action of pressure differential between the inside and the outside of the curtain (Fig. 1). The convergence length L is defined as a distance from the nozzle exit to the apex of the liquid curtain.

The concept of utilizing a liquid curtain as a sealed reactor chamber was proposed for the design of an inertial confinement fusion (ICF) reactor to alleviate several problems associated with a solid reactor chamber (Maniscalco and Meier, 1977). Interest in the dynamics of liquid curtains has grown in connection with a proposed design of a system for direct reduction of zirconium from zirconium tetrachloride ($ZrCl_4$) and sodium (Na) (Chigier et al., 1987). The conventional Kroll process involves mixing of $ZrCl_4$ and Na by injecting them separately into a solid reactor chamber. The reduction efficiency of Zr is very low since the molecular diffusion force that drives Zr into a molten pool is weak. However, if the $ZrCl_4$ spray were surrounded by a curtain of liquid sodium so that the reduced Zr could be driven through the apex of the conical curtain, a viable reactor with an improved reduction efficiency would be achieved. The liquid curtain also prevents the escape and/or the evaporation of homogeneously formed zirconium.

The history of the quantitative study of liquid curtains goes back at least to the 19th century when Boussinesq (1869) proposed a mathematical model for water bells. Amongst many studies (Lance and Perry, 1953, and Taylor, 1959) that have been devoted to establish the relevant phenomena, Binnie and Squire (1941) first employed the basic models to derive nonlinear differential equations that describe the behavior of liquid curtains. The differential equations were simplified and analytically solved for the flow at zero pressure differential. The study of Baird and Davidson (1962) is based on a similar analysis, but accounts for the presence of pressure differential across the curtain. However, both of these studies did not account for the gravity effect, and assumed that the thickness of the liquid sheet is negligibly thin.

The analysis of Holvingh (1977) accounts for the effect of gravitational acceleration and derives a solution for the convergence length analytically. Hoffman et al. (1980) generalized and improved Holvingh's analysis by including the surface

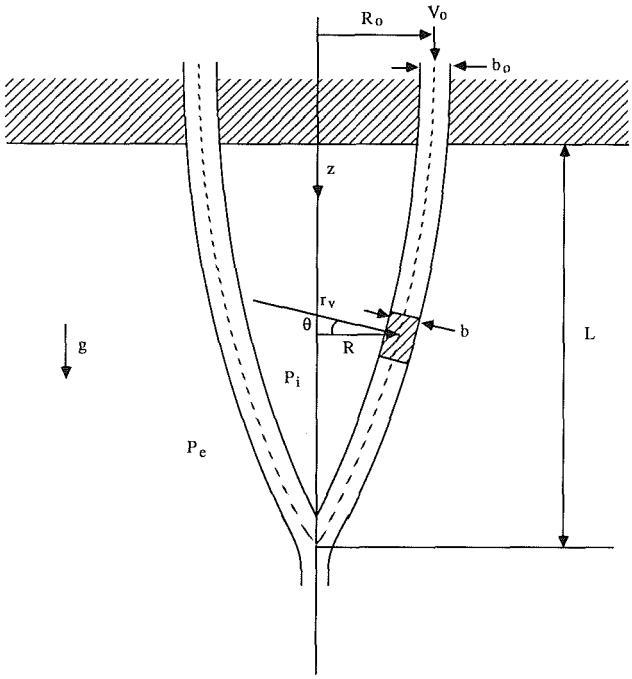

Fig. 1 Schematic diagram of liquid curtain from an annular nozzle

Contributed by the Fluids Engineering Division for publication in the JOURNAL OF FLUIDS ENGINEERING. Manuscript received by the Fluids Engineering Division August 23, 1988.

tension forces from both the inner and the outer surfaces of the curtain. Experimental verification of the theory was also attempted and results showed good agreement with the calculated convergence length at low flow velocities. At high flow velocities, the measured lengths were found to be significantly shorter than the calculated lengths. It is believed that this is due to the enhanced contractive action driven by the flow-induced partial vacuum inside the curtain. Unfortunately, both of these studies did not consider the influence of the pressure differential on the convergence length.

A more rigorous theory was developed by Esser and Abdel-Khalik (1984) who were motivated by the recognition that no purely analytical model can simultaneously account for all of the flow parameters of interest. The two-dimensional, steady-state, parabolic Navier-Stokes equations were applied to the flowing liquid and solved for the velocity and pressure distributions using the finite-difference computer code ANNJET. The calculated results agreed well with the measured convergence length with zero pressure differential obtained by Hoffman et al. (1980). For curtains with a nonzero pressure differential, more extensive measurement is needed to confirm the validity of the theory.

Ramos (1988) modified the Lagrangian formulation originally developed by Hoffman et al. (1980), and obtained analytical and numerical solutions. The analytical predictions, in which the radius of curvature in the vertical plane is neglected assuming a long curtain, showed longer convergence lengths than numerical predictions.

In the present study the convergence length is measured as a function of pressure differential $p_i - p_e$ for several combinations of the principal parameters: the ratio of the nozzle gap to the orifice radius b_o/R_o and initial liquid velocity V_o. The significant dimensionless parameters are the Froude number $Fr = V_o^2/gR_o$, the Weber number $W_e = \rho V_o^2 b_o/2\sigma$ where ρ and σ denote the liquid density and surface tension coefficient, respectively, and the pressure coefficient $C_p = Fr^2 (P_i - P_e/\rho V_o^2)$. The data have been compared with the analytical and numerical predictions obtained by Ramos (1988).

Using an argon-ion laser Doppler velocimeter, velocities of the flowing liquid have been measured and the results are compared with the theory for a long curtain with an approximation of $|dR/dz| << 1$ where R is the local curtain radius and z is the axial distance. Also, the evolution of the liquid curtains is photographically visualized as the pressure differential is progressively increased. It is demonstrated that the pressure differential force plays a major role in determining the characteristics of liquid curtains.

Experimental Apparatus

A schematic of the experimental apparatus is shown in Fig. 2. Liquid is injected vertically downward through a cylindrical annular nozzle into a tank. The nozzle is mounted in a three-dimensional traversing system which is positioned by computer-controlled stepping motors. Local tap water has been used for generating liquid curtains and the liquid is recirculated in a closed loop to maintain the same properties of the test fluid. The amount of natural seeding in the tap water was sufficient for providing good Doppler signals. Backward scattered signals from the LDA optical system were detected to avoid the attenuation of Doppler signals by the liquid curtain. The attenuation increases as the liquid velocity fluctuations in the curtain increase. The detected Doppler signal is processed by a counter type TSI 1980 processor and analyzed by a Digital MINC-23 data acquisition system. The anemometer was calibrated using a TSI calibrating wheel. The bias of the velocity measurement was found to be negligible and the discrepancy between the normal speed of the wheel and the actual measurement was less than 1 percent.

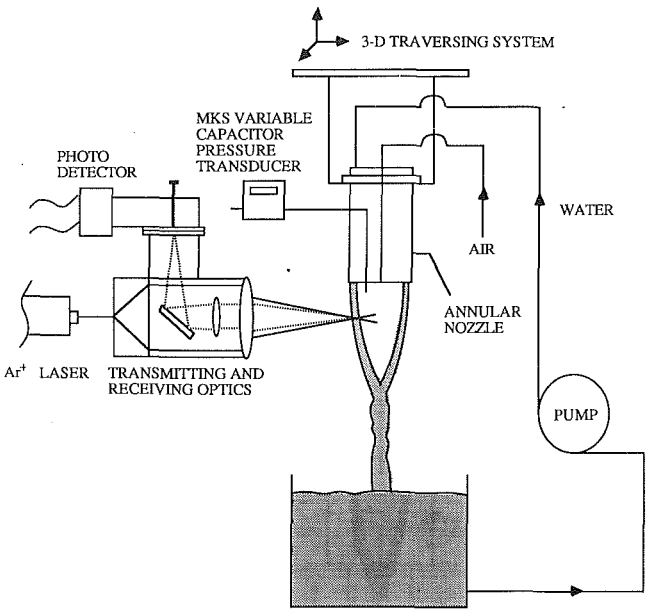

Fig. 2 Schematic diagram of experimental apparatus

The nozzle designed for the study is shown in Fig. 3. Water is pumped through the annular nozzle after passing through a filter and a settling chamber. The variation of the annular nozzle gap is achieved by installing inserts of different sizes. The nozzle outer diameter is 100 mm and two different inserts are used to provide gap thicknesses of 0.5 mm and 1.0 mm. The length/gap width ratio is 80 (for the 0.5 mm gap width) so that the flow at the nozzle exit is developed to a fully annular flow. An air inlet is located at the center of the center piece and the air supply is maintained at various pressures in order to study the effect of pressure differential on the curtain shape and stability. The minute pressure difference between the inner and outer regions of the curtain is measured using a MKS 398H

Nomenclature

b = local curtain film thickness
b_o = initial curtain thickness or nozzle gap thickness
C_p = pressure coefficient $[Fr^2(P_i - P_e)/\rho V_o^2]$
Fr = Froude number $[V_o^2/gR_o]$
g = gravitational acceleration
L = curtain convergence length
L^* = dimensionless convergence length $[L/R_o]$
N_c = convergence number $[\rho g^2 R_o b_o/2V_o^2\sigma]$
Pa = Pascal
P_i = pressure inside the curtain
P_e = pressure outside the curtain
ΔP = pressure differential $[P_i - P_e]$
R = local curtain radius in the horizontal plane
R_o = initial curtain radius or nozzle outer diameter
r_v = radius of curvature of the curtain in the vertical plane
t = time
V = axial mean velocity (local)
V = axial mean velocity at the nozzle exit
V^* = dimensionless axial mean velocity $[V/V_o]$
We = Weber number $[\rho V_o^2 b_o/2\sigma]$
z = axial distance
z^* = dimensional axial distance $[z/R_o]$
ρ = liquid density
σ = surface tension coefficient
θ = angle between r_v and R in the vertical plane

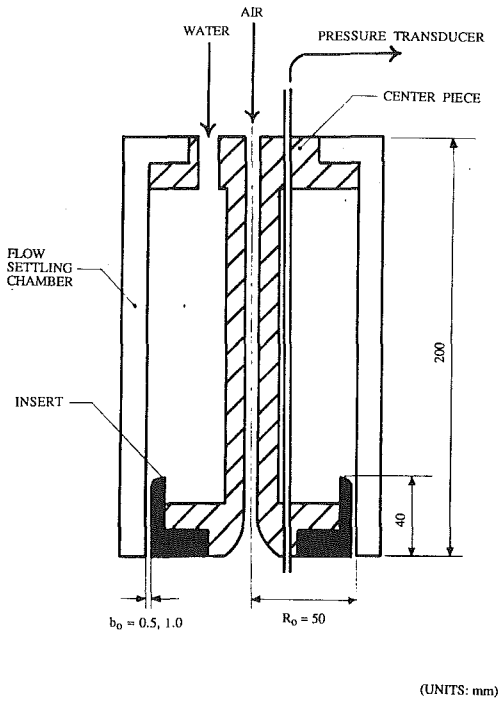

Fig. 3 Annular nozzle for generating liquid curtain

variable capacitor type differential pressure transducer with maximum range of 1 torr. By directly connecting the high and the low (ambient) pressure ports of the transducer, the zero calibration was checked within the accuracy of 10^{-3} Pascal. For oscillating curtains, the pressure readings fluctuated with time and the mean value was measured for an average pressure differential. According to the factory calibration performed with a pressure chamber and a dead weight, less than one percent of measurement is estimated for the bias of the instrument. The precision of the pressure differential measurement is estimated as three percent or less including the reading error from the digital display of the instrument.

Visualization of Liquid Curtains

The geometry of liquid curtains is shaped as a result of the combined effects of surface tension, gravity, inertia, and pressure differential. When these effects are in equilibrium, a curtain remains stable (steady or harmonically oscillating) until the balance is broken by a disturbance. As long as the magnitude of the disturbance is below a critical value, the curtain readjusts to a new equilibrium resulting in shorter or longer curtains. However, when the disturbance exceeds the critical value, the curtain is no longer able to maintain its closed and stable shape. Instead, the curtain collapses or is punctured near the apex. The primary length scale for curtain shape is the convergence L for a given nozzle geometry b_o/R_o.

The convergence length usually increases as the pressure differential is progressively increased. Typical modes of different curtain formations depending on the pressure differential are shown in Figs. 4(*a*) to 4(*d*). Without pressurization (Fig. 4(*a*)), slow reduction of the air inside the curtain driven by the flowing liquid through the apex results in a partial vacuum within the curtain with a small pressure differential. This pressure differential force plus surface tension act radially inward, which increases as the pressure continuously decreases inside the curtain. The convergence length decreases gradually and the curtain eventually collapses, unless the air supply is continued in order to compensate for the small amount of air entrained by the flowing liquid and, at the same time, to prevent the reduction in pressure inside the curtain.

In order to maintain a steady curtain, a small amount of

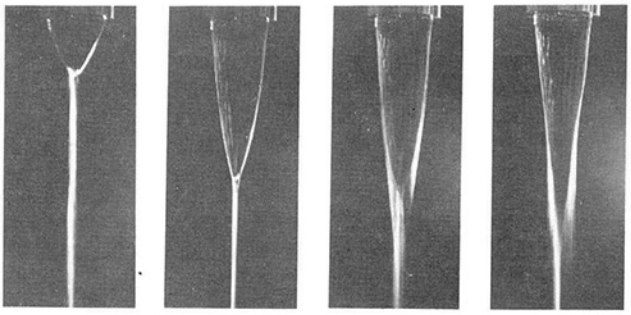

Fig. 4 Various types of liquid curtains

air, which balances the air leakage, needs to be introduced into the curtain. The steady curtain (Fig. 4(*b*)) is maintained as a result of the balance between the surface tension, pressure differential, inertial and gravitational forces. Inertial forces are axially downwards at the nozzle exit and for the period during which the curtain remains cylindrical. When the curtain begins to converge, which is caused by the contractive action of surface tension, a radially inward component appears in the inertial forces. By pressurizing the curtain, the pressure forces act radially outward causing an increase in the local diameter and thus extending the length of the cylindrical region until a new equilibrium between the forces is reached. Therefore, the more the curtain is pressurized, the longer the curtain (convergence) length.

When the curtain is pressurized with a pressure differential beyond a certain value, the contractive surface tensions can no longer hold the curtain steady because of the strong expanding action of the pressure forces. The curtain is expanded until the expansion reaches a limit in which the surface tensions start pulling the curtain upward (or radially inward). The curtain contracts until the contraction reaches the other limit in which the internal pressure becomes high enough to initiate an expansion of the curtain. As a result of this overshooting, the expansion and the contraction repeat like a simple harmonic oscillation attributed to the pressure fluctuation. A photograph of an oscillating curtain is shown in Fig. 4(*c*). The exposure time for the camera aperture was two seconds. The recorded inside apex of the curtain represents one instant of time (minimum length) while the blurred section of the photograph is due to the curtain fluctuations which are of the order of 2 Hz.

When the pressure differential exceeds a critical value, the surface tension is not able to initiate the curtain convergence since the expanding pressure forces are high enough to override the contractive action of surface tension. This results in a sudden decrease in curtain length and internal pressure as shown in Fig. 4(*d*). The curtain must now be considered as an open ended flow system with a jet flow from the air nozzle on the axis to the punctured opening. Increasing the supply air pressure increases the flow rate of air through the system without raising the pressure inside the curtain. The curtain near the apex fluctuates with a high frequency of the order of 10 Hz. Kendall (1986) showed experimentally and Lee and Wang (1986) showed theoretically that at specific conditions a sealing-off and encapsulation of the core-gas results in spherical liquid shell formation.

Review of the Theory

Lance and Perry (1953) presented the general differential equations for a "water bell" based on the Lagrangian formulation using a tangential-normal coordinate system. Transforming the differential equations into a cylindrical coordinate system, Hoffman et al. (1980) derived the vertical and radial momentum equations valid for a thin jet with zero pressure differential. Ramos (1988) accounted for the effect of nonzero pressure differential and obtained similar differential equations for $R(t)$ and $z(t)$, i.e.,

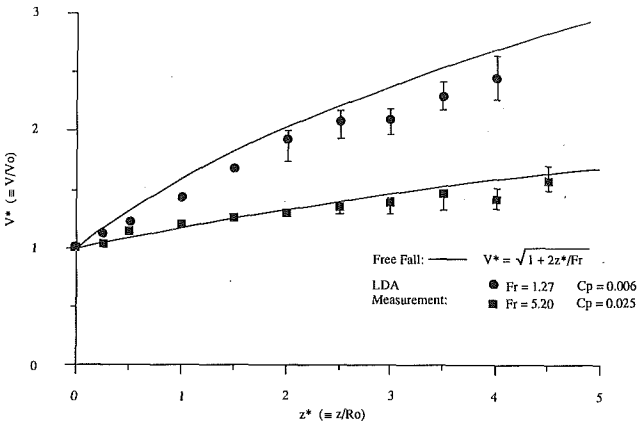

Fig. 5 Axial mean velocity normalized by the nozzle exit velocity V^* ($\equiv V/V_o$) as a function of z^* ($\equiv z/R_o$) for two different Froude numbers: b_o/R_o = 0.01 and Δp = 2.4 Pa for V_o = 0.8 m/s and 1.61 m/s

$$\frac{d^2R}{dt^2} = -\frac{2\sigma\cos\theta}{\rho b}\left(\frac{\cos\theta}{\rho b}+\frac{1}{r_v}\right)+\cos\theta(P_i-P_e) \tag{1}$$

$$\frac{d^2z}{dt^2} = g-\frac{2\sigma\sin\theta}{\rho b}\left(\frac{\cos\theta}{R}+\frac{1}{r_v}\right)+\sin\theta(P_i-P_e) \tag{2}$$

where r_v is the radius of curvature in the vertical plane at a particular axial location (Fig. 1), R is the local radius of the curtain in the horizontal plane and b is the local thickness of the curtain. The angle θ is defined in the vertical plane between the radius of curvature r_v and the curtain radius R.

The set of equations (1) and (2) together with the continuity and the curvature equation ($r_v = r_v$ (R, z)) was solved analytically and numerically by Ramos (1988). A closed form of analytical solutions was obtained for a very long curtain that converges very slowly, i.e, $|dR/dz| << 1$ and $\theta = 0$. In his numerical approach, the angle θ was expressed as a function of t, R and z, and the resulting equations were numerically integrated. Both of these solutions are compared with the measured convergence lengths in Figs. 7 through 11.

Results and Discussion

Mean velocity components of the flowing liquid have been measured using an argon-ion laser Doppler anemometer and results are shown for two different flow rates with the same pressure differential but with different C_p because of different liquid velocities (Fig. 5). The laser beams were focused onto the center of the curtain width at each axial station. Since it is expected that a nonuniform velocity profile due to shear stress along the nozzle walls relaxes rapidly at a short distance from the nozzle exit, the velocity distribution is assumed to be uniform across the liquid film. The dimension of the LDA probe volume was 5 mm in length and 0.25 mm in diameter so that the average velocity across the film thickness (~ 0.5 mm) can be obtained at each measurement location. For most regions of the curtain, except for the convergence point, zero tangential velocity was measured at each measurement location showing that no swirl was generated in the nozzle or liquid film. There may have arisen some swirl at the convergence point because of the small radial dimension where the flow is almost three dimensional. The rms fluctuations of the liquid flow gradually increase with distance downstream but never exceed 10 percent. The flow unsteadiness is initiated by the shear between the liquid and nozzle inner walls. The gradual increase of the unsteadiness outside the nozzle is attributed to the role of air friction on the liquid sheet as a weak but non-negligible force. The repeatability of the measurement was excellent near the nozzle exit. As indicated by the extended error bars, the uncertainty of mean velocity increased as the

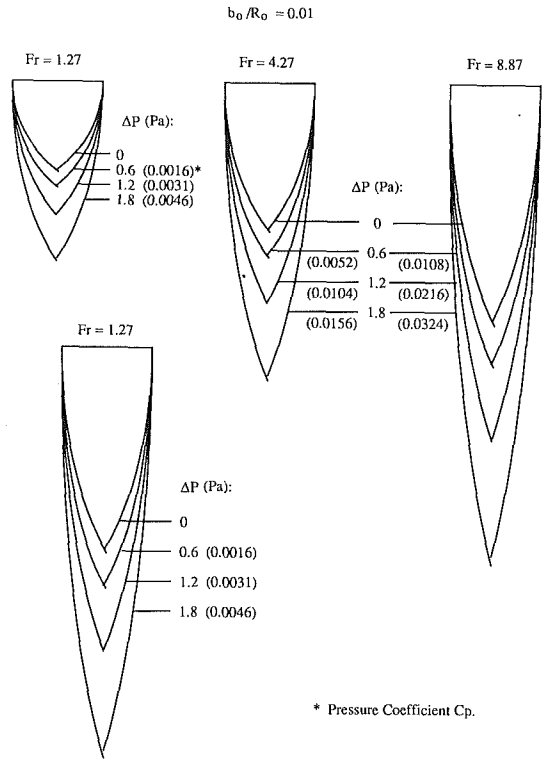

Fig. 6 Curtain shape and length as a function of $\Delta P (\equiv P_i - P_e 3)$ for three different Froude numbers and for two different values of b_o/R_o

convergence point was approached. Comparisons have been made between the measured velocities near the nozzle exit and the calculated mean velocities, based on the liquid mass flow rate. Good agreement was observed between the two values with the maximum deviations of 3 percent or less.

For a long curtain ($\theta = 0$), it can easily be seen from equation (2) that the axial velocity $V(=dz/dt)$ is identical to the free falling velocity, i.e.,

$$V = Vo + gt \text{ or } V^* = \sqrt{1+2z^*/\mathrm{Fr}} \tag{3}$$

where the dimensionless velocity V^* and the axial coordinate z^* are V/V_o and z/R_o, respectively. For the higher flow rate (Froude number = 5.20 and Weber number = 8.77), with an exit velocity of 1.6 m/s, the measured velocity agrees well with the free falling velocity, while the measured velocity for the lower flow rate (Fr = 1.27, We = 2.19 and V_o = 0.8 m/s) shows a lower value compared to the free falling velocity. The convergence length of the curtain increases as the flow rate is increased. The longer the curtain is, the more slowly the curtain radius R decreases with z ensuring the conditions $|dR/dz| << 1$ and $R << r_v|$, which validate the approximate solution for free falling velocity. This is clearly seen for the case of the longer curtain with Fr = 5.20. For the shorter curtain, these conditions are no longer valid since the curtain radius decreases faster, and the contractive action of surface tensions tends to retard the falling motion of the liquid resulting in a slower velocity than free falling.

The convergence length $L^*(\equiv L/R_o)$ has been measured for the pressurized curtains which are either in the steady or oscillating mode using a photographic recording technique. For steady curtains, the exposure time of the camera aperture was 1/60 to 1/125 of a second. A longer time exposure of 0.5 to 2 seconds was applied for the oscillating curtain so that the average convergence length could be obtained from the minimum and the maximum curtain lengths of the multi-exposed picture (Fig. 4(c)). The convergence length was measured using

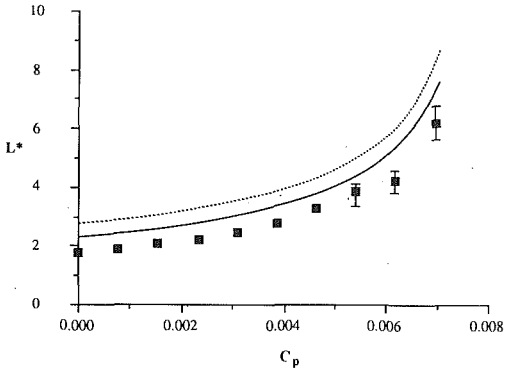

Fig. 7 Comparison of measured convergence length $L^*(\equiv L/R_o)$ versus C_p with theoretical predictions: N_c = 1.34 (Fr = 1.27 and We = 2.15), b_o/R_o = 0.01; ··· analytical solution, ——numerical solution (Ramos [1988])

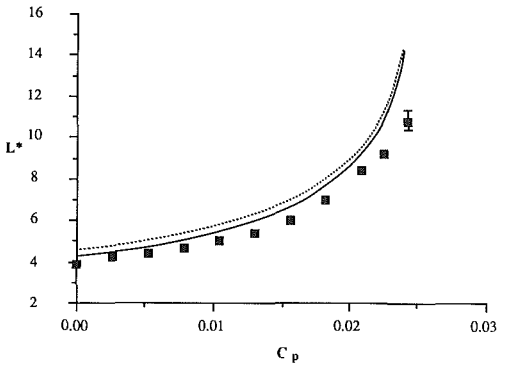

Fig. 8 Comparison of measured convergence length $L^*(\equiv L/R_o)$ versus C_p with theoretical predictions: N_c = 0.40 (Fr = 4.27 and We = 7.24), b_o/R_o = 0.01; ··· analytical solution, ——numerical solution (Ramos [1988])

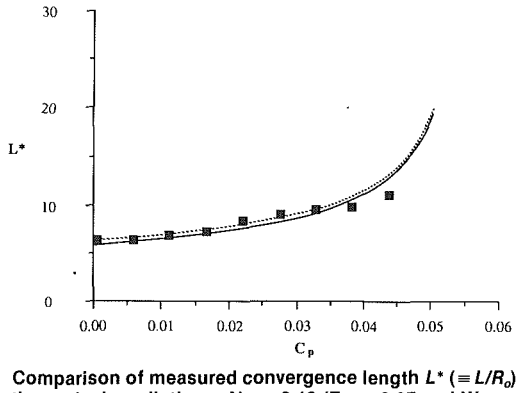

Fig. 9 Comparison of measured convergence length L^* ($\equiv L/R_o$) versus C_p with theoretical predictions: N_c = 0.19 (Fr = 8.87 and We = 15.03), b_o/R_o = 0.01; ··· analytical solution, —— numerical (Ramos [1988])

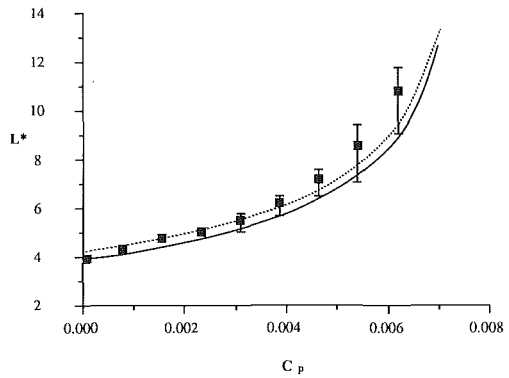

Fig. 10 Comparison of measured convergence length L^* ($\equiv L/R_o$) versus C_p with theoretical predictions: N_c = 2.67 (Fr = 1.27 and We = 4.31), b_o/R_o = 0.02; ··· analytical solution, —— numerical solution (Ramos [1988])

a ruler with a minimum resolution of 1 mm, which was attached to the nozzle and photographically recorded together with each curtain. The precision of the measurement was estimated as 1 percent or less with the reading error of one half of the minimum resolution, i.e., 0.5 mm for most curtains that were longer than 5 cm.

The average length and shape of the inside surface of steady curtains recorded by photographs are plotted in scale in Fig. 6. In each case, the initial curtain radius is 50 mm. Figure 6 shows the progressive increase in length, local radius, and internal volume of the curtain as ΔP is increased. Figure 6 also shows the benefits in terms of greater stability, larger length, and larger internal volume which are attained when the gap width is doubled for the same Froude number. For each value of ΔP, the curtain length is steadily increased by increasing the liquid flow rate, velocity, and Froude number.

The measured convergence lengths compared with the predictions are shown for b_o/R_o=0.01 in Figs. 7 to 9 and for b_o/R_o = 0.02 in Fig. 10. The symbol represents an averaged length of five individual recordings, while the extended bar indicates the range of measured lengths for each pressure differential. The nozzle radius R_o is fixed as a value of 50 mm for both cases. The solid curves represent the numerical solutions and the dashed curves denote the analytical solutions obtained from Ramos (1988). For all the cases considered, the numerical results predict a shorter convergence length compared to the analytical results. It is believed that the discrepancies between the two predictions are attributed to the terms including θ in the differential equations (1) and (2). In the numerical approach $\theta \neq 0$, while the analytical approach assumes $\theta = 0$ and neglects the contribution of surface tension in the second term on the right-hand side of equation (2). The major contribution of this term is to reduce both the falling velocity and the convergence length since the surface tension tends to hold the curtain, balancing the action of the gravitational and pressure differential forces. It can be seen from Figs. 7 to 9 that the discrepancies between the numerical and analytical solutions diminish as the flow rate is increased. For fixed nozzle geometry (R_o and b_o) and fluid properties (ρ and σ), both the Froude number and the Weber number increase with the flow rate. For long curtains with large flow rates, the angle θ becomes negligibly small in most regions except near the convergent apex. Therefore, the analytical solutions with $\theta = 0$ show close agreement with the numerical solutions as the Froude number and the Weber number increase with the flow rate. The influence of surface tension on the second term in equation (2) is very small for these cases.

The convergence length increases with increase of C_p, Fr, and We for a fixed value of $b_o/R = 0.01$. The variations of the convergence length with the pressure coefficient C_p show general agreement between the predictions and the measurements. For small values of C_p, curtains are steady with good repeatability of the measurements, and with good agreement with the theory. The curtain starts oscillating as the dimensionless pressure differential C_p increases. The lengths of the extended error bars are a measure of the magnitude of oscillation of the curtain apex, the convergence length. The degree of oscillation diminishes as the liquid flow rate is increased. This is due to the increased inertia overriding disturbances that cause the oscillation. For oscillating curtains, the unsteady formulation must be used to take into account the unsteady nature of the flow (Chigier et al., 1988).

The effect of b_o/R_o variation on the convergence length is shown in Fig. 10. Doubling the nozzle gap b_o while keeping the other parameters and dimensionless numbers the same, provides doubled mass and momentum flow rates. As expected, the convergence length is increased due to the increased

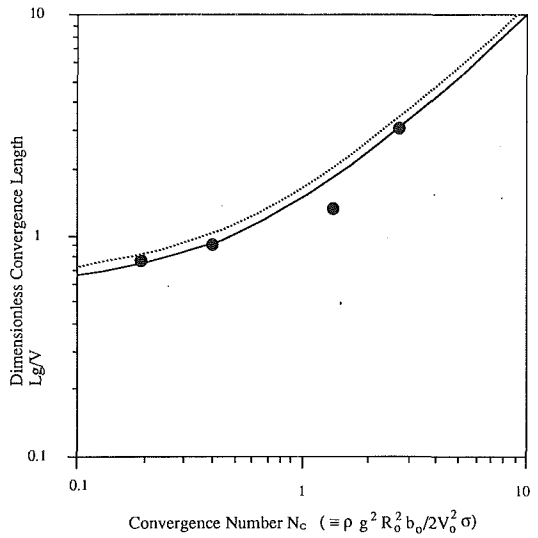

Fig. 11 Dimensionless convergence length Lg/Vo^2 versus convergence number N_c for Cp = 0: • measured data; ··· analytical solution, and —— numerical solution (Ramos [1988])

inertial (or momentum) forces. Compared to the similar condition but with the smaller nozzle gap of Fig. 6, the convergence length for low pressure differential has been nearly doubled. As we increase the pressure differential, the convergence length increases faster and has been almost tripled when C_p reaches 0.006. Again, the deviation of the predictions from the measurement increases as the curtain starts oscillating.

The dependence of convergence length upon the convergence number N_c, which is defined as $N_c = \rho g^2 R_o^2 b_o/2\ V_o^2 \sigma$ ($\equiv$ We/Fr^2), is examined in Fig. 11. For the case of zero pressure differential, i.e., $C_p = 0$, the dimensionless convergence length Lg/V_o^2 increases with the convergence number N_c showing close agreement between the measurement and the predictions. It must be emphasized that the convergence number is not the only parameter that determines the convergence length. The pressure coefficient C_p as well as N_p must be included in determining the convergence length of pressurized liquid curtains.

Conclusions

The dynamics of liquid curtains have been investigated by studying the convergence length and liquid velocity distributions experimentally. The experimental data have been compared with the analytical and numerical predictions of Ramos (1988). Also, different modes of curtain formation have been characterized using a photographic visualization technique. The main conclusions are listed below:

1. Steady curtains are formed when a steady pressure is maintained inside the curtain by providing a small air supply to compensate for the air leakage. As the pressure differential $P_i - P_e$ is increased, the curtain starts oscillating, and the curtain will be punctured above a critical pressure differential.

2. It has been shown that the convergence length of liquid curtains progressively increases with pressure coefficient C_p, Froude number Fr, Weber number We and nozzle gap to radius ratio b_o/R_o. For the case of $C_p = 0$, the dimensionless convergence length Lg/V_o^2 increases with the increase of the convergence number N_c.

3. For steady curtains, both analytical and numerical models provide good predictions of convergence length showing fairly good agreement with the experimental results. The theory deviates from the measurement for oscillating curtains since the modeling is based on curtains with steady flow.

4. Laser Doppler velocimetry measurements show that the curtain flow is in free falling motion when the Froude number is high (Fr = 5.20). When the Froude number is low (Fr = 1.27), the liquid falling velocity was measured to be lower than that of free fall due to the enhanced holding action of surface tension.

Acknowledgments

The authors gratefully acknowledge the assistance of and discussions with Frank Sun, Zalman Shapiro, and Mike Roidt. Financial assistance was provided by DOE Basic Energy Sciences.

References

Abramowitz, M., and Stegun, I. A., 1972, *Handbook of Mathematical Functions*, Dover Publications Inc., 1962.

Baird, M. H. I., and Davidson, J. F., "Annular Jets—I (Fluid Dynamics)," *Chem. Eng. Sci.*. Vol. 17, 1941, pp. 467–472.

Binnie, A. H., and Squire, H. B., 1941, "Liquid Jets of Annular Cross-Section," *The Engineer*, Vol. 171, London, 1941, pp. 236–238.

Boussinesq, J., 1869, "Comptes Rendus de l'Academie des Sciences," Vol. 69, p. 128.

Chigier, N. A., Ramos, J. I., and Sun, T-Y. 1987, "Experimental and Theoretical Studies of Vertical Annular Liquid Jets," Technical Report No. 1 prepared for the U.S. Department of Energy. Department of Mechanical Engineering, Carnegie-Mellon University, Pittsburgh, PA.

Chigier, N. A., Ramos, J. I., and Kihm, K. D., 1988, "Experimental and Theoretical Studies of Vertical Annular Liquid Jets," Technical Report No. 2 prepared for the U.S. Department of Energy. Department of Mechanical Engineering, Carnegie-Mellon University, Pittsburgh, PA.

Esser, P. D., and Abdel-Khalik, S. I., "Dynamics of Vertical Annular Liquid Jets," ASME JOURNAL OF FLUIDS ENGINEERING, Vol. 106, 1980, pp. 45–51.

Hoffman, M. A., Takahashi, R. K., and Monson, R. D., 1980, "Annular Liquid Jet Experiments," ASME JOURNAL OF FLUIDS ENGINEERING, Vol. 102, 1980, pp. 344–349.

Holvingh, J., 1977, "Stability of a Flowing Circular Annular Liquid Curtain with a Vertical Axis Subjected to Surface Tension Forces," Internal Memorandom No. 598A-77-108, Lawrence Livermore National Lab., Calif.

Kendall, J. M., 1986, "Experiments on Annular Liquid Jet Instability and on the Formation of Liquid Shells," *Phys. Fluids*, Vol. 29, pp. 2086–2094.

Lance, G. N., and Perry, R. L., "Water Bells," *Proceedings of the Physical Society*, London, Series B, Vol. 66, 1953, pp. 1067–1072.

Lee, C. P., and Wang, T. G., 1985, "A Theoretical Model for the Annular Jet Instability," *Phys. Fluids*, Vol. 29, 1977, pp. 2076–2085.

Maniscalco, J. A., and Meier, W. R., 1977, "Liquid Lithium 'Waterfall' Inertial Confinement Fusion Reactor Concept," Transactions of the American Nuclear Society, Vol. 26, 1977, pp. 62–63.

Ramos, J. I., 1988, "Liquid Curtains: I. Fluid Mechanics," *Chemical Engineering Science* (in press).

Taylor, G. I., 1959, "The Dynamics of Thin Sheets of Fluid. 1. Water Bells," *Proceedings of the Royal Society*, Series A, Vol. 253, 1959, pp. 289–295.

Effects of a Few Small Air Bubbles on the Performance of Circular Cylinder at Critical Flow Range in Water

H. Watanabe
Research Associate.

A. Ihara
Associate Professor.

S. Onuma
Technical Assistant.

Institute of Fluid Science,
Tohoku University,
Sendai, Japan

In a horizontal flow channel an experimental study was made on the effects of a small amount of air bubbles on the performance of a circular cylinder at a critical flow range where the drag coefficient of the test model decreased as Reynolds number increased. The measurements of the pressure distribution and fluid forces on the cylinder, the longitudinal turbulence level in water phase and the bubble size distribution in a free stream were taken. The results indicated that a large reduction in the drag coefficient and a change of the pressure distribution around the test model were caused at the low critical flow range by introducing a very small quantity of air bubbles such as 0.05 percent, though the turbulence level in water phase did not increase.

Introduction

A bubble flow can be found widely in the power industry such as conventional steam plants, nuclear power systems, and other industries. In order to design such systems it is important to know the characteristics of the internal and external flow phenomena around the bubble flow. On the internal flow problems such as a flow loss coefficient, a number of researches [for example, 1, 2, and 3] can be found. But reports about the external flow problems, e.g., a fluid force acting on a body, are fewer than those about the internal flow problems, though the industrial importance is equivalent in both cases.

The aim of this research is to investigate experimentally the effects of air bubbles in very small concentration in a water flow on the performance of a circular cylinder at a critical flow range. The term of the critical flow range is usually applied in a single-phase flow to the range where the drag coefficient of a circular cylinder decreases abruptly when Reynolds number increases. In this study we will use the term for a two-phase flow in the same sense that is generally used for a single-phase flow. The reason why we selected a circular cylinder as a test model is that its performance, such as a drag coefficient, pressure distribution, and Strouhal number in a single-phase flow, is well-known.

It is not new to use a circular cylinder as a test model in the study of a bubble flow. Hara [4] and Yokosawa et al. [5] have reported that flow characteristics around a circular cylinder change noticeably when bubbles are introduced into the stream in a subcritical flow range. The reason has been explained by them: The presence of bubbles increases the intensity of turbulence in the liquid phase, and this free-stream turbulence makes a turbulent transition of the boundary layer on the cylinder surface. There are some other experimental researches [6, 7] which seem to support the above reasoning. The researches just described were concerned with a vertical up and down flow with a very low mean velocity of less than 2.0 m/s. The diameters of individual bubbles were 3 ~ 5mm [5], which were relatively large in comparison with the diameter of the test cylinder. The slip ratio between both phases was also large. However, in case of the small slip ratio which will be realized in the horizontal bubble flow, the effects of air bubbles on the performance of the test model cannot be found in literature. The present study aims at such a case.

Experimental Equipment and Method

Water Tunnel. Experiments were conducted by using a closed circuit water tunnel [9] installed in the Scale Effect Cavitation Tunnel Laboratory of the Institute of the Fluid Science, Tohoku University. The schema around the working section of the water tunnel is shown in Fig. 1. It has a dimension of 200 mm in width, 610 mm in height, and 1000 mm in length.

The velocity profile in the working section was measured by a Pitot traverse method at the mid-height where a test cylinder was installed to check the uniformity of the flow field and to calibrate the flow nozzle shown in Fig. 1. The velocity profile was nearly plane outside the boundary layers on both side walls. The boundary-layer thickness and the displacement thickness were about 12 and 1.7 percent, respectively, of the width of the working section on each side wall. As this water tunnel had a large reservoir ($150m^3$) to remove air bubbles, the injected air bubbles scarcely returned to the working section, and hence during the following experiments the velocity and the flow rate of water in the working section could be related to the pressure difference across the flow nozzle. It was

Contributed by the Fluids Engineering Division for publication in the JOURNAL OF FLUIDS ENGINEERING. Manuscript received by the Fluids Engineering Division August 23, 1988.

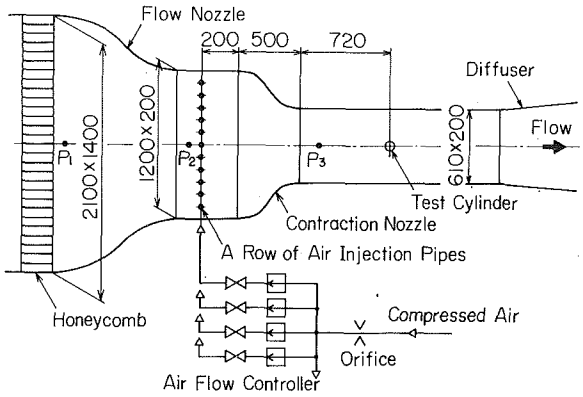

Fig. 1 Schema around the working section

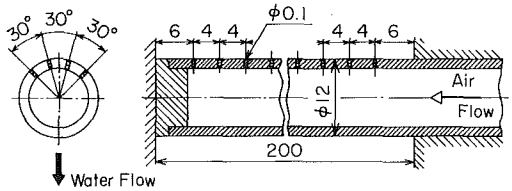

Fig. 2 Air injection pipe

assumed that the velocity profile in the working section did not change when air bubbles were introduced into water.

Air Injection Pipes. Air bubbles were introduced through the injection pipes arranged vertically at the upstream part of the working section with a rectangular cross section of 1200mm × 200mm, as shown in Fig. 1. The number of the air injection pipes was 23, and they were arranged at intervals of about 50mm. As shown in Fig. 2, each pipe (12mm in the outer diameter and 9mm in the inner diameter) had 192 small holes bored by laser rays with about 0.1mm in diameter. The holes were arranged to form 4 lines each 30 deg apart on the circumference between two adjacent lines, and each line had 48 holes located at regular intervals of 4mm in the direction of the pipe axis. Air was injected through those holes against the incoming flow in order to make the uniform bubble flow.

Air Fraction. Air was supplied from an air reservoir through 6 air flow controllers arranged in parallel after its flow rate and static pressure were measured by an orifice meter and a pressure gauge, as shown in Fig. 1. The controllers composed of air regulators and valves. They were separately adjusted to compensate the gravitational static pressure gradient which existed in the vertical direction at the air-injection plane. The air fraction at the working section was defined as follows:

$$\alpha = V_a / (V_a + V_w) \tag{1}$$

where V_w and V_a were the volumetric flow rate of water and air, respectively. V_a was calculated from the measured pressure difference across the orifice meter in consideration of the static pressure and the temperature differences between the working section and the orifice meter. In the preliminary experiment the air fraction was also measured with an optical probe (DISA 55S type) at the working section. The results of measurement by two different methods almost agreed with one another within the experimental uncertainty.

The static pressure at the working section was kept at 0.16MPa in all test runs. The temperature of water was between 293K and 301K at the working section. The air temperature inside the bubble was assumed to be equal to that of the surrounding water. The experiments were conducted under the conditions where the air fraction and the Reynolds number were between 0.0 and 0.48 percent, and between 1.3×10^5 and 2.7×10^5, respectively.

Test Cylinders. Two circular cylinders, one for force measurement and the other for the measurement of surface pressure distribution, were arranged in this research. Each cylinder was made of brass and had a diameter $d = 30$mm and a length $\ell = 200$mm. Its surface was polished so that its maximum roughness height should be within 1 μm. The force acting on the test model was measured by a force balance. The balance mounted at the end of the cylinder could decompose the force into two perpendicular components, the drag D, and the lift L, and measure them simultaneously. This force measurement system had a flat frequency response up to about 170Hz. The cylinder for the pressure distribution measurement had an orifice of 0.5mm in diameter on its surface at the center of its span. The pressure was led to a semiconductor pressure transducer installed inside the cylinder through the orifice and Helmholtz chamber which were filled with degassed silicon oil. This pressure measurement system had a flat frequency response up to about 1.8kHz. The cylinder could be turned freely around its longitudinal axis from $\theta = 0$deg to $\theta = 360$deg. Further information on the equipment and methods of the force and pressure-distribution measurements has been described in references [10,11].

Turbulence Measurement. The longitudinal turbulent velocity fluctuations in the bubble flow were measured with a total pressure probe which was previously developed by Murai and Ihara [9]. Owing to them, the longitudinal fluctuating velocity, u, can approximately be related to the total pressure fluctuations, p_t by the following equation.

$$u = p_t / (\rho_w U) \tag{2}$$

where, U and ρ_w were velocity and water density, respectively. The probe was composed of a miniature semiconductor pressure transducer with a high sensitivity and a probe cap installed at the head of the transducer. The probe cap which sensed the pressure at one end and led it to the pressure transducer equipped at the other end had a small tube with the inner diameter 0.4mm, outer diameter 0.6mm and length 5.8mm. The frequency response of this total pressure probe was flat

Nomenclature

C_D, C_L = drag and lift coefficients of the test cylinder
C_p = pressure coefficient
d = diameter of the test cylinder (30mm)
f = frequency
ℓ = length of the test cylinder (200mm)
p_t = total pressure
Re = Reynolds number
u = longitudinal fluctuating velocity, equation (2)
U = velocity
V = volumetric flow rate
α = air fraction, equation (1)
θ = azimuthal angle of the orifice on the surface of the test cylinder measured from the upstream stagnation point
ν = kinematic viscosity
ρ = density

Subscripts

a = air
RMS = root-mean-square value
t = two-phase-flow
w = water

Others

$'$ (prime) = fluctuating part of a quantity
$\bar{}$ (over bar) = mean value

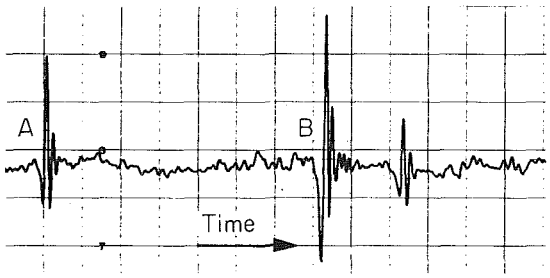

Fig. 3 Output signal from the total pressure probe

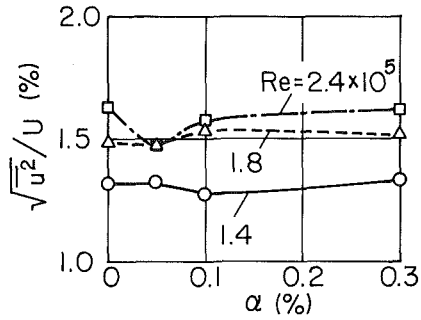

Fig. 4 Longitudinal turbulence level in water-phase

up to about 2.0kHz. It was inserted in the working section by replacing it with the test cylinder to measure the turbulence under the same experimental conditions when the force and pressure measurements were made.

Data Analysis and Bubble Observations. Electronic signals from those different transducers were recorded on magnetic tapes by a data recorder and were reproduced later to analyze statistically. A minicomputer equipped with an analogue-digital converter was used for analysis.

The output signal from the total pressure probe had a waveform, as shown in Fig. 3. It had information both of the longitudinal velocity fluctuations in a water phase and of the existence of air bubbles. While an air bubble was passing the sensing area of the probe, the total pressure decreased considerably due to the low density of air, as shown at A or B in Fig. 3. Therefore in calculating the longitudinal turbulence level of the water phase, the parts of the signal showing the existence of the bubble were left out of account.

The output from the force balance was used to calculate the mean lift and drag coefficients, the root-mean-square value of the lift and drag force fluctuations and their power spectrums. Corrections of the blockage effects were not made to the results. The distributions of the mean pressure coefficient and root-mean-square values of the pressure fluctuations around the test cylinder were calculated with the output of the pressure transducer installed inside the test cylinder. The power spectrum of the fluctuating pressure was also obtained.

To normalize the measured forces the velocity averaged in a full span of the working section, U_0, was used because the test cylinder extended into the side-wall boundary layers. But the velocity outside the boundary layers, U, was used to calculate the pressure coefficients and the turbulence level because the orifice on the test cylinder and the sensing area of the total pressure probe were located at the mid-span of the working section.

Flashlight photography with an electronic flash of the exposure time of 4 μs was employed to measure the diameters of bubbles in the free stream.

High speed cinematography was also employed to measure the bubble speed. It was found through the analysis of the bubble motion on the film that the horizontal velocity of each

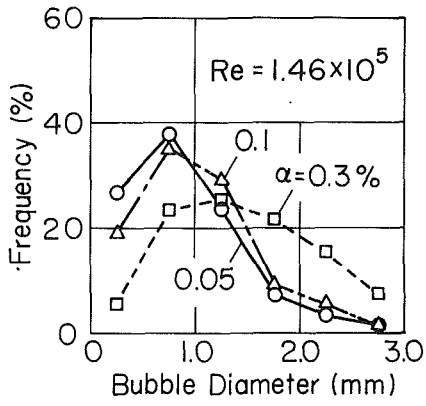

Fig. 5(*a*)

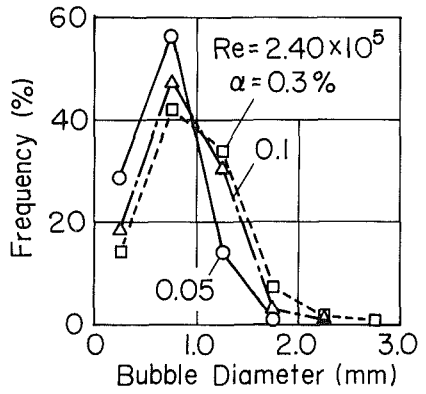

Fig. 5(*b*)

Fig. 5 Probability distribution functions of the bubble diameters at (*a*) Re = 1.46 × 10^5 and (*b*) Re = 2.40 × 10^5

bubble was almost equal to that calculated by dividing the volumetric sum of water and air flow rate by the cross sectional area of the test section.

Then, the density of the bubble flow, ρ_t, was given by

$$\rho_t = (1 - \alpha)\,\rho_w + \alpha\rho_a \tag{3}$$

and was used in the following to normalize the measured force and pressure. Here ρ_a and ρ_w were the densities of the air and water phases, respectively.

Since the air fraction was extremely small in our experiments, the viscosity of the air-water mixture, which was calculated with the formula presented by Einstein [12], proved almost equal to that of water, ν_w. Hence ν_w was used in the definition of Reynolds number in this study; that is, $\mathrm{Re} = dU/\nu_w$.

Experimental Results and Discussions

Turbulence Level in Water-Phase Flow. The longitudinal turbulence level in water phase is shown in Fig. 4.

As Reynolds number increases, the turbulence level increases slightly, but it is scarcely affected by the air fraction. This result seemed contradictory to those obtained by others [6,7]. Yokosawa et al. [5] explained that the increase in turbulence level in the bubble flow was, firstly, caused by the random motion of air bubbles and, secondly, by the wakes developed behind the bubbles. In our study, however, the velocity of each bubble was almost coincident with that of water, and the air fraction was very low, as stated before. Therefore the random motions of air bubbles and the wakes behind the bubbles could scarcely be realized, so that the turbulence level in water phase could not increase.

Distribution of Bubble Diameters and Observation of Bubbles. The probability distribution functions of bubble diam-

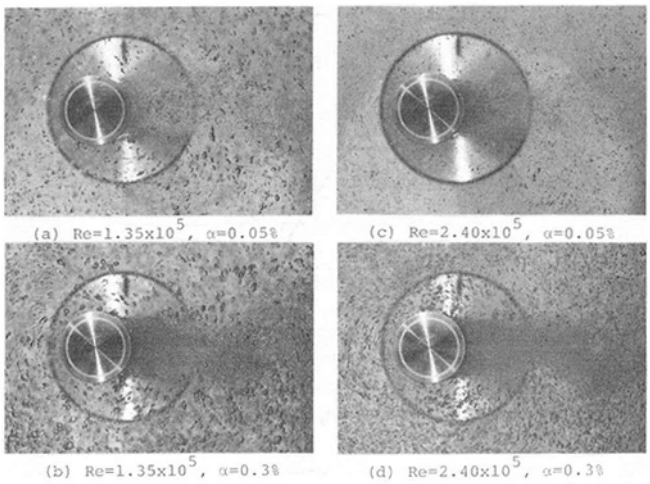

Fig. 6 Instantaneous photographs of the flow around the test cylinder

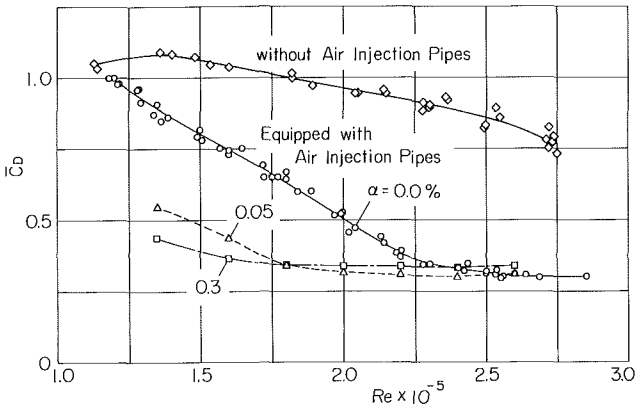

Fig. 7 Mean drag coefficients against the Reynolds number

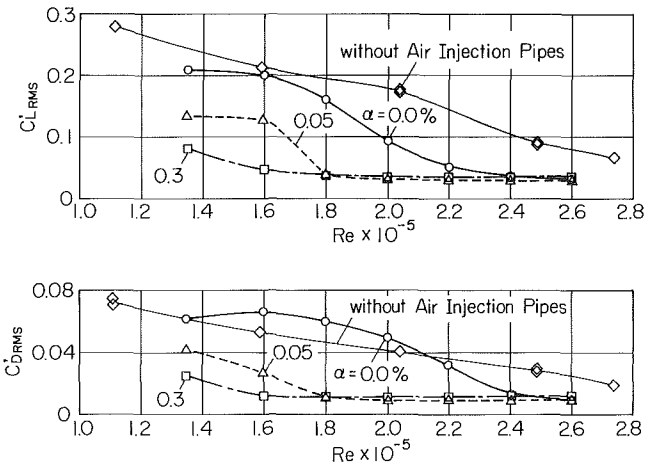

Fig. 8 Root-mean-square values of the fluctuations of the lift (top) and drag (bottom) against the Reynolds number

eters are shown in Fig. 5. At $Re = 1.46 \times 10^5$, the bubble diameters are widely distributed from 0.5mm to 3.0mm, and as the air fraction increases, the number of the bubbles of a large diameter increases. But the maximum diameter scarcely exceeds 3.0mm. The peak of the distribution shifts to a smaller diameter with an increase in Reynolds number. The mean diameter ranges between 0.7mm ($Re = 2.4 \times 10^5$, $\alpha = 0.05$ percent) and 1.5mm ($Re = 1.46 \times 10^5$, $\alpha = 0.3$ percent), as far as the measurements were made.

Figure 6 shows the instantaneous photographs of the flow

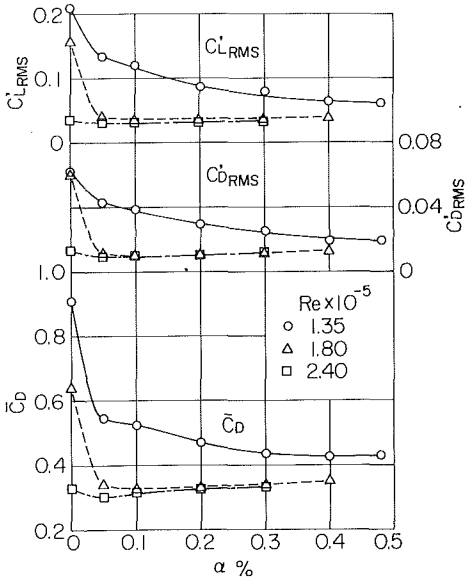

Fig. 9 Root-mean-square values of the fluctuations of the lift (top) and drag (middle) coefficients, and the mean drag coefficient (bottom) against the air fraction

around the test cylinder. It can be observed that bubbles disperse homogeneously in water and deform their contours according to the pressure gradient around the test cylinder. A lot of minute bubbles are observed in the region behind the cylinder. As such minute bubbles cannot be found in the flow upstream the cylinder, the bubbles which fall into the wake of the test cylinder by the effect of the pressure gradient around the cylinder should be crushed by the violent turbulence in the wake and brought away by water.

Force Coefficients and Pressure Distribution. The mean drag coefficient $\bar{C}_D$ and the root-mean-square values of the fluctuating lift and drag coefficients are plotted in Figs. 7 and 8 against the Reynolds number taking the air fraction as a parameter. To investigate the effects of the air fraction more explicitly, the data shown in Figs. 7 and 8 were rearranged against the air fraction, as shown in Fig. 9. From these figures, it can be said that the critical Reynolds number in a fully wetted flow (α = 0.0 percent) under the flow condition in which the air injection pipes are inserted is ranging in a relatively low range from 1.3×10^5 to 2.6×10^5. This may be due to the high turbulence level caused by the air injection pipes. The effect of air bubbles is remarkable at the critical flow range. In particular, at the low critical flow range a slight addition of air bubbles such as 0.05 percent makes a 60 percent reduction in $\bar{C}_D$ of that in the single-phase flow. In the high critical and supercritical flow ranges, on the contrary, we cannot find such a drag reduction as has been reported on a flat plate [13,14] and an axisymmetric body [15] covered with the turbulent boundary layer. The root-mean-square values of fluctuations of both of the force coefficients have the same tendency as $\bar{C}_D$ in regard to the air fraction and Reynolds number.

It is also an interesting problem to see a variation of the pressure distribution around the test cylinder when bubbles are added to the stream. The results of measurement at the different Reynolds numbers are shown in Figs. 10 (*a*) and (*b*) against the azimuthal angle θ with the air fraction as a parameter. The upper column shows the root-mean-square value of the pressure coefficient fluctuations, and the lower one shows the mean value. At $Re = 1.4 \times 10^5$ in the low critical flow range, the flow separates at $\theta \simeq 80$deg in the fully wetted flow. In this case, the addition of a small amount of air bubbles such as 0.05 percent makes a remarkable change as well as $\bar{C}_D$ in the mean pressure coefficient distribution, and transforms the

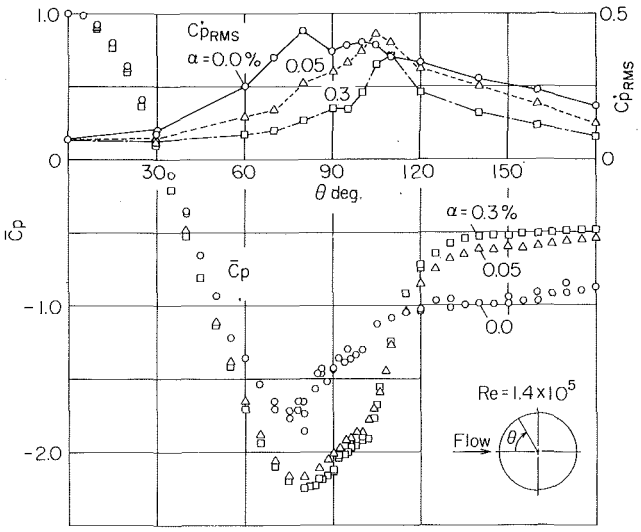

Fig. 10(*a*)

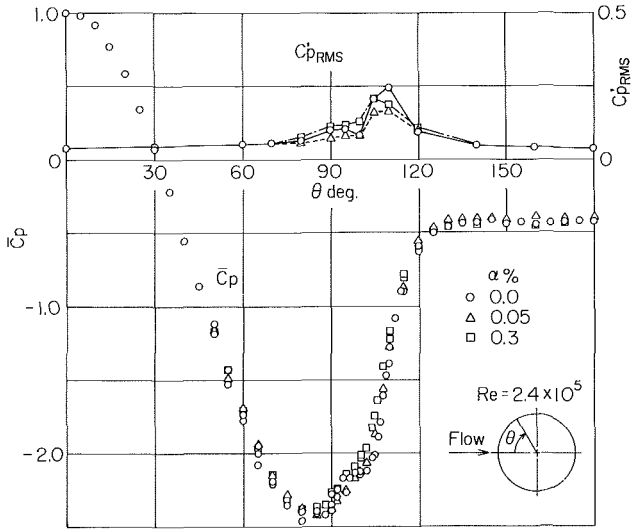

Fig. 10(*b*)

Fig. 10 Pressure distribution on the test cylinder at (*a*) Re = 1.40 × 10^5 and (*b*) Re = 2.4 × 10^5

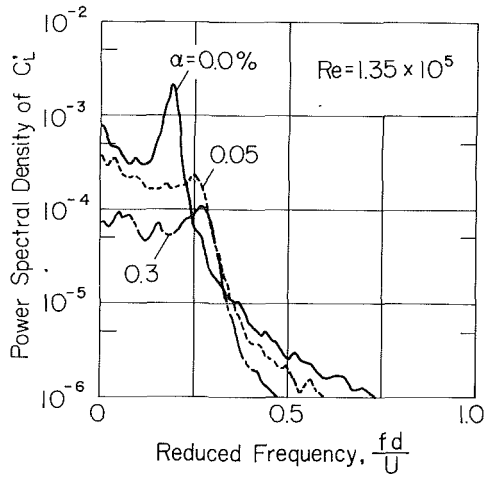

Fig. 11(*a*)

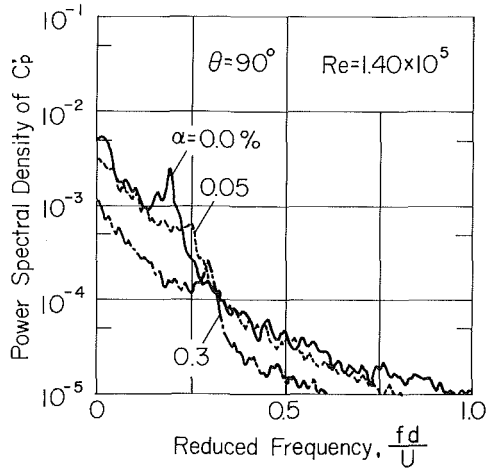

Fig. 11(*b*)

Fig. 11 Power spectral density of (*a*) the fluctuating lift and (*b*) the pressure fluctuations at θ = 90 deg

pressure distribution into what can be seen in the supercritical flow range. These changes of the pressure distribution and the mean drag coefficient are considered to be the consequence of the earlier transition in the boundary layer caused by the added air bubbles. As the amount of air bubbles increases, the change becomes more evident, and the point of separation moves further downstream. On the contrary, in the high critical flow range, noticeable changes in the mean pressure coefficient distribution cannot be noticed all over the surface except the region of 80deg $< \theta <$ 105deg, as can be seen in Fig. 10 (*b*), because the transition has almost been completed before the air bubbles are added.

As for the root-mean-square values of the pressure coefficient fluctuations at the low critical flow range, the values measured in the fully wetted condition are superior to those measured in the bubble flow all over the model surface except in the reattachment region. It can also be said that an increase in the air fraction decreases the static pressure fluctuations, in particular, on the surface just upstream of the flow separation point. This seems to contradict the fact that the static pressure fluctuations in the turbulent boundary layer are superior to those in the laminar boundary layer. The reason can be thought as follows: As will be stated later, the vortex shedding from the cylinder surface in the fully wetted flow at the Reynolds number stated here is most distinct. These vortices may cause the strongest static pressure fluctuation superior to those caused by the turbulent boundary layer.

Vortex Shedding in Bubble Flow. It is an interesting problem to observe how the vortex shedding behaves in the bubble flow. On the Kármán vortex in a bubbly two-phase flow Hulin et al. [16] reported the shedding frequency and the fluctuation of bubble number density in the wake behind the cylinder with trapezoidal cross section. They reported the good stability of vortex emission with void fraction up to 10 percent ($Re \leq 10^5$). The variations of the corresponding Strouhal number with the void fraction followed a law independent of the water flow rate at such a void fraction. Experimental researches were made by Yokosawa et al. [17], using a flat plate and a circular cylinder in a vertical bubbly flow. Their results indicated that two kinds of flow patterns appeared alternately in the wake. One of them corresponded to the Kármán vortex type in a single-phase flow and the other was similar to the twin-eddy type which was observed under the low Reynolds number ($Re < 10^2$) in a single-phase flow. However the range of the Reynolds number of their experiments was different and lower than ours.

To investigate the shedding frequency and the intensity of the vortex, the power spectral density distribution of the static pressure at θ = 90 deg and the lift force were calculated. Results at the low critical flow range are shown in Figs. 11 (*a*) and (*b*)

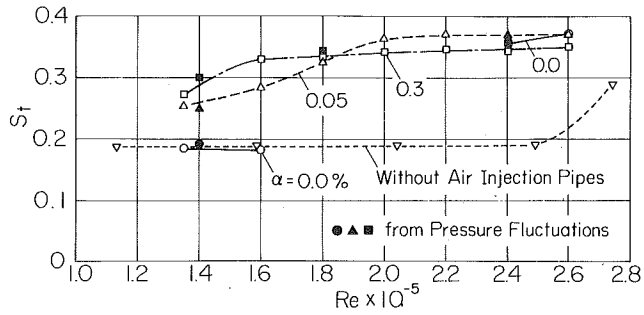

Fig. 12 Change of the peak reduced frequency of the fluctuation lift against the Reynolds number

against the reduced frequency, $S_t = fd/U$, where f is a frequency. We can find the resonant peaks which indicate the vortex shedding from the cylinder surface in both figures. The peak height decreases with an increase in the air fraction. This fact suggest that the strongest vortex takes place in the fully wetted flow. The peak frequencies are almost coincident in both cases of lift and pressure fluctuations, and increase with the air fraction. These peak frequencies are summarized in Fig. 12 against the Reynolds number. The reduced peak frequency in the fully wetted flow at the subcritical flow range is almost coincident with Strouhal number of the vortex shedding frequency reported by others [18-20] in a single-phase flow. The reduced frequency increases by about 45 percent when the air fraction varies from 0 to 0.3 percent at $Re = 1.35 \times 10^5$. This increase is far greater than those reported by Hulin, et al. [16] using the cylinder with the trapezoidal cross section at $0.3 \times 10^5 < Re < 1.1 \times 10^5$ and those reported by Yokosawa et al. [17] using the circular cylinder and the flat plate at $0.16 \times 10^5 < Re < 0.66 \times 10^5$. At the mid-critical flow range, the resonant peak on the spectra in the fully wetted flow becomes indistinct, but in the bubble flow this peak can be found, and its reduced frequency seems to attain some constant value with an increase in the Reynolds number. At the high critical flow range such as $Re = 2.4 \times 10^5$, the resonant peak can be recognized once more on the spectra in the fully wetted flow, and its reduced frequency is almost coincident with those in the bubble flow. These values of the reduced frequency are almost equal to those of the Strouhal number reported by Schewe [20] in a single-phase flow at the critical or supercritical flow range.

On the Boundary Layer Transition. As previously stated, the addition of a small amount of air bubbles, such as 0.05 percent in volume, caused a drastic change in both $\bar{C}_D$ and the pressure distribution at the low critical flow range. It was also found that the addition of air bubbles did not cause any increment in the turbulence level in the water phase. We can conclude, therefore, that the transition just stated may be caused by the direct interaction of air bubbles with the boundary layer on the cylinder surface. These results tell us that small air bubbles included in water have a possibility of playing an important role in spite of its small amount, just as the surface roughness, free stream turbulence and Reynolds number play in the experiment for obtaining a critical Reynolds number of the blunt nosed body such as a circular cylinder.

Experimental Uncertainty. The velocity had a maximum uncertainty of about ±1 percent. It composed of the uncertainties due to the zero drift of the differential pressure transducer of strain gauge type and the dynamic strain amplifier which were used to measure the differential pressure across the flow nozzle. The air fraction had a maximum uncertainty of about ±5 percent, which was associated with the pressure and temperature measurements at the orifice meter. The maximum uncertainties of C_L and C_D were about ±4 percent. They were mainly due to the hysteresis of the balance and the zero drift of the system. C_P and the longitudinal turbulence level had maximum uncertainties of about ±3 and ±6 percent, respectively. They were caused mainly by the pressure measurements with the semiconductor pressure transducers. In the turbulence level, the uncertainty due to the approximate measuring method was also included.

Conclusions

The following conclusions are obtained through the measurements of the pressure distribution and fluid forces in a horizontal bubble flow at the low air fraction using a circular cylinder as a test model and through the measurements of the longitudinal turbulent level in water phase and bubble size distribution.

1. The addition of air bubbles at the critical flow range causes a reduction in the drag coefficient. It also increases the frequency of vortex shedding to the value seen in a supercritical flow range, and decreases the intensity of the shedding vortices.
2. The reduction in the drag coefficient is due to the change in the pressure distribution around the test cylinder, and is caused by transition in the boundary layer.
3. The minimum amount of air bubbles necessary for making the changes described above is 0.05 percent in the volume flow rate.
4. The addition of air bubbles at the high critical and supercritical flow range does not cause a reduction in the drag coefficient and a change in the pressure distribution. Both the frequency and the intensity of the vortex shedding are not affected by the air fraction either.
5. The turbulence level in the water phase in the horizontal bubble flow does not increase by the addition of a small amount of air bubbles due to a small velocity difference between the air bubble and the surrounding water.

Acknowledgment

The authors would very much like to express their thanks to Mr. M. Kato and other staff of the factory of the Institute for their help in preparing the experimental equipment, and would also like to thank Miss E. Kikuchi and Mrs. M. Kusaka for their help in putting the manuscript in order for publication.

References

1 Lockhart, R. W., and Martinelli, R. C., "Proposed Correlation of Data for Isothermal Two-Phase Two-Component Flow in Pipes," *Chemical Engineering Progress*, Vol. 45, No. 1, 1949, pp. 39-48.

2 Levy, S., "Prediction of Two-Phase Pressure Drop and Density Distribution from Mixing Length Theory," ASME *Journal of Heat Transfer*, Vol. 85, No. 2, May 1963, pp. 137-152.

3 Chisholm, D., "Predicting Two-Phase Pressure Drop," *Encyclopedia of Fluid Mechanics*, Vol. 3, Gulf Publishing Co., Houston, 1986, pp. 532-561.

4 Hara, F., "Two-Phase Cross Flow Induced Vibrations in a Cylindrical System (2nd Report: Characteristics of Unsteady Lift and Drag Force)," *Transactions of JSME*, C, Vol. 48, No. 433, Sept. 1982, pp. 1371-1379.

5 Yokosawa, M. et al., "Studies on Two-Phase Cross Flow. Part II: Transition Reynolds Number and Drag Coefficient," *International Journal of Multiphase Flow*, Vol. 12, No. 2, 1986, pp. 169-184.

6 Serizawa, A., et al., "Turbulence Structure of Air-Water Bubbly Flow - II. Local Properties," *International Journal of Multiphase Flow*, Vol. 2, No. 3, 1975, pp. 235-246.

7 Wang, S. K., "3-D Turbulence Structure and Phase Distribution Measurements in Bubbly Two-Phase Flows," *International Journal of Multiphase Flow*, Vol. 13, No. 3, 1987, pp. 327-343.

8 Mandhane, J. M., et al., "A Flow Pattern Map for Gas-Liquid Flow in Horizontal Pipes," *International Journal of Multiphase Flow*, Vol. 1, No. 4, 1974, pp.537-554.

9 Murai, H. and Ihara, A., "A Handy Method for Measuring Turbulence in Water by Total Probes," The Reports of Institute of High Speed Mechanics, Tohoku University, Vol. 41, 1980, pp. 37-62.

10 Ihara, A., "Effects of Yaw Angle to Unsteady Hydraulic Forces Acting on a Cavitating Circular Cylinder," *Proceedings of International Symposium on Cavitation*, Vol. 1, Sendai, 1986, pp. 145-150.

11 Ihara, A. and Murai, H., "Cavitation Inception on a Circular Cylinder at Critical and Supercritical Flow Range," ASME JOURNAL OF FLUIDS ENGINEERING, Vol. 108, No. 4, Dec. 1986, pp. 421-427.

12 Brady, J. F., "The Einstein Viscosity Correction in n Dimensions," *International Journal of Multiphase Flow*, Vol. 10, No. 1, 1984, pp. 113-114.

13 Legner, H. H., "A Simple Model for Gas Bubble Drag Reduction," *Physics of Fluids*, Vol. 27, No. 12, Dec. 1984, pp. 2788-2790.

14 Madavan, N. K., Deutsch, S., and Merkle, C. L., "Measurements of Local Skin Friction in a Microbubble-Modified Turbulent Boundary Layer," *Journal of Fluid Mechanics*, Vol. 156, Jul. 1985, pp. 237-256.

15 Deutsch, S., and Castano, J., "Microbubble Skin Friction Reduction on an Axisymmetric Body," *Physics of Fluids*, Vol. 29, No. 11, 1986, pp. 3590-3597.

16 Hulin, J-P., Fierfort, C., and Coudol, R., "Experimental Study of Vortex Emission behind Bluff Obstacles in a Gas Liquid Vertical Two-Phase Flow," *International Journal of Multiphase Flow*, Vol. 8, No. 5, 1982, pp. 475-490.

17 Yokosawa, M. et al., "Studies on Two-Phase Cross Flow, Part III: Characteristics of Unsteady Flow Behavior," *International Journal of Multiphase Flow*, Vol. 12, No. 2, 1986, pp. 185-202.

18 Bearman, P. W., "On Vortex Shedding from a Circular Cylinder in the Critical Reynolds Number Regime," *Journal of Fluid Mechanics*, Vol. 37, Part 3, Jul. 1969, pp. 577-585.

19 Achenbach, E. and Heinecke, E., "On Vortex Shedding from Smooth and Rough Cylinders in the Range of Reynolds Numbers 6×10^3 to 5×10^6," *Journal of Fluid Mechanics*, Vol. 109, Aug. 1981, pp. 239-251.

20 Schewe, G., "On the Force Fluctuations Acting on a Circular Cylinder in Crossflow From Subcritical up to Transcritical Reynolds Number," *Journal of Fluid Mechanics*, Vol. 133, Aug. 1983, pp. 265-285.

Horizontal Slug Flow: A Comparison of Existing Theories

E. Kordyban
University of Detroit,
Detroit, MI 48221

Over the last twenty years a number of papers have appeared in literature concerning the transition to slug flow in horizontal two-phase flow. The theories proposed in these papers are described, and compared to each other and to results of experiments. It is found that most writers accept that the transition is due to Kelvin-Helmholtz instability of the waves, but if this is studied on the basis of wave motion equations, the transition is found to be dependent on wavelength which contradicts experimental data. A number of authors look at this instability by studying the Bernoulli equation, but this does not predict the wave height. Various approaches are taken by the authors to determine this quantity.

Introduction

Two-phase flow, the simultaneous flow of a liquid and a gas, occurs in many industrial processes, as well as in nature and, although it has been intensively studied over the last fifty years, its basic complexity has still not yielded to complete analysis. It was discovered early in the investigation that the two-phase flow can take on many forms, known as flow patterns or flow regimes. A number of general correlations not based on flow pattern such as those of Lockhart and Martinelli [1], have been developed and permit the determination of such quantities as pressure loss in a duct or void fraction, but it is clear that an understanding of the two-phase flow cannot be gained, unless the factors governing the existence of various flow patterns and their transitions are determined.

One of the first and probably the most widely used maps of the flow patterns has been presented by Baker in 1954 [2] and is shown in Fig. 1. Baker was not concerned with the mechanisms which govern the existence of the flow patterns and developed the map strictly on the basis of experimental data, but even presently the theories developed on various assumptions are still compared to his map. As may be seen in Fig. 1, the coordinates are not dimensionless and involve such variables as gas and liquid flow rates, densities, viscosities and surface tension.

A rather central position in the Baker's map is occupied by the slug flow, a flow pattern in which large liquid waves are periodically picked up by the rapidly moving gas. Such waves block, or partially block, the whole cross section of the channel and are then driven like a piston down the channel with resulting large fluctuations in pressure and discharge.

The conditions under which slugs form may be determined from Baker's map, but it does not tell the whole story. It is possible to produce slugging on essentially stagnant liquid and this, in fact, occurs in nominally horizontal steam pipes, when condensate collects at low spots. The resulting slugs have been known to break off blind flanges and even elbows at the end of a run of pipe.

Contributed by the Fluids Engineering Division for publication in the JOURNAL OF FLUIDS ENGINEERING. Manuscript received by the Fluids Engineering Division August 22, 1988.

Photographs of a slug early in its stage of development and one somewhat later are shown in Fig. 2.

Over the last twenty years a number of experimental and theoretical studies have appeared in the literature involving the transition to slug flow. It is the purpose of this paper to present the summary of these studies and to compare them with each other and with experimental data.

Description of Slug Flow Studies

Experimental and Analytical Work of Kordyban and Ranov [3]. In 1970 Kordyban and Ranov have published the results of their investigation into the mechanism of slug formation. Their experiments were performed in a channel of rectangular cross section 2.54 cm deep and 15.2 cm wide using air and water at essentially atmospheric pressure. Their results, shown in Fig. 4, present the transition to slug flow, plotted on coordinates of average air velocity and the depth of air channel which, for rectangular cross section, is proportional to the void fraction.

The authors proposed that the slugs form as a consequence of the Kelvin-Helmholtz instability of the liquid waves, in this

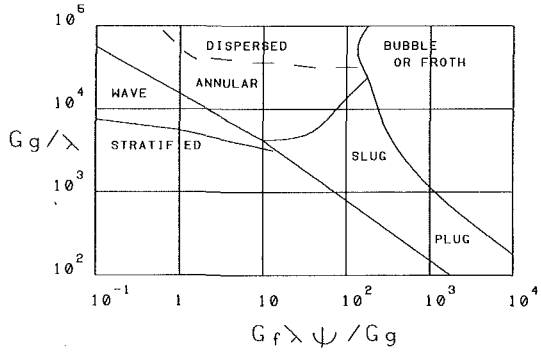

Fig. 1 Baker's flow pattern chart, $\lambda = [(\rho_G / .075)(\rho_L / 62.3)]^{1/2}$; $\psi = [(73/\sigma)\mu_F (62.3/\rho_G)^2]^{1/2}$; ρ_g, ρ_L in lb/ft³; G_g, G_f in lb/hr ft²; σ in dyn/cm; μ_f in centipoise.

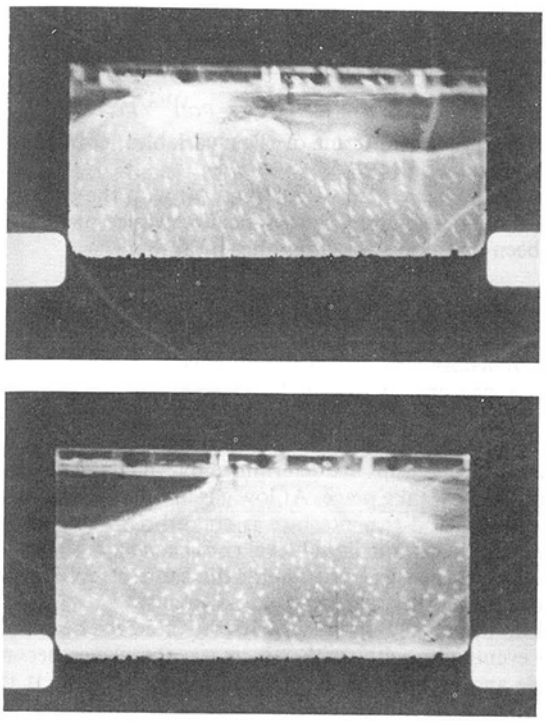

Fig. 2 Photographs of a Slug.
(*a*) Initial stage of formation;
(*b*) A slug somewhat further developed.

case significantly enhanced by the presence of the upper wall. They considered the stability of finite amplitude waves on shallow water and derived the following approximate condition for instability:

$$(U_G - U_L)^2 \geq \frac{\rho_L}{\rho_G} \cdot \frac{g}{k} \cdot \frac{1}{\coth (kh_G - 0.9) + 0.45 \coth (kh_G - 0.9)} \quad (1)$$

In order to obtain equation (1) it was necessary to assume the limiting steepness for largest waves and this was taken as

$$(k\eta)\ \max = 0.9 \quad (2)$$

It should be also noted that from equation (1) the transition is also a function of the wavelength.

The observed wavelengths in their tests were between 2.5 and 5 cm and when those were used in equation (1) the resulting curves are superimposed upon the data in Fig. 4. It may be seen that a reasonable agreement is obtained.

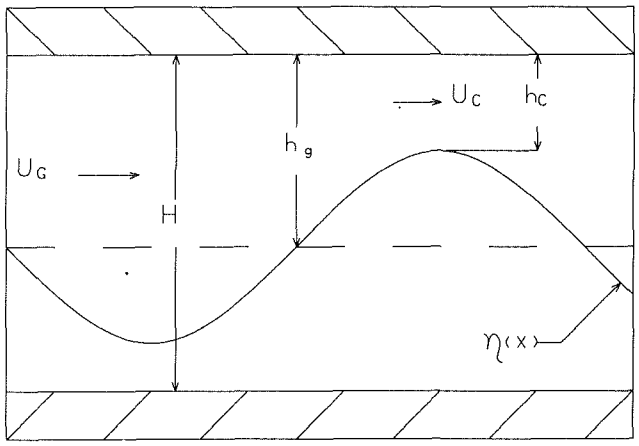

Fig. 3 Flow configuration and notations

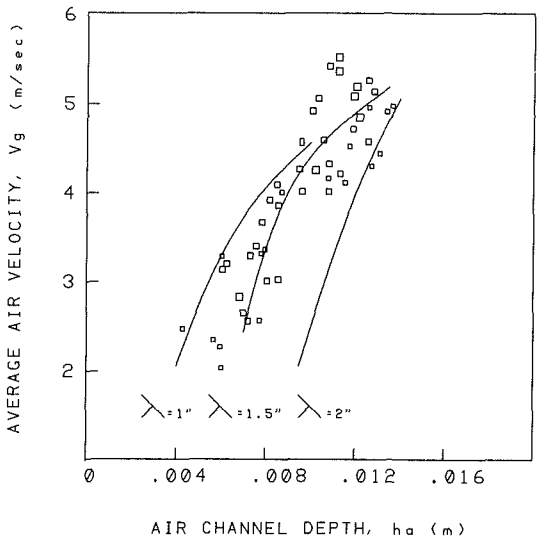

Fig. 4 Transition to slug flow. Work of Kordyban and Ranov [3].

The Work of Wallis and Dobson [4]. In 1973 Wallis and Dobson have published the result of an experimental and analytical study of transition to slug flow in essentially horizontal rectangular channels. They used two sizes of channels in their tests, 2.54 × 2.54 and 30.5 × 8.9 cm in cross section.

The tests were conducted under various conditions, such as counter — and cocurrent flow, as well as stagnant liquid; for some tests the waves were produced by a paddle and other

Nomenclature

C_1 = constant, defined in text
D = hydraulic diameter
F_G = parameter, defined in text
$F_{1\Delta}$ = parameter, defined in text
g = acceleration of gravity
H = total channel depth
h_c = depth of gas channel at crest
h_G = depth of gas channel at equilibrium level
h_L = depth of liquid at equilibrium level
J_G = volumetric gas flux (superficial gas velocity)
J_G^* = dimensionless gas flux, defined in text
K = experimental constant in Bernoulli equation
k = wave number
L = net lift force on wave
p = pressure at wave surface
p_c = pressure at crest
P = $\sqrt{\rho_L/\rho_G}$
ΔP_g = force on wave due to gas acceleration
ΔP_G = force on wave due to gravity
ΔP_K = force on wave due to liquid kinetic energy change
U = gas velocity
U_C = gas velocity at crest
U_G = gas velocity at equilibrium level
U_L = liquid velocity at equilibrium level
x = coordinate in the direction of flow
α = void fraction at equilibrium level
α_c = void fraction at crest
λ = wave length
ρ_G = density of gas
ρ_L = density of liquid
$\Delta\rho$ = $\rho_L - \rho_G$
σ = surface tension
η = wave profile

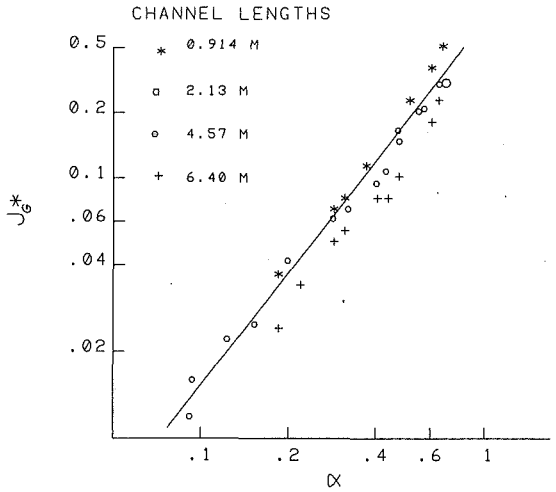

Fig. 5 Transition to slug flow. Work of Wallis and Dobson [4].

unusual conditions were introduced. All tests were conducted with air and water at approximately atmospheric pressure. A special emphasis is placed on the fact that during the tests the slope of the channel was varied to maintain a constant liquid level throughout the channel and a good consistency of the results is attributed to this fact

The authors describe the visual appearance of the flow in detail for various conditions, but the only measurements taken were those of air and water flow rates, as well as that of the liquid level, the latter accomplished by micrometers placed along the channel.

The data, shown in Fig. 5 are plotted on a graph of modified Froude number

$$J_G^* = J_G \{\rho_G [gH (\rho_L - \rho_G)]\}^{1/2} \tag{3}$$

versus the void fraction α.

The authors point out that this parameter represents a balance between gravitational effects and inertia forces in the gas which describe the aerodynamic lift on the wave sufficient to overcome the hydrostatic forces.

It was found that the data for both channels and for most conditions fell on one curve which can be expressed by the equation

$$J_G^* = 0.5\alpha^{3/2} \tag{4}$$

The only data that fell somewhat below the curve was obtained under conditions which the authors describe as "premature slugging." These were the slugs resulting from waves produced by the paddle, from reflected waves and from sufficiently large disturbances which produced high liquid levels.

The authors compared their work with the data of Kordyban and Ranov and found that they fell somewhat below the curve of equation (4); they attribute this to premature slugging, because the liquid depth was not maintained constant in the channel.

To provide an analytical explanation for their result, Wallis and Dobson examined the Kelvin-Helmholtz instability for small sinusoidal waves and found that, expressed in terms of their variables, it becomes

$$J_G^* = \alpha^{3/2} \tag{5}$$

and thus differs only by a constant from equation (4). They conclude that small wave theory is not applicable to slug flow transition, because the latter involves large waves.

They then considered Benjamin's [5] work with a long gas bubble held stationary by the liquid flow. This occurs at a unique velocity which is equal to

$$U_L = 0.5 [gH (\rho_L - \rho_G)]^{1/2}/\rho_L^{1/2} \tag{6}$$

Considering the transition to slug flow an inverse of this phenomenon, they express the gas velocity needed to hold a liquid wave stationary as

$$U_G = 0.5 [gH (\rho_L - \rho_G)]^{1/2}/\rho_G^{1/2} \tag{7}$$

which, expressed in terms of their variables, corresponds exactly to equation (4).

While the agreement of equation (4) with the experimental data is unquestionable, the physical relevance of their theory has been questioned by a number of authors.

Taitel and Dukler Study [6]. In 1976 Taitel and Dukler published the results of a study in which they tried to provide a rational basis for the transitions between all the flow patterns, so that the transition to slug flow was only a part of this study.

The process of analyzing the transitions between various flow patterns begins from consideration of stratified flow and then the mechanisms are determined by which the change from stratified flow take place. At low gas and liquid rates the flow is stratified and the interface is smooth. As the liquid flow rate is increased, the liquid level rises causing a higher relative velocity between gas and liquid; the same effect is produced by increasing the gas flow rate.

With increased relative velocity the interface becomes wavy and eventually, with further increase, the waves become unstable and grow to block the whole cross section. If there is insufficient liquid to form a stable slug, the liquid is swept around the pipe forming annular flow with some dispersed liquid in the core. Thus, according to the authors, the mechanism of transition from stratified to either slug or annular is exactly the same.

To analyze the stability of the waves the authors consider the Kelvin-Helmholtz instability to occur when the low pressure at the crest overcomes the stabilizing effect of gravity.

The condition for wave growth is

$$p - p_c > (h_G - h_c) (\rho_L - \rho_G) g \tag{8}$$

with

$$p - p_c = \frac{1}{2} \rho_G (U_C^2 - U_G^2) \tag{9}$$

and the criterion for instability becomes

$$U_G > C_1 \left[\frac{g(\rho_L - \rho_G) h_G}{\rho_G}\right] \tag{10}$$

where C_1 depends on the size of the wave

$$C_1 = \left[\frac{2}{\frac{h_G}{h_C}\left(\frac{h_G}{h_C} + 1\right)}\right]^{1/2} \tag{11}$$

The authors point out that for infinitesimal disturbances $\frac{h_G}{h_C} \longrightarrow 1$ and $C_1 \longrightarrow 1.0$, so that the classical instability equation is obtained. For finite waves C_1 is less than unity and thus such waves are less stable. They further speculate that C_1 can be estimated from the following relationship

$$C_1 = 1 - \frac{h_L}{D} \tag{12}$$

Using $h_L/D = 0.5$, $C_1 = 0.5$ and this yields the results of Wallis and Dobson, while C_1 obtained from equation (12) produces good agreement with the data of Kordyban and Ranov [3].

The Work of Kordyban [7]. In this study the author points out that Wallis and Dobson as well as Taitel and Dukler have presented the methods by which the transition to slug flow may be predicted without the necessity of knowing the characteristics of interfacial waves. If the instability of the wave, however, is indeed the cause of the slug formation then the

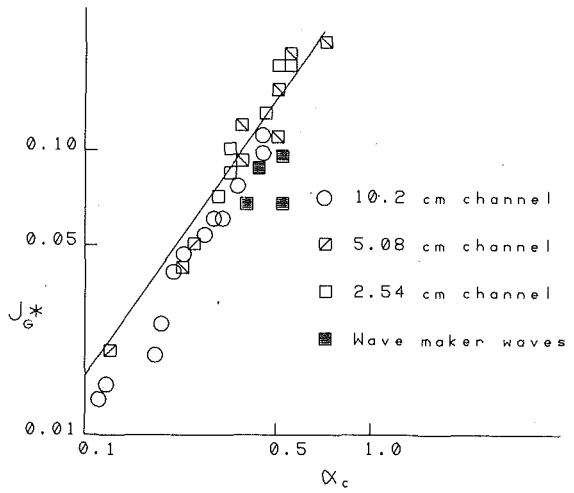

Fig. 6 Transition to slug flow. Data of Kordyban [7] compared to prediction of Wallis and Dobson and Taitel and Dukler.

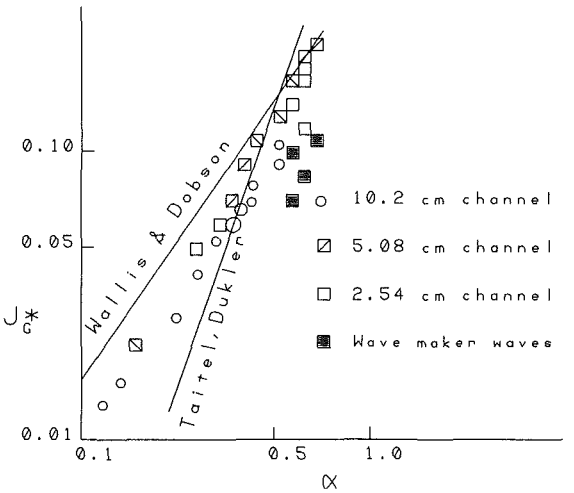

Fig. 7 Transition to slug flow. Data of Kordyban and calculated based on the basis of wave crests.

wave height and its proximity to the channel ought to be of central importance.

With this in mind the work was undertaken in which the transition to slug flow was determined and the height of the waves just prior to transition was measured. The tests were performed with air and water in a rectangular channel 15.2 cm wide; the tests were performed at three depths, 2.54, 5.08, and 10.2 cm. The air velocity at the transition to slug was determined for both spontaneously produced waves and also for waves produced by the wave maker which were longer and more regular. Electrical conductivity probes were used to measure the height of the waves. To duplicate the conditions of Wallis and Dobson the slope of the channel was adjusted during the tests to produce a constant average void fraction.

The results of the tests, when plotted against Wallis and Dobson coordinates, fell on one curve for all channel depths as shown in Fig. 6, but this curve does not agree with Wallis and Dobson prediction. A better agreement is obtained with the prediction of Taitel and Dukler when the following expression was used for C_1

$$C_1 = 1 - \frac{h_L}{D}$$

It is interesting that a much better agreement with Wallis and Dobson prediction can be obtained, as shown in Fig. 7, if the void fraction is calculated on the basis of wave crests.

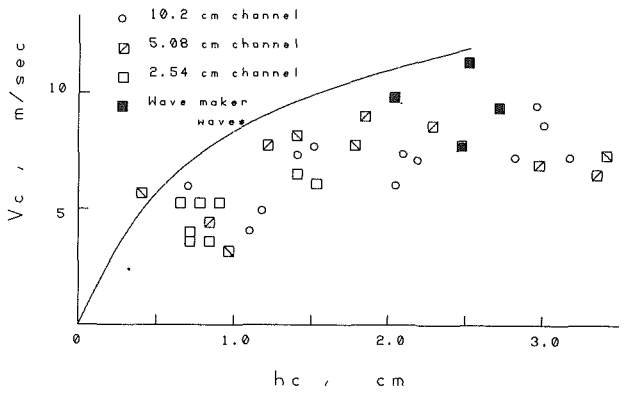

Fig. 8 Critical gas velocity at crest as a function of the gas channel depth at crest compared to highest waves just prior to slugging

In a previous paper this author [8] has proposed that the wave instability occurs in the vicinity of

$$\frac{1.35\ U_c^2}{gh_c} \cdot \frac{\rho_G}{\rho_L - \rho_G} = 1 \tag{13}$$

This equation was derived by considering the highest waves as presented by Michell [9]. The constant 1.35 was obtained from the measurements of pressure difference across the waves [10]. The critical gas velocity calculated from equation (13) is plotted against the distance from the wave crest to the top of the channel in Fig. 8. The highest waves just prior to the appearance of slugs are also plotted for comparison. The agreement is not unreasonable, since the curve is expected to form an upper bound to the data. It is also interesting to note that the waves produced by the wave maker show better agreement with the curve here, while falling noticeably below other points in Fig. 6. This seems to indicate that, in the final analysis, it is only the distance to the top of the channel that is important.

The Study of Gardner [11]. In 1979 an interesting paper authored by Gardner appeared in which he developed a theory of slug formation based on energy flux.

The author considered the analysis of Wallis and Dobson as well as that of Taitel and Dukler and stated that the basic flaw on both of those theories is that they assumed the liquid velocity to be the same both at high and low liquid levels. Since the basic liquid flow at low level is held zero in the experiments, it is therefore assumed that the waves have also zero velocity, which is contrary to experimental evidence.

The author then proceeds to derive the equations for the conservation of energy in both phases assuming that the velocity is uniform throughout. This is the basis for determination of the velocity of the waves with respect to the rest of the liquid.

An additional hypothesis is needed to derive a criterion for the transition to slugging. To obtain this the author studied the energy flux difference between the sections at high and low liquid level. Plotting this energy flux difference against the difference of gas and liquid velocity a maximum is observed. The author considered that it is unreasonable to expect that an increase in velocity difference would reduce the energy input into the system, and thus he proposed that the maximum in energy difference defines the onset of slugging.

This criterion was found to be

$$1 - \left(1 - \frac{1}{P}\right)\frac{h_L}{H} = \frac{4F_1\Delta - 3(3+P)F_1\Delta^2 - 4(1+P)F_1\Delta^3}{2 - 2(3+P)F_1\Delta + 3(1+P)F_1\Delta^2} \tag{14}$$

where

$$F_1\Delta = \left(\frac{\rho_G}{\Delta\rho g H}\right)^{1/2}(U_G - U_L) \tag{15}$$

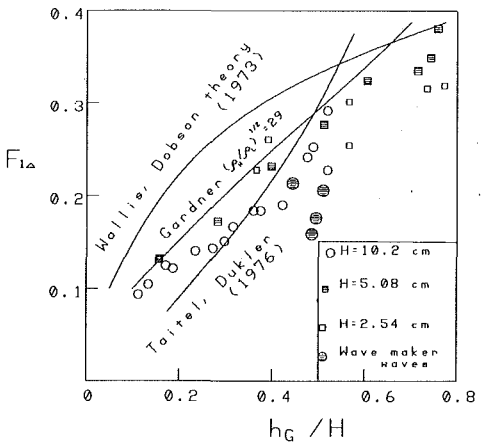

Fig. 9 Transition to slug flow. Work of Gardner [11] compared to prediction of Wallis and Dobson and Taitel and Dukler and to data of Kordyban [7].

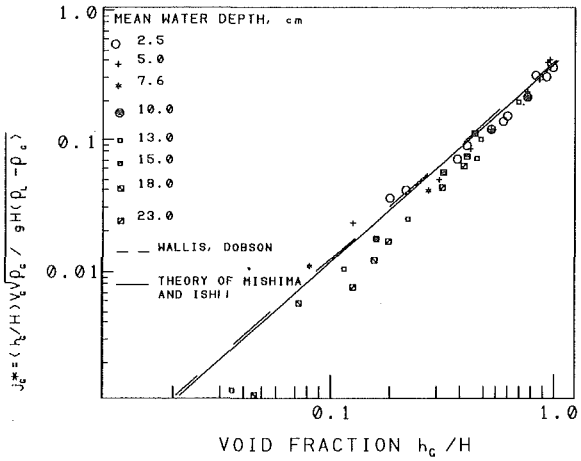

Fig. 11 Prediction of Mishima and Ishii (12) as compared to prediction and data of Wallis and Dobson

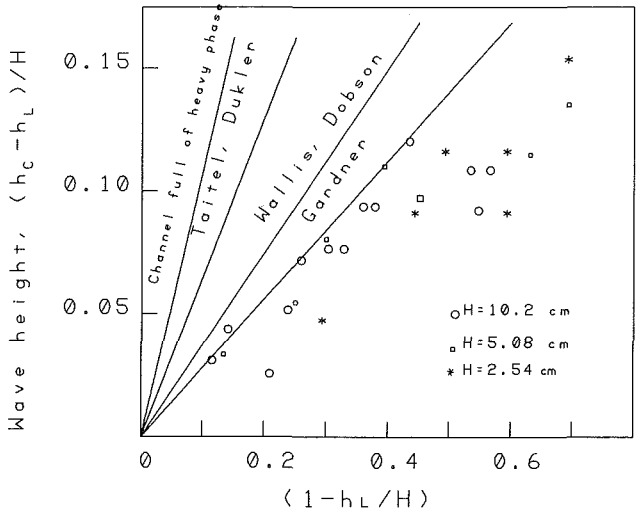

Fig. 10 Wave heights prior to slugging as predicted by various investigators and compared to data of Kordyban [7]

Figure 9 shows the comparison of results of equation (14) with those of Wallis and Dobson and Taitel and Dukler as well as the data of Kordyban [7]. Figure 10 shows wave heights as predicted by various investigators compared with the data of Kordyban. It may be seen that the predictions of this paper are in best agreement with the data.

The Study of Mishima and Ishii [12]. The authors based their study on the analysis of Kordyban and Ranov [3], then introduced further assumptions, namely:

$$\rho_L >> \rho_g$$
$$k\eta_{\max} = 1$$

They obtain the following criterion for the instability of waves

$$U_G^2 \geq \frac{\rho_L\, gh_G/\rho_G}{kh_G\, F_G\,(kh_G)} \tag{16}$$

where

$$F_G\,(kh_G) = \coth\,(kh_G - 1)\,[1 + 0.5\coth\,(kh_{G-1})] \tag{17}$$

This relationship is still dependent upon the wave length and at this point the authors introduce the concept of a "most dangerous" wave, that is the wave with the largest growth rate. By examining their equations they conclude that for such a wave $kh_G = 2.26$ and their criterion for instability becomes

$$U_G - U_L \geq 0.487\sqrt{(\rho_L - \rho_G)\, gh_G/\rho_G} \tag{18}$$

This criterion is in excellent agreement with both the prediction of Wallis and Dobson and their data as may be seen in Fig. 11.

While their agreement with the data is unquestionable, their assumption of $k\eta_{\max} = 1$, being equivalent to a height-to-length ratio of 0.318, does not appear to be reasonable. The height-to-length ratio of the highest waves was found analytically by Michell [9] to be 0.14 and the actual waves are probably somewhat lower than that. This author has observed and photographed numerous waves just prior to formation of slugs, but he never found one with a height-to-length ratio higher than 0.1. With this ratio in equation (17), equation (18) would overpredict the critical velocity by a considerable amount.

Work of Hihara and Saito [13]. The authors have investigated the transition from stratified to slug flow in circular and square tubes under the usual conditions, as well as in the presence of a bore travelling upstream from the tube exit.

In developing their model they consider that the waves will grow when the lift force produced by the aerodynamic pressure overcomes the restoring force of gravity. Unlike other investigators, who assume that the instability occurs when these forces are equal, they consider that the difference between them is equal to a constant. This constant is then established empirically.

Their model is similar to that of Taitel and Dukler in that a factor is introduced and determined from experimental data.

Photographic Study of Slug Formation by Kordyban [14]. In 1985 Kordyban has published the results of a photographic study of slug formation which was carried out in a rectangular channel 10.2 cm deep and 15 cm wide. To obtain a pictorial history of slug development the air velocity was set slightly below the critical value and then a large wave was produced by a single stroke of the wave maker. The progress of this wave was followed and photographed by a motion picture camera until it developed into a slug.

One of the significant observations of this work was the fact that, just prior to the rapid growth of wave into the slug, ripples appeared on the hitherto smooth crest of the wave in every case; a representative example of this is shown in Fig. 12. Ordinarily such ripples, having a lower speed, would be left behind by the large wave, but these remained at the crest. It is interesting to note that a similar phenomenon was observed by Mahony [15] in the ocean; he proposed that this may be due to Kelvin-Helmholtz instability.

It is also of interest that the wave growth originates from

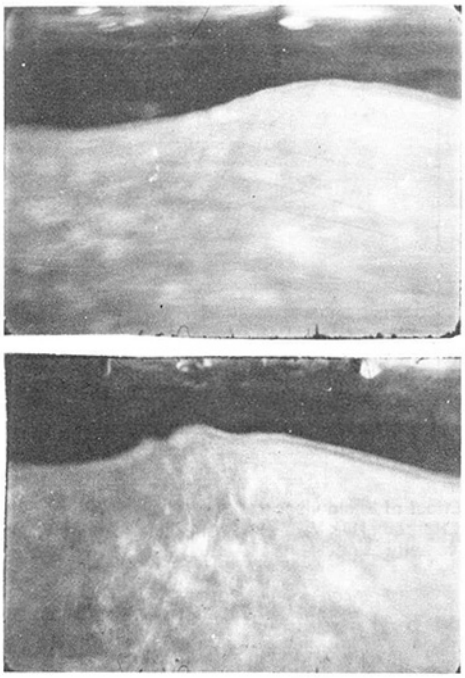

Fig. 12 Photographs showing sudden appearance of ripples at the crest of the wave. Time between frames 0.08S.

one of the ripples as may be observed in a series of photographs in Fig. 13.

Based on these observations the author proposed that the Kelvin-Helmholtz instability occurs at the crest only rather than over the whole wave, as is usually assumed. The reasoning behind this supposition is as follows. If the liquid surface is $\eta = \eta(x)$ and the pressure over the liquid is $p(x)$ then, neglecting surface tension, the criterion for instability is

$$\frac{dp/dx}{d\eta/dx} = (\rho_L - \rho_G)\, g \tag{19}$$

In accordance with this equation the liquid surface is particularly susceptible to instability where its slope is low and pressure gradient is high. For a wave in a closed channel equation (19) may be rewritten as

$$(\rho_L - \rho_G)\, g = K\rho_G U \cdot \frac{U_G\, h_G}{(h_G - \eta)^2} \tag{20}$$

As the wave approaches the channel top the crest will become unstable before the main portion of the wave, since both U and η have the highest values at the crest.

The proposition that the instability occurs at the crest only may explain a discrepancy between the theory and experiment. Kelvin-Helmholtz instability requires that, at instability, the waves be stationary with respect to the liquid current, but such waves have never been observed in an experiment. The particle velocity at the crest is practically equal to the wave speed for high waves; thus the ripples which remain at the crest are, in fact, stationary with respect to the local liquid current.

The Work of Ahmed and Banerjee [16]. The authors undertook this work, since, in their opinion, there is a lack of understanding as to why the transition to slug flow occurs well below the velocities predicted by the linear Kelvin-Helmholtz instability. The predictions of Wallis and Dobson as well as those of Taitel and Dukler agree well with experimental data, but they are not grounded in theory. In fact, the authors point out, the nonlinear interfacial instability has not yet been investigated and this they propose to do.

The authors formulate the problem in a rather standard

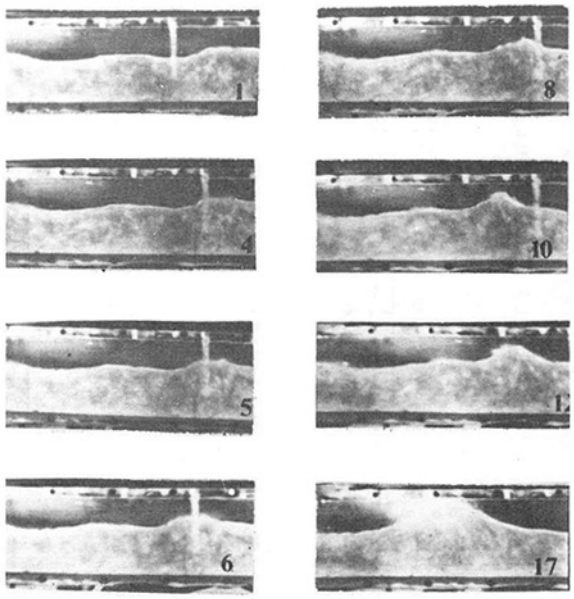

Fig. 13 Growth of ripples into a slug.

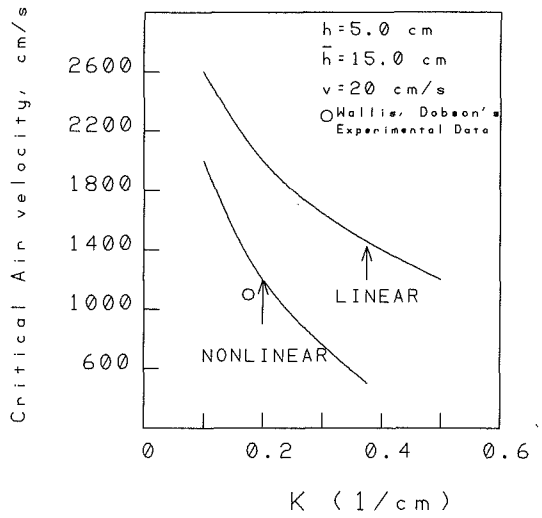

Fig. 14 Critical gas velocity for nonlinear waves from work of Ahmed and Bannerjee

manner by assuming incompressible, inviscid, two-dimensional flow. The problem is solved by a perturbation technique based on the method of multiple scales. The solution up to third order is obtained and, based on this, the stability of the waves is analyzed.

The results of this work have been obtained by the use of a computer and are shown in Fig. 14. Two different types of instability mechanisms were uncovered. One is possible in the absence of air velocity and leads to a complete disintegration of the wave train. The second, at high air velocity, may be responsible for the explosive growth of wave amplitude which is due to Kelvin-Helmholtz instability.

Figure 14 shows that the nonlinear waves are indeed more unstable than the linear waves and there is a qualitative agreement with a single experimental point. The instability also is a strong function of the wave length.

The Work of Minato, Ikeda and Naitoh [17]. A new, mechanistic model of transition to slug flow in horizontal circular tubes is developed by incorporating the contribution of the liquid kinetic energy to the growth of interfacial waves.

Aside from the usual lifting forces due to acceleration of gas over the wave crests, the authors propose that there is

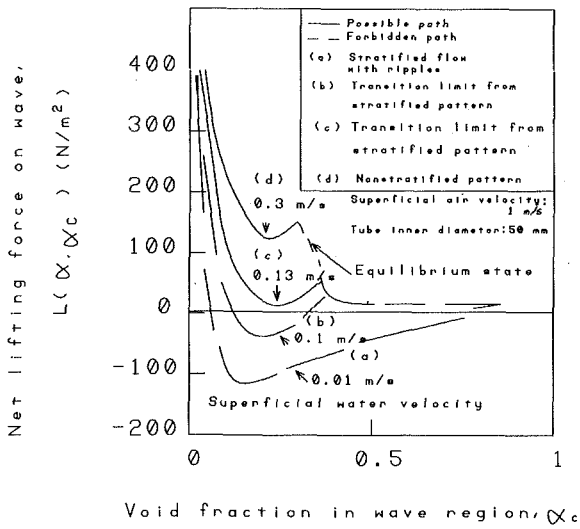

Fig. 15 Relationship between lifting force on wave air void fraction

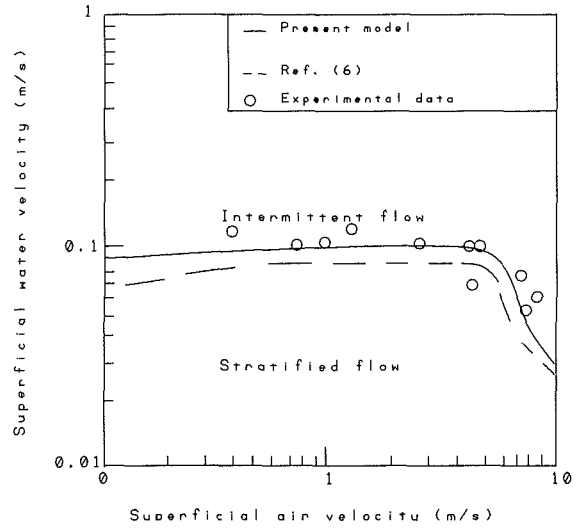

Fig. 16 Transition to slug flow. Work of Minato et al. [16] compared to prediction of Taitel and Dukler [6].

another lifting force due to the kinetic energy of the liquid, since its velocity becomes lower as the flow area in the wave increases.

The net force to promote the wave growth was found to be

$$L(\alpha,\alpha_c) = \Delta P_g + \Delta P_K - \Delta P_G = 1/2\,\rho_G U_G^2\,[(\alpha/\alpha_c)^2 - 1] + 1/2\,\rho_L U_L^2\,(1-\alpha)\,(2-\alpha-\alpha_c)/(1-\alpha_c) - g\,(\rho_L - \rho_G)\,(H - h_c - h_L) \quad (21)$$

The equilibrium void fraction α is found from the balance of gas and liquid pressure losses which are attributable to the tube wall and interface shear forces. The numerical calculation procedure then is described which determines the transition between the stratified and slug flow patterns. The results of calculations are shown in Fig. 15. It should be noted that the waves grow while the lift force is positive, but they cannot pass into the region of negative lift. Thus, for curves (*a*) and (*b*), the waves grow only a small amount and then remain stable. Curve (*d*) shows unstable interface, while curve (*c*) represents the transition to slug flow.

The authors also performed experiments with air and water in tubes of 2.5 and 5 cm diameters, as well as one with a 10.4 cm diameter which was equipped with a rod bundle. Typical comparison between the prediction and the experimental data is shown in Fig. 16. The dashed line represents the prediction of Taitel and Dukler [16].

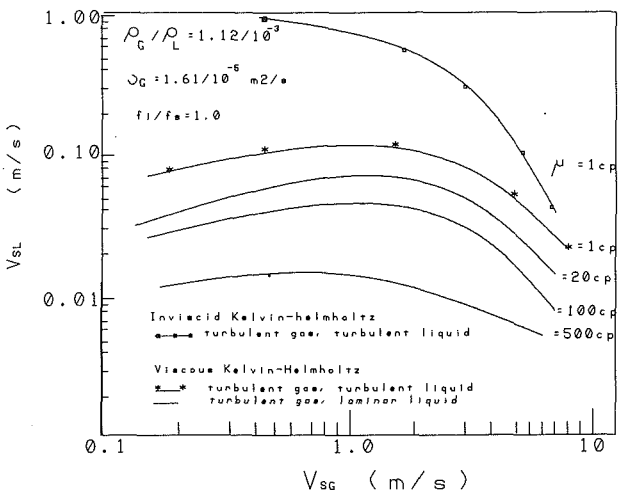

Fig. 17 Effect of liquid viscosity on neutral stability based on theory of Lin and Hanratty [17]; V_{SL} — superficial liquid velocity; V_{SG} — superficial gas velocity

Lin and Hanratty Model [18]. In this work the authors examine the stability of an infinitesimal disturbance by a method differing from the classical Kelvin-Helmholtz instability theory in that liquid phase viscous and inertia terms are included. The inclusion of these effects causes the wave velocity to be greater than the average liquid velocity at instability instead of being equal to it. The inertia terms become destabilizing and the instability occurs at the lower gas velocities.

To develop this theory the authors write basic continuity and momentum equations for the stratified flow and impose upon it a small sinusoidal disturbance. They then examine the conditions under which this disturbance will grow. For complete solution it is necessary to provide the relationship for wall and interfacial shear.

The comparison of resulting instability criteria as compared to inviscid Kelvin-Helmholtz instability is shown in Fig. 17. Now the instability criterion is a function of viscosity.

The authors compare the developed theory to experimental results of Lin [19] and a good agreement is obtained. A comparison with Taitel and Dukler relationship shows that it works correctly for air and water, but not for fluids of other viscosities.

Analysis of Fershneider et al. [20]. The authors study specifically the two-phase flow of gas and oil in pipe lines and point out that the classical methods of calculating the transitions between different flow regimes produce high errors. In their analysis they start with the basic equations as in previous work and consider linear stability theory. They point out that the inclusion of the friction terms in the stability criterion make it different from the classical Kelvin-Helmholtz instability. A good agreement with experimental data for the flow of oil and natural gas in a 6 in. dia pipe is obtained.

The Work of Wu et al. [21]. Here, again, the two-phase flow in the oil pipe lines is examined. The analysis is quite similar to the previous papers. The authors consider the analysis of Wallis [22] which is based on linear stability theory. In this analysis it is assumed that at instability the phase velocity of the continuity wave is greater than the wave speed. The results of this development compare well with the relationship of Taitel and Dukler for air and water in a 1 in. dia pipe, but differ significantly for the flow of hydrocarbons in an 8 in. dia pipe at high pressure. Of particular interest is the authors' observation of the existence of what they call "wall wetting and droplets" flow regime between the stratified and slug flow as shown in Fig. 19. This has not been observed with air and water and it certainly merits further investigation.

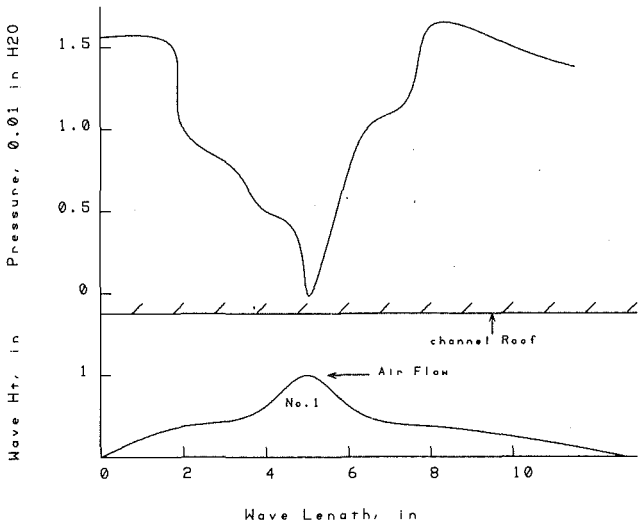

Fig. 18 Aerodynamic pressure gradient over a wave

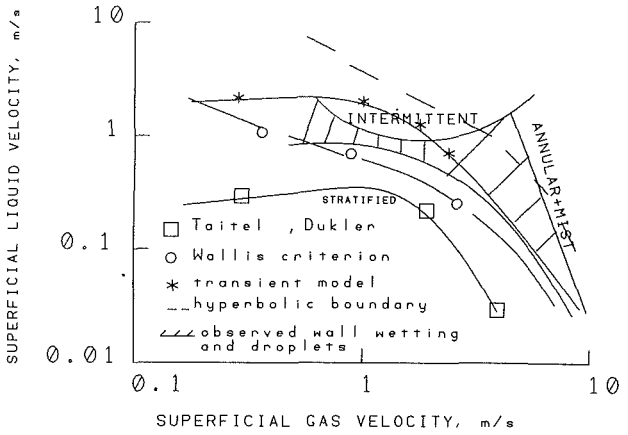

Fig. 19 Comparison of observed and predicted flow-regime boundaries from Wu et al. (21).

The Comparison Between the Theories

The various studies presented here can be divided roughly into four groups. In the first group the authors consider the Kelvin-Helmholtz instability as the cause for the formation and analyze the stability of waves on the basis of wave motion equations.

The propagation equation for small, sinusoidal waves is given by Milne-Thompson [23]

$$k\rho_L(U_L - C)^2 \coth kh_L + k\rho_G(U_G - C)^2 \coth kh_G = g(\rho_L - \rho_G) + \sigma k^2 \quad (22)$$

The waves are assumed to be stable as long as the expression for wave speed is real. For long waves, when the surface tension can be neglected, the predicted instability equation reduces to

$$(U_G - U_L)^2 > (\rho_L - \rho_G)\, g(h\rho_L/\rho_L + h_G/\rho_G) \quad (23)$$

For $\rho_L \gg \rho_G$ and $U_G \gg U_L$ the above equation becomes

$$\rho_G U_G^2 \geq g\,(\rho_L - \rho_G)\, h_G \quad (24)$$

As shown by a number of authors this relationship overpredicts the critical gas velocity by a factor of two and, consequently, various investigators turned to the analysis of finite amplitude waves. There are actually two factors to be considered here, first, the finite amplitude waves may be inherently less stable and second, as the waves approach the top of a closed channel the pressure variation increases with the square of velocities thus enhancing Kelvin-Helmholtz instability.

Kordyban and Ranov performed an approximate analysis on finite amplitude waves and Mishima and Ishii extended their theory. Ahmed and Banerjee, on the other hand, used more sophisticated mathematical techniques to analyze the stability of the finite waves.

The results of all these analyses indicate that the transition to slug flow is a rather strong function of the wave length in the sense that the shorter waves are less stable. This is at variance with experimental observations. Since most observed waves seem to have similar steepness, it is the longest waves which are the highest and they are invariably the ones which grow into slugs. Moreover, the experimental data do not indicate any sensitivity to wave length. The wavelengths in Fig. 6 varied from about 2 to 15 cm and yet, no trend is evident in this figure.

One possible explanation may be offered, if one accepts the supposition that the Kelvin-Helmholtz instability occurs at the crest only, made on the basis of photographic details of slug formation. In this case the large wave is only a vehicle which brings the liquid surface into proximity of the top wall of the channel and its length is not significant for Kelvin-Helmholtz instability.

The second group of papers consists of the theories in which the authors also consider that the slugs form due to Kelvin-Helmholtz instability, but analyze the stability on the basis of Bernoulli equation. Basically, the two approaches should be identical, but in that case the authors usually ignore the wave motion and simply consider the high and the low liquid level in the channel. They then calculate the pressure variation over the wave on the basis of continuity for gas phase and Bernoulli equation. The papers in this group include those of Taitel and Dukler [6] and Kordyban [7], but Wallis and Dobson [4] and Minato et al. [17] refer to it.

This approach appears to be more in the spirit of experimental data, because it indicates that the transition is insensitive to wave shape or length and seems to be only dependent on how close the liquid surface is brought to the top of the channel and on gas velocity. The work of Wallis and Dobson may serve as an example. Their tests include cocurrent and countercurrent flow as well as stagnant liquid and they describe in detail a variety of wave shapes and behavior and yet, the transition to slug flow was the same under all conditions.

This approach, however, is not free of problems, with the first being the inability to determine the wave height from Bernoulli equation; the authors here take different approaches. Kordyban does not provide any means for the determination of wave heights, but simply compares the results from Bernoulli equation to measured wave heights. Wallis and Dobson's theory results in the wave length being one-half of the depth of gas passage, while Taitel and Dukler introduce an empirical factor

$$C_1 = 1 - \frac{h_L}{D}$$

which, according to Gardner [11], results in the wave height being

$$\frac{H - h_c - h_L}{H - h_L} = 1 - 0.25\left[1 - \frac{h_L}{H}\right]^2 - 0.25\left[1 - \frac{h_L}{H}\right]\left\{\left[1 - \frac{h_L}{H}\right]^2 + 8\right\}^{1/2} \quad (25)$$

One may refer to Fig. 10 which compares various wave height predictions to experimental data of Kordyban [7].

The second problem with this approach is that, even with various empirical factors introduced, the Bernoulli equation still overpredicts the critical gas velocity. Again, if we consider the possibility of the instability occurring at the crest of the

wave only, then we should be considering the steepness of the pressure gradient at the crest, rather than the pressure difference across the whole wave. It is not an easy task to determine this local pressure gradient either experimentally or analytically, but from some measurements of pressure at the wave surface the pressure gradient appears to be particularly steep at the wave crest as shown in Fig. 17; this would explain the lower critical velocity.

The third group of papers consists of work in which the kinetic energy comes into consideration. Wallis and Dobson paper appears to fall into this category, even though they do not refer specifically to energy. The best developed theory here appears to be due to Gardner. He calculates the kinetic energy in both phases and determines the energy flux difference between the high and low liquid level; the maximum of this difference is considered to be the transition to slug flow.

Because of a good agreement with other theories and experimental data and because the same variables are involved, it appears that the Kelvin-Helmholtz instability and energy maximum, are the same physical phenomenon examined from two different viewpoints. The significant fact about Gardner's theory is that it permits the prediction to slug flow without the necessity of predicting the wave height from some other relationship.

The work of Minato and others also considers the energy, but the results are plotted on coordinates of superficial liquid versus gas velocity. While the agreement is good with their own experimental data, it is difficult to compare their relationship with data of other investigators, because reliable values of interfacial shear are needed for that purpose and it is not clear whether such values are available.

The fourth group consists of fairly recent analyses such as those of Lin and Hanratty and others. The common thread which runs through these analyses is that a linear instability is introduced which includes the effects of inertia and friction which results in the lowering of the gas velocity at instability. There is no question that the inclusion of these terms represents an advance in the analysis of instability and will eventually lead to a solution of this problem. The weak point in these analyses is the assumption of a small amplitude instability. It is assumed that the slugs develop from essentially smooth liquid level. The experimental observations from air and water indicate that waves grow at first without becoming slugs, probably by Miles' mechanism and it is only the steep waves that eventually become unstable and grow explosively to become slugs. There is no reason to believe that this situation is different at higher pressures or at different viscosities. For steep waves with variation of gas velocity from crest to trough and with separation at the crest the linear theory is not well applicable. On the other hand, the inclusion of friction and inertia terms for high waves would go far towards a complete understanding of the transition to slug flow.

Discussion

It may be seen from foregoing presentation that the transition to slug flow has been studied intensively by a number of investigators and much has been learned about this phenomenon. The experimental data appear to be quite good and there is considerable agreement between different workers. The analyses vary from mathematically simple to quite sophisticated and they agree well with experimental data.

In the opinion of this writer there is little doubt that the slugs form as a consequence of the Kelvin-Helmholtz instability of liquid waves enhanced by the proximity of the upper wall of the channel. This instability has been studied both by analyzing the wave amotion and by the use of a simple Bernoulli equation to determine the pressure difference across the wave. The latter method appears to agree better with experimental results. These results seem to indicate that the shape or the length does not matter; it is only necessary to raise the liquid surface to a certain distance to the top of the channel. This approach, however, does not predict the wavelength, but excellent correlation of experimental data when plotted on Wallis and Dobson coordinates indicates that there must be some relationship between the wave height and the transition to slug flow. Thus far this relationship has not been theoretically explained, except possibly by Gardner.

Further refinement in the analyses will have to take into account a number of details which have been ignored thus far. The wave instability depends vitally on the pressure distribution at the wave surface and this, in turn, depends on velocity profile. This is where available experimental data was not considered. Most authors assume inviscid flow, while Miles [24] assumed a logarithmic velocity profile, such as would occur over a rough surface. Chang [25] however, measured the velocity profile in the gas in the vicinity of the wave surface and found that at the crest the velocity has a value higher than the free stream velocity. Experimental evidence also indicates a separation at the crest.

A number of investigators ignore the wave motion in the liquid. Gardner and Minato et al. consider the high and the low liquid level in computing the kinetic energy of the liquid. Experimental evidence indicates that, in the initial stages of instability, the wave still possess orbital motions away from the crest.

Further refinements in the theories are also unlikely unless additional experimental data are obtained. Two areas in particular are lacking experimental information. A more complete understanding of the transition to slug flow requires the measurement of velocity profiles and pressure distribution in the vicinity of the waves, as well as the determination of flow patterns in the liquid waves.

The other area, of more practical nature, should cover the transition to slug flow for fluids of different density ratios, viscosities and surface tension. The early data are almost entirely limited to air and water at atmospheric pressure. The early theories, of course, predict the transition over the whole range of density ratios. They also indicate that the viscosity is not a variable of importance while surface tension may be significant or not, depending on the size of the wave in question. The more recent data [21, 22, 26] which involve hydrocarbon fluids, some at high pressure, indicate that the classical theories do not represent them well and it appears that the inclusion of interfacial friction is important. Thus, inspite of detailed explanation of the instability for the case of air and water, we are still far from the complete solution of this problem.

References

1 Lockhart, R. W., and Martinelli, R. C., "Proposed Correlation for Isothermal Two-Phase, Two-Component Flow in Pipes," *Chem. Eng. Progress*, Vol. 45, 1949, p. 39.

2 Baker, O., "Design of Pipe Line for the Simultaneous Flow of Oil and Gas," *The Oil and Gas Journal*, July 26, 1954.

3 Kordyban, E. S., and Ranov, T., "Mechanism of Slug Formation in Horizontal Two-Phase Flow," ASME *Journal of Basic Engineering*, Vol. 92, 1970, pp. 857–864.

4 Wallis, G. B., and Dobson, J. E., "The Onset of Slugging in Horizontal Stratified Air-Water Flow," *Int. J. Multiphase Flow*, Vol. 1, 1973, pp. 173–193.

5 Benjamin, T. B., "Gravity Currents and Related Phenomena," *J. Fluid Mech.*, Vol. 31, 1968, pp. 209–248.

6 Taitel, Y., and Dukler, A. E., "A Model for Predicting Flow Regime Transitions in Horizontal and Near Horizontal Gas-Liquid Flow," *AIChE J.*, Vol. 22, 1976, p. 47.

7 Kordyban, E., "The Transition to Slug Flow in the Presence of Large Waves," *Int. J. Multiphase Flow*, Vol. 3, 1977, pp. 603–607.

8 Kordyban, E., "Some Characteristics of High Waves in Closed Channels Approaching Kelvin-Helmholtz Instability," ASME JOURNAL OF FLUIDS ENGINEERING, Vol. 99, 1977, p. 339.

9 Michell, J. H., "The Highest Waves in Water," *Phil. Mag.*, Vol. 5, No. 36, 1893, p. 430.

10 Kordyban, E., "Some Characteristics of Aerodynamic Pressure Over High Waves in Closed Channels," ASME Paper No. 73-FE-6, 1973.

11 Gardner, G. C., "Onset of Slugging in Horizontal Ducts," *Int. J. Multiphase Flow*, Vol. 5, 1979, p. 201.

12 Mishima, K., and Ishii, M., "Theoretical Prediction of Onset of Horizontal Slug Flow," ASME JOURNAL OF FLUIDS ENGINEERING, Vol. 102, 1980, p. 441.

13 Hihara, E., and Saito, T., "Slug Flow Transition in Horizontal Gas-Liquid Flow," *Bull JSME*, Vol. 27, No.234, 1984, pp. 2771-2778.

14 Kordyban, E. S., Some Details of Developing Slugs in Horizontal Two-Phase Flow," *AIChE J.*, Vol. 31, 1985, p. 802.

15 Mahony, J. J., "Kelvin-Helmholtz Waves on the Ocean?," *J. Fluid Mech.*, Vol. 82, No. 1, 1977, pp. 1-16.

16 Ahmed, R., and Banerjee, S., "Finite Amplitude Waves in Stratified Two-Phase Flow: Transition to Slug Flow," *AIChE J.*, Vol. 31, 1985, p. 1480.

17 Minato, A., Ikeda, T., and Naitoh, M., "Mechanistic Model of Slugging Onset in Horizontal Circular Tube," *J. Nuclear Science and Technology*, Vol. 23, 1986, pp. 761-768.

18 Lin, P. Y., and Hanratty, T. J., "Prediction of the Initiation of Slugs with Linear Instability Theory," *Int. J. Multiphase Flow*, Vol. 12 (1), 1986, pp. 79-95.

19 Lin, P. Y., "Flow Regime Transitions in Horizontal Gas-Liquid Flow," Ph.D. dissertation, University of Illinois, Urbana, Ill., 1985.

20 Ferschneider, G., Laqiere, M., Bourgeois, T., and Fitreman, J-M, "How to Calculate Two-Phase Flow of Gas and Oil in Pipe Lines," *Pipe Line Industry*, Vol. 63, No. 2, 1985, pp. 35-39.

21 Wu, H. L., Pots, B. F. M., Hollenberg, J. F., and Meertroff, R., "Flow Pattern Transitions in Two-phase Gas/Condensate Flow at a High Pressure in an 8 in. Horizontal Pipe," *Proceedings of 3rd International Conference on Multiphase Flow*, Hague, Netherlands, 18-20 May 1987, pp. 13-21.

22 Wallis, G. B., *One-Dimensional Two-phase Flow*, McGraw-Hill, 1969.

23 Milne-Thompson, L. M., *Theoretical Hydrodynamics*, The MacMillan Co., New York, 1960.

24 Miles, J. W., "On the Generation of Surface Waves by Shear Flows," *J. Fluid Mech.*, Vol. 3, 1957, p. 185.

25 Chang, P. C., "Laboratory Measurements of Air Flow Over Wind Waves Following the Moving Water Surface," CER68-69PCC18, Colorado State Univ, Ford Collins, CO, 1968.

26 Bendiksen, K. H., "Two-phase Flow Research at SINTEF and IFE: Some Experimental Results and a Demonstration of the Dynamic Two-phase Flow Simulator OLGA," Offshore Northern Seas Conference, 1986, Stavanger, Norway.

This paper is dedicated to Professor Theodor Ranov on the occasion of his 80th birthday.

The Influence of the Wall on Flow Through Pipes Packed With Spheres

R. M. Fand

R. Thinakaran

Department of Mechanical Engineering,
University of Hawaii at Manoa,
Honolulu, Hawaii 96822

This paper presents the results of an experimental investigation that is a sequel to a previously published study of the flow of fluids through porous media whose matrices are composed of randomly packed spheres. The objective of the previous study was to accurately determine the ranges of the Reynolds number for which Darcy, Forchheimer and turbulent flow occur, and also the values of the controlling flow parameters—namely, the Kozeny-Carman constant for Darcy flow and the Ergun constants for Forchheimer and turbulent flow—for porous beds that are infinite in extent; that is, practically speaking, for sufficiently large values of the dimension ratio, D/d, where D is a measure of the extent of the bed and d is the diameter of a single spherical particle of which the porous matrix is composed. The porous media studied in the previous and present experiments were confined within circular cylinders (pipes), for which the dimension D is taken to be the diameter of the confining cylinder. The previous study showed that the flow parameters are substantially independent of the dimension ration for $D/d \geq 40$. For $D/d < 40$, the so-called "wall effect" becomes significant, and the flow parameters become functionally dependent upon this ratio. The present paper presents simple empirical equations that express the porosity and the flow parameters as functions of D/d for $1.4 \leq D/d < 40$. Transitions from one type to another were found to be independent of D/d and occur at values of the Reynolds number identical to those reported in the previous study.

Introduction and Statement of Objectives

Asymptotic Values of Flow Parameters. The present paper presents the results of an experimental investigation that is a sequel to a previously published study by Fand et al. [1] of the flow of fluids through simple and complex porous media whose matrices are compared of randomly packed spheres. In this context the term "simple" refers to porous media whose matrices are composed of spheres of uniform diameter, while "complex" refers to matrices composed of spheres having different diameters. The objective of the previous study was to accurately determine the ranges of the Reynolds number for which Darcy, Forchheimer and turbulent flow occur, and also the values of the controlling flow parameters—namely, the Kozeny-Carman constant for Darcy flow and the Ergun constants for Forchheimer and turbulent flow—for porous beds that are infinite in extent; that is, practically speaking, for sufficiently large values of the dimension ratio, D/d, where D is a measure of the extent of the bed and d is the diameter of a single spherical particle of which the porous matrix is composed. The porous media studied in the previous and present experiments were confined within circular cylinders (pipes), for which the dimension D is taken to be the diameter of the confining cylinder. The previous study showed that the flow parameters are substantially independent of D/d for $D/d \geq 40$ and can be evaluated in the manner described in what follows.

For relatively low Reynolds numbers and for $D/d > 40$, viscosity-dominated Darcy flow occurs and can be represented by the following well known equation:

$$\frac{P'd}{\mu v} = \frac{d}{K}, \tag{1}$$

where, for spheres, the permeability, K, is given by

$$K = \frac{d^2}{36\kappa\alpha}; \ \alpha = \frac{(1-\epsilon)^2}{\epsilon^3}, \tag{2}$$

and κ is a dimensionless constant called the Kozeny-Carman constant. Forchheimer flow, which is a region of laminar flow that occurs at moderate Reynolds numbers, wherein both viscous and inertial forces are significant, can be represented, for $D/d > 40$, by Ergun's well known equation:

$$P' = \left(\frac{A\alpha\mu}{d^2}\right) v + \left(\frac{B\beta\rho}{d}\right) v^2; \tag{3}$$

$$\alpha = \frac{(1-\epsilon)^2}{\epsilon^3} \text{ and } \beta = \frac{(1-\epsilon)}{\epsilon^3},$$

where A and B are dimensionless constants, called the first

Contributed by the Fluids Engineering Division for publication in the JOURNAL OF FLUIDS ENGINEERING. Manuscript received by the Fluids Engineering Division November 9, 1988.

Table 1 Bounds of flow regimes and asymptotic values of flow parameters

Flow Regime	Lower Bound for Simple Media	Upper Bound for Simple Media	Asymptotic Values of of Flow Parameters
Darcy Flow	$Re_{DL} < 10^{-5}$	$Re_{DH} = 2.3$	$\kappa = 5.34$
Forchheimer Flow	$Re_{FL} = 5$	$Re_{FH} = 80$	$A = 182$, $A_w = 173$ $B = 1.92$, $B_w = 1.87$
Turbulent Flow	$Re_{TL} = 120$	None	$A' = 225$, $A'_w = 214$ $B' = 1.61$, $B'_w = 1.57$

Fictitious point of transition from Darcy to Forchheimer Flow, $Re_{DF} = 3$
Fictitious point of transition from Forchheimer to Turbulent Flow, $Re_{FT} = 100$

and second Ergun constants for Forchheimer flow, respectively. Equation (3) also represents the flow at relatively high Reynolds numbers, where the flow is turbulent. For turbulent flow, the Ergun constants are denoted by A' and B'.

It will be useful to note that equation (3) can be written as follows:

$$f' = \frac{A}{\mathrm{Re}'} + B, \tag{4}$$

where $f' = dP'/\rho v^2\beta$ and $\mathrm{Re}' = \mathrm{Re}/(1-\epsilon)$ are called the modified friction factor and modified Reynolds number, respectively.

Fand et al. determined experimentally the bounds of the Darcy, Forchheimer and turbulent flow regimes and the values of the parameters κ, A, B, A', and B' as listed in Table 1. In order to facilitate the mathematical characterization of the transition regions which lie between the Darcy and Forchheimer and between the Forchheimer and turbulent regions, they defined two fictitious "points of transition," Re_{DF} and Re_{FT}, whose numerical values are indicated beneath Table 1. The values of the flow parameters listed in Table 1 and the conditions relating thereto will be referred to as "asymptotic" values and conditions, in recognition of the fact that they pertain to large values of the dimension ration (in practice, for $D/d \geq 40$).

The Dimension Ratio and Wall Effect: Objectives of the Investigation. The pressure gradient associated with the flow of a fluid through a porous medium depends upon the density and viscosity of the fluid, the magnitude of the Reynolds number that characterizes the flow, and the detailed geometry of the matrix of the medium. The porosity, ϵ, defined as the fraction of the total volume of a porous medium represented by the voids in its matrix, is a primary controlling geometrical parameter. When a porous medium whose matrix is composed of discrete solid particles is confined in a duct, the wall of the duct affects the local magnitude of the porosity, because the spatial distribution of the particles must conform with the shape of the wall—this is the so-called the "wall effect." For the case of spherical particles contained in a circular cylinder, to which the present study is restricted, the porosity tends toward unity upon approach to the cylinder wall. Further, Roblee et al. [2] have observed that the local porosity near a confining cylindrical wall varies cyclically in a zone extending to three particle diameters from the wall into a bed of spheres of uniform diameter. Benenati and Brosilow [3] have reported that the zone, within which oscillations in local porosity occur, extends inward from a cylindrical wall a distance of approximately five spherical particle diameters. Within this annular "zone of the wall" the average porosity is greater than it is without; and hence, in the presence of a uniform pressure gradient, the average velocity of flow is higher within the zone than without—this effect is commonly referred to as "channeling." Clearly, the annular zone of the wall comprises an increasing fraction of the cross-sectional area of a cylinder as D/d decreases. Therefore, the influence of the wall upon the

Nomenclature

A = first Ergun constant for Forchheimer flow (asymptotic conditions
A' = first Ergun constant for turbulent flow (asymptotic conditions)
Aw = first Ergun-Riechelt parameter for Forchheimer flow
A'_w = first Ergun-Riechelt parameter for turbulent flow
B = second Ergun constant for Forchheimer flow (asymptotic conditions)
B' = second Ergun constant for turbulent flow (asymptotic conditions)
Bw = second Ergun-Riechelt parameter for Forchheimer flow
B'_w = second Ergun-Riechelt parameter for turbulent flow
d = diameter of sphere
D = diameter of cylindrical test section
f' = modified friction factor: $f' = \dfrac{d_p P'}{\rho v^2 \beta}$
f_w = wall-modified friction factor: $f_w = f'/M$
K = permeability
L = length of the test section
M = wall correction factor: $M = 1 = \dfrac{2}{3}\dfrac{d}{D(1-\epsilon)}$
n = number of data points
P' = negative of the pressure gradient
Re = Reynolds number: $\mathrm{Re} = \dfrac{dv}{\nu}$
Re′ = modified Reynolds number: $\mathrm{Re}' = \mathrm{Re}/(1-\epsilon)$
Re_w = wall modified Reynolds number: $\mathrm{Re}_w = \mathrm{Re}'/M$
R_h = hydraulic radius = void volume/wetted surface: $R_h = \epsilon/S$
S = total particle surface area per unit volume of bed
v = superficial velocity of fluid (volume rate of flow per unit area)
α = a parameter: $\alpha = (1-\epsilon)^2/\epsilon^3$
β = a parameter: $\beta = (1-\epsilon)/\epsilon^3$
ϵ = porosity
κ = Kozeny-Carman constant
μ = dynamic viscosity
ν = kinematic viscosity: $\nu = \omega/\beta$
ρ = density of fluid

Error Notation

E = percent error, $E = 100\,(Z_{\mathrm{cal}} - Z_{\mathrm{exp}})/Z_{\mathrm{exp}}$
$|E|$ = absolute percent error
E_m = percent mean error: $E_n = \sum_{i=1}^{n} E_i/n$
E_{md} = percent mean deviation error: $E_{\mathrm{md}} = \sum_{i=1}^{n} |E_i|/n$
E_{rms} = percent root mean square error: $E_{\mathrm{rms}} = \left(\sum_{i=1}^{n} E_i^2/n\right)^{1/2}$
E_{sd} = percent standard deviation of error: $E_{\mathrm{sd}} = \left\{\left[\left(\sum_{i=1}^{n} E_i^2\right) - \left(\sum_{i=1}^{n} E_i\right)^2/n\right]/(n-1)\right\}^{1/2}$
Z_{cal} = a calculated quantity
Z_{exp} = an experimentally determined quantity

flow (via channeling) becomes more significant as D/d progressively decreases. Schwartz and Smith [4] have reported that the velocity profile for gases flowing through a packed bed has a maximum value at approximately one particle diameter from a pipe wall, and that this maximum increases up to twice the centerline velocity as the dimension ratio decreases.

Fand et al. have reported that, for cylindrical ducts packed with spheres, the "wall effect" becomes significant for $D/d < 40$, and consequently the flow parameters become functionally dependent upon D/d for $D/d < 40$. The objectives of the present investigation were to determine the precise functional dependence of the flow parameters upon D/d for $D/d < 40$, and also to determine the influence, if any, of D/d upon the bounds of the Darcy, Forchheimer and turbulent regimes of flow for simple porous media.

Review of the Literature

Many investigators have studied the effect of the wall. Especially noteworthy among them are Carman [5], Metha and Hawly [6], and Riechelt [7].

Carman included in [5], as an appendix, a discussion of the porosity in pipes packed with spheres that is interesting and relevant to the present study. Clearly, since the effect of the wall upon porosity propagates inward several sphere diameters, the packing diverges progressively from being "random" with decreasing values of D/d. In fact, for $D/d \leq 2$, the porosity is completely determined by geometry. Carman derived the following formulas for ϵ:

$$\epsilon = \left[1 - \frac{2}{3}\left(\frac{d}{D}\right)^3 \Big/ \sqrt{\frac{2d}{D} - 1}\right] \quad \text{for } 1 < \frac{D}{d} \leq 1.866; \tag{5}$$

and

$$\epsilon = \left(1 - \frac{\sqrt{2}}{3}\right) = 0.528 \text{ for } \frac{D}{d} = 2. \tag{6}$$

The calculation of ϵ for values of D/d between 1.866 and 2 is very complex, and so Carman recommended that interpolation based on equations (5) and (6) be used to determine ϵ for $1.866 < D/d < 2$. To summarize, the packing is completely deterministic for sufficiently low values of D/d, and it only approaches a condition that is called "random" as D/d increases beyond measure (practically speaking, beyond 40).

In order to account for the wall effect, Metha and Hawley defined a hydraulic radius, R_H, as follows:

$$R_H = \frac{\epsilon d}{6(1-\epsilon)M}, \tag{7}$$

where

$$M = 1 + \frac{2}{3}\left[\frac{d}{D(1-\epsilon)}\right]. \tag{8}$$

Based on this definition, they derived the following modification of equation (4):

$$f' = \frac{A}{\mathrm{Re}'} M^2 + BM; \; A = 150, \; B = 1.75. \tag{9}$$

Metha and Hawley concluded that wall effects are not significant if the diameter ratio is greater than 50. Careful scrutiny of the experimental data obtained by Metha and Hawley indicates that this last conclusion is somewhat overly conservative, and that, in fact, wall effects are not significant if the diameter ratio is greater than 40, in agreement with the findings of Fand et al.

Riechelt further modified equation (9). He defined a wall-modified hydraulic radius,

$$R_{hw} = R_h / M, \tag{10}$$

which, when inserted into the defining equations for f' and Re', yield corresponding "wall-modified" parameters:

$$f_w = f'/M, \tag{11}$$

and

$$\mathrm{Re}_w = \mathrm{Re}'/M, \tag{12}$$

with which he obtained the following modification of equation (9):

$$f_w = \frac{A_w}{\mathrm{Re}_w} + B_w \tag{13}$$

or

$$f_w \mathrm{Re}_w = A_w + B_w \mathrm{Re}_w \tag{14}$$

Riechelt carried out experiments with spherical particles for dimension ratios between 1.73 and 14.32 and Re_w between 0.2 and 30000. For spherical particles, Riechelt determined A_w to be 150 and he concluded that the value of B_w can be calculated from the following empirical formula:

$$\frac{1}{\sqrt{B_w}} = \frac{1.5}{(D/d)^2} + 0.88. \tag{15}$$

The quantities A_w and B_w will be referred to hereinafter as the first and second Ergun-Riechelt parameters.

Table 2 Experimental values of geometric parameters

Ratio No.	D	d	L	ε	D/d
1	0.005588	3.994	1.0696	0.6168	1.399
2	0.005588	3.040	1.0696	0.5916	1.838
3	0.005588	2.067	1.0696	0.4593	2.704
4	0.01273	3.994	1.0700	0.4257	3.186
5.	0.01563	3.994	1.0700	0.4129	3.914
6	0.01273	3.040	1.0700	0.4029	4.186
7	0.01563	3.040	1.0700	0.3925	5.143
8	0.02672	3.994	1.0708	0.3861	6.690
9	0.02672	3.040	1.0708	0.3714	8.789
10	0.04104	3.994	1.0704	0.3731	10.27
11	0.04104	3.040	1.0704	0.3589	13.50
12*	0.0866	4.029	0.4572	0.3586	21.50
13*	0.0866	3.072	0.4572	0.3602	28.19
14*	0.0866	2.098	0.4572	0.3571	41.28

* From previous investigation by Fand et al.

Table 3 Uncertainties in experimental and derived variables at 20:1 odds

Experimental Variables	U	Derived Variables	U
v	2.0%	Re	2.0
ΔP*	2.0%	Re_w	2.0
ε	0.3%	f_w	4.7
d	0.1%	$f_w \mathrm{Re}_w$	5.1
D	0.1%	κ	4.8
L	0.1%	A_w, A'_w	3.2
ρ	0.1%	B_w, B'_w	4.0

*Pressure drop across test section whose length is L

Table 4 Experimentally determined values of flow parameters

Ratio No.	D/d	κ	A_w	B_w	A'_w	B'_w
1	1.399	4.76	104	0.750	108	0.567
2	1.838	4.79	105	0.821	107	0.746
3	2.704	4.82	107	1.08	120	0.852
4	3.186	4.84	111	1.18	126	0.943
5	3.914	4.92	113	1.23	129	0.961
6	4.186	4.89	118	1.25	132	0.980
7	5.143	4.94	116	1.35	149	1.08
8	6.690	5.04	134	1.25	175	1.10
9	8.789	5.12	144	1.52	175	1.25
10	10.27	5.09	144	1.59	196	1.28
11	13.50	5.14	148	1.59	185	1.35
12*	21.49	5.12	158	1.73	197	1.47
13*	28.19	5.28	165	1.83	203	1.58
14*	41.28	5.33	173	1.87	215	1.57

*From previous investigation by Fand et al.

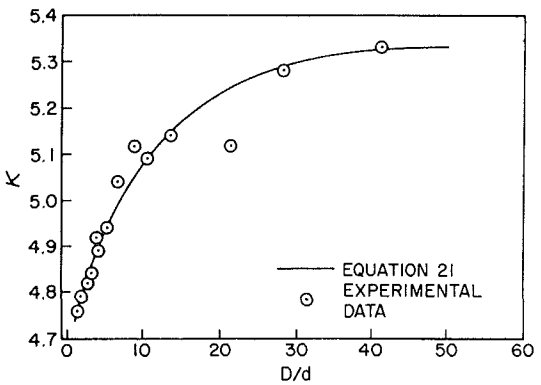

Fig. 1 Kozeny-Carman constant as a function of the dimension ratio

Experimental Apparatus and Procedure

The experimental apparatus employed in the present study consisted of a precision-built stainless steel water tunnel into which were incorporated a series of interchangeable circular cylindrical test sections that were packed with glass spheres. The apparatus and general procedures employed were identical with those described in detail in the previous publication by Fand et al. except for a change (increase) in the lengths of the packed test sections and variations in D/d. Eleven different values of D/d were used in the present study, ranging from 1.4 to 13.5. The length-to-diameter ratios of the test sections ranged from a minimum of 27 to a maximum of 191, thereby, it is believed, rendering entrance effects negligible. Table 2 lists the experimental values of the geometric parameters.

A test consisted of a set of simultaneous steady state measurements of water temperature and velocity, plus the pressure drop across the entire test section, for which the porosity was determined by weighing and computing the volume of the glass spheres comprising the packing. For low rates of flow, a gravity feed system was used and the velocity was determined by weighing the effluent of water collected during a measured interval of time. For high flow rates, the water was pumped through the tunnel loop and its flow rate was measured by means of calibrated orifices. A total of 718 tests were performed in the range $0.62 \leq \mathrm{Re} \leq 869$. The uncertainties in the experimentally measured and derived variables at 20:1 odds are listed in Table 3.

The packings that were employed in the present study were achieved by randomly dropping small batches of dry spheres into lengths of dry pipe that were held vertical during the packing process. Further, the packings that were studied were "stable," where the adjective stable implies that the flow parameters for the packing *remain unchanged* after the packing had been subjected to the maximum pressure gradients that were employed in the study. Whether a particular packing satisfied this criterion was determined by checking whether its measured Darcy permeability was unaltered after the packing had been subjected to the highest attainable turbulent flow rates. Stable packings were achieved by subjecting the pipes to repeated small shocks by tapping the pipes with a metal rod during the packing process.

Table 5 Asymptotic values and correlation constants to be used in conjunction with equation (21)

Y	Y_∞	a	p	q	r
κ	5.340	0.6545	0	0	0.09034
A_W	172.9	82.18	0.0001125	-0.003931	0.1314
B_W	1.871	1.636	0.0004908	-0.01665	0.2925
A'_W	213.7	129.7	0.00003852	-0.003376	0.1510
B'_W	1.569	1.350	0.0003688	-0.01465	0.2646

Table 6 Error-analysis of correlation equations for flow parameters

Parameter	E_m	E_{md}	E_{rms}	E_{sd}
κ	-0.1	0.5	0.9	0.5
A_w	2.8	3.2	4.2	3.0
B_w	1.6	3.0	5.0	4.6
B'_w	0.3	3.9	5.2	5.1
B'_w	0.5	2.5	3.6	3.4

Experimental Results

For each experimental value of D/d, three types of flow were identified: Darcy flow, characterized by equation (1) and the single flow parameter, κ; Forchheimer flow, characterized by equation (14) and the two flow parameters, A_w and B_w; and turbulent flow, characterized by the same equation as is Forchheimer flow but for which the flow parameters are denoted by A'_w and B'_w. The bounds for these three types of flow were found to be identical with those observed by Fand et al. in the previous study and are listed in Table 1. The experimentally determined values of the flow parameters, obtained by linear regression analysis of the data based upon equations (1) and (14), are listed in Table 4.

Analysis of Results

Correlation Equations for Flow Parameters. The experimentally determined values of each of the five flow parameters listed in Table 4 were plotted versus D/d as shown, by way of example, in Fig. 1 for κ. All five plots exhibited the same general pattern, which, it was found, could be represented by correlation equations having the following common form:

$$Y = Y_\infty - ae^{-f(D/d)} \tag{16}$$

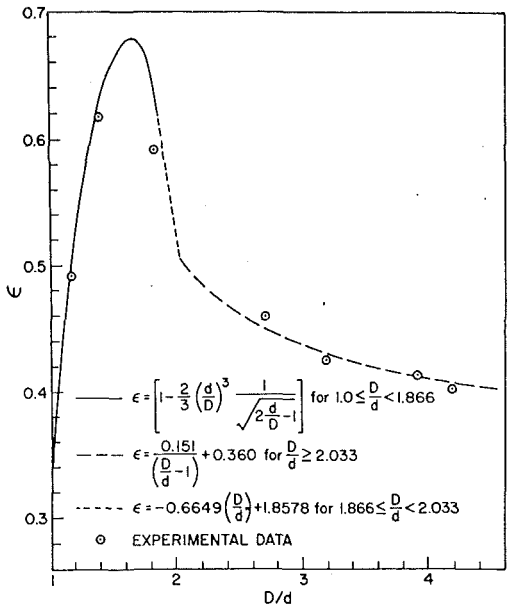

Fig. 2 Porosity as a function of the dimension ratio

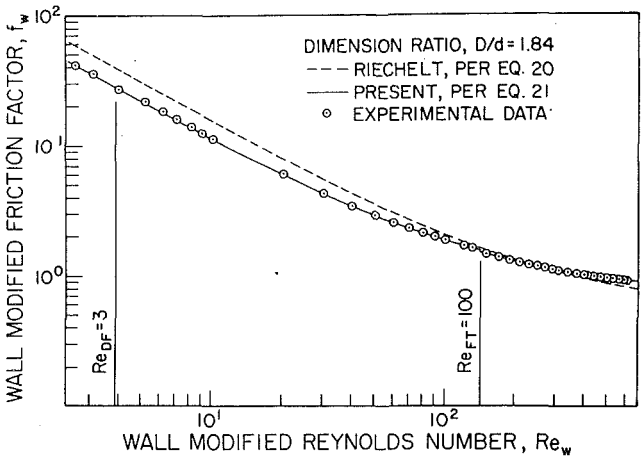

Fig. 3 Comparison of present results with those of Riechelt

where Y represents a parameter whose asymptotic value is Y_∞, $f(D/d) = p(D/d)^3 + q(D/d)^2 + r(D/d)$ and a, p, q, r are numerical correlation constants. The values of Y_∞ and the correlation constants for all five flow parameters are listed in Table 5. Figure 1 includes a graph of κ calculated per equation (16), in order to demonstrate visually the degree to which equation (16) typically represents the experimentally measured values of the flow parameters.

Table 6 exhibits the errors incurred by equation (16) vis-a-vis the experimental data. The mean deviation is less than 4 percent in every case.

Correlation Equation for Porosity. The experimentally determined values of the 14 values of ϵ listed in Table 2, plus two additional values obtained at $D/d = 1.16$ and $D/d = 1.84$, were plotted versus D/d. Figure 2 is a reproduction of this plot for D/d up to approximately 4. A graph of Carman's equations (5) and (6), with linear interpolation between, is indicated in Fig. 2 for purposes of comparison with the experimental data (for $D/d < 2$). For values of $D/d \ge 2$ (more precisely, for $D/d \ge 2.033$), it was found that the experimentally determined values of ϵ could be correlated by the following equation of a hyperbola:

$$\epsilon = \frac{0.151}{(D/d-1)} + 0.360;\ D/d \ge 2.033. \qquad (17)$$

This hyperbola intersects the linear portion of Carman's representation at $D/d = 2.033$; thus, Carman's equations together with equation (17) provide a continuous analytical representation of ϵ for all D/d. The errors incurred by using these analytical expressions to represent ϵ are less than 2.4 percent for all but two experimental data points.

Conclusions

The correlation equations developed in the present study provide means whereby the porosity and the pressure gradient (as a function of velocity) can be calculated for fluid flow through pipes packed with spheres of uniform diameter for $D/d \ge 1.4$. The existence of Darcy, Forchheimer and turbulent flow was verified. The ranges of the Reynolds number within which these three types of flow occur have been determined to be identical with those found in the previous study by Fand et al.

The correlations equations presented herein represent the experimental data with greater accuracy than can be achieved with previously published equations—this conclusion is substantiated by the curves in Fig. 3, which provides a comparison of the present results with those of Riechelt. It is worth mentioning that Riechelt did not identify three different flow regimes, as was done here.

Some preliminary experimental data were obtained for a value of D/d substantially lower ($D/d = 1.16$) than the minimum value ($D/d = 1.4$) investigated here. These preliminary results indicate that the correlations equations for the flow parameters presented here, per equation (16), should not be extrapolated to values below $D/d = 1.4$. Further, a preliminary test employing a complex medium revealed that the results obtained in the present study using simple media cannot be applied directly to complex media, as has been shown to be feasible in the asymptotic case, by simply using the mean harmonic diameter of the packing. The wall effect in the presence of complex media represents a more complex problem.

Acknowledgment

Sunil K. Sinha assisted with the performance of calculations.

References

1 Fand, R. M., Kim, B. Y. K., Lam, A. C. C., and Phan, R. T., "Resistance to the Flow of Fluids Through Simple and Complex Porous Media Whose Matrices Are Composed of Randomly Packed Spheres," ASME JOURNAL OF FLUIDS ENGINEERING, Vol. 109, 1987, pp. 268-274.

2 Roblee, L. H. S., Baird, R. M., and Tierney, J. W., "Radial Porosity Variations in Packed Beds," *A.I.Ch.E.J.*, Vol. 4, No. 4, 1958, pp. 460-464.

3 Benenati, R. F., and Brosilow, C. B., "Void Fraction Distribution in Beds of Spheres," *A.I.Ch.E.J.*, Vol. 8, No. 3, 1962, pp. 359-351.

4 Schwartz, C. E., and Smith, J. M., "Flow Distribution in Packed Beds," *Ind. and Eng. Chem.*, Vol. 45, No. 4, 1953, pp. 1209-1218.

5 Carman, P. C., "Fluid Flow Through Grannular Beds," *Trans. Inst. Chem. Engg.*, London, Vol. 15, 1937, p. 150.

6 Metha, D., and Hawley, M. C., "Wall Effect in Packed Columns," *I & EC Process Design and Development*, Vol. 8, No. 2, 1969, pp. 280-282.

7 Riechelt, W., "Zur Berechmeng des Druckverlustes einphasig durchstromter Kuger-ung Zyhnderschuthungen," *Chemie. Ing. Tech.*, Vol. 44, No. 18, 1972.

S. K. Wang

S. J. Lee

O. C. Jones, Jr.

R. T. Lahey, Jr.

Department of Nuclear Engineering,
& Engineering Physics,
Rensselaer Polytechnic Institute,
Troy, NY 12180-3590

Statistical Analysis of Turbulent Two-Phase Pipe Flow

The statistical characteristics of turbulent two-phase pipe flow have been evaluated. In particular, the autocorrelation functions and the power spectral density functions of the axial turbulence fluctuations in the liquid phase were determined. The high frequency content of the power spectrum in bubbly two-phase pipe flow was found to be significantly larger than in single-phase pipe flow and, in agreement with previous studies of homogeneous two-phase flows (Lance et al., 1983), diminished asymptotically with a characteristic −8/3 slope at high frequency. The power spectrum and the autocorrelation functions in two-phase pipe flow, although distinctively different from those in single-phase pipe flow, were insensitive to the local void fraction and the mean liquid velocity when plotted against wave number and spatial separation, respectively. Finally, the dissipation scale, determined from the shape of the autocorrelation function, indicated that the turbulent dissipation rate in two-phase pipe flow was significantly greater than that in single-phase pipe flow.

Introduction

As more accurate and detailed numerical simulations are required for two-phase flows, multidimensional two-fluid modeling is becoming widely used. However, in two-fluid models, the interfacial and wall transfer laws, and the turbulent structure must be constituted to achieve closure. Unfortunately, in vapor/liquid two-phase systems, the turbulent structure is more complicated than in single-phase flow because of the interaction between interface and the turbulence in the continuous phase.

Realistic modeling of two-phase turbulence calls for a thorough understanding of its structure. According to the current understanding of turbulence, eddies are initially evolved from the strain in the mean flow field. The well-known turbulent "bursts" near rigid boundaries is a typical strain-related production mechanism. Once large eddies are created, they start to break-up into smaller eddies, transferring turbulent kinetic energy through the eddy-size spectrum, from bigger to smaller eddies, until they are dissipated into heat.

In bubbly two-phase flow, the dispersed phase tends to break-up the large eddies and creates smaller eddies in bubble's wakes. Moreover, buoyancy creates high strain regions around the bubble's interface, generating an additional source of small eddies. In contrast, the vapor/liquid interface can absorb some of the energy of the eddies which impact it (Serizawa, 1988). Thus, measuring the space/time correlation of the turbulent field of the continuous phase can help reveal the structure and dynamics of turbulence in two-phase flows and may aid in the development of a more realistic model of the turbulence transport process.

It can be noted in Fig. 1 that when an intrusive probe encounters the disperse phase (i.e., the gas bubbles) the signal representing the turbulence of the continuous phase is lost. Indeed, as will be discussed subsequently, the data from t_A to t_D must be discarded. Thus, a controversy on the spectral analysis of two-phase flow signals arises concerning how to treat the discontinuity in the data of the continuous (i.e., liquid) phase. Various methods have been proposed. Gherson et al. (1984) simply patched together the liquid-phase segments of the signal. Tsuji et al. (1984) interpolated linearly the missing signal due to the voids, while Lance (1979) and Lee (1982) inserted the liquid mean velocity into the data gaps.

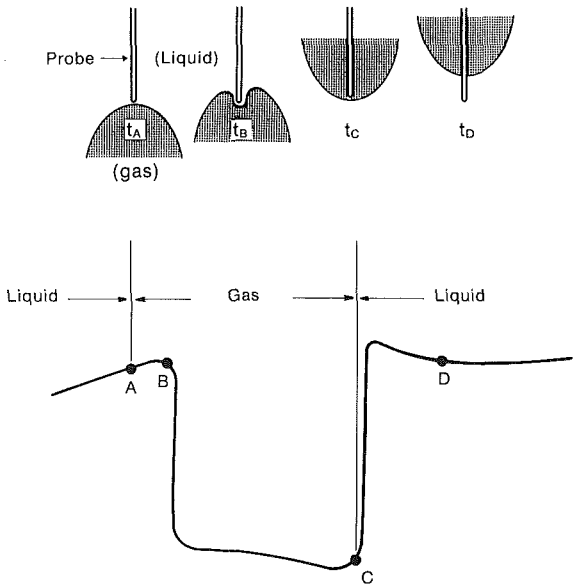

Fig. 1 Schematic of bubble passage and probe response

Contributed by the Fluids Engineering Division for publication in the JOURNAL OF FLUIDS ENGINEERING. Manuscript received by the Fluids Engineering Division September 22, 1986.

Unfortunately, all of these methods inevitably distort the "true" turbulence spectrum of the continuous phase. Thus, because of the inherent nature of the problem we must estimate the turbulence spectrum from a discontinuous set of time histories. The method of replacing the void signal with the known mean value is preferred because, as will be shown later, the effect of this operation on the true spectrum can be analyzed.

It should be noted that Lance et al. (1989) have recently proposed that, in addition to inserting the mean value into the gaps, a sequence of smoothing windows be applied to each segment of liquid phase signal to minimize the distortion of the "true" spectrum. This approach was not adopted in this paper because such operations do not allow one to easily analyze the effect on the "true" spectrum.

Lance et al. (1983) used both hot-film and Laser Doppler Anemometry (LDA) to measure homogeneous grid generated turbulence in bubbly two-phase flow. They observed that the one-dimensional spectra did not exhibit the classical $-5/3$ law at high frequencies, but rather had an extended high frequency region which followed a $-8/3$ law. They also observed that the autocorrelation of the two-phase signal was insensitive to variation of void fraction, at least for low void fractions which they tested. Moreover, the dependence of their correlation functions on the axial liquid mean velocity U_L could be removed by replotting as a function of $U_L\tau$ instead of τ. This implies that if Taylor's hypothesis of a frozen turbulence field was applicable, the axial space correlation is independent of the void fraction and the liquid mean velocity.

In this paper, many of these findings were found to also be valid for wall generated turbulence in two-phase pipe flow. In addition, the dissipation length scale and the Kolmogoroff scale were estimated for two-phase pipe flow from the measured autocorrelation functions.

Discussion

Summary of the Experiment. The test section used in this experiment was a 2-1/4 in. (57mm) inside diameter plexiglass pipe. Air was injected through a specially designed mixing tee at the bottom of the vertical test section. At a length of approximately thirty-five pipe diameters above the mixing tee, a hot-film anemometer probe and a pitot tube were mounted at positions 90 deg apart. The hot-film anemometer was calibrated against the pitot tube reading in single-phase flow. This calibration curve was used to determine the instantaneous velocity sensed by the hot-film element when the probe was in liquid phase of the bubbly two-phase flows.

The significantly lower signal level sensed when the probe was in the gas phase and was used to discriminate liquid-phase and gas-phase signals. The instantaneous axial liquid-phase velocity was recorded at various radial positions using a single-sensor cylindrical probe (TSI-1218-20W) for 16 different combinations of water flow rates (j_L = 0.41, 0.71, 0.94, 1.08 m/s) and air flow rates (j_G = 0.0, 0.10, 0.27, 0.40 m/s). A thorough description of the test loop has been given previously (Wang et al., 1987) and thus will not be repeated here.

Signal Processing. The anemometer's signal was sampled at 10 KHz using an A/D converter and the result was fed into a VAX-750 digital computer for processing. After the anemometer signal was digitized and stored in computer memory, the data reduction was performed using a set of FORTRAN programs. These data reduction programs perform basically two tasks: to recognize and separate out segments of the signal corresponding to the liquid phase, and then to compute the flow parameters of interest from the liquid phase data. This section is concerned with the former task. First, we will discuss how voids show up in the anemometer output signal. Then the computer algorithm used to automate the signal processing will be described.

Figure 1 is a schematic of a typical signal and a schematic of the corresponding position of the bubble with respect to the probe. This figure is similar to that observed by Delhaye (1969) using high speed photography. At time t_A, the bubble interface reaches the sensor element on the probe. However, due to surface tension, the interface deforms around the probe and penetration does not occur until time t_B, at which point the signal drops rapidly. At time t_C, the rear interface of the bubble makes contact with the sensor. Although data points in time interval $t_D - t_C$ belong to the liquid phase, they should be excluded in computing liquid phase flow parameters because they are strongly influenced by the thermal inertia of the sensor's substrate, and thus do not represent realistic liquid-phase velocities. Visual examination of the signal of the probe indicated that after about 2 ms the spurious signal returns to the level of the liquid phase. Thus, we assumed in this study that $t_D \cong t_C + 2$ ms.

From Fig. 1, it is clear that the gas phase spans an interval of time form t_A to t_C. Unfortunately, sharp changes in the signal occur only at t_B and t_C; thus time t_A must be estimated using other methods. The phase determination algorithm described herein used t_B and t_C to compute the local void fraction. Therefore, it is expected to predict lower void fraction than the actual value. This signal was later corrected using a gamma-densitometer standard as described by Wang et al. (1984). In this way the time interval, $t_B - t_A$, was implicitly determined.

The data sampling rate, 10 KHz, was found to be sufficient to resolve rapid variation of the signal during phase changes.

Basically, the phase discrimination algorithm consists of various sets of tests to be applied to the signal to decide whether to switch from one phase to the other. When in the liquid phase, any one of the following three conditions caused a switch to the gas phase:

(1) A data sample point falls below a specified level threshold.
(2) A data sample point dropped by more than twice the slope threshold times Δt.
(3) Two consecutive drops in data points are each greater than the slope threshold times Δt.

Having determined that a change in phase has occurred, the point which initiated the change is stored. Usually the second and the third criteria detect t_B precisely. However, rare, but

Nomenclature

E_{11} = power spectral density function
f = longitudinal correlation function
f = frequency
R_{11} = autocorrelation function
j = volumetric flux
t = time
z = distance (spatial separation)
R = radius of pipe
U = mean axial velocity
U = Fourier transform of u'
u' = fluctuating component of velocity
$(u')^2$ = mean axial turbulent fluctuations squared
u^* = friction velocity
X = phase indicator function
y = distance from the wall
α = local void fraction
α_c = void fraction at the centerline of the pipe
ϵ = dissipation rate
ν = kinematic viscosity
ν = Kolmogoroff length scale
λ = dissipation length scale
χ_L = Fourier transform of X_L

Subscripts

G = gas phase
L = liquid phase

otherwise catastrophic, failure of the slope thresholding criteria will immediately be corrected by the less precise level thresholding criterion.

When in the gas phase, the gas-to-liquid phase transition is triggered when either:

(1) The data point rises by more than the slope threshold times Δt.

(2) The probe has been in gas phase for more than 2 ms and the data sample point is above the level threshold. (This value of 2 ms is not expected to be universal, but has sufficed for our experiments.)

The gas-to-liquid transition is followed by the probe rewetting transient period ($t_D - t_C$), during which the signal does not reflect realistic liquid-phase parameters.

Spectral Analysis of the Segmented Signal. In two-phase flow, the liquid-phase signal is frequently interrupted by void passages. Hence, as discussed previously, we must process a segmented signal since data is not available between each segment. Any attempt to interpolate the data in these gaps produces artificial components in the power spectrum. For simplicity, we inserted the liquid-phase mean velocity signal into the missing segments. This method has the merit that we know the exact implication of zero insertion on the "true" power spectrum.

That is, inserting the mean value into the missing segments is equivalent to applying a rectangular window to the "true" continuous data. Note that this window function is identical to the local liquid phase indicator function, $X_L(t)$, where:

$$X_L(t) = \begin{cases} 1.0, \text{ when the probe is in the liquid phase at time, } t. \\ 0.0, \text{ otherwise.} \end{cases} \quad (1)$$

Recalling that multiplication by the window function in time domain is equivalent to convolution of the window function in frequency domain, the power spectrum of the two-phase liquid-phase velocity is given by:

$$E_{11}(f) = \lim_{T\to\infty} 1/T\left(\int_0^T u_L'(t)X_L(t)\exp(-j2\pi ft)dt\right)^* \times \left(\int_0^T u_L'(t)X_L(t)\exp(-j2\pi ft)dt\right) \quad (2)$$

or,

$$E_{11}(f) = \lim_{T\to\infty} 1/T[U_L(f,T)\chi_L(f,T)]^*[U(f,T)\chi_L(f,T)] \quad (3)$$

where U_L (f, T) and $\chi_L(f, T)$ are finite Fourier transforms of $u_L'(t)$ and $X_L(t)$, respectively. Thus, the effect of mean value insertion is to smooth the "true" power spectrum by convoluting the finite Fourier transform of the "true" signal with the finite Fourier transform of the liquid phase indicator function. Figure 2 shows power spectra of the liquid phase indicator functions ($X_L(t)$) for two different local void fractions, 24 and 6.3 percent. Since the mean value has not been removed from the phase indicator function, the power spectra are characterized by a single spike at the origin, reflecting the nonzero mean value. The spike is superimposed on a relatively broad band which tapers off starting at about 300 Hz. The slope of these curves for higher frequencies is about -1.82.

Clearly, for the limiting case of single-phase flow, the power spectra of the (constant) liquid phase indicator function would be a delta function at the origin. Convoluting the power spectrum of the single-phase turbulence signal with this delta function does not alter the original power spectrum. On the other hand, as shown in Fig. 2, the amount of interruption of the signal due to voids increases the amplitude of the broad band region of the power spectrum of the phase-indicator function. When this phase indicator power spectrum is convoluted with

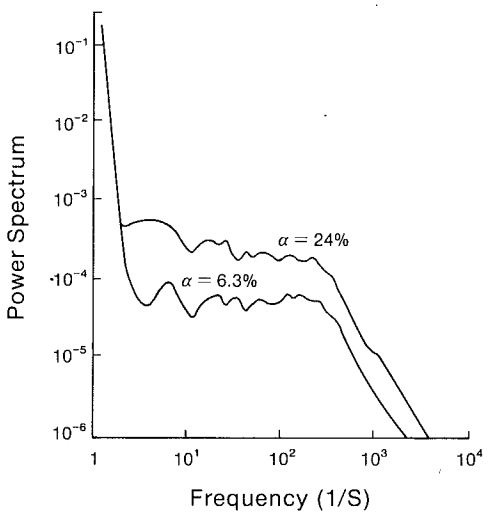

Fig. 2 Power spectrum of the liquid phase indicator function, $X_L(t)$

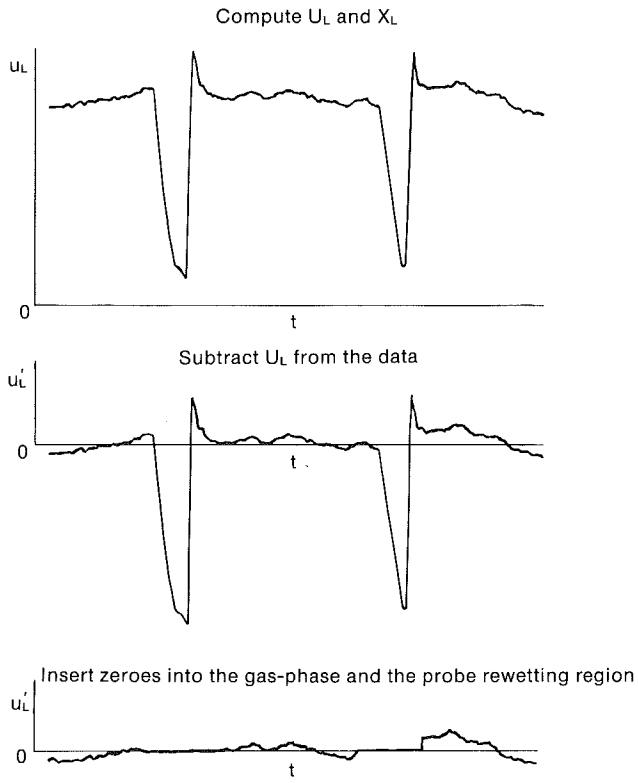

Fig. 3 Schematic of the two-phase data processing prior to Fourier transformation

the true turbulence power spectrum, the actual shape of the power spectrum is lost due to the averaging process. Thus, we expect some distortion of power spectral density results, particularly for high void fraction two-phase flows.

Figure 3 is the schematic of the mean value insertion process employed to compute the estimated power spectrum of the liquid phase fluctuating axial velocity (u_L') for two-phase pipe flow. First, the phase discrimination algorithm was applied on the data to obtain the mean liquid velocity (U_L) and the liquid phase indicator function (X_L). Next, the mean liquid velocity was subtracted from the data. Then, the resulting data was masked with the phase indicator function by inserting zeros into the missing parts. Lastly, a digital signal processing program was used to calculate the autocorrelation functions and the power spectrum for the turbulent two-phase flow data.

The Fast Fourier Transform (FFT) algorithm used in this

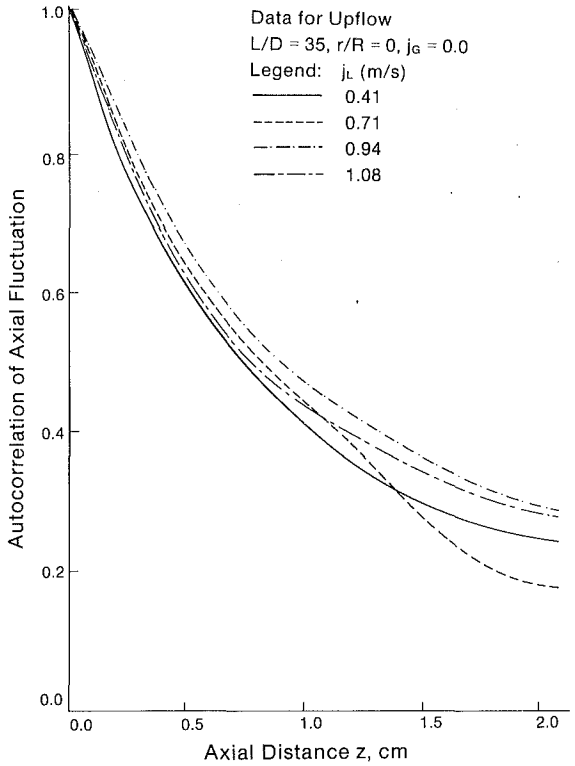

Fig. 4 Axial correlation at centerline (single-phase liquid)

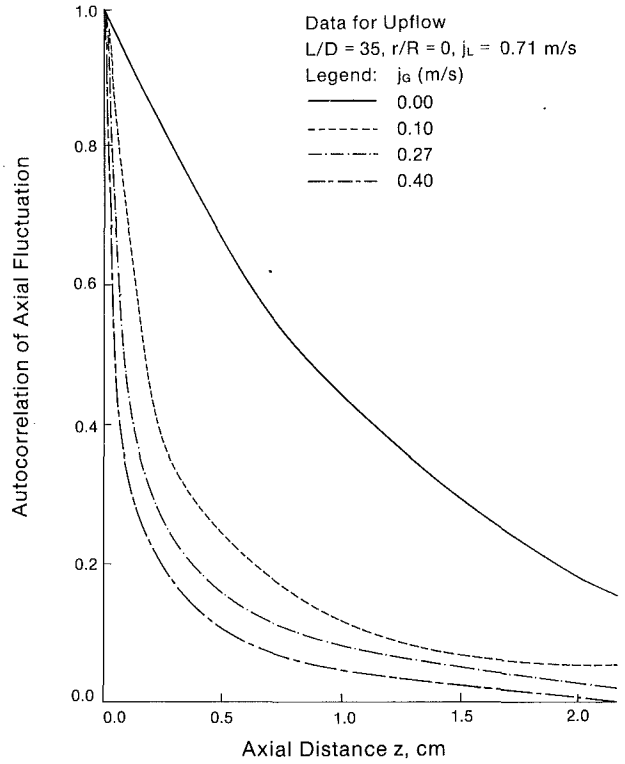

Fig. 5 Axial correlation at centerline

study gave good frequency resolution between 2 Hz and 500 Hz for each 256 point data record processed. Twenty such records were then ensemble averaged to obtain statistically stationary estimate of the power spectrum.

Results

Autocorrelation Functions. In this study, the time correlation function, $\overline{u_L'(t_0)u_L'(t_0-t)}$, was related to the spatial correlation function, $\overline{u_L'(z_0)u_L'(z_0-z)}$, assuming Taylor's "frozen" field hypothesis (Hinze, 1976). That is,

$$f(z)=R_{11}(t); \qquad z=U_L t$$

where,

$$f(z)=\frac{\overline{u_L'(z_0)u_L'(z_0-z)}}{\overline{(u_L')^2}} \tag{4}$$

is the axial correlation coefficient, and,

$$R_{11}(t)=\frac{\overline{u_L'(t_0)u_L'(t_0-t)}}{\overline{(u_L')^2}} \tag{5}$$

is the autocorrelation coefficient.

As shown in Fig. 4, for single-phase liquid flows, this transformation eliminated the dependency of the correlation function on the mean velocity. The axial correlation function changed significantly when voids were introduced into the flow. However, as shown in Fig. 5, the two-phase axial correlation function is insensitive to void fraction. Indeed, it appears there is an abrupt transition in the basic structure of the turbulence of the continuous phase when going from single-phase to two-phase flow. Although not shown, the two-phase turbulence structure was also insensitive to the mean liquid-phase velocity.

The autocorrelation function for two-phase flow has a sharper drop near the origin. This indicates a much shorter distance over which the turbulence correlates. Apparently it is the relatively smaller eddies, which are characteristic of two-phase flow, that are responsible for this shorter correlation distance. Since the curvature at the origin is also related to the dissipation scale, it will be shown that two-phase flow has a higher dissipation rate than corresponding single-phase flows.

The Power Spectrum. Figure 6 shows the normalized power spectrum of the liquid phase turbulence for two-phase pipe flows of various void content. The spectrum is much flatter than for single-phase flows. Analogous to the well-known $-5/3$ slope in the high frequency region of the single-phase flow spectrum, a $-8/3$ slope appeared to fit our two-phase pipe flow data quite well in high frequency range. Interestingly, this same frequency dependence was also found by Lance (1979) for homogeneous turbulence. Also, the spectrum were insensitive to the actual void content except in the low frequency region where flows with high void content exhibited lower amplitude.

Thus it appears that, unlike in single-phase flows where much of the turbulent kinetic energy is contained in large eddies, in two-phase flows an appreciable fraction of the energy is associated with small eddies. This implies that turbulence models having a single set of velocity and length scales should not work well for two-phase flows. One obvious alternative would be to divide the spectral range into large and small scales and use two sets of velocity and length scales to characterize the dynamics of the different scale turbulence.

Turbulence Length Scales and Turbulent Kinetic Energy Dissipation Rate. As previously discussed by Hinze (1976), the turbulent kinetic energy dissipation rate is closely related to the axial dissipation length scale, λ_L. For example, for isotropic turbulence:

$$\epsilon_L=30\nu_L\frac{\overline{(u_L')^2}}{\lambda_L^2} \tag{6}$$

where ϵ_L is the dissipation rate of turbulent kinetic energy.

The dissipation length scale, λ_L, is defined from the following relationship:

$$\frac{U_L^2}{\lambda_L^2}=-\frac{1}{2}\left[\frac{d^2R_{11}(t)}{dt^2}\right]_{t=0} \tag{7}$$

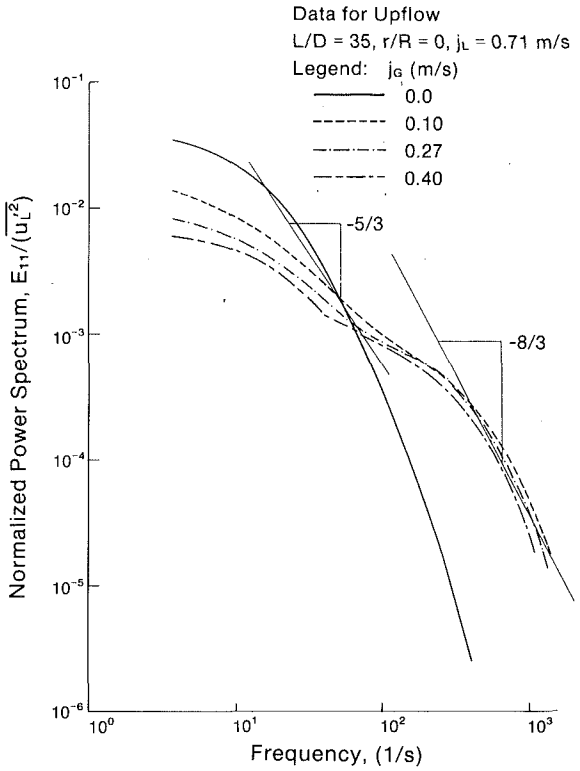

Fig. 6 Two-phase power spectrum

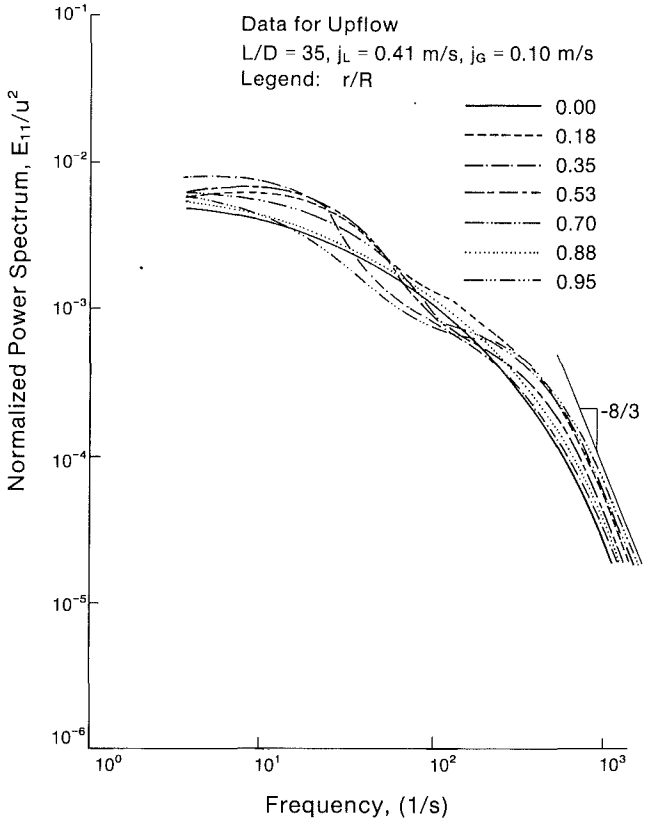

Fig. 7 Two-phase power spectrum at different radial position

Several methods have been reported to measure the length scale, λ_L. Townsend (1947) proposed that λ_L be computed from the following relation:

$$\overline{\left(\frac{\partial u_L'}{\partial t}\right)^2} = U_L^2 \overline{\left(\frac{\partial u_L'}{\partial x}\right)^2} = U_L^2 \frac{\overline{(u_L')^2}}{\lambda_L^2} \tag{8}$$

Liepmann (1951) employed an oscillograph trace and counted the zero crossings of the axial fluctuations. From these crossings λ_L was calculated by assuming a normal and independent distribution for both u_L' and $\frac{\partial u_L'}{\partial x}$. This procedure resulted in:

$$\frac{1}{\lambda_L} = \frac{\pi}{U_L} \times \left[\begin{array}{c}\text{average number of zeros} \\ \text{of } u_L' \text{ per second}\end{array}\right] \tag{9}$$

For convenience, in this study the axial length scale, λ_L, of the current data was evaluated from the autocorrelation of the axial fluctuations. For isotropic turbulence, λ_L can be expressed as (Hinze, 1976):

$$\frac{1}{\lambda_L^2} = -\frac{1}{2}\left(\frac{\partial^2 f}{\partial z^2}\right)_0 \tag{10}$$

where $\left(\frac{\partial^2 f}{\partial z^2}\right)_0$ is the value of second derivative of the axial correlation function at $z = 0$. Using Taylor's expansion, the derivative term can be approximated by (Hinze, 1976):

$$\left(\frac{\partial^2 f}{\partial z^2}\right)_0 \cong -2 \lim_{z\to 0}\left(\frac{1-f(z)}{z^2}\right) \tag{11}$$

Thus, if f can be approximated by a parabola, the intersection of the parabola and the abscissa will be the length scale, λ_L. That is, $f(z)$ and λ_L are related by,

$$f(z) = 1 - \frac{z^2}{\lambda_L^2} \tag{12}$$

Unfortunately, the value of λ_L depends on the position where the data are fitted, thus it is very difficult to determine λ_L by fitting a parabola to the data. Since the autocorrelation and the PSD are Fourier transfer pairs, we obtain:

$$E_{11}(f) = \overline{4(u_L')^2}\int_0^\infty R_{11}(t)\mathrm{Cos}(2\pi f t)\,dt \tag{13}$$

and inverse transform yields,

$$R_{11}(t) = \frac{1}{\overline{(u_L')^2}}\int_0^\infty E_{11}(f)\mathrm{Cos}(2\pi f t)\,dn \tag{14}$$

We can relate the autocorrelation function, $R_{11}(t)$, to the axial correlation, $f(z)$, using Taylor's hypothesis. Thus equation (14) becomes,

$$f(z) = \frac{1}{\overline{(u_L')^2}}\int_0^\infty E_{11}(f)\mathrm{Cos}\left(\frac{2\pi f z}{U_L}\right)df \tag{15}$$

If we take the second derivative of $f(z)$ at $z=0$, equation (15) yields,

$$\left(\frac{\partial^2 f}{\partial z^2}\right)_0 = \frac{-4\pi^2}{\overline{(u_L')^2}}\left[\frac{1}{U_L^2}\int_0^\infty f^2 E_{11}(f)\,df\right] \tag{16}$$

Combining equations (10) and (16), the dissipation length scale, λ_L, can be expressed as,

$$\frac{1}{\lambda_L^2} = \frac{2\pi^2}{\overline{(u_L')^2}}\left[\frac{1}{U_L^2}\int_0^\infty f^2 E_{11}(f)\,df\right] \tag{17}$$

For convenience, equation (17), which is the same result obtained previously by Hinze (1976), was used in this study to calculate λ_L. While the dissipation length scales and dissipation rates presented herein are not completely accurate for pipe flows, they do provide realistic trends concerning the effect of the dispersed phase on dissipation. Moreover, equation (17) was only used near the centerline of the pipe where the turbulence was found to be nearly isotropic (Wang et al., 1987).

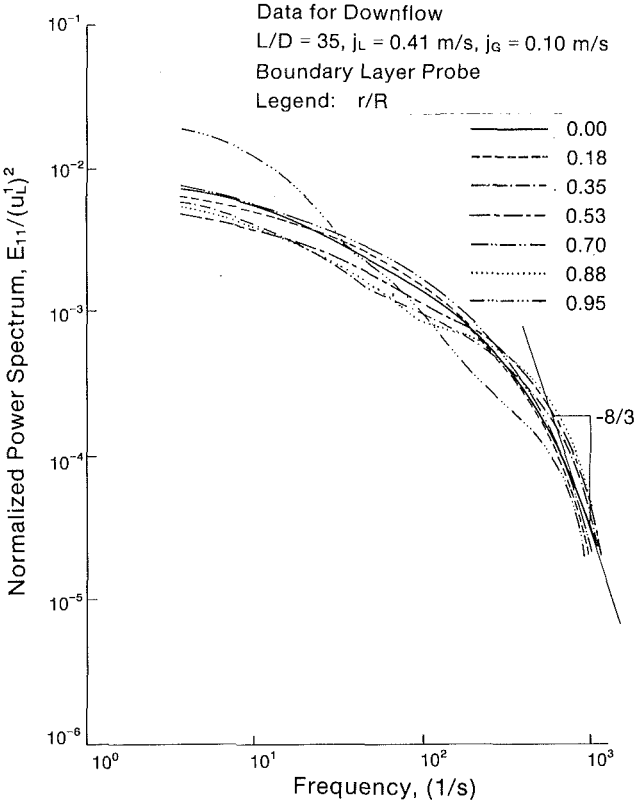

Fig. 8 Two-phase power spectrum at different radial positions

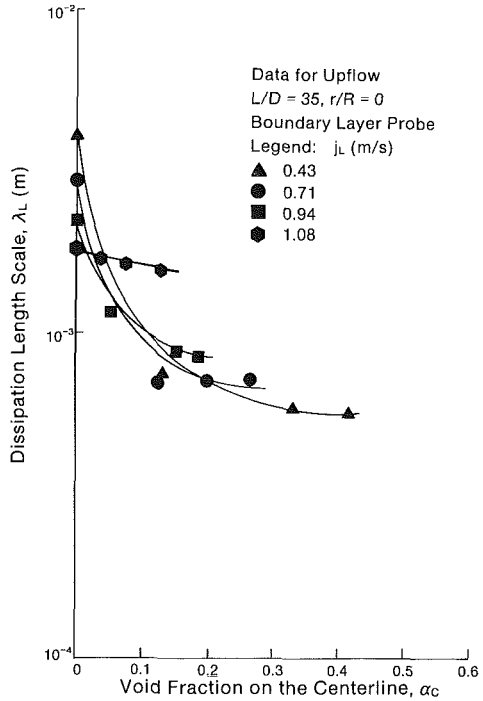

Fig. 9 Dissipation length scale

The results are shown in Fig. 9 and where α_c is the void fraction on the centerline. In two-phase bubbly flow, the bubbles apparently interact with the liquid eddies which causes more dissipation. That is, the dissipation length scale was always smaller in two-phase flow than in single-phase flow. As a result, Fig. 10 shows that the dissipation rate at the centerline of the pipe, calculated using equation (6), was always higher in two-phase flow than in single-phase flow.

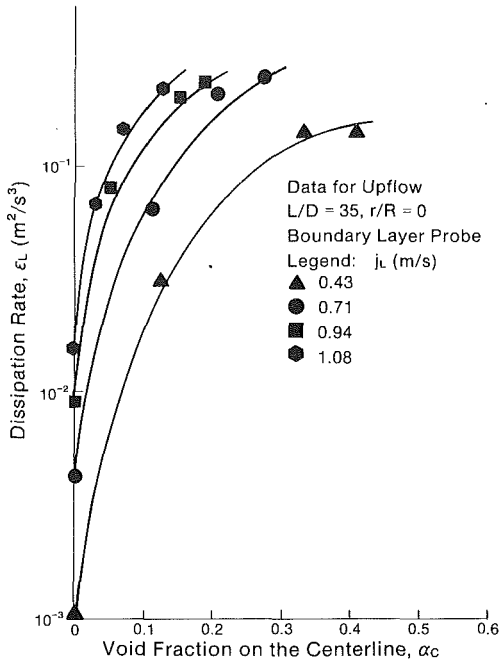

Fig. 10 Dissipation rate of turbulent kinetic energy

The dissipation length scale, λ_L, estimated in this research was also compared with the results of other investigators. Afzal (1982) studied single-phase turbulence in a pipe and presented a semi-empirical equation for the length scale, λ_L:

$$\lambda_L = \left\{ 30\nu_L \frac{\overline{(u_L')^2}R}{u_L^{*3}\left(\frac{2.44}{y/R} - 0.24\right)} \right\}^{1/2} \tag{18}$$

As can be seen in Fig. 11, the agreement is very good between the single-phase dissipation length scale calculated using equation (17) and equation (18).

Finally, let us consider the so-called Kolmogoroff scale, η_L. This scale is defined as,

$$\eta_L \triangleq (\nu_L^3/\epsilon_L)^{1/4} \tag{19}$$

The Kolmogoroff scale may be considered to be a measure of the smallest eddies responsible for the dissipation of turbulent kinetic energy. This parameter was also calculated for our data and is shown in Fig. 12. Interestingly, as can be seen in Figs. 13 and 14, Kolmogoroff length scale and the dissipation rate seen in our study are similar to the values reported previously by Lance (1979) for grid-generated turbulence. This again implies that for two-phase bubbly flows the turbulent structure in general, and the dissipation in particular, are controlled by bubble-induced effects rather than wall effects.

Summary and Conclusions

The statistical characteristics of turbulent two-phase pipe flow were evaluated by measuring its power spectrum and autocorrelation functions. The power spectrum in two-phase flow turbulence has a flatter profile than single-phase flow, and has appreciable high frequency content. A $-8/3$ slope in the high frequency range characterized the two-phase flow power spectrums.

From the measured autocorrelation functions, the dissipation rate of the turbulent kinetic energy at the pipe's centerline was estimated. The dissipation rate in two-phase flows was found to be an order of magnitude higher than in single-phase flows. It is significant that these pipe flow results are similar to grid-generated turbulence data. This implies that bubble-

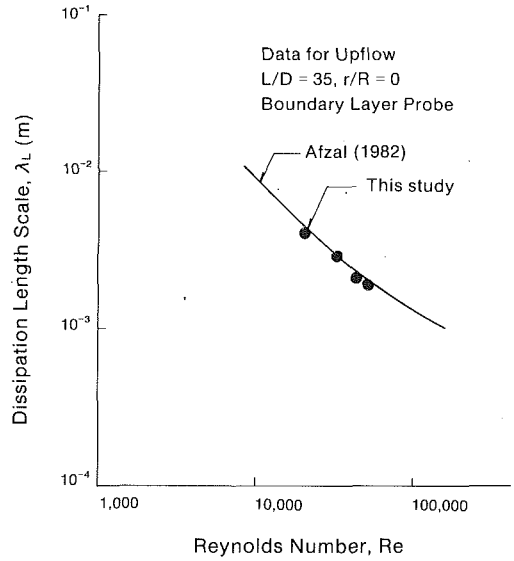

Fig. 11 Comparisons of dissipation length scale (single-phase liquid)

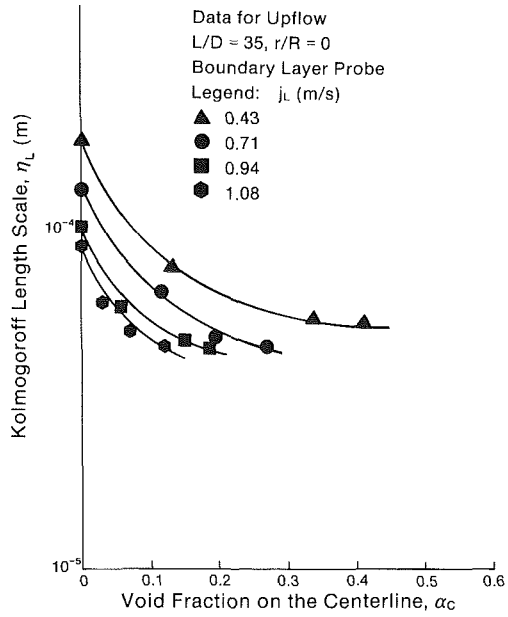

Fig. 12 Kolmogoroff length scale

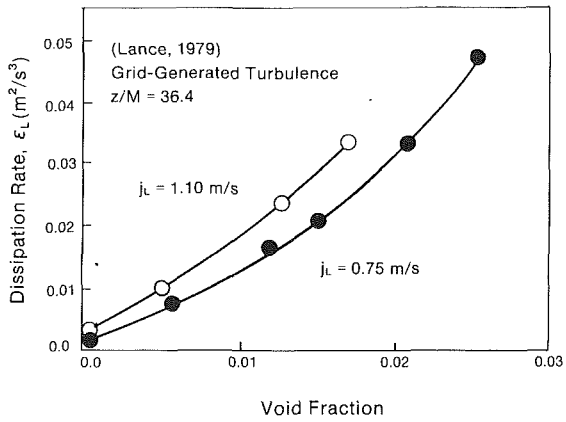

Fig. 13 Dissipation rate of turbulence kinetic energy

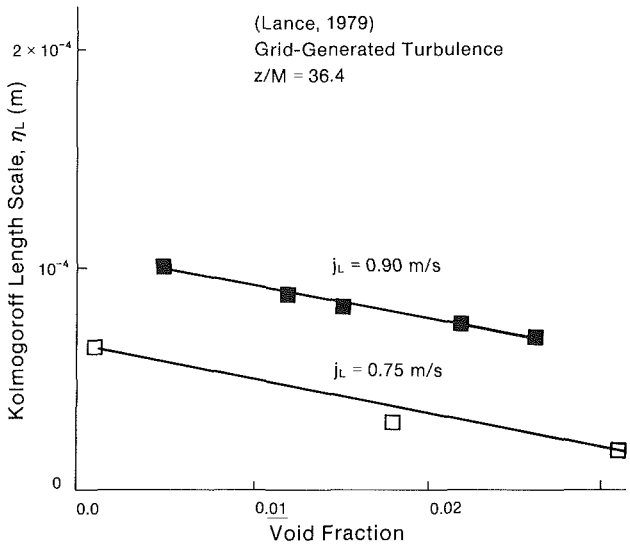

Fig. 14 Kolmogoroff length scale

induced turbulence, rather than the wall-induced or grid-generated turbulence, primarily determines the turbulence structure in two-phase flows.

Acknowledgments

The authors wish to acknowledge the support given this research by the NSF.

References

Afzal, H., 1982, "Fully Developed Turbulence Flow in a Pipe: An Intermediate Layer," *Ing. Arch.*, 52, p. 355.

Delhaye, J. M., 1969, "Hot-Film Anemometry in Two-Phase Flow," Proc. 11th National Heat Transfer Conference, Minneapolis, Minn., p. 58.

Gherson, P., and Lykoudis, P. S., 1984, "Local Measurements in Two-Phase Liquid-Metal Magneto-Fluid-Mechanic Flow," *J. Fluid Mech.*, Vol. 147, pp. 81–104.

Hinze, J. O., 1976, *Turbulence*, 2nd Ed., McGraw-Hill.

Lance, M., 1979, "Contribution A L'etude De La Turbulence Dans La Phase Liquid Des Ecoulements a Bulles," Ph.D. thesis, L'Universite Claude Bernard De Lyon.

Lance, M., and Bataille, J., 1983, "Turbulence in the Liquid Phase of a Bubbly Air-Water Flow," *Proceedings of NATO Specialist's Meeting*, Spitzingsee, FRG, Martinus Nijhoff Publishers.

Lance, M., and Bataille, J., 1989, "Turbulence in the Liquid Phase of a Uniform Bubbly Air-Water Flow," accepted for publication, *J. Fluid Mech.*

Lee, S. J., 1982, "The Development of a Digital Data Processing System for Two-Phase Turbulence Data," M.S. thesis, Rensselaer Polytechnic Institute, Troy, New York.

Liepmann, H. W., 1951, "On the Spectrum of Isotropic Turbulence," NACA TN 2473.

Serizawa, A., 1988, "Turbulence Suppression in Bubbly Two-Phase Flow," *Proceedings of the Third International Topical Meeting on Nuclear Power Plant Thermal Hydraulics and Operations*, Vol. 1, p. A1-1.

Townsend, A. A., 1947, "Measurement of Double and Triple Correlation Derivatives in Isotropic Turbulence," *Proc. Cambridge Phil. Soc.*, Vol. 43, Part 4, p. 560.

Tsuji, Y., Morikawa, Y., and Shiomi, H., 1984, "LDV Measurements of an Air-Solid Two-Phase Flow in a Vertical Pipe," *J. Fluid Mech.*, 139, p. 417.

Wang, S. K., Lee, S. J., Jones, O. C., Jr., and Lahey, R. T., Jr., 1984, "Local Void Fraction Measurement Techniques in Two-Phase Bubbly Flows Using Hot-Film Anemometry," *Proc. 22nd National Heat Transfer Conference*, Niagara Falls, New York.

Wang, S. K., Lee, S. J., Jones, O. C., Jr., and Lahey, R. T., Jr., 1987, "3-D Turbulence Structure and Phase Distribution Measurements in Bubbly Two-Phase Flows," *Int. J. Multiphase Flow*, Vol. 13, pp. 327–343.

Design and Uncertainty Analysis of a Series of Atomization Experiments in Seven Variables

F. Ruiz
Department of Mechanical and Aerospace Engineering, Illinois Institute of Technology, Chicago, IL 60616

N. A. Chigier
Department of Mechanical Engineering, Carnegie Mellon University, Pittsburgh, PA 15213

Atomization of liquids is a phenomenon that involves many variables. In order to find correlations for the effects of an extended set of variables, dimensional analysis and experimental design are used, resulting in experimental plans with very reduced number of necessary data points. Means were found to further reduce the cost of the experiments by adjustments of the ranges of the variables and the selection of the parameters and experimental sources of variability. The generation and propagation of uncertainties in the experiments are discussed, and estimates for the true lack of fit of the approximations obtained are found. The selection of a quadratic polynomial approximation seems adequate, given the relative magnitude of the other sources of uncertainty. The effects of some dimensionless parameters with physical meaning are isolated for the first time.

Introduction

The typical atomization process involves a number of variables that may affect the final result considerably, as several investigators have pointed out [1–15]. The most important variables are schematically shown in Fig. 1. They are:

1. Densities and viscosities of both liquid and outside gas, and surface tension between them: ρ_1, ρ_g, μ_1, μ_g, σ.
2. Velocities of liquid and gas (axial and tangential).
3. Injection pressure, P_1, and gas pressure, P_2.
4. Geometrical dimensions of the injector, mostly those of the final orifice (diameter, D, length, L, inlet curvature, R) and of the swirler (diameter, d, port area, As, number of ports, N), if a tangential velocity is induced in the liquid.

The tangential velocity component is directly related to the dimensions of the swirler and the injector, and to the mean aixal velocity (Taylor [4], Dombrowski [10]). The only parameter necessary to include the effect of swirl is the Taylor swirl number, $\Delta = (N\,As)/(D\,d)$. Also, it has been shown that the effect of gas velocity can be better represented by the relative velocity between liquid and gas (Taylor [3], Lefebvre [11], Ruiz and Chigier [17]). It is sufficient to test the effect of absolute liquid velocity when injecting into a stagnant gas, and substitute absolute by relative velocity in the processes and correlation terms related to the external flow problem. A complete discussion can be found in references [19] and [32].

For a steady-state case, the set above can be reduced to twelve variables. If the response of the atomization characteristics to all the variables is to be found experimentally, the experiment becomes too large to carry out. Consider, for instance, that five points per variable are required, and the variation with each variable is tested, for all constant values of the other variables. In such case, as many as $5^{12} \approx 240$ million data points would be necessary. A technique must be sought to reduce the number of tests required, while sacrificing the resolution of the results as little as possible.

Dimensional Analysis

The twelve variables under consideration are composed of three fundamental dimensions: mass, length, and time. If the problem is expressed in dimensionless terms, three of the variables, used to non-dimensionalize the others, will be eliminated from the set. Thus, when expressed in dimensionless terms, the general problem has only nine degrees of freedom to be controlled in an experiment [5].

There is a considerable freedom in the selection of the dimensionless groups, which can be chosen in such a way that they carry a clear physical meaning or help simplify the experiments. The set finally chosen, was:

External flow parameters:

gas/liquid density ratios:

$$\rho^* = \frac{\rho_g}{\rho_1} \tag{1}$$

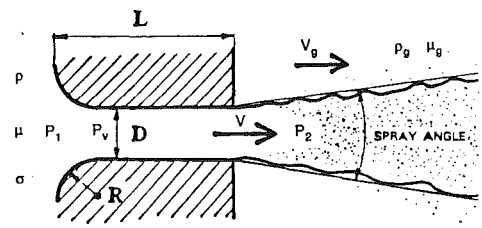

Fig. 1 Schematic diagram of high speed atomization

Contributed by the Fluids Engineering Division for publication in the JOURNAL OF FLUIDS ENGINEERING. Manuscript received by the Fluids Engineering Division August 4, 1989; revised manuscript received September 28, 1989.

gas/liquid viscosity ratio:

$$\mu^* = \frac{\mu_g}{\mu_l} \tag{2}$$

Taylor's number:

$$\frac{\mathrm{Re}}{\mathrm{We}} = \frac{\sigma}{\mu V} \tag{3}$$

Internal flow parameters:

Reynolds number, based on the orifice diameter and the average flow velocity:

$$\mathrm{Re} = \frac{\rho D V}{\mu} \tag{4}$$

cavitation number:

$$K = \frac{P_2}{\frac{1}{2}\rho V^2} \tag{5}$$

orifice length/diameter ratio:

$$L/D$$

orifice inlet curvature radius/diameter ratio:

$$R/D$$

swirl number:

$$Sw = \Delta^{-1} = \frac{D\,d}{N\,As} \tag{6}$$

And last:

discharge (flow) coefficient:

$$Cd = \frac{V}{(2(P_1 - P_2)/\rho)^{1/2}} \tag{7}$$

There is an additional advantage in separating the parameters into two groups, one of them comprising only variables of the internal flow of the liquid within the injector, and the other comprising variables of the external flow of the liquid surrounded by a gas. When only the internal flow problem is posed (variables ρ^*, μ^*, D, L, R, V, P_1, P_2, for plain atomizers), dimensional analysis shows that there are only five dimensionless parameters involved. In other words, one of the parameters of the subset for internal flow depends on the others. Traditionally [1, 5, 6, 20], it is the discharge coefficient Cd that is expressed as a function of the other parameters. The atomization problem of this study has, in fact, only eight degrees of freedom. The discharge coefficient, which represents the ratio between the real flow and the flow predicted by Bernoulli's equation, must be determined as a function of the internal flow parameters, before the dependence of the atomization measurements on the remaining parameters is established. A separate experiment is to be carried out for this purpose.

Atomization from plain cylindrical orifices (no swirl induced) corresponds to the case $Sw = 0$. Therefore, Sw is not a variable for plain atomizers. In the same way, due to the flow pattern induced by swirl, the minimum pressure within the injector orifice is found at the center line, usually occupied by a gaseous core open to the outside. There is little chance for the pressure to drop locally below the vapor pressure of the liquid and, therefore, cavitation is unlikely to occur when swirl is present. Atomization from swirl injectors can be expected to be independent of the cavitation parameter K.

We have thus reduced the original set to seven simultaneous dimensionless parameters affecting the atomization process. Four experiments were conducted, for measurement of atomization characteristics and discharge coefficients, in plain orifice and swirl injectors, each one involving a different set of variables, represented in Table 1.

Table 1 Variables controlled in the experiments

EXPERIMENTS PERFORMED:		
PLAIN ATOMIZERS:		Variables
	• Cd:	Re, K, L/D, R/D
	• Spray:	ρ^*, μ^*, Re, Re/We, K, L/D, R/D
SWIRL ATOMIZERS:		
	• Cd:	Re, Sw, L/D, R/D
	• Spray:	ρ^*, μ^*, Re, Re/We, Sw, L/D, R/D

Experimental Design

Seven degrees of freedom is the minimum that can be considered without giving up generality in the study. A full parametric study, using five values of each variable, would need $5^7 = 78125$ different data points, still unfeasible. A reduction can be obtained by decreasing the number of different values taken by each variable, at the expense of losing resolution in the results. In many practical instances, variations with individual parameters do not have inflection points: the curvature has a constant sign. Such are the variations expected with ρ^*, Sw, and L/D, reported by several investigators [1, 2, 4, 8, 10, 12, 13, 14, 15]. For these parameters, a parabolic approximation to the real variation is appropriate, only needing three values or "levels" of the variable, to be determined. The

Nomenclature

As = swirler port cross-sectional area
B = bias error
c_j = influence coefficient (power product correlation)
C_{ij} = coefficient in polynomial correlation
Cd = discharge coefficient
d = swirl chamber diameter
D = orifice diameter
K = cavitation parameter
L = orifice length
m = mass
M = gas molecular weight
n = number of data points
N = number of variable/number of swirler ports
P_1 = injection pressure
P_2 = gas pressure
R = orifice inlet curvature radius
$\mathfrak{R}$ = molar constant of gases
Re = Reynolds' number
Re/We = Taylor's number
S = standard deviation
Sw = swirl number
t = time/t-ratio
T = absolute temperature
U = uncertainty
V = liquid velocity
X_i = independent variable
Y = dependent variable
θ = average spray angle
μ = liquid viscosity
μ_g = gas viscosity
μ^* = viscosity ratio
ρ = liquid density
ρ_g = gas density
ρ^* = density ratio
σ = surface tension
i, j = summation indices
I = ideal flow
Δ = increment/error
$'$ = time derivative

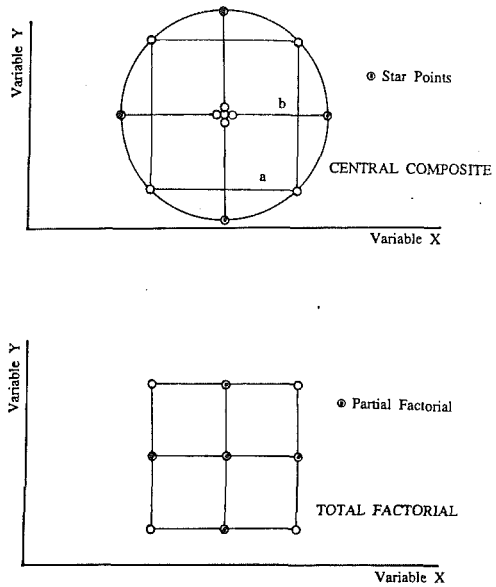

Fig. 2 Comparison of central composite and three level experimental designs

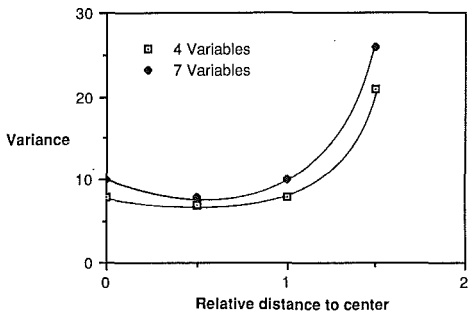

Fig. 3 Variance vs. distance to the center in the experimental designs (after Box and Behnen [22])

other variations (K, Re, μ^*, R/D, Re/We) are expected to be so for limited ranges. For a "full factorial" experiment, using three levels of seven variables, a second order polynomial approximation can be obtained by using $3^7 = 2187$ different experimental conditions. This represents a substantial reduction in the size of the experiment from the previous estimate (2187 versus 78125 points), but at the cost of incurring a lack-of-fit error if the real variation with each parameter does not follow a parabola.

The problem can also be seen from the point of view of polynomial fit. A second degree polynomial in 7 variables contains only 36 coefficients. It would be sufficient to test 36 different experimental conditions, in order to establish a linear system of equations from which the 36 coefficients can be determined. On the other hand, if any of the measurements in the 36 point experiment is affected by error, this would be directly reflected in the correlation. A certain degree of replication is necessary, in order to make the correlations less sensitive to measurement uncertainty. This replication can be introduced by repeating measurements under the same conditions or, even better, by adding new conditions.

For quantitative measurements, a number of designs have been produced to obtain linear or quadratic approximations, also called "response surfaces" (see Box, Hunter and Hunter [21], or Diamond [23]). For an experimental design to be efficient, the experimental conditions should be as far apart as possible, in order to reduce the sensitivity of the correlation to individual uncertainty. Some conditions should be placed close to the center of the domain, to reduce the effect of uncertainty on the curvature of the quadratic fit. A common type of experimental design fulfilling these criteria is the "central composite" design. In this design, the experimental conditions are placed at the surface or the center of a hypersphere in the domain of the variables, in our case, seven-dimensional. This experimental design consists of three sets of conditions:

-points at the center (0, 0, 0, . . .)

-points at the vertices of the included hypercube (± 1, ± 1, ± 1, . . .)

-star points ($\pm r$, 0, 0, . . .), (0, $\pm r$, 0, . . .), (0, 0, $\pm r$, . . .) etc.

The quantity r is determined by the condition that all points not at the center must be on the surface of the N-dimensional hypersphere of radius r. Hence: $r = N^{1/2}$.

This type of design always has the property of rotatability: since it has spherical symmetry, the variance of the coefficients and other statistical properties of the polynomial fit have no preferred direction and, in fact, can be made almost uniform within the domain, by selecting the number of data taken at the center of the domain. This design, however, needs five different values for each variable, denoted here by 0, ± 1, and $\pm r$. A central composite design for seven variables needs only 78 points on the boundary of the domain (one half of the hypercube points is sufficient), plus 14 points taken at the center. Figure 2 shows a comparison between a central composite design and a full factorial design, in two variables.

There are other types of quantitative experimental design with similar properties [21, 22]. A "partial factorial" design, taking a subset of the 2187 points of the full factorial design for three levels of seven variables can also have the property of rotatability. For instance, some of the designs of the family described by Box and Behnken [22] are rotatable, but they require only three levels of each variable. In the designs of this family, for 4 and 7 variables, the boundary points are located on the surface of a hypersphere. These designs are represented, in expanded form, in Table 2 (values denoted by -1, 0, and $+1$), and the plots of variance vs. distance to the center are shown in Fig. 3. The design in 7 variables consists of 56 points on the boundary, plus 6 points at the center.

These designs were the best found, because they are rotatable (nearly uniform variance), and fulfill the following criteria:

Accuracy. The degree of replication should be sufficient

Table 2 Schematic matrix form of the experimental designs used in this research

4 variables

A	B	C	D
±1	±1	0	0
0	0	±1	±1
±1	0	0	±1
0	±1	±1	0
±1	0	±1	0
0	±1	0	±1
0	0	0	0 (3 times)

7 variables

A	B	C	D	E	F	G
0	0	0	±1	±1	±1	0
±1	0	0	0	0	±1	±1
0	±1	0	0	±1	0	±1
±1	±1	0	±1	0	0	0
0	0	±1	±1	0	0	±1
±1	0	±1	0	±1	0	0
0	±1	±1	0	0	±1	0
0	0	0	0	0	0	0 (6 times)

to reduce the sensitivity of the correlation to errors in the individual points (62 points for 36 parameters: replication 1.72). The points should be far from each other, for the same reason.

Cost. A three-level partial factorial design is the most economical solution for a quadratic approximation, because it involves fewer experimental conditions to be tested and requires less variation in the parameters. For the atomization experiments, using three levels only in geometrical ratios implies that fewer different nozzles had to be made and fewer different working fluids had to be used. The cost and time involved in the experiment depended critically on the number of nozzles and liquids required.

Resolution. After analyzing the data, the effect of each parameter on the final result should be separable from the effects of all the others. For instance, changing the liquid velocity affects Re, Re/We, and K (see the results of Bracco [12, 13], and Hiroyasu [14, 15]). Other experimental variables affect these parameters in a different way, since they are independent. The combination of data points must be such that the effect of each one of the dimensionless parameters on the atomization characteristics is isolated.

The experimental designs of Box and Behnken [22], therefore, were chosen for the atomization experiments (seven variables), and for the discharge coefficient experiments (four variables). The required degrees of freedom were obtained by varying some of the natural variables of the system, described in the introduction. Only seven of the twelve variables available need to be varied to provide the necessary degrees of freedom. There is a choice that can be exploited to minimize the complexity of the experiment. The appropriate values of these experimental variables can be found from the values of the dimensionless parameters, by solving the system of equations (1)-(7) that define the dimensionless parameters.

For example, consider a procedure in which the composition of the gaseous atmosphere is held constant, but some properties of the liquid are varied (μ, σ), as well as the dimensions of the injecting orifice (D, L, R), and the injection and gas pressures (P_1, P_2). These variables are found from the definitions of the dimensionless parameters by the equations:

$$P_2 = \rho^* \frac{\rho R T}{M} \tag{8}$$

$$Cd^2(P_1 - P_2) = \rho^* K^{-1} \frac{\rho \mathcal{R} T}{M} \tag{9}$$

$$\mu = \mu^{*-1} \mu_g \tag{10}$$

$$\sigma = \frac{\mathrm{Re}}{\mathrm{We}} \mu^{*-1} \rho^{*1/2} K^{-1/2} \left(\frac{2\mathcal{R}T}{M}\right)^{1/2} \mu_g \tag{11}$$

$$D = \mathrm{Re}\ \mu^{*-1} \rho^{*-1/2} K^{1/2} \frac{\mu_g}{\rho} \left(\frac{2\mathcal{R}T}{\mu}\right)^{-1/2} \tag{12}$$

$$L = L/D \times D(\mathrm{Re}, \mu^*, \rho^*, K) \tag{13}$$

$$R = R/D \times D(\mathrm{Re}, \mu^*, \rho^*, K) \tag{14}$$

where the gas is considered to be ideal of molecular weight M ($\mathcal{R}$ is the universal constant of gases). With this choice of variables, the different combinations of dimensionless parameters of the design would require $3^4 = 81$ different values of the diameter, D, or the surface tension of the liquid, σ, to be tested. This problem can be reduced by the adjustment of the dynamic range of the parameters (dynamic range is the ratio of upper value to lower value of a parameter). Still, it would be better if each experimental variable were dependent on a limited number of parameters: two or three at most.

If the dynamic ranges of the dimensionless parameters are large, much larger ranges are required for the experimenal variables. If, for instance, all Re, μ^*, ρ^*, and K are to vary by 10 times, then $P_1 - P_2$ may need to vary by 100 times (equation (9)), and D by over 316 times (equation (12)), which is totally out of the possible range of variation. The ranges of the dimensionless parameters, for which the final correlations are valid, are fundamentally limited by the possible ranges of the experimental parameters. This situation is worse, the more parameters appear in each equation yielding the value of a specific experimental variable.

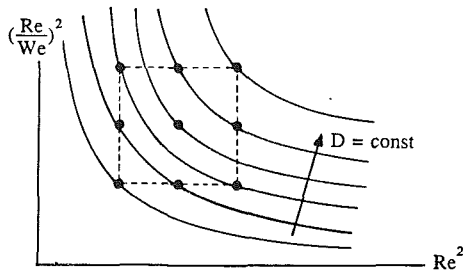

Fig. 4 Coincidence of calculated orifice diameters

Due to these considerations, the choice was made to maintain constant the liquid composition (σ and ρ have small dynamic ranges), but to vary the viscosity and the molecular weight of the gas. The equations that give the experimental variables are, then:

$$\mu_g = \mu^* \mu \tag{15}$$

$$D = (\mathrm{Re}^2)^{1/2}((\mathrm{Re/We})^2)^{1/2} \frac{\mu^2}{\sigma\rho} \tag{16}$$

$$Cd^2(P_1 - P_2) = ((\mathrm{Re/We})^2)^{-1} \frac{\sigma^2\rho}{2\mu^2} \tag{17}$$

$$P_2 = (K^{-1})^{-1}((\mathrm{Re/We})^2)^{-1} \frac{\sigma^2\rho}{2\mu^2} \tag{18}$$

$$M = \rho^* K^{-1} (\mathrm{Re/We})^2 \frac{2^2 \mu \mathcal{R} T}{\sigma^2} \tag{19}$$

$$L = L/D \times D(\mathrm{Re}^2, (\mathrm{Re/We})^2) \tag{20}$$

$$R = R/D \times D(\mathrm{Re}^2, (\mathrm{Re/We})^2) \tag{21}$$

The parameters Re^2, $(\mathrm{Re/We})^2$, and K^{-1} were chosen for the design, instead of simply Re, Re/We, and K, because they allow for "coincidences" to occur that simplify the experiment. The equation that gives the nozzle diameter (16), yields as many as nine different values of D, for three levels of the two design parameters (Re^2, $(\mathrm{Re/We})^2$) that take part in it. However, if the dynamic ranges of Re and Re/We are the same (see Fig. 4), several coincidences in the calculated value of D occur. This occurs also in other equations (18, 19) if the following conditions are met:

(a) The dynamic ranges of all parameters are equal
(b) The exponents of all parameters in the equation are the same

The dynamic ranges of the parameters are mostly limited by the variability of the gas molecular weight, M, from $M = 4$ (helium) to $M = 81$ (mixtures of freon-12 and other gases). The best dynamic range obtainable was 4.5 times, for Re^2, $(\mathrm{Re/We})^2$, K^{-1}, and ρ^*, and 1.7 times for μ^*. The parameters L/D, R/D, and Sw are not affected by these considerations, and so their ranges were chosen so that the expected variation would not be far from the quadratic approximation provided by the experiment: $L/D = 1$ to 5, $R/D = 0$ to 1, $Sw = 0$ to about 4 (two swirler ports). The final ranges of conditions used in the experiments are summarized in Tables 3 and 4. Table 3 also includes the normal ranges found in diesel injection.

The selection of the columns of the design matrix that is to represent each parameter is not trivial. A close examination of

Table 3 Ranges for the parameters in the plain orifice experiments

Parameter	Min.	Max.	Min. (diesel)	Max. (diesel)
Re	8250	17500	15000	30000
Re/We	0.047	0.099	0.02	0.08
ρ^*	0.004	0.021	0.012	0.032
K	0.081	0.367	0.08	0.9
μ^*	0.003	0.005	0.018	0.03
L/D	1	5	2	4
R/D	0	1	0	0
Sw	0	4	0	0

Table 4 Ranges for the parameters in the swirl experiments

Parameter	Minimum value	Maximum value
ρ^*	0.004	0.023
Re	9514	20177
Sw	0	4.05
Re/We	0.0407	0.0865
μ^*	0.0024	0.0066
L/D	1	5
R/D	0	1

Table 5 Measurement uncertainties of the experimental variables

Variables	Precision (tS)	Bias (B)
D, L, R, d	10 μm ≈ 3%	no
P_1, P_2	1%	no
ρ, μ, σ	no	1%
ρ_g, μ_g	3%	no
t	1 msec ≈ 0.01%	no
volume	1%	no
mass	0.02%	no
spray angle	2 deg ≈ 13%	1 deg ≈ 6.6%

the design matrix (Table 2(*b*)) reveals that some sets of three columns contain conditions where the three parameters take the extreme values at the same time (± 1, ± 1, ± 1), while other sets of three columns do not contain those conditions. This situation is to be avoided for the parameters that take part in the equation to determine the gas molecular weight: ρ^*, K^{-1}, and $(\mathrm{Re/We})^2$, otherwise the necessary dynamic range for M would be larger than is possible, or the dynamic ranges of ρ^*, K^{-1} and $(\mathrm{Re/We})^2$ would need to be reduced.

For a similar reason, the selection of the four columns to represent Re^2, $(\mathrm{Re/We})^2$, L/D, and R/D affects the number of nozzles to be made, if coincidences in the calculated diameter occur. Choosing the adequate set, it is possible to run all the conditions with a set of only 16 different nozzles. When swirl is introduced, similar considerations are made to choose the column in the design matrix that is to represent the number of swirler ports N (or which the intensity of swirl depends). With the best choice, only 25 combinations of nozzle and swirler are required; the second best requires 37.

Experimental Apparatus

Two installations were necessary for the tests: one for atomization (Fig. 5), the other for measurements of the discharge coefficient (Fig. 6). The uncertainties associated with all the measurements made in the experiment are summarized in Table 5.

The same set of nozzles was used for the two types of experiment. The nozzles were made by drilling brass plates with a high speed mechanical drill. Rounding off the nozzle inlets was produced by a chamfer at a 120° angle and variable depth, later smoothed out with a layer or epoxy resin. It is suspected, however, that the rounding obtained was not perfect, in some cases, and angles could still exit at the inlet. The orifice diameters were individually measured under an optical microscope. The maximum roughness of the orifice walls was estimated to be about 10 μm. For the swirl experiments (Fig. 7), the nozzles were provided with internal swirlers, each one with a different number, N, of equal tangential ports. One of the swirlers had radial ports, to represent the condition $Sw = 0$.

The composition of the gas within the spray chamber had to be varied, in order to obtain the required values of gas viscosi-

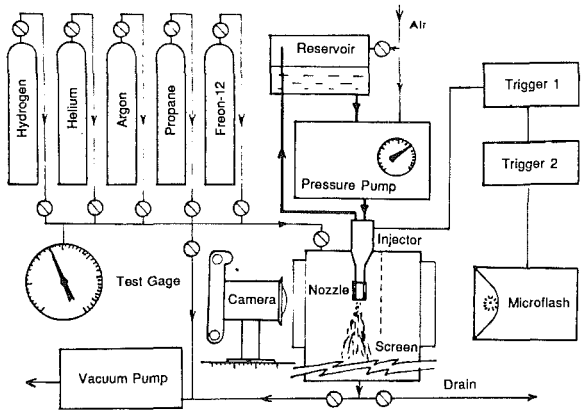

Fig. 5 Experimental apparatus for the atomization tests

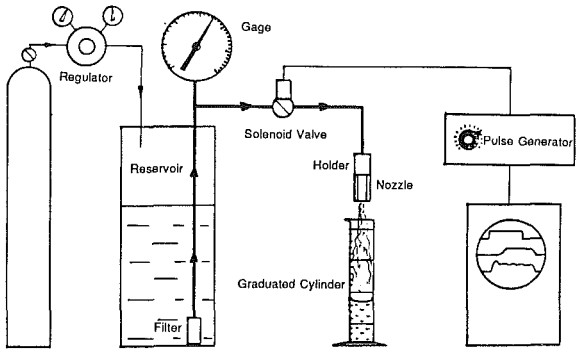

Fig. 6 Experimental apparatus for the flow tests

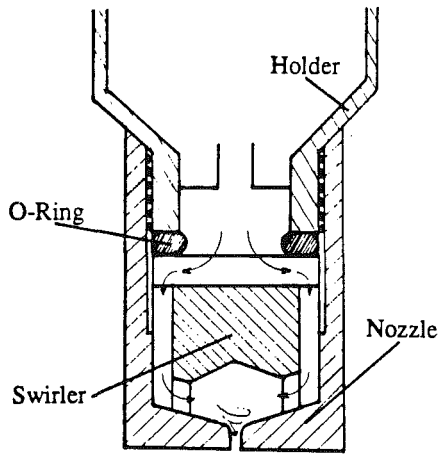

Fig. 7 Typical nozzle and swirler assembly

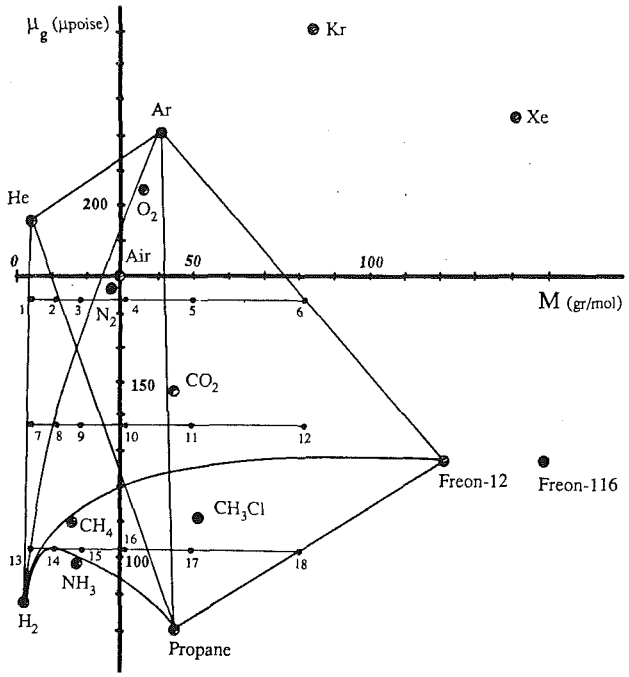

Fig. 8 Gas properties required for the experiments on plain orifice atomization

ty, μ_g, and molecular weight, M. In Fig. 8 the experimental conditions are represented in $\mu_g - M$ coordinates, together with the points corresponding to common gases at ambient temperature. The required values of μ_g and M were obtained by making ternary mixtures of the following five gases: hydrogen helium, argon, propane, and freon-12 (CF_2Cl_2). An algorithm was devised to calculate the compositions from the values of μ_g and M. Given an initial guess, μ_g was calculated using Wilke's equation [24] (accurate to 2 percent), and M is the molar average of the molecular weights of the component gases. Successive iterations were performed, until μ_g and M were within 1 percent of the required values.

Several measurement techniques were tried in the atomization apparatus:

Laser Diagnostics (Malvern). The Fraunhoffer diffraction particle sizer is based on the collection of the light scattered by the spray droplets, out of a cylindrical laser beam. The light is received on an array of semicircular photosensors and the intensity information is deconvoluted to obtain the droplet size distribution producing that scattering pattern. Although some investigators have been able to use this technique in the outer envelope of diesel sprays (Arai et al. [15], Sangeorzan et al. [25]), our efforts were unsuccessful, for the most part, due to the high opacity (large scattering power) of our sprays. Some data were obtained for the thin regions of the spray, but they are not reported here.

Cinematography. Motion pictures were taken with a Hicam high speed camera, operating at up to 20,000 frames per second. However, a strong motion blur was observed in the pictures, even at that high speed, and the framing rate was not sufficient to follow the motion of the spray during its initiation period.

Still Photography. The best results were obtained with diffused back illumination of the spray produced by a 0.5 μs strobe light (E.G.&G. Microflash). Photographs were taken in Kodak Technical Pan film (variable speed 25-100 ASA), with direct magnifications up to 1.5 times. The grain of the photographs was fine enough to allow further magnification in the prints, without loss of detail. A very slight motion blur could still be observed, in some cases. The problems associated with this technique are discussed in the next section.

Uncertainty Analysis

Locating the possible sources of uncertainty should precede the experiment itself, because sometimes small details in the procedure can have a significant effect in the uncertainty of the results [26]. There are three main types of uncertainty associated with our experiments:

1. Uncertainty of the measurements: U_1 (precision and bias)
2. Uncertainty of the values calculated by the final quadratic corrections, as a consequence of the uncertainties in the determination of the dimensionless parameters, that is transmitted to the predictions: U_2 (precision and bias)
3. Lack of fit of the quadratic correlation to the real variation with the parameters: U_3 (precision)

The total uncertainty or "error" of the values predicted by the correlation with respect to the experimental measurement is composed of these three terms. If these uncertainties are independent from each other, then the total uncertainty can be estimated by the following equation (reference [27]):

$$U = (U_1^2 + U_2^2 + U_3^2)^{1/2} \tag{22}$$

The total uncertainty can be reduced by reducing the uncertainties in the measurements, U_1, and transmitted from the variables, U_2. The error due to lack of fit, U_3, is inherent to the quadratic approximation and could only be reduced if a higher degree polynomial approximation were used.

Both uncertainties, U_1 and U_2, are composed of two elements: bias, B, and precision, tS, according to the A.S.M.E. definitions [27]. Bias is the systematic error of the measurement (average value of the measurement with respect to the true value). It can be reduced by calibration of the instruments. The precision error depends on the resolution of the instruments, the method employed, and the repeatability of the physical quantity measured. The uncertainty is calculated from these two components by:

$$U^2 = B^2 + tS^2 \tag{23}$$

The uncertainty transmitted through the correlation, U_2, depends on the uncertainties of the independent variables (dimensionless parameters), which affect the calculated value of the dependent variable (Cd or spray angle). In a simplified way, if a variable Y is given by a product of powers of the variables X_i:

$$Y = \prod_{i=1}^{N} X_i^{C_i} \tag{24}$$

then its relative uncertainty, $\Delta Y/Y$, is a function of those of the independent variables, $\Delta X_i/X_i$, by:

$$(\Delta Y/Y)^2 = \sum_{i=1}^{N} (c_i \Delta X_i/X_i)^2 \tag{25}$$

Although the final correlations reported here are not power products, the transmitted uncertainty is estimated from the values of the influence coefficients of each variable [26]:

$$c_i = \frac{\partial \ln Y}{\partial \ln X_i} \tag{26}$$

An easy way to obtain those coefficients is to correlate the measured variable, Y, by a power product equation, in addition to the approximation by a quadratic polynomial that is our main objective. The transmitted uncertainty was, in all cases, much smaller than the other contributions to the total uncertainty (see Table 6).

If the experimental method is to help minimize the uncer-

Table 6 Uncertainties of the parameters and the results

Parameter	Uncertainty (%)	c_i (Cd plain)	c_i (Cd swirl)	c_i (angle plain)	c_i (angle swirl)
ρ^*	5.2	0	0	0.32	-0.1
μ^*	5.1	0	0	0.03	0.1
Re	5.6	0.062	0.09	0.44	0.54
K	16.3	0.004	0	0.69	0
Re/We	8.3	0	0	-0.13	-0.1
Sw	4.4	0	-0.46	0	0.55
L/D	3.2	-0.06	-0.22	-0.24	-0.24
R/D	3.2	0.59	0.1	0.04	0.08
Precision components of the uncertainty					
Measurement	U_1	0.06	0.04	2.0 deg	2.0 deg
Transmitted	U_2	0.009	0.008	1.0 deg	1.6 deg
Lack of fit	U_3	0.07	0.09	2.5 deg	5.4 deg
Total	U	0.08	0.1	3.4 deg	6.0 deg

tainty, it is necessary to find the magnitudes whose accuracy is critical to the accuracy of the measurements and of the dimensionless variables. For instance, the discharge coefficient, Cd, is calculated from flow measurements, by the equation:

$$Cd = \frac{m/t}{\frac{\pi D^2}{4}\,[2(P_1 - P_2)\rho]^{1/2}} \tag{27}$$

where m is the mass that flows in the time t, through an orifice of diameter D. According to equation (25), the coefficient Cd is most sensitive to errors in D (2nd power), m and t (1st power), its sensitivity to errors in pressures and density being much smaller. A problem may arise, though, if P_1 and P_2 are close, large numbers.

The measurement of flow is based on the collection of the liquid injected during a relatively short injection pulse. The typical flowrate for one of these pulses is represented in Fig. 9, as a function of time. The flowrate is fairly constant during most of the injection time, but there are two highly transient flow conditions, at the beginning and the end of the pulse. The response of the flow is delayed with respect to the electric signal that controls the solenoid used in the experiments.

In order to eliminate this transient effect from the measurements, flow measurements were made at two different control timings, t_1 and t_2. Since the duration of the steady state part of the pulse, the steady-state flow can be obtained by subtracting the mass measurements taken with the two timings:

$$Cd = \frac{m_2 - m_1}{t_2 - t_1}\,\frac{4}{\pi D^2}\,\frac{1}{(2(P_1 - P_2)\rho)^{1/2}} \tag{28}$$

The relative uncertainty of Cd, assuming that all errors are of the same type, would be:

$$\left(\frac{\Delta Cd}{Cd}\right)^2 = \left(2\,\frac{\Delta m}{(m_2 - m_1)}\right)^2 + \left(2\,\frac{\Delta t}{(t_2 - t_1)}\right)^2 + \left(2\,\frac{\Delta D}{D}\right)^2 + \left(\frac{\Delta P}{(P_1 - P_2)}\right)^2 + \left(\frac{1}{2}\,\frac{\Delta\rho}{\rho}\right)^2 \tag{29}$$

The critical uncertainties are those of D, m, and t. Values for the different measurements were:

$\Delta D \approx 10\ \mu$m (microscope), for $D \approx 300\ \mu$m

$\Delta m \approx 0.01$ g (balance), or 0.5 g (volume measurement) from $m \approx 50$ g

$\Delta t \approx 1$ ms (due to the AC solenoid valve)

$\Delta P \approx 5$ psig (gages), for $P_1 \approx 100$ psig and P_2 atmospheric

$\Delta\rho \approx 0.01$ g/cm^3, for $\rho \approx 1$ g/cm^3

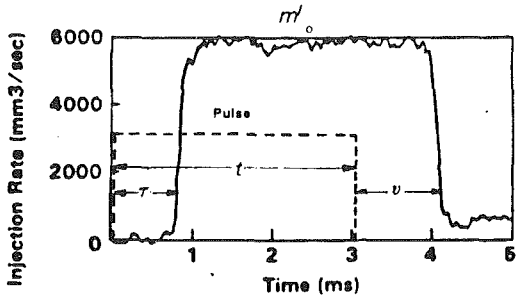

Fig. 9 Typical flow rate as a function of time (after Sinnamon et al. [31])

The instruments had been calibrated, in order to reduce bias. The error $\Delta\rho$ is of bias type, since ρ was a constant in all measurements. The error ΔD was constant for each nozzle; however, since 16 different nozzles were used in the experiments, it was considered that the ΔD errors of different nozzles affected the results as a precision error, not a bias.

In order to reduce the effect of the uncertainties of m and t, the difference between the timings t_1 and t_2 (and, therefore, between the collected masses m_1 and m_2) must be as large as possible. The larger timing t_2 was chosen to be about 10 sec (10010 ms), while t_1 was chosen to be 10 ms, barely long enough to allow the flow to reach steady state conditions before the shut-off transient period starts. With this choice, the uncertainty in the determination of m ceases to be important (1 percent, if obtained by volume measurement) the main factor being the uncertainty in the measurement of the orifice diameter (3.3 percent). The orifices were measured under a traversing microscope, with negligible bias error. Since the orifices were never perfectly circular, an uncertainty of 10 μm was taken, lacking a more perfect method of measuring the orifice cross-sectional area. This causes the relative uncertainty transmitted to Cd to be 8.4 percent, which means $\Delta Cd \approx 0.06$ for plain cylindrical orifice injector, and $\Delta Cd \approx 0.04$ for a swirl injector.

The determination of the spray angle from photographs of atomizing sprays was affected by several types of uncertainty:

Bias Caused by the Photographic Technique. Depending on the exposure and developing time of the film, the contrast of the photographs is altered. An overexposed or underdeveloped film has a weaker contrast in the lighter regions than in the darker regions [28]. The spray outline can be located in different positions, depending on photographic exposure and developing time. If the photographic procedure is the same for all conditions, this uncertainty represents a bias of the spray angle measurements. If the procedure is not the same for all conditions, uniformity can be obtained by photographing a gray scale together with the spray, and adjusting the developing of the final positive prints to achieve the same contrast of the gray scale in all the prints. Calibration for the photographic spray angle is not possible, unless sprays of known angle are independently available. A reduction of the bias can be expected, however, by selecting the exposure and developing process that produces a more uniform degree of contrast throughout the whole image. In this case, the image density of the photograph is nearly proportional to the logarithm of the light intensity received at each picture element [29]. The problem of determination of the spray boundary becomes rather a problem of selection of an adequate definition of spray boundary.

Uncertainty Due to the Definition of Spray Angle Itself. Most investigators using photographic determination of spray angle [12–15] rely on the absolute conical envelope of the spray, outside which no droplets can be found. This definition has a physical sense, because it is related to the maximum

growth rate of the liquid surface instabilities, but its practical significance is questionable. First, the position of the very outer limit of the spray depends on small, relatively isolated droplets. A variation in the photographic technique can produce changes in the visibility of those droplets in the photographs [28], causing large variations in the measured spray angle. This definition is also very dependent on lighting conditions: small droplets tend to disappear under diffused background illumination, because they scatter light more easily than large droplets, and their contrast is reduced [25, 28]. Alternative methods, based on image density measurements, have been suggested by Kamimoto and co-workers [29]. The image density is directly related to the line of sight absorption and scattering of light, which is a function of the optical properties of the liquid in the spray, and the surface density of droplets (droplet surface per unit volume of spray). The spray angle reported is that of a cone enclosing the same volume as the spray boundary thus defined (average angle).

Uncertainty in the Determination of the Equivalent Cone. This uncertainty depends on the reliability of the instrument used to determine the conventionally defined spray boundary and draw the equivalent cone. If these processes are done by automatic image analysis, this uncertainty is related to the resolution of the digitized image, and the sensitivity to error of the calculation procedures uses to determine the position of the cone (which involve numerical differentiation). If, as is usual [1–15], the determination of the equivalent cone is done by human visual inspection, then the uncertainty depends on many other factors, such as fatigue, expectation of a particular value, the precision of the observer's perception, and other uncontrollable factors.

Working figures for all the discussed types of uncertainty were measured or estimated, and are summarized in Table 6. The measurement uncertainties were calculated from equations (23) and (25). The uncertainties of the dimensionless parameters were calculated from equations of the type of (25), derived from their definitions in equations (1) to (6). Finally, the uncertainties transmitted to the predicted values, U_2, were calculated by equation (25), using the coefficients of a power-product fit to the experimental data, as discussed before. The coefficients are also represented in Table 6.

The main source of error is the uncertainty in the value of the discharge coefficient Cd, that is needed to calculate the dimensionless parameters Re, Re/We, and K. Consequently, these parameters are affected by a relatively large uncertainty (over 15 percent for K). Fortunately, the coefficients corresponding to these parameters are rather small, and so the uncertainty transmitted to the predicted spray angles, U_2, is still smaller than the uncertainty of the measurements, U_1, and has a much less significant effect in the total uncertainty of the correlation, U.

Results

The sets of experimental conditions, and the corresponding measurements, are too long to be shown here, but can be found in ref. [19] (summary in ref. [32]). Those data were fit by a full quadratic polynomial in the dimensionless variables. A standard statistical computer package, MINITAB (reference [30]), was used to find the coefficients of the polynomial, and other statistical quantities. Among these, the most important were:

Standard Deviation of the Estimation, S. This is related to the total uncertainty or "error", U, of the approximation, but does not include the bias. Following the ASME standard [27], precision limits are defined as the points separated a distance $\pm 2S$ from the mean value, for a 95 percent coverage. In our case, we have assumed that bias only comes by transmission from the liquid properties (bias 0.07 percent, according to Table 6) and from the measurement bias of the spray angle.

Correlation coefficient "*R*-squared," R^2, which is the square of the common regression coefficient "ρ" [30]. This parameter measures the dispersion of the data around the prediction equation (a coefficient of 100 percent would be a perfect match of data and polynomial prediction). Since this number naturally increases every time a new term is added to the polynomial, a better indicator of the true degree of correlation is the R-squared, corrected by degrees of freedom coefficient, R^{2*}, defined by:

$$R^{2*} = \frac{n-1}{n-N-1} R^2 - \frac{N}{n-N-1} \tag{30}$$

for $N+1$ terms in the polynomial, and n data points. This is the value that is reported in this paper.

Significance ratios or "*t*-ratios" of the coefficients, defined as the ratio $t_i = s_i/c_i$, of the value of the ith coefficient of the correlation, c_i, and its standard deviation, s_i. The t-ratio indicates the relative contribution of each term to the approximation. If $|t_i| > 2$ (and samples larger than 30 data points, like in our case), the coefficient is different from zero, at least with a 95 percent certainty. The t-ratios of absolute value less than 2 are commonly considered a symptom of insignificance of the corresponding term [21, 30]. However, one must be cautious in dropping those terms from the correlations, since a small confidence interval does not mean that the term is really insignificant, and physical meaning could be lost in dropping some of these terms.

Relative Residuals. For some data points, the difference between measured and predicted values (residual) is considerably larger than the standard deviation. For instance, for the measurements of spray angle produced by plain orifice injectors, it was found that the points of codes aVI and aVIII [19] were far from the predicted values. These points were dropped from the database, and a special experiment designed to detect the causes producing their anomalous behavior. Upon examination, it was discovered that a different atomization mechanism, based on the Coanda effect, was being triggered under those conditions [18, 19]. The normal mode was still possible, but the photographs detected the occurrence of this extraordinary mechanism in some cases, and so the average value of the spray angle was misleading.

The data were approximated first by a full quadratic polynomial in all the parameters: linear, quadratic, and cross-product terms of ρ^*, Re, Re/We, μ^*, L/D, R/D, and K or Sw. A term was dropped from the correlation, if it had a low t-ratio ($-1 < t < 1$), or it was such that $-2 < t < 2$, and contained parameters that consistently produced terms of low significance level. The viscosity ratio, μ^*, was eventually dropped altogether from the correlations, and so was the R/D ratio, for the spray angle measured in plain orifices without swirl. Successive regressions were repeated until the R^{2*} coefficient was a maximum. In some cases, individual examination of some data points of high residual, followed by remeasuring, produced a small increase in the correlation coefficient, R^{*2}. Approximations were obtained for five definitions of the spray angle, but only the coefficients for the "average" spray angle, discussed above, are presented here. The coefficients are shown, in double-entry form, in Tables 7 and 8. The dependent variable Y (Cd or average spray angle) can be calculated by:

$$Y = \sum_{i,j=1}^{8} C_{ij} X_i X_j \tag{31}$$

where C_{ij} are the coefficients, and X_i X_j are dimensionless variables of set: 1, ρ^*, Re, Re/We, K, Sw, L/D, R/D. The dimensionless unity "1" is included to represent the linear terms, in the cross-product equation (31).

Notice that the dimensionless parameters used in the cor-

Table 7 Coefficients of the correlations for plain orifice injectors

DISCHARGE COEFFICIENT $R^2 = 85.5\%$ sd = 0.04

	1	Re	K	L/D	R/D
1	-0.2860	9.584E-5	2.1741	-0.18611	1.5778
Re		-2.469E-9	0	0	-4.117E-5
K			-3.0869	0	-1.4359
L/D				0.029314	0
R/D					-0.42287

AVERAGE ANGLE $R^2 = 82.7\%$ sd = 1.7 deg

	1	ρ*	Re	K	Re/We	L/D
1	60.026	0	-2.5284E-3	31.53	-850.07	-5.9007
ρ*		25193	-2.3959E-2	-1254.3	0	0
Re			6.0238E-8	0	1.7996E-2	0
K				48.73	-415.59	-2.688
Re/We					3666.4	45.057
L/D						0.38002

Table 8 Coefficients of the correlations for swirl injectors

DISCHARGE COEFFICIENT $R^2 = 91.3\%$ sd = 0.054

	1	Sw	L/D
1	1.12	-0.189	-0.219
Sw		0.0202	0
L/D			0.0313

AVERAGE ANGLE $R^2 = 93.1\%$ sd = 3 deg

	1	ρ*	Re	Sw	Re/We	L/D	R/D
1	39.80	-494.3	5.564E-3	-95.863	0	11.418	24.522
ρ*		0	0	0	0	217.82	0
Re			-3.097E-7	6.4623E-3	-2.9017E-2	-1.662E-3	0
Sw				2.9690	198.03	0	3.226
Re/We					796.6	-43.35	-108.69
L/D						1.0854	-3.534
R/D							-11.167

relations are not exactly the same as those used in the experimental design (Re versus Re^2, Re/We versus $(Re/We)^2$, K versus K^{-1}, Sw versus N). The design points are not exactly placed on a spherical surface in the domain of the variables, and the variance of the correlation cannot be expected to be uniform throughout the domain. However, the deformation induced by these transformations is small, as long as the dynamic range of the variables is small (4.5 times only, for these experiments), and the power of separating the effects of the different parameters is not damaged. For instance, if the design values of Re^2 were 1, 2.25, and 4.5 (in normalized form), the corresponding values of Re are 1, 1.5, and 2.12. The middle value, 1.5, is no longer the average of the extreme values, 1.56, but the deviation is only a 10.8 percent of the distance between average and extreme values. The use of the parameters mentioned above has a clearer physical meaning, whereas the parameters used in the experimental design

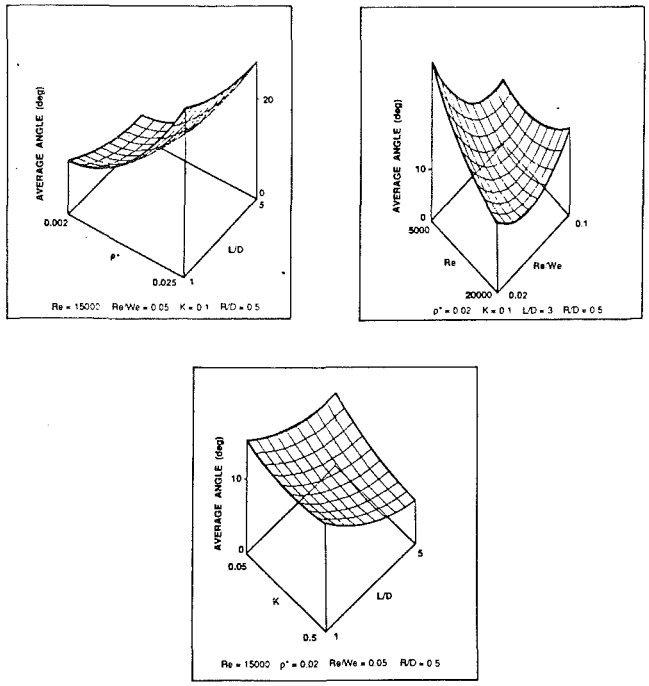

Fig. 10 Some variations observed in plain orifice injectors

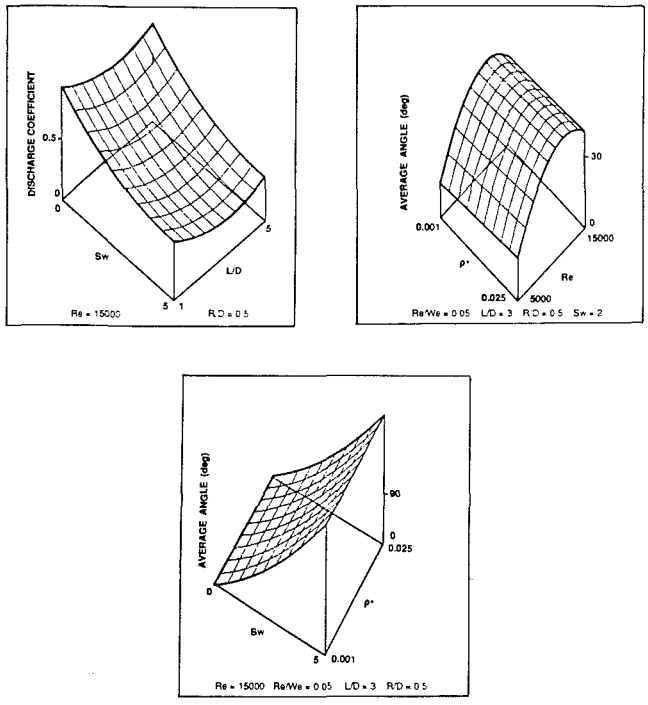

Fig. 11 Some variations observed in swirl injectors

simplify the experiment and allow coincidences in experimental variables to occur, greatly reducing the cost of the experiments. The correlation coefficient, R^2, is approximately the same with either set of variables, confirming the validity of the change.

Examples of the values predicted by the correlations are shown in Figs. 10 and 11. A few consequences can be drawn from them. The spray angle tends to increase with ρ^*, for plain orifice injectors, whereas it decreases with ρ^* for swirl injectors. The reason is to be found in a different interaction with the gas flow field induced by entrainment into the spray: the droplets in a wide spray (like that produced by a swirl in-

jector) tend to be drawn inwards by drag forces in the predominantly radial gas flow field that they find away from the axis; if the spray is narrow, the local flow field is almost parallel to the axis, and has no reducing effect on the spray angle, which naturally increases with the gas density [5]. The curvature of the variation of spray angle with ρ^* is opposite to that reported by other authors [12–15], but still correct in its average slope. This is, however, within the scope of the design, which is not expected to yield perfectly accurate variations for each one of the parameters, but to optimize the fit in the domain of all the parameters, considered simultaneously. If a detailed description of the variation of the spray angle with a specific parameter is sought, an experiment focusing on that parameter alone should be run independently. For the same reason, it is possible that the parameter R/D be significant to the spray angle of plain injectors, as reported elsewhere [12], but that in this case its effect has been shielded by more significant variations. It is also possible that the rounding of the nozzles used in our experiments, being obtained in a different way, is not so smooth as that used by Reitz and Bracco [12], and does not cause the same stabilizing effect of the liquid jet. An analysis of the effect of R/D should maintain constant the parameters with stronger influences, such as ρ^*, Re, Sw, or L/D.

It was found that the influence of the parameter Re/We was, in general, opposite to the predictions of Taylor's aerodynamic theory [3], on which the traditional Ranz's equation for the spray angle is based [7]. The spray angle tends to decrease as Re/We increases, while the theory predicts a slow increase. The theory was found to work fairly well in the range of $\mathrm{Re/We} < 10^{-2}$, in a different experiment [17]. Other authors [1, 2, 5, 12–15] have reported an increase of the spray angle with increased liquid velocity (decreased Re/We), but they do not separate the effects of Re/We, Re, and K, and so a discussion of the validity of Taylor's aerodynamic theory is not possible. This theory, which is based on a linear stability analysis, would need to be extended to a higher order, if these effects are to be included. The linear theory can be made to represent correctly the effect of Re/We if an additional factor (roughly $(\mathrm{Re/We})^{-1/4}$) is added to Ranz's equation (see references [19], [32]).

Spray angles were monotonically decreasing functions of L/D. This agrees with the results of Gelalles [1], and Reitz and Braco [12], but disagrees with those of Wu et al. [13], and Hiroyasu and Kadota [14], who found a maximum for $L/D = 10$ and 20, respectively. In a later paper, Hiroyasu et al. [15], reported a steep maximum for $L/D = 4$. Details of the orifice geometry, not reported in the published papers, could be responsible for this discrepancy. It is known that the flow at the entrance of cylindrical orifices tends to separate from the walls, to reattach further downstream. Late reattachment could be the cause of the increase in spray angle with L/D, in certain ranges, found by some investigators.

After the correlations were made, an estimate of the lack of fit, U_3, was indirectly found from the precision components of the uncertainty by the following equation, derived from equation (22) (the bias errors do not compound with the lack of fit):

$$U_3 = (tS)_3 = ((tS)^2 - (tS)_1{}^2 - (tS)_2{}^2)^{1/2} \tag{32}$$

The lack of fit of each correlation was estimated through equation (32), and is shown in Table 6. The lack of fit is comparable, in any case, to the measurement uncertainty and considerably larger than the transmitted uncertainty of the predicted values. The choice of a quadratic approximation seems adequate. A higher degree polynomial approximation would be efficient only if the uncertainty in the measurements of spray angle (see the related discussion) or orifice diameter is considerably reduced. Neither would a reduction in the measurement uncertainty be efficient, if only a quadratic polynomial fit is required.

Conclusions

1. Dimensional analysis is an effective technique to reduce the number of degrees of freedom necessary in a parametric experiment. There exists a freedom in the selection of the dimensionless variables that can be advantageously used to represent physical effects. Grouping the parameters related to the same part of the problem (internal or external flow) can produce further reductions.

2. Experimental designs in up to seven variables, taken in three levels, have been used to simplify parametric experiments prepared to yield second degree polynomial approximations. Certain classes of rotatable designs offer the smallest cost for the same performance as a full factorial experiment.

3. The selection of experimental variables and ranges of the design variables is crucial for the feasibility of the experiments. Homogeneity in the dynamic ranges of the design variables produces coincidences in the required values of the experimental variables, with considerable cost savings.

4. A procedure was devised to eliminate the effect of flow transients for experiments designed to measure the steady-state flow in injectors where the transients occupy a substantial fraction of the total injection time. The uncertainty in the determination of the discharge coefficient of small orifices is controlled by the errors in the measurement of orifice diameter.

5. The uncertainty involved in the photographic measurement of spray angles is discussed. There exists a bias due to the photographic technique, and several sources of precision error, some inherent to the spray, some due to the observer.

6. Estimations for the lack of fit of the correlations are indirectly obtained from the uncertainties in the measurements and the predictions, and the scatter of the date around the predicted values. It was found that both an improvement in the measurement uncertainty and a higher degree polynomial approximation would be required to reduce the global uncertainty.

7. The measurements mostly confirm the trends discussed by other authors [1, 2, 5, 6, 7, 10, 12, 13, 14, 15], but point out variations that previously had been overlooked (effects of Re/We, μ^*, K). Correlations are presented that, although with a relatively high uncertainty (around 10 percent), isolate the contributions of different parameters to the discharge coefficient and the spray angle characteristic of plain orifice and swirl injectors, at high operating pressures.

References

1 Gelalles, A. G., "Effect of Orifice Length-Diameter Ratio on Fuel Sprays for Compression-Ignition Engines," NACA Technical Report No. 402. 1931.

2 Schweitzer, P. H., "Mechanism of Disintegration of Liquid Jets," *Journal of Applied Physics*, Vol. 8, 1937, p. 513.

3 Taylor, G. I., "Generation of Ripples by Wind Blowing over a Viscous Fluid," *The Scientific Papers of G. I. Taylor*, Vol. 3, Cambridge University Press, 1940, p. 244.

4 Taylor, G. I., *The Mechanics of Swirl Atomisers*, op. cit., 1948, p. 429.

5 Giffen, E., and Muraszew, A. *The Atomisation of Liquid Fuels*, John Wiley, New York, 1953.

6 Bergwerk, W., "Flow Pattern in Diesel Nozzle Spray Holes," *Proceedings of the Institution of Mechanical Engineers*, Vol. 173, No. 25, 1959, p. 655.

7 Ranz, W. E., "Some Experiments on Orifice Sprays," *Canadian Journal of Chemical Engineering*, Aug. 1958, p. 175.

8 Miesse, C. C., "Correlation of Experimental Data on the Disintegration of Liquid Jets," *Industrial and Engineering Chemistry*, Vol. 47, No. 9, 1955, p. 1690.

9 Rupe, J. H., "On the Dynamic Characteristics of Free-Liquid Jets and a Partial Correlation with Orifice Geometry," JPL Technical Report No. 32-207, 1962.

10 Dombrowski, N., and Hasson, D., "The Flow Characteristics of Swirl (Centrifugal) Spray Pressure Nozzles with Low Viscosity Liquids," *A.I.Ch.E. Journal*, Vol. 15, No. 4, 1969, p. 604.

11 Lefebvre, A. H., "Airblast Atomization," *Progress in Energy and Combustion Science*, Vol. 6, 1980, p. 233.

12 Reitz, R. D., and Bracco, F. V., "Mechanism of Atomization of a Liquid Jet," *Physics of Fluids*, Vol. 25, No. 10, 1982, p. 1730.

13 Wu, K.-J., Su, C. C., Steinberger, R. L., Santavicca, D. A., and Bracco, F. V., "Measurements of the Spray Angle of Atomizing Jets," ASME JOURNAL OF FLUIDS ENGINEERING, Vol. 105, No. 12, 1983, p. 406.

14 Hiroyasu, H., and Kadota, T., "Fuel Droplet Size Distribution in Diesel Combustion Chamber," SAE Paper No. 740715. 1974.

15 Arai, M., Tabata, M., Hiroyasu, H., and Shimizu, M., "Disintegrating Process and Spray Characterization of Fuel Jet Injected by a Diesel Nozzle," SAE Paper No. 840275, 1984.

16 Hoyt, J. W., and Taylor, J. J., "Waves on Water Jets," *Journal of Fluid Mechanics*, Vol. 83, 1977, p. 119.

17 Ruiz, F., and Chigier, N. A., "The Mechanics of High Speed Atomization," *Proceedings of ICLASS'85*, London. The Institute of Energy, 1985, p. IVB/3/1.

18 Ruiz, F., and Chigier, N. A., "The Effects of Design and Operating Conditions on Flow and Atomization in Diesel Engines," SAE Paper No. 870100, 1987.

19 Ruiz, F., "Experimental and Theoretical Analysis of HighSpeed Atomization, and its Application to Diesel Fuel Injection," Ph.D. thesis, Carnegie Mellon University, Pittsburgh, 1987.

20 Spikes, R. H., and Pennington, G. A., "Discharge Coefficients of Small Submerged Orifices," *Proceedings of the Institution of Mechanical Engineers*, Vol. 173, No. 25, 1959, p. 661.

21 Box, G. E. P., Hunter, W. G., and Hunter, J. S., *Statistics for Experimenters*, Chapter 15, Wiley, New York, 1978.

22 Box, G. E. P., and Behnken, D. W., "Some New Three Level Designs for the Study of Quantitative Variables," *Technometrics*, Vol. 2, No. 4, 1960, p. 455.

23 Diamond, J. W., *Practical Experimental Designs for Engineers and Scientists*, Chapter 15. Lifetime Learning Publishers, Belmont, CA, 1981.

24 Reid, R. C., Prausnitz, J. M., and Sherwood, T. K., *The Properties of Gases and Liquids*, McGraw-Hill, New York, 1977.

25 Sangeorzan, B. P., Uyehara, O. A., and Myers, P. S., "Time-Resolved Drop Size Measurements in an Intermittent High Pressure Fuel Spray," SAE Paper No. 841361, 1984.

26 Kline, S. J., "The Purposes of Uncertainty Analysis," ASME JOURNAL OF FLUIDS ENGINEERING, Vol. 107, 1985, p. 153.

27 Abernethy, R. B., Benedict, R. P., and Dowell, R. B., "Measurement Uncertainty," ASME JOURNAL OF FLUIDS ENGINEERING, Vol. 107, 1985, p. 161.

28 Azzopardi, B. J., "Measurement of Drop Sizes," *International Journal of Heat and Mass Transfer*, Vol. 22, 1979, p. 1245.

29 Kamimoto, T., Ahu, S.-K., Chang, Y., Kabayashi, H., and Matsouka, S., "Measurement of Droplet Diameter and Fuel Concentration in a Non-Evaporating Diesel Spray by Means of an Image Analysis of Shadow Photographs," SAE Paper No. 840276. 1984.

30 Ryan, T. A., Joiner, B., and Ryan, B., *MINITAB Student Handbook*, Duxbury Press, N. Scituate, MA, 1981.

31 Sinnamon, S. F., Lancaster, D. R., and Steiner, S. C., "An Experimental and Analytical Sutyd of Engine Fuel Spray Trajectories," SAE Paper No. 800135, 1980.

32 Ruiz, F., and Chigier, N. A., "Parametric Experiments on Liquid Jet Atomization," *Atomization and Sprays*, Vol. 1, No. 1, 1990.

M. Lopez de Bertodano

S-J. Lee

R. T. Lahey, Jr.

D. A. Drew

Rensselaer Polytechnic Institute,
Troy, NY 12180-3590

The Prediction of Two-Phase Turbulence and Phase Distribution Phenomena Using a Reynolds Stress Model

The void fraction distribution for turbulent bubbly air/water upflows and downflows in a pipe was analyzed using a three-dimensional two-fluid model. A $\tau-\epsilon$ (i.e., Reynolds stress) turbulence model was used for the continuous (liquid) phase. The $\tau-\epsilon$ transport equations yield all components of the Reynolds stress tensor for the liquid phase momentum equations. The effect of these stresses is to create a lateral pressure gradient that acts on the bubbles and effects their distribution. The lateral lift force on the bubbles has also been modelled. This lift force arises due to the relative motion of the bubble with respect to a nonuniform liquid velocity field. It has been observed experimentally that for upflows the bubbles concentrate near the wall while for downflows they move toward the center of the conduit. The model presented herein predicts these trends.

Introduction

Two-phase flow models are often one-dimensional and involve the use of many correlations. These correlations do not normally take into account the detailed three-dimensional structure of the flow nor do they consider all the physical phenomena involved. In recent years there has been a trend toward more rigorous multidimensional analyses. This paper presents such an analysis.

The object of this study was to predict the lateral phase distribution in a vertical pipe for upward and downward bubbly flows. The lateral forces that most strongly effect the void distribution were found to be the turbulent stresses, and the lateral lift force.

For single-phase turbulent flow in a pipe there is a radial pressure gradient induced by the turbulence. In contrast, for laminar flows the radial pressure gradient is zero. Any transverse pressure gradient exerts a lateral force on the bubbles, which they respond to due to their relatively low axial inertia. The key to calculating the lateral pressure gradient is to properly compute the turbulence structure. Various turbulence transport models developed in recent years have had some success when applied to two-phase flows. For example, a $K-\epsilon$ model has been used by Lee et al. (1988). This paper presents an extension to that research. In particular, a $\tau-\epsilon$ model has been used instead of a $K-\epsilon$ model. This model is more detailed since it replaces the equation for the turbulent kinetic energy by a set of coupled differential equations for the individual Reynolds stress components. As a consequence, nonisotropy is automatically predicted.

The bubbles may also experience a lateral lift force as they move relative to the liquid in a nonuniform velocity field. The model proposed by Drew and Lahey (1987) was used for this force.

Experimental measurements of void fraction and turbulence in pipes have been made by a number of investigators, including Serizawa (1974) and Wang et al. (1987). For bubbly upflow, both sets of data show void peaking near the wall, similar to that shown in Figs. 1 and 2(*a*). In contrast for downflows, as can be seen in Fig. 2(*b*), the data of Wang et al. (1987) show the opposite trend.

Discussion

The Conservation Equations. For convenience, the PHOENICS code (Spalding et al., 1986) was used to carry out the computations presented herein. This code contains a three-dimensional set of two-fluid conservation equations that can be modified by adding other terms to those equations and by inserting addition transport equations. In our case the full $\tau-\epsilon$ turbulence model was implemented, as well as a lateral lift force.

A derivation of the time-averaged three-dimensional two-fluid conservation equations has been given by Ishii (1975) and has been the subject of many studies since then. Following Ishii (1975) the mass conservation equations are:

$$\frac{D_k}{Dt}\alpha_k + \alpha_k \nabla \cdot \underline{\bar{u}}_k = 0 \quad , \qquad (k = l, v) \qquad (1)$$

where the subscript k refers to the liquid or vapor phase, the overbars indicate time-averaged quantities, the underbars indicate vector quantities, α_k is the volumetric fraction of

Contributed by the Fluids Engineering Division and presented at the Winter Annual Meeting Chicago, Ill., November 27-December 2, 1988 of THE AMERICAN SOCIETY OF MECHANICAL ENGINEERS. Manuscript received by the Fluids Engineering Division February 13, 1989.

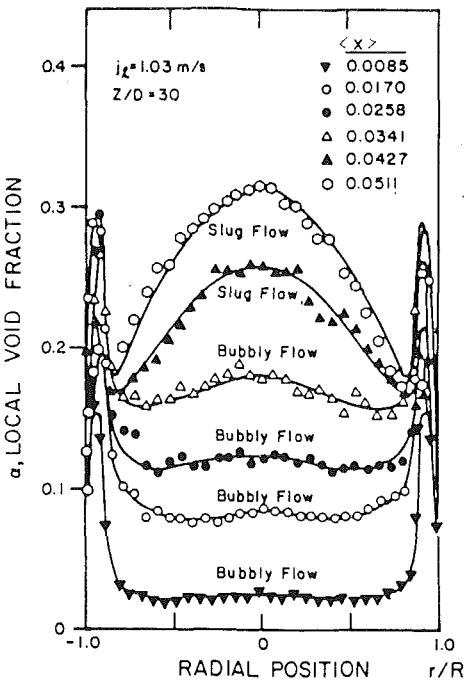

Fig. 1 Radial void distribution (upflow)—Serizawa (1974)

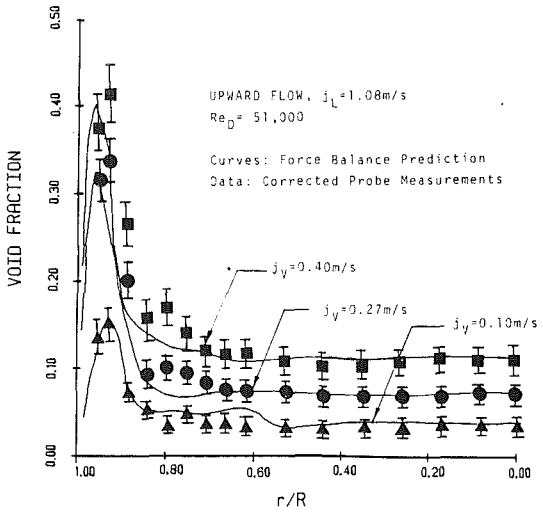

Fig. 2(*a*) Void fraction profiles (upflow)—Wang et al. (1987)

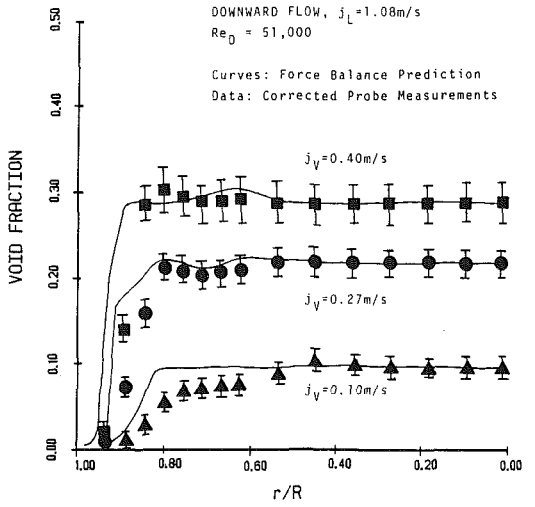

Fig. 2(*b*) Void fraction profiles (downflow)—Wang et al. (1987)

phase-k, $\underline{u}_k$ is the corresponding velocity and D_k/Dt represents the material derivative of phase-k.

Similarly, the phasic momentum equations are:

$$\alpha_k\rho_k\frac{D\tilde{u}_k}{Dt}=\alpha_k(\nabla\cdot\underline{\underline{\tilde{T}}}_k+\rho_k\underline{g})-(\underline{\underline{\tilde{T}}}_{ki}-\underline{\underline{\tilde{T}}}_k)\cdot\nabla\alpha_k+\underline{M}_{ki} \qquad (2)$$

where, neglecting viscous stresses, the stress tensor for phase-k is given by,

$$\underline{\underline{\tilde{T}}}_k=-\tilde{p}_k\underline{\underline{I}}-\rho_k\overline{\underline{u}_k'\underline{u}_k'}$$

and the instantaneous velocity of phase-k is:

$$\underline{u}_k=\tilde{\underline{u}}_k+\underline{u}_k'$$

Nomenclature

c = coefficient
g = gravitational constant
$\underline{\underline{I}}$ = identity matrix
k = turbulent kinetic energy
$\underline{M}$ = interfacial force vector between liquid and gas phases
p = pressure
P = production of turbulence
u = velocity
α = void fraction
γ = constant in pressure-strain term
ϵ = turbulence dissipation
ν = kinematic viscosity
ρ = density
τ = characteristic time
ϕ = pressure-strain term in Reynolds-stress equations

Subscripts

b = bubble
d = drag
i = interface
k = phase-k
l = liquid
L = lift
s = for coefficient of turbulence characteristic time
t = turbulence
v = gas (vapor)

Superscripts

$( )'$ = fluctuating component
$( )^T$ = transpose

Derivatives

$\frac{D}{DT}=\frac{\partial}{\partial t}+u\cdot\nabla$ = material derivative
∇ = gradient

Other Symbols

$(\bar{\ })$ = averaged quality
$(\underline{\ })$ = vector quantity
$(\underline{\underline{\ }})$ = tensor quantity (second order)
$\underline{u}\,\underline{u}$ = tensor (second order)
$\underline{u}\,\underline{u}\,\underline{u}$ = tensor (third order)

The phasic density is ρ_k (assumed constant), $\bar{p}_k$ is the static pressure, $\underline{g}$ is the gravitational acceleration and $\underline{M}_{ki}$ is the interfacial force on phase-k. The term $-\rho_k \underline{u}_k' \underline{u}_k'$ is the Reynolds stress tensor. In the vapor momentum equation the Reynolds stresses are small in comparison to the pressure gradient and the interfacial forces, so they can be neglected. This assumption is quite good for low pressure air/water flows where the vapor density is relatively small. Hence, from here on, the subscripts in the term $\underline{u}_k' \underline{u}_k'$ will be dropped with the understanding that this term corresponds to the liquid phase.

The phasic interfacial force terms in the momentum equation are assumed to be equal and opposite:

$$\underline{M}_{vi} = -\underline{M}_{li} = -\underline{M}_i \tag{3}$$

The forces at the interface can be decomposed into the drag force and the lift:

$$\underline{M}_i = \underline{M}_i^D + \underline{M}_i^L$$

where the interfacial drag force per unit volume is given by:

$$\underline{M}_i^D = \frac{3}{4} C_D \frac{\rho_l}{D_b} \alpha_v |\underline{\bar{u}}_v - \underline{\bar{u}}_l| (\underline{\bar{u}}_v - \underline{\bar{u}}_l) \tag{4}$$

Here, D_b is the bubble diameter and C_D was taken as the "dirty water" drag coefficient of Wallis (1969):

$$C_D = \frac{6.3}{\mathrm{Re}_b^{0.385}} \quad , \quad \mathrm{Re}_b = \frac{D_b |\underline{\bar{u}}_v - \underline{\bar{u}}_l|}{\nu_l} \tag{5}$$

The model of Drew and Lahey (1987) for the lateral lift force was used in the form:

$$\underline{M}_i^L = -C_L \rho_l \alpha_v (\underline{\bar{u}}_v - \underline{\bar{u}}_l) \times (\nabla \times \underline{\bar{u}}_l) \tag{6}$$

In previous work (Wang et al., 1987) it was shown that the lift coefficient (C_L) can vary from 0.5 (inviscid flow) to about 0.01 (highly viscous flows). In this study we used the value, $C_L = 0.05$.

Inviscid calculations (Lamb, 1932) indicate that:

$$\bar{p}_{li} = \bar{p}_l - \frac{1}{4} \rho_l |\underline{\bar{u}}_v - \underline{\bar{u}}_l|^2 \tag{7}$$

In contrast, neglecting surface tension and assuming that $\rho_v \ll \rho_l$, we have for the gas phase:

$$\bar{p}_v = \bar{p}_{vi} = \bar{p}_{li}$$

Thus, for the interfacial stress tensor it was assumed that:

$$\underline{\bar{T}}_{li} = -\bar{p}_{li} \underline{\underline{I}} - \rho_l \overline{\underline{u}' \underline{u}'} \tag{8}$$

For adiabatic air/water flow no energy equations are necessary and the thermodynamic and transport properties were assumed to be constant. This is not rigorously true because there is viscous dissipation, however this effect is negligible.

These conservation equations are closed once $-\rho_l \overline{\underline{u}' \underline{u}'}$ is related to the state variables of the problem (i.e., the velocity field). Since none of the available algebraic closure models (e.g., mixing length models) were appropriate (Lee et al., 1988), a Reynolds stress (τ-ϵ) model was used.

The Reynolds Stress Equations. A single-phase τ-ϵ model has been developed by Launder et al. (1975). The basic procedure they used was to subtract the product of the averaged velocity times the averaged Navier-Stokes equation, from the average of the product of the instantaneous velocity times the instantaneous Navier-Stokes equation. Because of the nonlinear convection term in the Navier Stokes equation a triple product appears in the Reynolds stress equations. Also additional double product terms other than the Reynolds stresses result. All these terms need to be constituted in order to close the set of equations. Nevertheless, applying the same procedure to two-phase flow, the resulting set of liquid phase equations is:

$$\alpha_l \frac{D_l}{Dt} \overline{\underline{u}' \underline{u}'} = \alpha_l (\nabla \cdot \underline{\underline{\bar{D}}} + \underline{\underline{\bar{P}}} + \underline{\underline{\bar{\phi}}} - 2 \underline{\underline{I}} \bar{\epsilon}) - (\underline{\underline{\bar{D}}}_i - \underline{\underline{\bar{D}}}) \cdot \nabla \alpha_l + \underline{\underline{\bar{P}}}_i \tag{9}$$

where $\underline{\underline{\bar{D}}}$ is the so-called diffusion tensor,

$$\underline{\underline{\bar{D}}} = -\overline{\underline{u}' \underline{u}' \underline{u}'}$$

and viscous transport has again been neglected.

The tensor $\underline{\underline{P}}$ is the turbulence production tensor, and $\underline{\underline{\phi}}$ is the pressure-strain tensor, which acts to exchange kinetic energy between the various Reynolds stress tensor components. The parameter $\bar{\epsilon}$ is the dissipation of liquid phase turbulence. $\underline{\underline{\bar{P}}}_i$ is an additional tensor which represents the source of turbulence due to the bubbles. This term does not exist in the single-phase flow equations.

The turbulence production tensor can be obtained from a rigorous mathematical derivation of the Reynolds stress equation:

$$\underline{\underline{\bar{P}}} = -\overline{\underline{u}' \underline{u}'} \cdot (\nabla \underline{\bar{u}}_l + \nabla \underline{\bar{u}}_l^T) \tag{10}$$

where the quantity in brackets is twice the strain rate tensor. This production term represents an exchange of kinetic energy between the mean flow and the turbulence (Tennekes et al., 1972).

The source of turbulence due to the work that the bubbles do as they move through the liquid is (per unit volume):

$$\bar{P}_i = C_i \underline{M}_i^D \cdot (\underline{\bar{u}}_v - \underline{\bar{u}}_l) \tag{11}$$

where $C_i (\leq 1.0)$ is a parameter that is needed because the turbulence induced by the bubbles is of smaller length scale than that due to wall-induced turbulence. Introducing equation (4) into equation (11) yields:

$$\bar{P}_i = C_i \frac{3}{4} C_D \frac{\rho_l}{D_b} \alpha_v |\underline{\bar{u}}_v - \underline{\bar{u}}_l|^3 \tag{12}$$

At present it appears that the best way to split this source of turbulence among the components of the Reynolds stress is:

$$\underline{\underline{\bar{P}}}_i = \begin{bmatrix} 4/5 & 0 & 0 \\ 0 & 3/5 & 0 \\ 0 & 0 & 3/5 \end{bmatrix} \bar{P}_i \tag{13}$$

That is, in accordance with potential flow theory, all the bubble-induced turbulence is partitioned among the normal components.

A value of 0.02 was used for C_i. This is consistent with previous investigators (Lee et al., 1988) and indicates that only a small percentage (i.e., 2 percent) of the bubble-induced turbulence goes into the large eddy structure of the continuous phase.

The pressure-strain tensor is modeled as:

$$\underline{\underline{\phi}} = -C_1 \frac{\bar{k}}{\bar{\epsilon}} \left(\overline{\underline{u}' \underline{u}'} - \frac{2}{3} \underline{\underline{I}} \bar{k} \right) - \gamma \left(\underline{\underline{\bar{P}}} - \frac{2}{3} \underline{\underline{I}} \bar{P} \right) - \gamma \left(\underline{\underline{\bar{P}}}_i - \frac{2}{3} \underline{\underline{I}} \bar{P}_i \right) \tag{14}$$

where,

$$\bar{k} = \frac{1}{2} \text{ Trace } (\overline{\underline{u}' \underline{u}'}) \tag{15}$$

is the turbulence kinetic energy, and,

$$\bar{P} = \frac{1}{2} \text{ Trace } (\underline{\underline{\bar{P}}}) \quad , \quad \bar{P}_i = \frac{1}{2} \text{ Trace } (\underline{\underline{\bar{P}}}_i) \tag{16}$$

are terms associated with the production of turbulence kinetic energy.

The triple product term correlation proposed by Launder et al. (1972) is:

$$\overline{\underline{u}'\underline{u}'\underline{u}'} = -\tau_t \overline{\underline{u}'\underline{u}'} \cdot \nabla \overline{\underline{u}'\underline{u}'} \tag{17}$$

where,

$$\tau_t \triangleq C_s \frac{\bar{k}}{\bar{\epsilon}} \tag{18}$$

is a mean turbulence time constant. This expression is a simplification of the exact transport equation for $\overline{\underline{u}'\underline{u}'\underline{u}'}$.

For the interfacial terms it was assumed that:

$$\bar{\underline{\underline{D}}}_i = \bar{\underline{\underline{D}}} \tag{19}$$

The dissipation of turbulence is also modeled with a transport equation:

$$\alpha_l \frac{D\bar{\epsilon}}{Dt} = \alpha_l(\nabla \cdot \bar{\underline{D}}_\epsilon + \bar{P}_\epsilon - \bar{\epsilon}_\epsilon) - (\bar{\underline{D}}_{\epsilon i} - \bar{\underline{D}}_\epsilon) \cdot \nabla \alpha_l + \bar{P}_{\epsilon i} \tag{20}$$

where the dissipative diffusion vector is given by:

$$\bar{\underline{D}}_\epsilon = -\overline{\underline{u}'\epsilon'}$$

and $\overline{\underline{u}'\epsilon'}$ is the turbulent transport of dissipation, $\bar{P}_\epsilon$ is the production of dissipation and $\bar{\epsilon}_\epsilon$ is the reduction of dissipation. The closure models used for these terms are (Rodi, 1984):

$$\overline{\underline{u}'\epsilon'} = C_\epsilon \frac{\bar{\epsilon}}{\bar{k}} \overline{\underline{u}'\underline{u}'} \cdot \nabla \bar{\epsilon} \tag{21a}$$

$$\bar{P}_\epsilon = C_{\epsilon 1} \frac{\bar{\epsilon}}{\bar{k}} \bar{P} \tag{21b}$$

$$\bar{\epsilon}_\epsilon = C_{\epsilon 2} \frac{\bar{\epsilon}}{\bar{k}} \bar{\epsilon} \tag{21c}$$

$$\bar{P}_{\epsilon i} = C_{\epsilon 3} \frac{\epsilon}{\bar{k}} \bar{P}_i \tag{21d}$$

Again, as in the previous cases, the interfacial term was assumed to be equal to the bulk value:

$$\bar{\underline{D}}_{\epsilon i} = \bar{\underline{D}}_\epsilon \tag{22}$$

The constants used in this model were the well known single-phase values (Launder et al., 1975):

$$\gamma = 0.6 \qquad C_{\epsilon 1} = 1.44$$

$$C_S = 0.25 \qquad C_{\epsilon 2} = 1.92$$

$$C_1 = 1.5 \qquad C_{\epsilon 3} = 1.92$$

$$C_\epsilon = 0.15$$

Boundary Conditions. The boundary conditions at the wall are an essential part of this model. Because of computational complexity it is impractical to numerically evaluate the flows in the buffer zone and the sublaminar layer. Instead the boundary conditions are normally placed at the inertial sublayer where the logarithmic "law of the wall" is assumed to be valid. This assumption, which is known to work well for single-phase flows, has been used in this study for two-phase flow. While the validity of the single-phase "law of the wall" has not been completely verified for two-phase flows, it appears to be a reasonable assumption (Marié, 1987).

Thus the momentum equation's boundary conditions at the "wall" are zero normal velocities, and tangential velocities given by:

$$\frac{\bar{u}_l}{u^*} = 2.5 \ln y^+ + 5 \tag{23}$$

where, y is the distance from the wall and,

$$y^+ = \frac{yu^*}{\nu} \quad , \quad u_* = \sqrt{\tau_W/\rho_l} \tag{24}$$

The boundary conditions for the $\tau - \epsilon$ equations are:

$$\overline{\underline{u}'\underline{u}'} = \underline{\underline{C}} u_*^2 \tag{25}$$

where, for axisymmetric pipe flows,

$$\underline{\underline{C}} = \begin{bmatrix} 5.1 & 0 & 1.0 \\ 0 & 2.3 & 0 \\ 1.0 & 0 & 1.0 \end{bmatrix} \tag{26}$$

For the dissipation at the "wall":

$$\bar{\epsilon} = \frac{1}{\kappa} \frac{u_*}{y} u_*^2 \tag{27}$$

where, κ is the von Karman constant ($\kappa = 0.435$).

Comparison With Experiments

According to equation (6) the lift force for steady axisymmetric pipe flow is:

$$\underline{M}_i^L = -C_L \rho_l \alpha_v (\bar{u}_v - \bar{u}_l) \frac{\partial \bar{u}_l}{\partial r} \underline{e}_r \tag{28}$$

where $\bar{u}_k$ is the axial component of the velocity vector, $\bar{\underline{u}}_k$. Since the velocity gradient in equation (28) changes sign with flow direction, the lift force also changes sign. Hence, for upflow the lift force pushes the bubbles toward the wall while for downflow it pushes them toward the center.

The effect of turbulence on bubble distribution may be illustrated by the lateral momentum equation for fully developed, single-phase, plane channel flow:

$$\frac{\partial}{\partial y}(\bar{p} + \rho_l \overline{v'v'}) = 0 \tag{29}$$

where $\overline{v'v'}$ is the normal Reynolds stress in the lateral direction. This equation resembles Bernoulli's equation in that it shows that when the normal lateral component of turbulence increases the static pressure decreases.

Experimental data for single-phase pipe flows indicate that the turbulence intensity is highest near the wall so that the static pressure is a minumum there. Due to their relatively small axial inertia the bubbles tend to migrate into the low pressure region near the wall. This illustration provides a partial explanation of the effect of turbulence. In order to complete the picture let us now consider the lateral momentum equation for the vapor phase in fully developed, two-phase flow. For simplicity we again examine planar flows. For this case the vapor momentum equation is:

$$-\alpha v \frac{\partial \bar{p}}{\partial y} - M_i^L = 0 \tag{30}$$

Now let us assume that $C_L = 0$ such that the lift force is zero. Then the product of the local void fraction and the local pressure gradient must be zero. In general it is the lateral pressure gradient that must vanish. This shows that for fully developed conditions, as the vapor flow is increased, the pressure profile changes from the single-phase profile (with a minimum near the wall) to a flat profile due to interaction with the local voids. That is, the positively buoyant bubbles interact with the turbulence structure, modifying the lateral static pressure profile.

Naturally, once fully developed conditions are achieved the

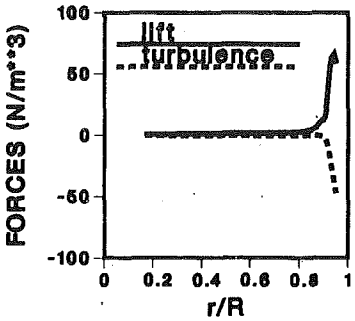

Fig. 3(*a*) Radial forces on the bubbles for upflow ($j_l = 1.08$ m/s; $j_g = 0.10$ m/s)

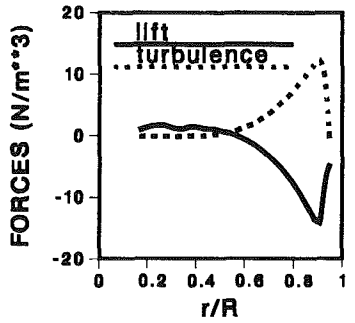

Fig. 3(*b*) Radial forces on the bubbles for downflow ($j_l = 1.08$ m/s; $j_g = 0.10$ m/s)

net force on the bubbles is zero. In contrast, in the developing flow region the bubbles are pushed sideways by the turbulent-induced pressure gradient until they attain their final nonuniform lateral distribution.

In the more realistic case in which lift is nonzero, the final pressure profile is such that it balances the lift force. This is shown in Figs. 3(*a*) and 3(*b*) for upflow and downflow, respectively.

Significantly, when the lateral pressure gradients are modified due to the presence of the bubbles, this has an impact on the turbulence profiles as well, because the liquid momentum equation, which contains both the pressure and turbulence gradients, is effected. For example, it was observed that increasing the lift force in the model produces a reduction in the local shear stress.

Figures 4(*a*) to 4(*d*) show a comparison between computed results for a mean bubble diameter of 2 mm and the data of Wang et al. (1987).

Figures 5(*a*) to 5(*d*) show a similar comparison with the data of Serizawa et al. (1974). The mean bubble diameter used in these calculations was 5 mm, which was somewhat higher than reported. However, in order to reproduce Serizawa's relatively low shear stress data it was necessary to have a fairly large lift force. This was achieved by increasing the bubble size since, when maintaining a constant void fraction, the resultant reduction in interfacial area implies an increase in relative velocity which in turn implies more lift. It should also be noted that the two data points shown in Fig. 4(*d*) which are the closest to the wall are suspect since they do not satisfy a force balance.

Overall the sets of upflow data of Wang and Serizawa are almost equivalent, however, there are some other discrepancies. For example, the turbulent components of velocity near the wall measured by Wang et al. (1987) are lower than the computed values whereas Serizawa's measurements are higher. This lack of agreement made it impossible to assess the validity of the single-phase boundary conditions, equations (23)–(27), used for the two-phase flow calculations.

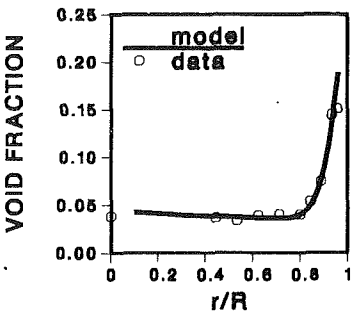

Fig. 4(*a*) Radial void profile. The data of Wang et al. (1987): upflow ($j_l = 1.08$ m/s; $j_g = 0.10$ m/s)

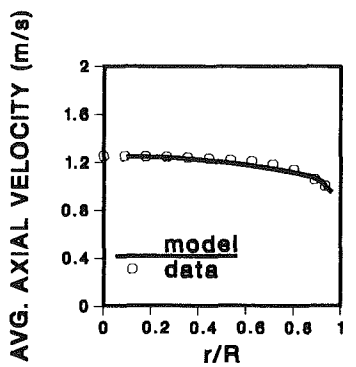

Fig. 4(*b*) Radial mean liquid velocity profile. The data of Wang et al. (1987): upflow ($j_l = 1.08$ m/s; $j_g = 0.10$ m/s)

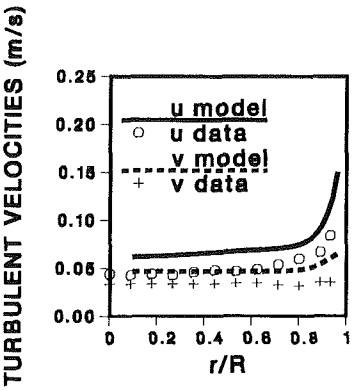

Fig. 4(*c*) Radial RMS turbulent fluctuations. The data of Wang et al. (1987): upflow ($j_l = 1.08$ m/s; $j_g = 0.10$ m/s)

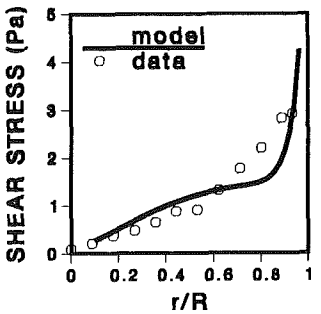

Fig. 4(*d*) Radial shear stress profile. The data of Wang et al. (1987): upflow ($j_l = 1.08$ m/s; $j_g = 0.10$ m/s)

Finally, Figs. 6(*a*) to 6(*d*) show a comparison with Wang's downflow data. The model was successful in reproducing the void fraction data trends and the peak in the mean liquid

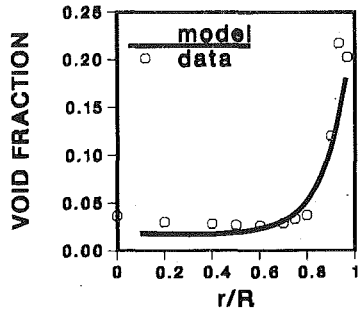

Fig. 5(*a*) Radial void profile. The data of Serizawa et al. (1974): upflow ($j_l = 1.36$ m/s; $j_g = 0.077$ m/s)

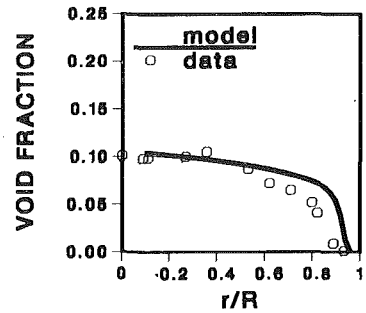

Fig. 6(*a*) Radial void profile. The data of Wang et al. (1987): downflow ($j_l = 1.08$ m/s; $j_g = 0.10$ m/s)

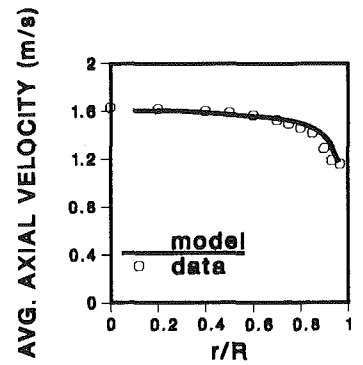

Fig. 5(*b*) Radial mean liquid velocity profile. The data of Serizawa et al. (1974): upflow ($j_l = 1.36$ m/s; $j_g = 0.077$ m/s)

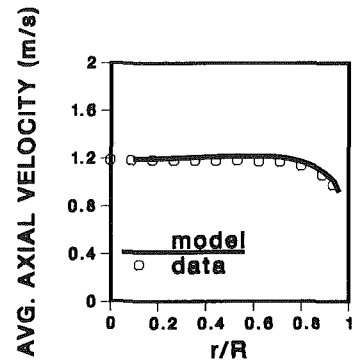

Fig. 6(*b*) Radial mean liquid velocity profile. The data of Wang et al. (1987): downflow ($j_l = 1.08$ m/s; $j_g = 0.10$ m/s)

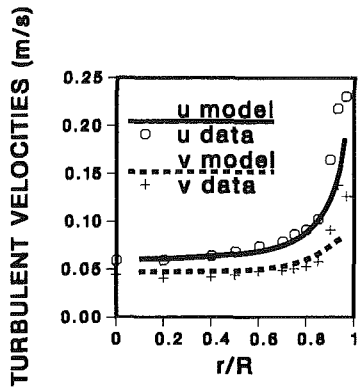

Fig. 5(*c*) Radial RMS turbulent fluctuations. The data of Serizawa et al. (1974): upflow ($j_l = 1.36$ m/s; $j_g = 0.077$ m/s)

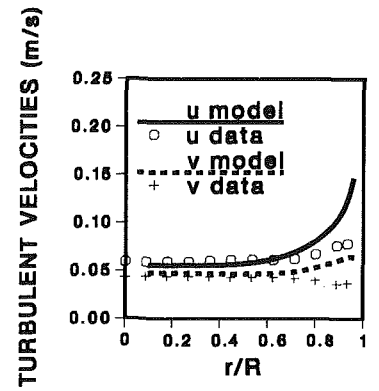

Fig. 6(*c*) Radial RMS turbulent fluctuations. The data of Wang et al. (1987): downflow ($j_l = 1.08$ m/s; $j_g = 0.10$ m/s)

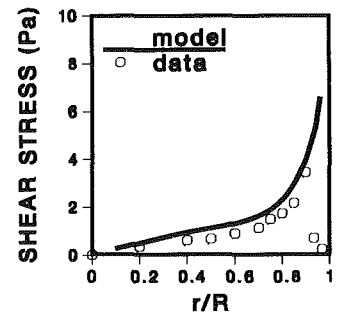

Fig. 5(*d*) Radial shear stress profile. The data of Serizawa et al. (1974): upflow ($j_l = 1.36$ m/s; $j_g = 0.077$ m/s)

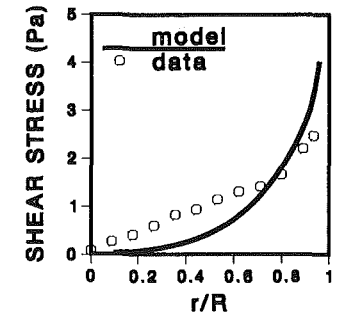

Fig. 6(*d*) Radial shear stress profile. The data of Wang et al. (1987): downflow ($j_l = 1.08$ m/s; $j_g = 0.10$ m/s)

velocity off the centerline. While model predictions of shear stress are not as good as for upflows, overall agreement seems satisfactory.

Future Work

So far a τ–ϵ turbulence model has been used with fairly simple two-phase closure relations. The model has been successful when compared with a certain range of data (i.e., low pressure air/water flows with water velocities up to 1 m/s and void fractions below 10 percent). However, it appears that more research is needed to develop more general closure laws and to extend the validity of the model to other ranges of data. For example, the high velocity data (i.e., 3 to 5 m/s) obtained by

Serizawa et al. (1987) indicate that as the flow is increased the wall peak in void fraction is dispersed. This may occur due to the diffusive effect of large eddies which become more intense at higher liquid velocity. Unfortunately, a suitable constitutive relation that accounts for this effect is not currently available. Moreover, other effects that were not considered very significant in this study, such as a lubrication-theory-like wall force, may also be needed if the model is to have wide applicability (e.g., to "laminar" two-phase flows).

Conclusions

A model has been devéloped to account for phase distribution in bubbly flow based on a simple but rigorous formulation of the averaged two-phase flow transport equations. A τ-ϵ model has been used to account for the effects of turbulence.

Comparisons of the model results with low pressure air/water data obtained at void fractions below 10 percent and intermediate velocities (i.e., up to approximately 1 m/s in a 5 cm diameter pipe) show good agreement. For turbulent two-phase flows the Reynolds stresses and the lift force appear to be the most significant mechanisms involved in lateral void distribution.

Although the results presented herein are very promising, further research is needed to extend the validity of multidimensional two-fluid models to other conditions of practical concern. It is hoped that this paper will help stimulate this research.

References

Drew, D. A., and Lahey, Jr., R. T., 1987, "The Virtual Mass and Lift Force on a Sphere in Rotating and Straining Flow," *J. Multiphase Flow*, Vol.-13, No. 1.

Ishii, M., 1975, "Thermofluid Dynamic Theory of Two-Phase Flow," Eyrolles.

Lamb, H., 1932, *Hydrodynamics* 6th Ed., New York, Cambridge University Press.

Launder, B. E., et al., 1975, "Progress in the Development of a Reynolds Stress Closure," *J. Fluid Mech.*, Vol. 68-3, pp. 537-566.

Launder, B. E., and Hanjalic, K., 1972, "A Reynolds Stress Model of Turbulence and its Application to Thin Shear Flows," *J. Fluid Mech.*, Vol. 52, p. 609.

Lee, S. J., Lahey, Jr., R. T., and Jones, Jr., O. C., 1988, "The Prediction of Two-Phases Turbulence and Phase Distribution Using a K-ϵ Model," to be published, *Japanese J. of Multiphase Flow*.

Marié, J. L., "Modelling of the Skin Friction and Heat Transfer in Turbulent Two-Component Bubbly Flow in Pipes," *J. Multiphase Flow*, Vol.-13, No. 3.

Rodi, W., 1984, "Turbulence Models and Their Applications in Hydraulics," IAHR Monograph.

Serizawa, A., et al., 1974, "Turbulent Structure of Air/Water Bubbly Flow," *J. Multiphase Flow*, Vol. 2.

Serizawa, A., et al., 1987, "Data Set 24, Phase Distribution in Bubbly Flows," *Proceedings of the Second International Workshop on Two-Phase Flow Fundamentals*, Rensselaer Polytechnic Institute, Troy, NY.

Spalding, D. B., et al., 1986, "PHOENICS-Beginner's Guide and User Manual," CHAM TR/100.

Tennekes, H., and Lumley, J. L., 1972, *A First Course in Turbulence*, MIT Press, Boston.

Wallis, G. B., 1969, *One Dimensional Two-Phase Flow*, McGraw-Hill, New York.

Wang, S. K., Lee, S-J., Jones, Jr., O. C., and Lahey, Jr., R. T., 1987, "3-D Turbulence Structure and Phase Distribution Measurements in Bubbly Two-Phase Flows," *J. Multiphase Flow*, Vol.-13, No. 3.

Analysis of Dispersion of Small Spherical Particles in a Random Velocity Field

H. Ounis

G. Ahmadi

Department of Mechanical and Industrial Engineering,
Clarkson University,
Potsdam, N.Y. 13676

The equation of motion of a small spherical rigid particle in a turbulent flow field, including the Stokes drag, the Basset force, and the virtual mass effects, is considered. For an isotropic field, the lift force and the velocity gradient effects are neglected. Using the spectral method, responses of the resulting constant coefficient stochastic integro-differential equation are studied. Analytical expressions relating the Lagrangian energy spectra of particle velocity to that of the fluid are developed and the results are used to evaluate various response statistics. Variations of the mean-square particle velocity and particle diffusivity with size, density ratio and response time are studied. The theoretical predictions are compared with the digital simulation results and the available data and good agreement is observed.

1 Introduction

The dispersion phenomena of small particles in a turbulent flow field have significant applications in various fields of engineering. The first detailed analysis of turbulent diffusion by continuous movement was carried out by G. I. Taylor [1]. Tchen [2] initiated the study of turbulent dispersion of finite size particles by analyzing the BBO (Boussinesq [3], Basset [4], Oseen [5]) equation for time varying flow fields. Corrsin and Lumley [6] offered certain corrections on the equation of motion and studied the diffusion of a small rigid sphere in a turbulent fluid. Experimental studies of turbulent diffusions of aerosols in an air jet were carried out by Goldschmidt and Eskinazi [7], Householder and Goldschmidt [8], and Yuu et al. [9]. Singametti [10] and Chuang [11] experimentally studied the dispersion of air bubbles in submerged water jets. Observations of particle diffusivities larger and smaller than that of fluid were reported in theses studies. The experimental study of Snyder and Lumley [12] clearly showed that the mass diffusivities of finite size particles are less than that of fluid particles for homogeneous nearly isotropic turbulent flows.

Applying the conditional averaging, Shirazi [13] reduced the BBO equation to a stochastic integro-differential equation. Levich and Kuchanov [14] neglected the pressure gradient and the Basset term and found that the mean square of particle velocity is always smaller than the mean square fluid velocity. Additional works on the subject were carried out by Hinze [15], Soo and Peskin [16], Peskin [17], and Chao [18]. Ahmadi and Goldschmidt [19–22] and Ahmadi [23] used digital simulation and analytical techniques to study the turbulent dispersion of small spherical particles. In [20], motions of particles in a numerically generated two-dimensional isotropic turbulent flow field was studied. Riley and Patterson [24] digitally simulated the particle diffusion process in a three-dimensional isotropic turbulent field. Recently, Maxey [25] studied the gravitational settling of aerosol particles in a random flow field.

Further analyses of motions of an isolated sphere at low Reynolds number in an incompressible viscous fluid were carried out by Arminski and Weinbaum [26], Gitterman and Steinberg [27], and Reeks and Mckee [28]. The results of [28] suggested that the initial conditions could affect the long-term particle diffusivity. Using an approximate analytical method, Rizk and Elghobashi [29] studied motions of particles suspended in a turbulent flow near a plane wall. Maxey and Riley [30] developed a new improved equation of motion for a small rigid particle in an undisturbed flow. Recently, Ounis and Ahmadi [31] simulated the motions of small suspended particles in a digitally generated three-dimensional random Gaussian flow field. Ensemble and time averaging were used for evaluating various statistical properties including the particle mass diffusivity.

In present study, the equation of motion of a small spherical particle is reduced to a linear integro-differential equation. For a homogeneous isotropic flow field, the statistical properties of the random excitations are estimated. The spectral method is used and various particle response statistics are evaluated. Variations of mean-square particle velocity, autocorrelation function and particle diffusivity with particle size, density ratio, flow Reynolds number and particle response time are studied. The results are also compared with the digital simulation and existing experimental data and discussed.

2 Equation of Motion

The equation of motion of a small solid spherical particle in a turbulent field which is referred to as the Basset-Boussinesq-

Contributed by the Fluids Engineering Division for publication in the JOURNAL OF FLUIDS ENGINEERING. Manuscript received by the Fluids Engineering Division January 9, 1989.

Oseen (BBO) equation in dimensionless form is given as

$$\frac{dv_i^{*p}}{dt^*}=\frac{2}{(2S+1)}\frac{Dv_i^{*f}}{Dt^*}\Big|_{x_i^{*p}}$$
$$+\frac{1}{(2S+1)}\frac{d}{dt^*}\left(v_i^{*f}+\frac{1}{40}d^{*2}\nabla^2 v_i^{*f}\right)\Big|_{x_i^{*p}}$$
$$-\frac{36}{(2S+1)}\frac{1}{\mathrm{Re}_l d^{*2}}\left(v_i^{*p}-v_i^{*f}\Big|_{x_i^{*p}}-\frac{1}{24}d^{*2}\nabla^2 v_i^{*f}\Big|_{x_i^{*p}}\right)$$
$$-\frac{18}{(2S+1)}\frac{1}{d^*\sqrt{\pi\mathrm{Re}_l}}\int_{-\infty}^{t^*}\frac{\frac{d}{d\tau^*}\left(v_i^{*p}-v_i^{*f}-\frac{1}{24}d^{*2}\nabla^2 v_i^{*f}\right)\Big|_{x_i^{*p}}}{\sqrt{(t^*-\tau^*)}}d\tau^*$$
$$+\frac{2}{(2S+1)}\frac{K}{d^*\sqrt{\mathrm{Re}_l}}\frac{d_{ij}^{*f}|_{x_i^{*p}}}{[(d_{lk}^{*f}d_{kl}^{*f})|_{x_i^{*p}}]^{1/4}}\left(v_j^{*f}\Big|_{x_i^{*p}}-v_j^{*p}\right)$$
$$+\frac{2(S-1)}{(2S+1)}g_i^*, \tag{1}$$

where v_i^* is the velocity vector, t^* is the time, d^* is the particle diameter, and $K=2.594$ is the constant coefficient of Saffman's lift force. Here, all quantities are nondimensionalized with the aid of a turbulent length macroscale l_o and the root-mean-square fluctuating velocity v_o, and the superscripts f and p refer to the fluid and the particle, respectively. The density ratio S, the Reynolds number Re_l, and the dimensionless acceleration of the body force g^* are defined as

$$S=\frac{\rho^p}{\rho^f},\quad \mathrm{Re}_l=\frac{v_o l}{\nu^f},\quad g_i^*=\frac{g_i l_o}{v_o^2}, \tag{2}$$

where ν is the kinematic viscosity and ρ is the mass density. All the terms on the right-hand side of equation (1) are evaluated at the location of the center of the particle $x_i^{*p}(t^*)$.

In equation (1), d_{ij}^* is the deformation rate tensor which is given by

$$d_{ij}^{*f}=\frac{1}{2}(v_{i,j}^{*f}+v_{j,i}^{*f}), \tag{3}$$

and d/dt^* denotes a time derivative following the moving particle, so that

$$\frac{dv_i^{*f}}{dt^*}=\frac{\partial v_i^{*f}}{\partial t^*}+v_j^{*p}\frac{\partial v_i^{*f}}{\partial x_j^*}, \tag{4}$$

while the fluid acceleration is given as

$$\frac{Dv_i^{*f}}{Dt^*}=\frac{\partial v_i^{*f}}{\partial t^*}+v_j^{*f}\frac{\partial v_i^{*f}}{\partial x_j^*}, \tag{5}$$

Note also that equation (1) is the nondimensional form of the corrected BBO equation as derived by Maxey and Riley [30] and it is modified by including the expression for the Saffman shear lift force [31–36].

The terms on the right-hand side of equation (1) are forces due to the pressure gradient, the acceleration of apparent mass, the Stokes drag, the Basset history term (the drag caused by unsteady motion of the particle in a viscous medium), the Saffman lift force, and the external body forces such as gravity. According to Maxey and Riley [30], equation (1) is valid provided that the quantities $\mathrm{Re}_l d^*|v_i^{*p}-v_i^{*f}|$ and $d^{*2}\mathrm{Re}_l$ are much less than unity. Since we are only concerned with the long-term dispersion, it is assumed that particles have been in the flow for a long time. Hence, the lower limit of the integral in the Basset history term in equation (1) is set equal to $-\infty$. According to Reeks and Mckee [28], for particles released at time zero, the statistics of the initial relative velocities affect the long-term diffusivity. This counter intuitive result which originates from the Basset history term could be avoided by the use of equation (1).

The BBO equation as given by (1) may be restated in a compact form as

$$\frac{dw_i^*}{dt^*}+aw_i^*+\gamma_{ij}(t^*)w_j^*+\eta\int_{-\infty}^{t^*}\frac{\frac{dw_i^*}{d\tau^*}}{\sqrt{(t^*-\tau^*)}}d\tau^*=\beta_i(t^*), \tag{6}$$

where the relative velocity w_i^* is defined as

$$w_i^*=v_i^{*p}-v_i^{*f}|_{x_i^{*p}}. \tag{7}$$

The coefficients $\gamma_{ij}(t^*)$ and $\beta_i(t^*)$ in equation (6) are related to the turbulent velocity field and are given by

$$\gamma_{ij}=\frac{2}{(2S+1)}\left(\frac{\partial v_i^{*f}}{\partial x_j^*}+\frac{K}{d^*\sqrt{\mathrm{Re}_l}}\frac{d_{ij}^{*f}}{(d_{lk}^{*f}d_{kl}^{*f})^{1/4}}\right)\Big|_{x_i^{*p}}, \tag{8}$$

Nomenclature

a = inverse particle response time
b = function of ω
d = particle diameter
d_{ij} = deformation rate tensor
D = diffusivity
D_{ij} = diffusivity tensor
E = three-dimensional energy spectrum
g = acceleration of the body force
k = wave number
K = constant of lift force
l_i = length scale
l_o = turbulent length scale
Re_l = flow Reynolds number
R_{ij} = velocity autocorrelation function
sgn = sgnum function
S = density ratio
$S_{v_iv_j}$ = power spectrum function
t = time
v = velocity vector
v_o = root-mean-square fluctuating velocity
w = relative velocity
x = position vector
$\alpha, \alpha_1, \alpha_2$ = functions of ω
β_i = random forcing function
γ_{ij} = random coefficient
γ_o = constant coefficient
δ_{ij} = Kronecker delta
η = Basset's force coefficient
λ_f = longitudinal Taylor microscale
ν = kinematic viscosity
ρ = mass density
τ = time
τ_p = particle relaxation time
ω = frequency

Superscripts

f = refers to fluid
p = refers to particle
$^\circ$ = zero size particle
* = dimensionless quantity

Other Notation

d/dt = time derivative following the moving particle
D/Dt = time derivative following the fluid particle
∇^2 = Laplacian
$|\ |$ = absolute value
$\langle\ \rangle$ = expected value overbar = Fourier transform

and

$$\beta_i(t^*)=\left[\frac{2(1-S)}{2S+1}\frac{dv_i^{*f}}{dt^*}+\frac{3}{2(2S+1)\mathrm{Re}_l}\nabla^2 v_i^{*f}\right.$$
$$\left.+\frac{d^{*2}}{40(2S+1)}\frac{d\nabla^2 v_i^{*f}}{dt^*}+\eta\frac{d^{*2}}{24}\int_{-\infty}^{t^*}\frac{\frac{d\nabla^2 v_i^{*f}}{d\tau^*}}{\sqrt{(t^*-\tau^*)}}d\tau^*\right]_{x_i^{*p}}. \quad (9)$$

In equation (6)

$$a=\frac{1}{\tau_p}=\frac{36}{(2S+1)\mathrm{Re}_l d^{*2}},\quad \eta=\frac{18}{(2S+1)d^*\sqrt{\pi\mathrm{Re}_l}}, \quad (10)$$

with τ_p being the particle response time.

Equation (6) is a set of coupled integro-differential equations with random coefficient γ_{ij} and random forcing function β_i. The exact general solution to (6) is not available. However, in the absence of a mean velocity gradient and in an isotropic flow field for small particles with high density ratio, the effects of coupling coefficient $\gamma_{ij}(t)$ may be insignificant. (In Appendix A, it is also shown that the least-square error estimates for the coupling term are negligible.) When γ_{ij} is neglected equation (6) reduces to

$$\frac{dw_i^*}{dt^*}+aw_i^*+\eta\int_{-\infty}^{t^*}\frac{\frac{dw_i^*}{d\tau^*}}{\sqrt{(t^*-\tau^*)}}d\tau^*=\beta_i(t^*), \quad (11)$$

which is a linear integro-differential equation in the Lagrangian frame of particle and can be solved by the spectral method. The approximation used in the derivation of (11) will be partially justified by comparison of the predicted particle response statistics with the simulation data which were obtained for the exact equation of motion.

When the Faxen terms in equation (9) are neglected, equation (11) becomes identical to the one used by Hinze [15]. In the subsequent sections, it will be shown that the inclusion of the Faxen terms leads to a more reasonable variation of turbulent diffusivity with particle diameter.

3 Fourier Analysis

Using the definition given in Appendix B, the Fourier transform of equation (11) leads to

$$\overline{w_i^*}(\omega)=\frac{\overline{\beta}_i(\omega)}{\left(a+\eta\sqrt{\frac{|\omega|}{2\pi}}\right)+i\left(\omega+\eta\sqrt{\frac{|\omega|}{2\pi}}\mathrm{sgn}(\omega)\right)}. \quad (12)$$

Here sgn is the sgnum function and $\overline{\beta}_i(\omega)$ is given by

$$\overline{\beta}_i(\omega)=[\alpha_1(\omega)+i\alpha_2(\omega)]\overline{v_i^{*f}}(\omega), \quad (13)$$

where $\alpha_1(\omega)$ and $\alpha_2(\omega)$ are given as

$$\alpha_1(\omega)=-5\frac{d^{*2}}{\lambda_f^2}\left(\frac{3}{(2S+1)\mathrm{Re}_l d^{*2}}+\frac{\eta}{12}\sqrt{\frac{|\omega|}{2\pi}}\right),$$

$$\alpha_2(\omega)=2\frac{(1-S)\omega}{(2S+1)}$$
$$-\frac{5}{4}\frac{d^{*2}}{\lambda_f^2}\left(\frac{\omega}{5(2S+1)}+\frac{\eta}{3}\sqrt{\frac{|\omega|}{2\pi}}\mathrm{sgn}(\omega)\right). \quad (14)$$

In the derivation of (13) and (14), it is assumed that the $\nabla^2 v_i^{*f}$ term in equation (9) may be approximated as

$$\nabla^2 v_i^{*f}|_{x_i^{*p}}=-\frac{10}{\lambda_f^2}v_i^{*f}|_{x_i^{*p}},\quad \text{(no sum on } i\text{)}, \quad (15)$$

where λ_f is the nondimensional longitudinal Taylor microscale. (The derivation of equation (15) is described in Appendix A.)

Taking Fourier transform of equation (7) and using (12) and (14), one finds

$$\overline{v_i^{*p}}(\omega)=H(\omega)\overline{v_i^{*f}}(\omega), \quad (16)$$

where the system function $H(\omega)$ is defined as

$$H(\omega)=\frac{\alpha(\omega)+i(\alpha_2(\omega)+b(\omega))}{a+\eta\sqrt{\frac{|\omega|}{2\pi}}+i\left(\omega+\eta\sqrt{\frac{|\omega|}{2\pi}}\mathrm{sgn}(\omega)\right)}, \quad (17)$$

where the coefficients $\alpha(\omega)$ and $b(\omega)$ are defined as

$$\alpha(\omega)=\left(1-\frac{5}{12}\frac{d^{*2}}{\lambda_f^2}\right)\left(a+\eta\sqrt{\frac{|\omega|}{2\pi}}\right),$$

$$b(\omega)=\omega+\eta\sqrt{\frac{|\omega|}{2\pi}}\mathrm{sgn}(\omega). \quad (18)$$

Equations (16)–(18) relate the particle velocity to the fluid velocity in the Fourier domain.

The power spectrum of particle velocity is then given by

$$S_{v_i^{*p}v_i^{*p}}(\omega)=|H(\omega)|^2 S_{v_i^{*f}v_i^{*f}}(\omega),\quad \text{(no sum on } i\text{)}, \quad (19)$$

where $S_{v_i^{*f}v_i^{*f}}(\omega)$ is the Lagrangian power spectrum of fluid velocity as is seen by the particle. Using (17), it follows that

$$S_{v_i^{*p}v_i^{*p}}(\omega)$$
$$=\frac{\alpha^2(\omega)+(\alpha_2(\omega)+b(\omega))^2}{\left(a+\eta\sqrt{\frac{|\omega|}{2\pi}}\right)^2+\left(\omega+\eta\sqrt{\frac{|\omega|}{2\pi}}\mathrm{sgn}(\omega)\right)^2}S_{v_i^{*f}v_i^{*f}}(\omega). \quad (20)$$

The mean-square particle and fluid velocities are now given as

$$\begin{cases}\langle v_i^{*p}v_i^{*p}\rangle=\int_0^\infty S_{v_i^{*p}v_i^{*p}}(\omega)d\omega,\\ \qquad\qquad\qquad\qquad\text{(no sum on } i\text{)},\\ \langle v_i^{*f}v_i^{*f}\rangle=\int_0^\infty S_{v_i^{*f}v_i^{*f}}(\omega)d\omega,\end{cases} \quad (21)$$

where the angular bracket '$\langle\ \rangle$' stands for the expected value (ensemble average). When the spectral density of the flow field is known, equations (20) and (21) may be used for evaluating the power spectrum and the mean-square particle velocity.

4 Turbulence Mass Diffusivity

The particle turbulent diffusivity tensor is given by

$$D_{ij}^p=\int_o^\infty R_{ij}^p(\tau^*)d\tau^*, \quad (22)$$

where R_{ij}^p is the autocorrelation function defined as

$$R_{ij}^p(t^*)=\langle v_i^{*p}(t^*)v_j^{*p}(t^*+\tau^*)\rangle. \quad (23)$$

Noting from Appendix B that

$$S_{v_i^{*p}v_j^{*p}}(\omega)=\frac{1}{\pi}\int_{-\infty}^{\infty}e^{-i\omega\tau^*}R_{ij}^p(\tau^*)d\tau^*, \quad (24)$$

equation (22) may be restated as

$$D_{ij}^p=\frac{\pi}{2}S_{v_i^{*p}v_j^{*p}}(0). \quad (25)$$

Using equation (20) in (25), the expression for the relative mass diffusivity follows, i.e.,

$$\frac{D^p}{D^o} = \left[1 - \frac{5}{12}\left(\frac{d^*}{\lambda_f}\right)^2\right]^2, \tag{26}$$

where D^o denotes the mass diffusivity of fluid (zero size) particles and for an isotropic field

$$\begin{cases} D_{ij} = 0 \text{ for } i \neq j \\ D_{11} = D_{22} = D_{33} = D, \end{cases} \tag{27}$$

are used. Equation (26) shows the effect of particle size on mass diffusivity. Since the present analysis is restricted to small particles, the second term in (26) is always less than unity. Thus, for an unbounded homogeneous isotropic turbulent flow field, the relative mass diffusivity decreases with an increase in the dimensionless particle diameter d^*. Equation (26) also indicates that the turbulent microscale λ_f plays an important role for the degree of the influence of d^* on the relative mass diffusivity. It also follows that the drag force and its Faxen correction only affect the particle diffusivity. In particular, in agreement with [19], the Basset force has no effect on the (long term) particle diffusivity in the stationary limit.

The effect of Faxen correction on particle diffusivity has not been considered in the earlier studies. This additional drag which is generated due to nonuniformity in the flow field is dissipative in nature. It is also independent of the instantaneous particle velocity. A simplified energy balance analysis reveals that there is an additional energy dissipation due to Faxen drag. As a result a finite size particle is exposed to only part of the fluid fluctuation energy and its diffusivity becomes less than that of a fluid particle.

The Taylor microscale may generally be related to the macroscale l_o. Using the expression given by Hinze [15] for an isotropic turbulence, in dimensionless form we find

$$\lambda_f = \sqrt{\frac{30}{A\mathrm{Re}_l}}, \tag{28}$$

where the coefficient $A = 0.764$ was suggested in [37]. Using (28), equation (26) becomes

$$\frac{D^p}{D^o} = \left[1 - \frac{d^{*2}\mathrm{Re}_l}{94.24}\right]^2. \tag{29}$$

This equation gives the explicit expression for the relative mass diffusivity as a function of d^* and Re_l. Equation (31) suggests that the relative diffusivity is independent of the density ratio. However, the particle relaxation time is directly proportional to the density and hence the time needed to approach the stationary condition limit is strongly affected by S.

5 Results and Discussion

To analyze the particle response statistics, an expression for the Lagrangian spectral density of the flow field as seen by the particle is needed. In [31], for simulating the particle diffusion process, a pseudo turbulent Gaussian velocity field with a three dimensional energy spectrum

$$E(k) = 16(2/\pi)^{1/2}k^{1/2}e^{-2k^2}, \tag{30}$$

was numerically generated. The exact BBO equation as given by (1) was integrated to generate a large number of particle trajectories. Ensemble and time averaging techniques were used and various particle velocity response statistics were evaluated. For evaluating the mean-square particle velocities 300 particle trajectories and 800 time steps were used. Thus, the statistical error is expected to be rather small. In this section, the simulation data of [31] are compared with the present analytical results.

Although the Lagrangian and the Eulerian spectra are generally different, an acceptable method for relating the two is not available (Lumley [38]). However, the data of Snyder and Lumley [12] showed that the corresponding autocorrelations are indistinguishable within the experimental scatter. Here it is assumed that the Lagrangian fluid velocity spectrum as it is seen by the particle is approximately equal to the Eulerian spectrum. From equation (30), it follows that

$$S_{v_i^{*f}v_j^{*f}}(\omega) = \frac{2}{\pi}e^{-\omega^2/\pi}\delta_{ij}. \tag{31}$$

Equation (31) provides an approximate expression for the Lagrangian fluid velocity spectrum.

Using equations (20) and (31), for different values of density ratio, fluid Reynolds number and dimensionless particle diameter, the particle power spectra are calculated. The fast Fourier transform (FFT) routine from the IMSL library is used and the particle autocorrelation functions under a variety of conditions are evaluated. The resulting spectral and correlation functions are used to determine the corresponding mean-square particle velocities and the relative mass diffusivities as given by equations (23) and (29).

Analysis of a reduced BBO equation which includes only the Stokes drag (e.g., [15], [31]) shows that the turbulent diffusivity and other statistical properties of particle depend on the particle response time. In the following, the presented results are correlated with τ_p whenever feasible.

Figure 1 displays variations of the particle relative power spectra ($S_{v_i^{*p}v_i^{*p}}/S_{v_i^{*f}v_i^{*f}}$) with frequency for $\mathrm{Re}_l = 100$, $S = 5$ and different dimensionless particle diameters. It is observed that the amplitude of the relative power spectrum decreases sharply as the particle size increases. For example, when $\omega = 50$, the amplitude of the relative spectrum drops from 0.95 to about 0.75 or 0.2 when d^* increases from 0.01 to 0.02 or 0.05. It is also observed that the particle power spectrum approaches that of the fluid when the particles become very small. Figure 1 also shows that the particle relative power spectra decreases with increasing frequency and tends to vanish for large values of ω. The rate of decrease is strongly affected by the particle size.

Figure 2 compares the particle correlation coefficient $(R^p(\tau)/R^p(0))$ for τ_p of 0.022 and 0.044 with the experimental data of Snyder and Lumley [12]. In that experimental study, the correlation coefficients for corn pollen, solid glass, and copper particles for a range of particle relaxation times between 0.022 and 0.05 were measured. The results of digital simulations of [31] are also shown in this figure for comparison. Figure 2 shows that the predicted particle correlation coefficients are in reasonable agreement with the simulation results and the experimental data.

Variations of the mean-square (MS) particle velocity $\langle v_i^{*p}v_i^{*p}\rangle/\langle v_i^{*f}v_i^{*f}\rangle$ with d^* for different density ratio S as predicted by the present analysis are shown in Fig. 3 by solid

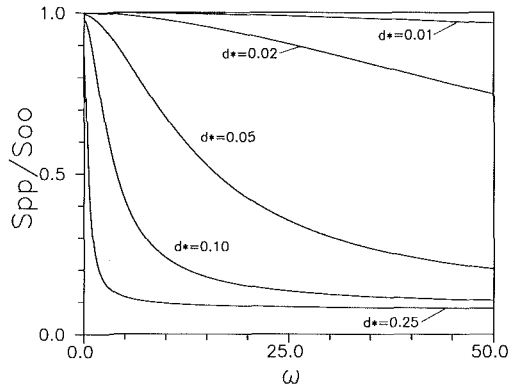

Fig. 1 Variation of the relative particle power spectra with frequency for rel = 100, $S = 5$ and different d

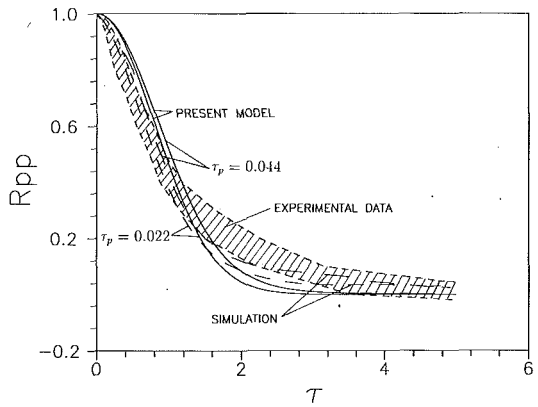

Fig. 2 Comparisons of predicted particle autocorrelation functions with experimental data of Snyder and Lumley [36] and simulation results of [29]

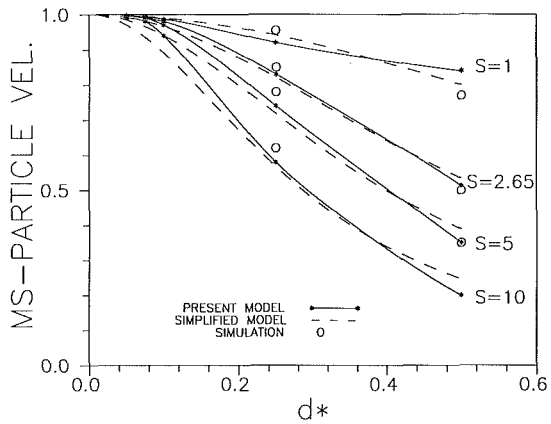

Fig. 3 Variations of relative mean-square particle velocity with dimensionless diameter *d*

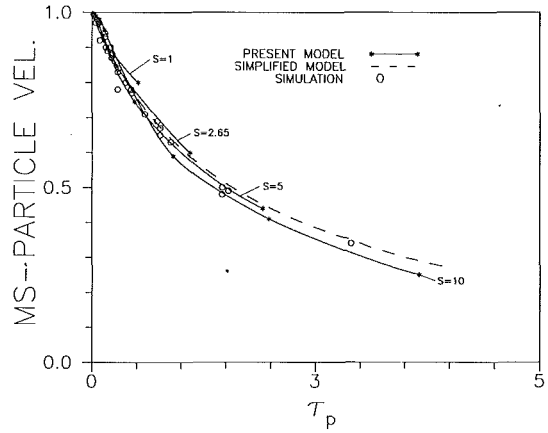

Fig. 4 Variation of mean-square particle velocity with particle response time

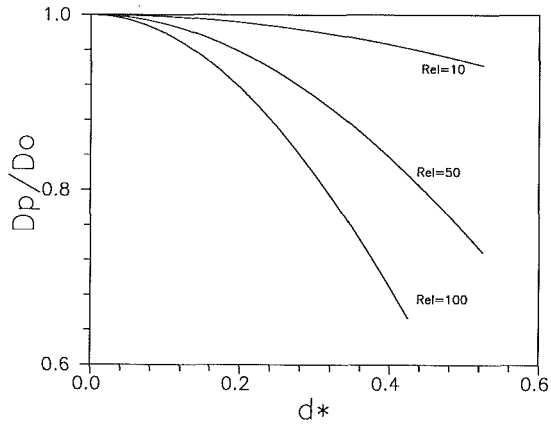

Fig. 5 Variation of relative difficulty with *d* for different Reynolds number Rel

lines. The prediction of the simplified model of [15, 31] along with the digital simulation results are also shown in this figure. It is observed that the agreement between the present and earlier theoretical predictions and the digital simulation results is generally good. Figure 3 shows that the mean-square particle velocity decreases with an increase in particle size or density ratio. As the density ratio approaches unity or particle size becomes small, the MS particle velocity fluctuation becomes comparable to that of the flow field.

Figure 4 displays variations of the mean-square particle velocity with particle relaxation time for different density ratios. The predictions of the simplified model as well as the digital simulation results of [31] are also plotted in this figure for comparison. It is observed that the mean-square particle velocity decreases rapidly with an increase in particle response time. As the density ratio increases, the mean-square particle fluctuation velocity decreases. Although the general agreement between the theoretical predictions and simulation results is reasonably good, certain differences are observed. The simplified model of [15, 31] leads to a single curve which implies that the MS-particle velocity is only a function of τ_p. The present model, however, predicts distinct curves for different density ratios which are slightly decreasing with S. This latter behavior seems to agree with the digital simulation results of [31].

It should be emphasized that the simulation results of [31] were obtained by using the particle equation of motion including the exact expressions for various forces. The present formulation, however, involves several approximate least mean-square error estimates for the Faxen terms and the Saffman lift force as described in Appendix A. The favorable agreement of the predicted mean-square particle velocities with the simulation data of [31] as shown in Figs. 3 and 4 partially justifies the approximation used.

Figure 5 shows variations of the relative mass diffusivity with the dimensionless particle diameter d^* for different Reynolds numbers as predicted by equation (29). It is observed that D^p/D^o decreases as particle size increases. The rate of decrease of the relative mass diffusivity is also a sensitive function of the flow Reynolds number and becomes more rapid as Re_l increases. The prediction of the simplified model of [15, 31] is not shown in this figure since it leads to the unrealistic results of $D^p = D^o$ for any d^*, Re_l or S.

The predicted variations of the relative diffusivity with the particle response time τ_p for $S = 1$ and $S = 2.65$ are shown by solid lines in Fig. 6. The digital simulation results of [31] and the experimental data of Yuu et al. [9], Snyder and Lumley [12] and Calabrese et al. [39] are also reproduced in this figure for comparison. For $S = 1$, the relative mass diffusivities as predicted by equation (29) appear to be in good agreement with the digital simulation results. Although, the experimental data which are for particle diffusivity in nearly isotropic turbulent flows are somewhat scattered, the qualitative agreement with theoretical predictions is reasonable. As noted before, the simplified model of [15, 31] leads to $D^p/D^o = 1$ and is incapable of predicting the proper decrease of the relative mass diffusivity with τ_p.

6 Conclusion

In this study, motions of small spherical particles in a random flow field are studied. The spectral method is used and

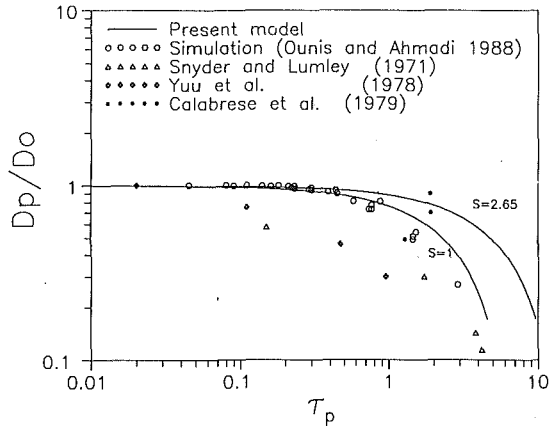

Fig. 6 Comparison of theoretical, simulated, and experimental relative diffusivity

analytical expressions for particle response statistics are developed. Variations of the relative mass diffusivity and mean-square particle velocity with particle size, density ratio and relaxation time are studied. Based on the present results, the following conclusions may be drawn:

1) The relative mass diffusivity decreases with an increase in particle size or relaxation time.

2) The mean-square particle velocity decreases with an increase in particle size, density or relaxation time.

3) For a small relaxation time, particles turbulent diffusivity approaches that of the fluid.

4) The Faxen terms in the BBO equation affects the long-term particle diffusivity.

5) The predicted mean-square particle velocities and mass diffusivities are in reasonable agreement with the digital simulation results and the available experimental data. In particular the decrease of relative mass diffusivity with particle size or relaxation time is properly predicted by the model.

While the favorable agreement between the analytical and simulation results, in part, justifies the assumption made, there are a number of questions left unanswered. For example, a systematic method for relating the Lagrangian fluid spectrum as is seen by the particle to that of the Eulerian field needs to be developed. The effect of the lift force in the presence of strong mean shear field must be addressed. However, providing answers to these questions are left for future studies.

Acknowledgment

This study is partially supported by the NSF Grant MSM-8714687, and the New York State Science and Technology Foundation through the Center for Advanced Material Processing (CAMP) of Clarkson University. The use of Cornell University supercomputer is gratefully acknowledged.

References

1 Taylor, G. I., "Diffusion by Continuous Movements," *Proc. Land. Math. Soc. 20*, Series 2, 1921, pp. 192–212.

2 Tchen, C. M., Ph.D. thesis, University of Delft, Martinus Nijhoff, Hague, 1947.

3 Basset, A. B., *Treatise on Hydrodynamics*, Deighton, London, Vol. 2, 1888, pp. 285–297.

4 Boussinesq, J., *Theory Analytique de la Chaleur*, L'Ecole Polytechnique, Paris, Vol. 2, 1903, p. 224.

5 Oseen, C. W., *Hydrodynamik*, Leizig, 1927, p. 132.

6 Corrsin, S., and Lumley, J. L., "On the Equation of Motion for a Particle in Turbulent Fluid," *Appl. Sci. Res.*, Vol. 6, 1956, pp. 114–116.

7 Goldschmidt, V. M., and Eskinazi, S., "Two-Phase Turbulent Flow in Plane Jet," ASME *Journal of Applied Mechanics*, Vol. 33, 1966, pp. 735–747.

8 Houserholder, M. K., and Goldschmidt, V. M., "Turbulent Diffusion and Schmidt Number of Particles," *ASCE J. Eng. Mech.*, Vol. 6, 1969, pp. 1345–67.

9 Yuu, S., Yasukouchi, Y., Hirosawa, Y., and Jotaki, T., "Particle Turbulent Diffusion in a Dust Laden Round Jet," *AIChE Journal*, Vol. 22, No. 3, 1978, pp. 509–519.

10 Singametti, S. R., "Diffusion of Sediment in a Submerged Jet," *ASCE J. Hydraul. Div.*, 1966, pp. 153–168.

11 Chuang, S. C., "Turbulent Diffusion of Small Gas Bubbles in an Axisymmetric Water Jet," Ph.D. thesis, Purdue University, Aug. 1970.

12 Snyder, W. H., and Lumley, J. L., "Some Measurements of Particle Velocity Autocorrelation Functions in Turbulent Flow," *J. Fluid Mech.*, Vol. 48, 1971, pp. 41–71.

13 Shirazi, M. A., "On the Motion of Small Particle in a Turbulent Field," Ph.D. thesis, University of Illinois, Urbana, 1967.

14 Levich, V. G., and Kuchanov, S. I., "Motion of Particle Suspended in Turbulent Flow," *Soviet Physics Doklady*, Vol. 12, 1967, pp. 546–548.

15 Hinze, J. O., *Turbulence*, Second Edition, McGraw-Hill, New York, 1975.

16 Soo, S. L., and Peskin, R. L., "Statistical Distribution of Solid Phase in Two Phase Turbulent Motion," Project SQUID Tech. Report PR-80-R (ONR), Princeton University, 1958.

17 Peskin, R. L., "Diffusivity of Small Suspended Particles in Turbulent Fluid," Presented at the National Meeting AIChE, Baltimore, 1962.

18 Chao, B. T., "Turbulent Behavior of Small Particles in Dilute Suspension," *Osterreich Ingenieur Archiv*, Vol. 18, 1964, pp. 7–21.

19 Ahmadi, G., and Goldschmidt, V. W., "Motion of Particle in a Turbulent Fluid—The Basset History Term," ASME *J. Appl. Mech.*, Vol. 38, 1971, pp. 561–563.

20 Ahmadi, G., and Goldschmidt, V. W., "Analytical Prediction of Turbulent Dispersion of Finite Size Particles," Purdue University, Technical Report FMTR-70-3, March 1970. (Also G. Ahmadi, Ph.D. thesis, Purdue University, 1970).

21 Ahmadi, G., and Goldschmidt, V. W., "Dynamic Simulation of the Turbulent Diffusion of Small Particles. Hydrotransport 1," First International Conference on the Hydraulic Transport of Solids in Pipes, University of Warwick, BHRA, Cranfield, Bedford, England, 1970.

22 Ahmadi, G., and Goldschmidt, V. W., "Kinematic Computer Simulation of the Turbulent Dispersion of Neutrally Buoyant Particles," *Developments in Mech.*, Vol. 5, Proc. 11th Midwestern Mech. Conf., 1969, pp. 201–210.

23 Ahmadi, G., "Motion of Particles in a Turbulent Fluid-on the Effect of Rotation on the Dispertion Coefficient," Pneumotransport 2, Second International Conference on the Pneumatic Transport of Solids in Pipes, BHRA, Cranfield, Bedford, England, 1973, pp. C1:1–C1:14.

24 Riley, J. J., and Patterson, G. S., Jr., "Diffusion Experiments With Numerically Integrated Isotropic Turbulence," *Phys. Fluids*, Vol. 17, 1974, pp. 292–297.

25 Maxey, M. R., "The Gravitational Settling of Aerosol Particles in Homogeneous Turbulence and Random Flow Fields," *J. Fluid Mech.*, Vol. 174, 1987, pp. 441–445.

26 Arminski, L., and Wienbaum, S., "Effect of Waveform and Duration of Impulse on the Solution to the Basset-Langevin Equation," *Phys. Fluids*, Vol. 22, 1979, pp. 404–411.

27 Gitterman, M., and Steinberg, V., "Memory Effects in the Motion of a Suspended Particle in a Turbulent Fluids," *Phys. Fluids*, Vol. 23, 1980, pp. 2154–2160.

28 Reeks, M. W., and Mckee, S., "The Dispersive Effect of Basset History Forces on Particle Motion in a Turbulent Flow," *Phys. Fluids*, Vol. 27, 1984, pp. 1573–1582.

29 Rizk, M. A., and Elghobashi, S. E., "The Motion of a Spherical Particle Suspended in a Turbulent Flow Near a Plane Wall," *Phys. Fluids*, Vol. 20, 1985, pp. 806–817.

30 Maxey, M. R., and Riley, J. J., "Equation of Motion for a Small Rigid Sphere in a Nonuniform Flow," *Phys. Fluids*, Vol. 26, 1983, pp. 883–889.

31 Ounis, H., and Ahmadi, G., "Motions of Small Rigid Spheres in a Simulated Random Velocity Field," Clarkson University, Report No. MIE-164, 1988. Also *ASCE J. Eng. Mech. Div.* (In press).

32 Saffman, P. G., "The Lift on a Small Sphere in a Slow Shear Flow," *J. Fluid Mech.*, Vol. 22, 1965, pp. 385–398.

33 Drew, D. A., "Constitutive Equations for Multiphase Mixture of Fluids," *Int. J. Multiphase Flow*, Vol. 10, 1976, pp. 273–305.

34 Ahmadi, G., "A Continuum Theory for Two Phase Media," *Acta Mech.*, Vol. 44, 1982, pp. 299–317.

35 McTique, D. F., Givler, R. C., and Nunziato, J. W., "Rheological Effects of Nonuniform Particle Distribution in Dilute Suspensions," *J. Rheology*, Vol. 30, 1986, pp. 1053–1076.

36 Ahmadi, G., and Ma, D., "A Thermodynamical Formulation for Dispersed Multiphase Turbulent Flows, Part 1: Basic Theory," Clarkson University, Report No. MIE-143, 1987. Also *J. Multiphase Flows* (In press).

37 Wolfshtein, M., "The Velocity and Temperature Distribution in One Dimensional Flow with Turbulence Augmentation and Pressure Gradient," *Int. J. Heat Mass Transfer*, Vol. 12, 1969, pp. 301–308.

38 Lumley, J. L., "Some Problems Connected with the Motion of Small Particles in Turbulent Fluid," Ph.D. thesis, The Johns Hopkins University, Baltimore, 1957.

39 Calabrese, R. V., and Middleman, S., "The Dispersion of Discrete Particles in Turbulent Fluid Field," *AIChE Journal*, Vol. 25, 1979, pp. 1025–1035.

40 Tennekes, H., and Lumley, J. L., *A First Course in Turbulence*, The MIT Press, Cambridge, Massachusetts, 1972.

APPENDIX A

Estimation of Parameters

In order to evaluate the statistics of the Faxen correction $\nabla^2 v_i^{*f}|_{x_i^{*p}}$ term in equation (9), it is assumed that $\nabla^2 v_i^{*f}|_{x_i^{*p}} = -(1/l_i^2) v_i^{*f}|_{x_i^{*p}}$ (no sum on i) where the length scale l_i may be estimated by minimizing the mean-square error. This leads to

$$l_i^{-2} = -\frac{\langle v_i^{*f} \nabla^2 v_i^{*f} \rangle}{\langle v_i^{*f} v_i^{*f} \rangle}, \tag{32}$$

or

$$l_i^{-2} = -\frac{\dfrac{\partial^2}{\partial x_j^2}\left\langle \dfrac{v_i^{*f} v_i^f}{2} \right\rangle}{\langle v_i^f v_i^{*f} \rangle} + \frac{\left\langle \dfrac{\partial v_i^{*f}}{\partial x_j} \dfrac{\partial v_i^{*f}}{\partial x_j} \right\rangle}{\langle v_i^f v_i^{*f} \rangle}, \tag{33}$$

where '$\langle\ \rangle$' denotes the expected value. Note that in equations (32) and (33), the summation on i is dropped and all quantities are evaluated at x_i^{*p}.

For a homogeneous and isotropic turbulent flow field

$$\frac{\partial^2}{\partial x_j^2}\left\langle \frac{v_i^{*f} v_i^{*f}}{2} \right\rangle = 0, \tag{34}$$

and according to [15, 23]

$$\left\langle \frac{\partial v_i^{*f}}{\partial x_k^*} \frac{\partial v_j^{*f}}{\partial x_l^*} \right\rangle = \frac{2v^2}{\lambda_f^2}\left(2\delta_{kl}\delta_{ij} - \frac{1}{2}\delta_{il}\delta_{jk} - \frac{1}{2}\delta_{jl}\delta_{ik}\right), \tag{35}$$

where λ_f is the nondimensional turbulent longitudinal microscale and v is the mean square of the fluctuating velocity.

Using (34) and (35) in (33) it follows that

$$\overline{l_i^{-2}} = \frac{\left\langle \dfrac{\partial v_i^{*f}}{\partial x_i^*} \dfrac{v_i^{*f}}{\partial x_i^*} \right\rangle}{\langle v_i^{*f} v_i^{*f} \rangle} = \frac{10}{\lambda_f^2}. \tag{36}$$

A similar attempt may be made to include the effect of the coupling term in equation (11). For example, $\gamma_{ij} w_j$ may be replaced by $\gamma_o w_i$, where γ_o is a constant. Minimizing the mean-square error, one finds

$$\gamma_o = \frac{\langle w_i \gamma_{ij} w_j \rangle}{\langle w_i w_i \rangle}. \tag{37}$$

Here, w_i is proportional to the fluid and particle velocities while γ_{ij} is essentially a velocity gradient term. According to [15, 40], these are, to first order of approximation, independent processes. Therefore,

$$\gamma_o = \frac{\langle w_i w_j \rangle \langle \gamma_{ij} \rangle}{\langle w_i w_j \rangle}. \tag{38}$$

However, $\langle \gamma_{ij} \rangle = 0$, which implies, $\gamma_o = 0$. Thus, the least-square error estimate does not produce a meaningful correction to equation (11). In [23], use of a perturbation method to include the coupling effects was suggested.

APPENDIX B

Fourier Transform

The power spectrum $S(\omega)$ and the autocorrelation function $R(\tau)$ are related by Fourier transform and its inverse as

$$S(\omega) = \frac{1}{\pi}\int_{-\infty}^{+\infty} e^{-i\omega\tau^*} R(\tau^*) d\tau^*, \tag{39}$$

$$R(\tau^*) = \frac{1}{2}\int_{-\infty}^{+\infty} e^{i\omega\tau^*} S(\omega) d\omega. \tag{40}$$

The mean-square (variance) then becomes

$$R(0) = \frac{1}{2}\int_{-\infty}^{+\infty} S(\omega) d\omega = \int_0^{\infty} S(\omega) d\omega. \tag{41}$$

It follows that

$$\frac{1}{\pi}\int_{-\infty}^{+\infty} e^{-i\omega\tau^*} \frac{U(\tau^*)}{\sqrt{\tau^*}} d\tau^* = \frac{1}{\pi}\int_0^{\infty} \frac{e^{-i\omega\tau^*}}{\sqrt{\tau^*}} d\tau^* = \frac{1 - i\,\mathrm{sgn}(\omega)}{\sqrt{2\pi|\omega|}}. \tag{42}$$

Analysis of Venturi Performance for Gas-Particle Flows

F. D. Shaffer
United States Department of Energy,
Pittsburgh Energy Technology Center,
Pittsburgh, PA 15236

R. A. Bajura
Energy and Water Research Center,
West Virginia University,
Morgantown, WV 26506

In recent years, use of the venturi for measurement of gas-particle flows has received considerable attention. The technology for the venturi as a single-phase flowmeter has matured to the point that application is routine. Much more research, however, is required to establish the venturi as an acceptable gas-particle flowmeter. The first part of this paper consists of a discusssion of the basic principles of venturi pressure-flow performance for gas-particle flows. This is followed by a description of the experimental calibration of a venturi for measurement of gas-particle flows with particle-to-gas mass-loading ratios up to 35. Next, a modified Stokes number is presented and shown to improve correlation of venturi pressure-flow data. Finally, the predictions of a model presented by Doss are compared with the pressure-flow data of the venturi calibration performed in this work. The Doss model provides good predictions of venturi differential pressures for particle-to-gas mass-loading ratios less than ten but tends to overpredict the differential pressure, by as much as 45 percent, for particle-to-gas mass-loading ratios above 10.

1 Introduction

Differential-pressure flow-metering elements, such as the venturi, nozzle, and orifice, are routinely applied for metering the flow of a single-phase gas or liquid. These flow elements provide a low-cost, simple, accurate, and reliable flow-metering device. Their theory is well developed, and standard designs and application principles have been established [1]. The success and advantages associated with differential pressure flow-metering elements for single-phase flows have generated interest in their use as gas-particle flow-metering devices. This interest has resulted in several experimental and theoretical studies over the past forty years.

The first attempt to develop a differential-pressure gas-particle flow meter was completed by Carlson et al. in 1948 [2]. A nozzle-orifice combination was used to meter the flow of air and pulverized coal in small-diameter (0.019–0.100 m) lines. High accuracy was achieved in the measurement of both coal and air flow rates. Following the successful small-scale testing, the meter was applied to several large-scale (0.3–0.5 m) lines from 1955 to 1960 [3]. Although it performed well on small-diameter lines, the meter did not perform well when applied to the larger diameter lines owing to poor correlation between differential pressure and coal flow rate.

The work of Carlson et al. was followed by that of Farbar in 1952 [4] and 1953 [5], who investigated both the venturi and the nozzle as gas-particle flowmeters. Farbar's works was followed by that of Antikayn in 1956 [6], Barth et al. in 1957 [7], and Graczyk in 1961 [8], who also studied the venturi as a gas-particle flowmeter. During the past ten years, Crowe et al. [9–15] have conducted several experimental studies of the venturi as a gas-particle flowmeter. All of the above-mentioned studies reported accurate measurement of the gas and particle flow rates with small-diameter lines (0.017–0.100 m).

Crowe and Lee [12] identified the dimensionless parameters, such as the Stokes number and the particle-to-gas mass-loading ratio, necessary for correlation of pressure-flow data for gas-particle flows through venturis. Such dimensionless parameters are essential for the design and scaling of venturis for varied operating conditions. Crowe and Lee [12] have suggested that an inadequate understanding of these dimensionless parameters may have caused the failure of the meter developed by Carlson et al. when applied to larger diameter lines.

In this paper, the Stokes number is modified to more accurately account for variations in venturi geometry. Venturi calibration data from this and other studies are employed to show that the modified Stokes number improves correlation of pressure-flow data. The modified Stokes number should prove to be a valuable tool for the design of venturi geometries.

In addition to the experimental studies mentioned above, several theoretical models have been developed to predict the pressure-flow performance of venturis for gas-particle flows [16–20]. The most common modeling approach consists of numerical integration of one-dimensional, differential forms of the conservation of mass and momentum equations. This type of model has been reviewed by Gidaspow [21]. A model presented by Doss [18] is adapted for comparison with the experimental results of this work because an attempt was made in the Doss model to account for the effect of particle-particle collisions.

The experimental aspects of this work include the design and calibration of a venturi for metering gas-particle flows. This experimental work provides new data for particle-to-gas mass-loading ratios from 10 to 35: the maximum particle-to-

Contributed by the Fluids Engineering Division for publication in the JOURNAL OF FLUIDS ENGINEERING. Manuscript received by the Fluids Engineering Division October 22, 1987.

gas mass-loading ratio reported in previous studies is 10. The venturi design and experimental calibration facility are described, and the experimental results are employed in the evaluation of the modified Stokes number and the Doss model predictions.

2 Basic Concepts

For single-phase gas flow in a venturi, the differential pressure between the inlet and throat is primarily due to gas acceleration. The pressure-flow relationship can be accurately predicted via the Bernoulli equation with corrections for viscous effects. When particles are entrained in the gas flow through a venturi, the particles also undergo an acceleration between the inlet and throat because of the drag force of the gas on the particles. The kinetic energy acquired by the particles through the venturi is supplied by the gas and results in an increased as differential pressure through the venturi. This increase in differential pressure is proportional to the particle flow rate and thus can be used to meter the particle flow rate.

The success enjoyed with prediction of venturi pressure-flow performance for single-phase gas flows has not yet been achieved for gas-particle flows. The ability to predict the pressure-flow performance of venturis is crucial to optimize their performance for gas-particle flows. Two means that can be used to predict venturi pressure-flow performance for gas-particle flows are discussed in this section: empirical correlation of pressure-flow data, and numerical solution of one-dimensional, differential forms of the conservation of mass and momentum equations.

2.1 Empirical Correlation of Venturi Pressure-Flow Data. Empirical correlation of venturi pressure-flow data provides one means to estimate venturi pressure-flow performance. Dimensional analyses have shown that venturi pressure-flow data should be correlated in terms of three dimensionless parameters: the mixture-to-gas pressure ratio, $\Delta P_{g-p}/\Delta P_g$; the Stokes number, St; and the particle-to-gas mass-loading ratio, Z [12]. Thus, the following functional relationship can be used to represent venturi pressure-flow data for gas-particle suspension flow in venturis:

$$\Delta P_{g-p}/\Delta P_g = f(ST, Z) \tag{1}$$

The mixture-to-gas pressure ratio, $\Delta P_{g-p}/\Delta P_g$, is a measure of the increase in differential pressure owing to the presence of particles in the flow. The magnitude of the increase in differential pressure (or mixture-to-gas pressure ratio) is proportional to the degree to which the particles accelerate through the venturi, and to the concentration of particles in the gas. The Stokes number, St, is a measure of the degree to which particles accelerate in a venturi; and the loading ratio, Z, is a measure of the concentration of particles in the gas.

The experimental data of this and other studies [4, 6–8, 12] have shown that a linear relationship exists between the mixture-to-gas pressure ratio and the loading ratio for a constant Stokes number condition. This linear relationship may be expressed as

$$\Delta P_{g-p}/\Delta P_g = mZ + 1.0 \tag{2}$$

The line slope, m, indicates the sensitivity of the venturi differential pressure to the particle flow rate. The line slope, m, is termed the pressure ratio parameter by Lee and Crowe [12] but will be referred to as the venturi sensitivity in this paper. Given the additional relationship of equation (2), only two dimensionless parameters—the Stokes number, St, and the line slope, m—are needed to correlate venturi pressure-flow data. The Stokes number, and the relationship between venturi sensitivity and the Stokes number, are discussed below.

2.1.1 The Stokes Number. For this work, the Stokes number is defined specifically for a venturi. The Stokes number is a measure of the degree to which a specific particle can accelerate in a given gas flow in a given venturi. The Stokes number is defined as the ratio of the time *required* for particle acceleration (aerodynamic response time) to the time *available* for particle acceleration in a venturi (gas residence time). The aerodynamic response and the gas residence times are discussed in detail below.

Aerodynamic Response Time. The particle aerodynamic response time gives an indication of the time required for particle acceleration when a particle is subjected to an increase in gas velocity. The particle aerodynamic response time is approximated by considering the case of a spherical particle ac-

Nomenclature

d = particle diameter
D = line diameter
ΔP_g = differential pressure for gas only
ΔP_{g-p} = differential pressure for gas-particle mixture
D_t = venturi throat diameter
f = indicates a functional relationship
F_g = gas drag force
F_{ki} = forces acting on a particle of size i
F_{p-p} = particle-particle collision force
g = gravitational acceleration
i = indicates a particle size range
L = characteristic length
L_v = length of venturi variable-area section
L_t = length of venturi throat up to throat pressure tap
m = venturi sensitivity
M_p = particle mass flow rate
M_{pi} = particle mass flow rate for particles of size i
M_g = gas mass flow rate
n = number of particle size ranges
P = gas pressure
$\Re$ = particle Reynolds number
St = stokes number
t = time
U = line gas velocity
U_t = gas velocity in venturi throat
U_v = gas velocity in variable-area section of a venturi
V = particle velocity
V_i = velocity for particles of size i
V_∞ = particle terminal velocity
x = axial distance in flow direction
Z = particle-to-gas mass-loading ratio
β = throat-to-inlet diameter ratio
ρ_g = gas density
ρ_p = particle density
ρ_{pi} = particle density for particles of size i
Φ = angle of inclination from the horizontal
ϕ_p = particle volume concentration
ϕ_{pi} = volume concentration of particles of size i
ϕ_g = gas volume concentration
τ_g = gas residence time
τ_p = aerodynamic response time
τ_t = throat gas residence time
τ_v = variable area section residence time
τ_w = wall shear stress
μ = gas viscosity

celerating from rest in a constant-velocity, free-stream gas flow. With the assumption of Stokes drag, a force balance of a particle results in the following differential equation:

$$\frac{dV}{dt}=\frac{18}{\Re}\left(\frac{\rho_g}{\rho_p}\right)\frac{(U-V)^2}{d} \tag{3}$$

with a solution:

$$V(t)=V_\infty\,[1-e^{(-t/\tau_p)}] \tag{4}$$

The aerodynamic response time is given by

$$\tau_p=\frac{\rho_p d^2}{18\mu} \tag{5}$$

Gas Residence Time. The gas residence time is a measure of the time available for particle acceleration between two specified points in a venturi. The two specified points are usually a pressure tap location just upstream of the venturi inlet, and a pressure tap location in the venturi throat. The gas residence time will be defined as the time required for a *gas particle* to flow between two specified points in a venturi (a *"gas particle"* will be defined as a particle moving with a velocity equal to that of the gas). The gas residence time in a venturi is approximated by

$$\tau_g=L/U \tag{6}$$

The characteristic length, L, is usually taken to be the throat diameter, D_t [12].

Based on the definitions listed above for the aerodynamic response time and gas residence time, the Stokes number for a venturi is given by

$$\mathrm{St}=\frac{\rho_p d^2 U}{18\mu D_t} \tag{7}$$

2.1.2 Relationship Between Stokes Number and Sensitivity. The general relationship between the sensitivity and the Stokes number is that sensitivity decreases with increasing Stokes numbers. For low Stokes number conditions, particle inertia is relatively low, so particles undergo a large acceleration in the venturi. For the extreme case of Stokes numbers approaching zero, the particles move with a velocity equal to the gas velocity; and consequently, the sensitivity approaches one. In this case, the differential pressure of the venturi responds as if the gas-particle flow were a single fluid with a density equal to the average density of the gas-particle mixture. For high Stokes numbers, particle inertia is relatively high, so particles undergo less acceleration in the venturi. For the extreme case of Stokes numbers approaching infinity, the particles undergo negligible acceleration through the venturi. The differential pressure of the venturi approaches that of the gas flow alone, i.e., the sensitivity, m, approaches zero.

2.2 Numerical Prediction of Venturi Pressure-Flow Performance. Numerical modeling provides a versatile and potentially more accurate tool for predicting venturi pressure-flow performance. The most common type of numerical model applied to predict venturi pressure-flow performance is based on one-dimensional, differential forms of the conservation of mass and momentum equations. The primary assumptions are steady, adiabatic flow with ideal gas behavior. The use of such models for prediction of gas-particle duct flows has been reviewed by Gidaspow [21]. The basic governing equations for this type of model are listed below:

Gas Continuity

$$\frac{d}{dx}(\rho_g\phi_g U)=0 \tag{8}$$

Particle Continuity

$$\frac{d}{dx}(\rho_p\phi_p V)=0 \tag{9}$$

Gas-Particle Mixture Momentum

$$\rho_g\phi_g U\frac{dU}{dx}+\rho_p\phi_p V\frac{dV}{dx}= -\frac{dP}{dx}+\frac{4\tau_w}{D}+(\rho_p\phi_p+\rho_g\phi_g)g\sin\Theta \tag{10}$$

These equations can also be written for a gas flow containing a range of particle sizes by dividing the particles into a number of discrete size ranges, with each size range represented by a mean particle diameter. Each particle size range is then considered as a separate phase. Equations (9) and (10) are rewritten for each particle size range (phase), with each size range denoted by a subscript i, where $i = 1, 2, \ldots, n$.

Particle Continuity for Each Discrete Size Range

$$\frac{d}{dx}(\rho_{pi}\phi_{pi}V_i)=0 \tag{11}$$

Gas-Particle Mixture Momentum

$$\rho_g\phi_g U\frac{dU}{dx}+\sum_{i=1}^{n}\rho_{pi}\phi_{pi}V_i\frac{dV_i}{dx}= -\frac{dP}{dx}+\frac{4\tau_w}{D}+(\rho_p\phi_p+\rho_g\phi_g)g\sin\Theta \tag{12}$$

Equations (8), (11), and (12) comprise a set of $2n+1$ equations with $2n+2$ unknowns: U, V_{pi}, ϕ_{pi}, and p. Therefore, another equation is required to close the set of equations. Gidaspow has reviewed and categorized the closure equations found in the literature [21]. The equation used for closure is usually a momentum balance on the particle phase. The particle phase momentum equation can be represented in a generalized form as

$$M_{pi}V_i\frac{dV_i}{dx}=\sum_{k=1}^{1}F_{ki} \tag{13}$$

where the forces, F_k, are those acting on the particles such as gas drag and gravity.

Equations (8) and (11–13) comprise a system of $2n+2$ first-order differential equations, which, with appropriate initial conditions, can be numerically integrated to yield the values of U, V_{pi}, ϕ_{pi}, and P at any point through a venturi.

3 Experimental

In this work, a venturi was calibrated for measurement of the flow rates of spent fluid cracking catalyst (FCC) particles and air. The dimensions of the venturi are shown in Fig. 1. The venturi geometry was designed to minimize obstruction of the particle flow. The throat-to-inlet diameter ratio was made large, $\beta = 0.9$, and the inlet angle was made low to reduce the angle of impaction of particles on the walls of the converging section. With the throat-to-inlet diameter ratio and the inlet angle set to minimize obstruction of the particle flow, the throat length was extended to increase the time available for particle acceleration. This increased the sensitivity of the venturi to the particle flow.

An experimental facility was constructed to calibrate the venturi [22, 23]. The main function of the facility was to create controlled gas and particle flow rates through a vertical section and to record the corresponding differential pressures across the venturi and other flow elements. The layout of the experimental facility is shown in Fig. 2.

The FCC particles were spherical and had a mean diameter of 61 ± 2 μm and a density of 2.3 ± 0.05 g /cc. The size distribution of the FCC particles is given in Table 1. The line

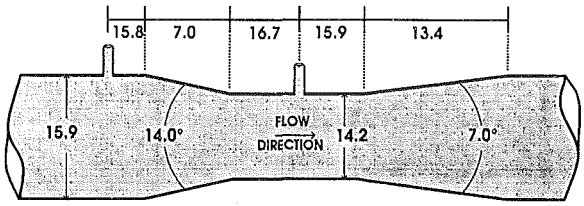

Fig. 1 Dimensions (in mm) of the venturi calibrated in this work

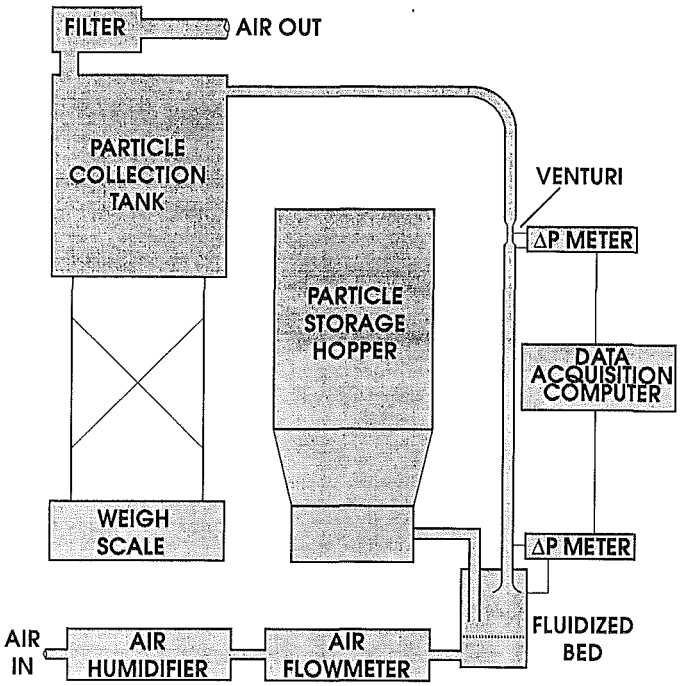

Fig. 2 Schematic of gas-particle flow facility used for venturi calibration

pressure of the air was maintained at 6.4 psig, and the relative humidity of the air was kept above 75 percent to mitigate electrostatic charging. The flow rate of the FCC was measured by weighing the accumulation of particles in a capture tank over a known period of time. The airflow rate was measured with a rotometer using the manufacturer's calibration and correction factors for pressure and temperature. The humidified air and FCC fed into a fluidized-bed mixing zone and then elutriated as a gas-particle suspension into a vertical pipe section. The FCC particles collected in the solids capture tank and returned to the powder-feeding system. The air exited the system through a filter.

Fifty test conditions were completed during calibration of the venturi. The experimental conditions covered gas flows from 1.5 to 7.2 g/s and particle flows up to 55 g/s. These flow ranges correspond to line gas line velocities from 5 to 25 m/s with particle-to-gas mass-loading ratios up to 35.

The main source of experimental uncertainty in the calibration was the rotometer used to measure the gas flow rate. The uncertainty of the rotometer was ±2 percent of the full scale (±0.15 g/s). The maximum uncertainty in the measurement of the particle flow rate was ±0.6 percent of the particle flow rate. The differential pressure ranged from 1.5 to 25 cm H_2O, and the measurement uncertainty was ± 0.025 cm H_2O.

4 Analysis of Venturi Pressure-Flow Performance

In this section, experimental results of the venturi calibration are presented. Then two means of predicting venturi pressure-flow performance—empirical correlation of pressure-flow data and numerical modeling—are discussed and evaluated in light of the experimental results of this work.

Table 1 FCC particle size distribution

Particle Diameter (μm)	% Volume
0–20	1.5
20–25	4.7
25–32	10.8
40– 51	22.4
51–64	20.2
51– 64	20.2
64–81	12.8
81–102	12.8
102–128	2.9
128–161	1.1
161–203	0.1

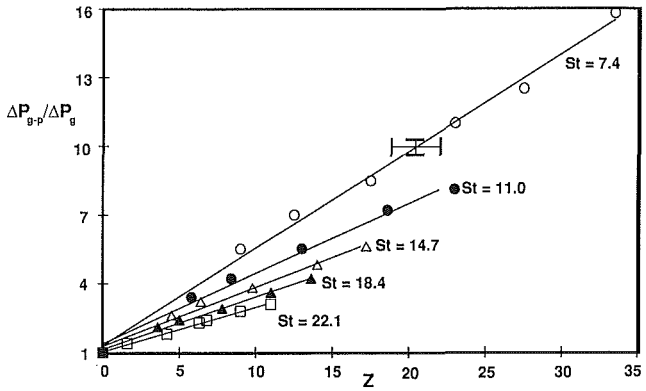

Fig. 3 Venturi calibration data for constant Stokes number groups with loading ratios above 10

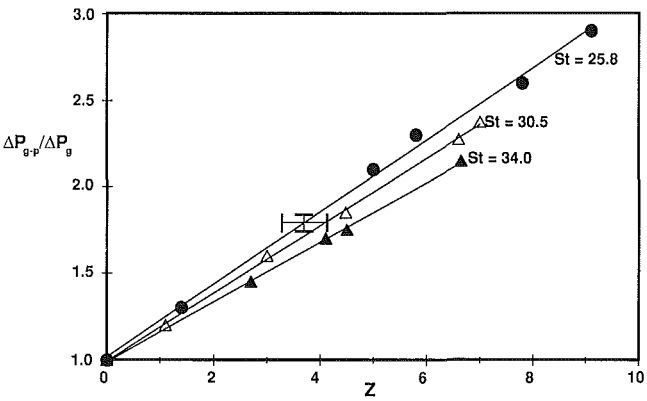

Fig. 4 Venturi calibration data for constant Stokes number groups with loading ratios less than 10

4.1 Experimental Results. The pressure-flow data from the venturi calibration are shown in Figs. 3 and 4. The pressure-flow data are represented in terms of the dimensionless parameters of equation (2): the venturi differential pressure is represented in terms of the mixture-to-gas pressure ratio, $\Delta P_{g-s}/\Delta P_g$, and the flow rates are represented in terms of the loading ratio, Z. The data are grouped according to constant Stokes number conditions. Data for constant Stokes number groups including loading ratios above 10 are shown in Fig. 3. Constant Stokes number groups with all loading ratios less than 10 are shown in Fig. 4.

Previous venturi calibrations [4, 6–15] have been limited to loading ratios less than 10. These calibrations have shown that a linear relationship exists between the mixture-to-gas pressure

Table 2(*a*) Dimensions of calibrated venturis used for Stokes number sensitivity correlation in Figure 5.

Source	Diameter Ratio	Inlet Angle	Line Diameter (mm)	Throat Length (mm)	Gas & Particle Properties*	Symbol**
Crowe and Lee [12]	0.5	21.0°	52.5	6.0	2,3,5	◆
Crowe and Lee [12]	0.6	21.0°	52.5	6.0	2,3,5	□
Crowe and Lee [12]	0.7	2.10°	52.5	6.0	2,3,5	◇
Payne and Crowe [9]	0.6	8.0°	52.5	6.0	1,2,5,6	●
Payne and Crowe [9]	0.6	4.0°	52.5	6.0	1,2,4,6	■
Shaffer [23]	0.9	14.0°	15.9	16.7	4	○

*See Table 2(*b*)
**See Figs. 5 and 6

Table 2(*b*) Particle and gas properties for venturi calibrations listed in Table 2(*a*)

No.	Particle	Mean Diameter (μm)	Density (kg/ms^3)	Shape	Gas
1	Small Glass Beads	23	4750	Spherical	Air
2	Microballons	29	325	Spherical	Air
3	Glass Beads	36	2900	Spherical	Air
4	Fluid Cracking Catalyst	61	2300	Spherical	Air
5	Ballotini Impact Balls	65	2420	Spherical	Air
6	Glass Beads	92	4446	Spherical	Air

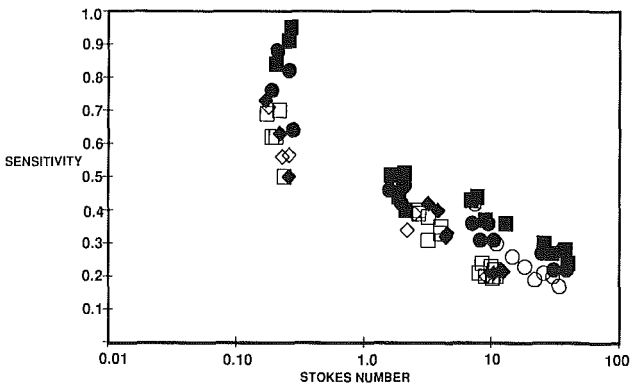

Fig. 5 Correlation of venturi sensitivity with Stokes number. Symbol legend and experimental conditions are listed in Tables 2(*a*) and 2(*b*)

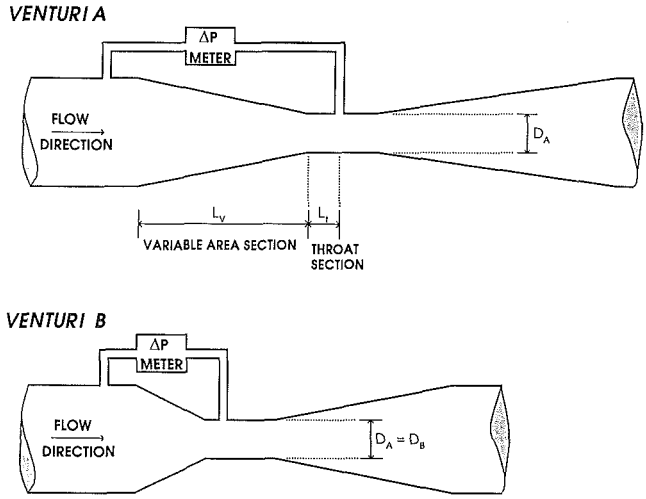

Fig. 6 Two venturis with equal thorat diameters but dissimilar geometries

for loading ratios less than 10 for a constant Stokes number condition. The data produced in this work indicate that this linear relationship extends to loading ratios of at least 35.

4.2 Correlation of Pressure-Flow Data by Sensitivity and Stokes Number. To test the ability of the sensitivity and Stokes number to correlate pressure-flow data, data from this and several other venturi calibrations were correlated in terms of the sensitivity and Stokes number. The sources of the venturi calibration data and the experimental conditions are listed in Tables 2(*a*) and 2(*b*). The correlation of the venturi pressure-flow data is shown in Fig. 5. Although the sensitivity data may show a general trend of decreasing with increasing Stokes number, the correlation is poor (correlation coefficient of 0.82). This is particularly true for Stokes numbers between 0.1 and 0.3, where the sensitivity data are scattered from 0.5 to 0.98. One reason for this poor correlation may be the failure of the Stokes number to account for variations in venturi geometry, such as inlet angle and throat length. To test this postulate, the Stokes number is modified in the next section to account for variations in venturi geometry. The venturi sensitivity data will then be recorrelated in terms of the modified Stokes number.

4.2.1 Modification of the Stokes Number. The Stokes number will be modified by deriving a characteristic length term that provides a better approximation of gas residence times for venturis with dissimilar geometries. The throat diameter as a characteristic length is suitable only for venturis with similar geometries and can lead to poor correlation of pressure-flow data for venturis with dissimilar geometries. For example, consider the two venturis shown in Fig. 6. Both venturis have equal throat diameters but different inlet angles. If each venturi is subjected to the same gas velocity, then the calculated residence time, based on the throat diameter, is equal for both venturis. However, the actual time required for a *"gas particle"* to flow between the pressure taps for venturi A is much greater than that for venturi B.

To derive a characteristic length parameter that provides a better approximation of gas residence times for venturis with dissimilar geometries, the gas residence time will be redefined. It will be defined as the sum of two gas residence times: a residence time for the variable area section, τ_v, and a residence time for the throat section of venturi, τ_t. The variable area and throat sections are shown in Fig. 6 for venturi A. The gas

residence time for the variable area section will be defined as the ratio of the length of the variable area section L_v, to the average gas velocity in the variable area section, U_v. The gas residence time for the variable are section is given by

$$\tau_v = \frac{L_v}{U_v} = \frac{2L_v}{U_t + U} \tag{14}$$

The gas residence time for the throat section is simply

$$\tau_t = \frac{L_t}{U_t} \tag{15}$$

Adding equations (14) and (15) gives the total gas residence time for the venturi:

$$\tau_g = \frac{2L_v}{U_t + U} + \frac{L_t}{U_t} \tag{16}$$

By use of the conservation of mass relationship for incompressible flow, the throat velocity can be written in terms of the line velocity:

$$\tau_g = \left[\left(\frac{\beta^2}{1+\beta^2} \right) 2L_v + \beta^2 L_t \right] / U \tag{17}$$

Thus, a new characteristic length is now defined as

$$L = \left(\frac{\beta^2}{1+\beta^2} \right) 2L_v + \beta^2 L_t \tag{18}$$

and modified Stokes is

$$\mathrm{St} = \frac{\rho_p d^2 U}{18\mu \left[\left(\frac{\beta^2}{1+\beta^2} \right) 2L_v + \beta^2 L_t \right]} \tag{19}$$

It should be noted that an assumption of incompressible flow (Mach No. < 0.3) was made in the derivation of the modified Stokes number.

The sensitivity data have been recorrelated in terms of the modified Stokes number and are shown in Fig. 7. The modified Stokes number shows improved correlation of sensitivity data (correlation coefficient of 0.94) over the previous Stokes number (correlation coefficient of 0.82). The sensitivity data can be represented by the following curve fit:

$$\begin{aligned} m &= \mathrm{St}^{-0.135} e^{(-0.8\mathrm{St}^{0.151})} && \text{for St} > 0.03 \\ m &= 1 && \text{for St} < 0.03 \end{aligned} \tag{20}$$

Equation (20) may be used to estimate venturi sensitivity. Given the experimental flow conditions from which equation (20) is derived, it is recommended only for inlet angles < 21 deg.

This relationship between the sensitivity and modified Stokes number may be used as a guide for the initial design of venturi geometries. To minimize obstruction of the particle flow and erosion of the venturi dimensions, it is recommended that the inlet angle be made small, less than the ASME standard of 21 deg for single-phase flow metering [1], and that the throat diameter should be made large. With these constraints placed on the inlet angle and throat diameter, the venturi throat can be extended to achieve a desired sensitivity.

4.3 Comparison of Doss Model Prediction With Pressure-Flow Data. In this section, a model for gas-particle flow through venturis presented by Doss [18] is briefly described. The capability of the model to predict pressure-flow data is tested by comparing the model predictions with the experimental data of this work. The Doss model is employed here as an example of models based on one-dimensional forms of the conservation of mass and momentum equations, with the assumptions of steady, adiabatic flow with ideal gas behavior. This type of one-dimensional model is described in section 2.2.

Doss has used a particle phase momentum balance equation that is similar to what Gidaspow categorizes as Case B [21]. The major difference with the Doss model is that a particle-particle collision force term developed by Soo [24] is added to the particle phase momentum equation. The particle phase momentum equation used by Doss may be represented, in a generalized form, by

$$M_{pi} V_i \frac{dV_i}{dx} = (F_g)_i + (F_{p-p})_i + F_{\text{gravity}} \tag{21}$$

The results of the comparison of the Doss model differential-pressure predictions with the experimental data of this work are summarized by plotting the prediction error, $(\Delta P_{\text{predicted}} - \Delta P_{\text{measured}}) / \Delta P_{\text{measured}}$, versus the loading ratio (see Fig. 8). The Doss model predictions of differential pressure show good agreement with the experimental data for loading ratios less than 10. However, as the loading ratio increased above 10, the Doss model tended to increasingly overpredict the experimental data by as much as 45 percent for loading ratios above 25.

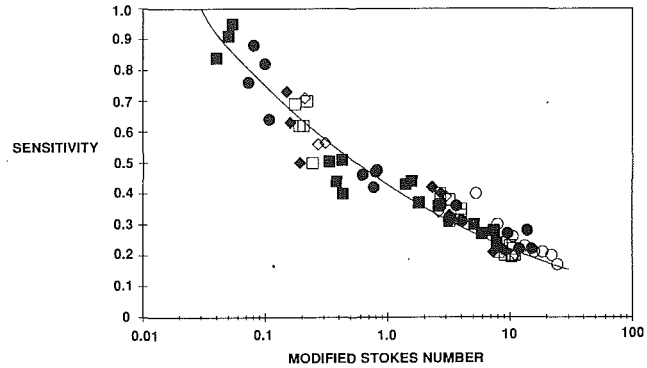

Fig. 7 Correlation of venturi sensitivity with modified Stokes number. Symbol legend and experimental conditions are given in Tables 2(*a*) and 2(*b*)

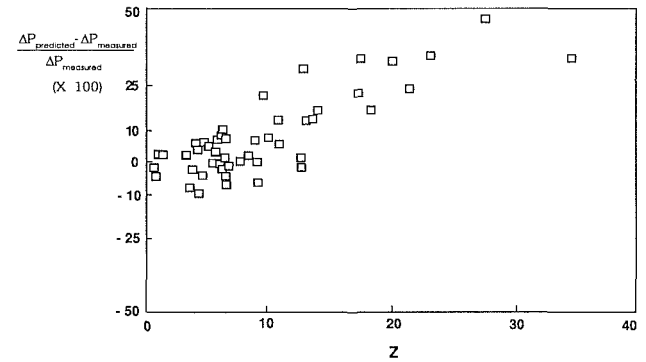

Fig. 8 Comparison of Doss model predictions with the experimental data of this work

6 Conclusion

In this paper, the basic concepts of venturi pressure-flow performance for gas-particle flows have been discussed. The results of the calibration of a venturi for gas-particle flows have been presented, the Stokes number has been modified to more accurately account for venturi geometry, and the predictions of a model by Doss have been evaluated.

An experimental facility was constructed to calibrate a venturi for measurement of air and FCC particles. In this venturi calibration, the particle flow rate was increased to yield loading ratios up to 35. Previous venturi calibrations were limited to loading ratios less than 10. The experimental data of this work indicate that a linear relationship between the mixture-to-gas pressure ratio and the loading ratio extends to loading ratios of 35.

The Stokes number was modified to more accurately account for variations in venturi geometry. The experimental data of this work and others were employed to show that the modified Stokes number provides improved corrrelation of venturi sensitivity data. The modified Stokes number may be used as a guide for the design of venturi geometries.

The predictions of a model by Doss were compared with the experimental data of this work. It was found that, for loading ratios up to 10, the Doss model provides good predictions of differential pressure, within ± 10 percent of the measured value. However, for loading ratios above 10, the Doss model tended to overpredict the experimental values of differential pressure by as much as 45 percent.

Disclaimer

Reference in this report to any specific commercial product, process, or service is to facilitate understanding and does not necessarily imply its endorsement or favoring by the United States Department of Energy.

References

1 Fluid Meters, Their Theory and Application, 6th ed., ASME, 1971.

2 Carlson, H. M., Frazier, P. M., and Engdahl, R. B., "Meter for Flowing Mixtures of Air and Pulverized Coal," Trans. ASME, Feb. 1948.

3 Saltsman, R. D., "The BCR Gas-Solids Flow Meter," *Proc. Inst. Gas Tech. and Bureau of Mines Symp. on Pneumatic Transport of Solids, Info. Circ. No. 8314*, Morgantown, W. Va, 1965.

4 Farbar, L., "The Venturi as a Meter for Gas-Solid Mixtures," Trans. ASME, July 1952.

5 Farbar, L., "Metering the Flow of Powdered Solids In Gas-Solid Mixtures," *Engr. and Proc. Dev.*, Vol. 44, No. 12, Dec. 1953.

6 Antikayn, P. A. "Measurement of Pulverized Coal Flow in an Air Stream," *Teploenergetika*, Vol. 3, No. 12, 1956.

7 Barth, W., Nagel, R., and Van Waveran, K., "Neues Verfahren zur Bestimmungder Augenblick Gefotderten Gutmengen in Lutftstrom Pneumatscher Forderung," *Chemie. Eng. Techn.*, Vol. 29, 1957.

8 Graczyk, C., "The Application of the Venturi tube to the Measurement of the Coal Dust Flow Transported by Air," *Acta Imeko*, 1961, pp. 251-275.

9 Crowe, C. T., and Payne, A. L., "Metering the Mass Flow of Gas-Solid Mixtures in Non-Standard Venturi Configurations," *Proc. Symp. on Instrumentation and Control for Fossil Energy Processes*, ANL-80-62, 1980.

10 Crowe, C.T., and Payne, A. L. "Optimization of the Inlet and Outlet Geometry for Metering the Mass Flow of Gas-Solid Mixtures in a Venturi, "*Proc. Symp. on Instrumentation and Control for Fossil Energy Processes*, ANL-81-62, 1981.

11 Crowe, C. T., Payne, A. L., Weber, M., and Plank, D., "Mass Flow Measurements of Gas-Solid Suspensions Using Venturimeters with Light Attenuation," *Proc. Symp. on Instrumentation and Control for Fossil Energy Processes*, ANL-82-62, 1982.

12 Lee, J., and Crowe, C. T., "Scaling Laws for Metering the Flow of Gas-Particle Suspensions Through Venturis, ASME JOURNAL OF FLUIDS ENGINEERING, Vol. 104, Mar. 1982.

13 Crowe, C. T., and Payne, A. L., "An Experimental Study of Gas-Solid Mixture Flows in a Venturi," *Proc. ASME Winter Annual Metering*, 1984.

14 Crowe, C. T., and Payne, A. L., "An Experimental Study of Gas-Solid Mixtures Flows in a Venturi," *Proc. 30th Int. Instrumentation Symp.*, 1984.

15 Crowe, C. T., "Extended Throat Venturimeter," *Proc. Cavitation and Multiphase Flow Forum*, ASME Fluids Engineering Meeting, 1987.

16 Neilson, J. H., and Gilchrist, A., "An Analytical and Experimental Investigation of the Velocities of Particles Entrained by the Gas Flow in Nozzles," ASME JOURNAL OF FLUID MECHANICS, Vol. 33, 1968.

17 Crowe, C. T., and Sharma, M. P., "Novel Physico-Computational Model for Quasi One-Dimensional Gas-Particle Flows," ASME JOURNAL OF FLUIDS ENGINEERING, Vol. 100, 1978.

18 Doss, E. D., Analysis and Application of Solid-Gas Flow Inside a Venturi with Particle Interactions, *Int. J. Multiphase Flow*, Vol. 11, No. 4, 1985.

19 Chung, M. K., Sung, H. J., and Lee, K. B., "Computational Study of Turbulent Gas-Particle Flow in a Venturi, *Proc. AIAA/ASME 4th Fluid Mechanics*, Plasma Dynamics and Lasers Conf., May 1986.

20 Kmiec, A., "An Analytical Study of Flow in Gas/Solid Injectors, Pneumatech 3, Third Int. Conf. on Pneumatic Conveying Tech., Mar. 1987.

21 Gidaspow, D., "Two-Phase Flow Pressure Drops," *China-U.S. Seminar on Two-Phase Flow and Heat Transfer*, May 1984.

22 Shaffer, F. D., "A Differential Pressure Based Gas-Solid Flow Metering Method Applicable to the Intensively Circulating Fluidized Bed System," M.S. thesis, West Virginia Univ., 1986.

23 Shaffer, F. D., and Bajura, R. A., "A Gas-Solid Flow Metering Based on Differential Pressure Measurements," *Proc. AIAA/ASME 4th Fluid Mechanics, Plasma Dynamics and Lasers Conf.*, May 1986.

24 Soo, S. L., *Fluid Dynamics of Multiphase Systems*, Blaisdell Press, 1967.